



**UNIVERSITA' DELLA CALABRIA**

Dipartimento di Chimica e Tecnologie Chimiche

**Scuola di Dottorato**

“Bernardino Telesio”

**Indirizzo**

Mesofasi e Materiali Molecolari

*Con il contributo di*

MIUR Fondo giovani

**CICLO**

XXVI

**Novel molecular materials for photo/electro conversion based on Palladium and Iridium organometallic complexes**

**Settore Scientifico Disciplinare CHIM/03**

**Direttore:** Prof. Roberto Bartolino

**Coordinatore:** Prof. Carlo Versace

**Supervisor:** Prof. Mauro Ghedini

Dott. Nicolas Godbert

**Dottoranda:** Dott.ssa Andreea Ionescu

*Andreea Ionescu*



# **Nuovi materiali molecolari per la foto/elettro conversione basati su complessi organometallici di Palladio e Iridio**

## *Sommario*

Questo lavoro di ricerca è dedicato allo sviluppo di nuovi materiali molecolari basati su complessi ciclo metallati di Pd(II) e di Ir(III) per la foto/elettro conversione.

Negli ultimi quindici anni, al fine di ottenere dispositivi più flessibili, più leggeri e più facilmente processabili, sono stati studiati principalmente materiali a base organica.

Tali materiali presentano però, proprio a causa della loro natura organica, molteplici svantaggi, tra i quali scarsa qualità delle interfacce formate, limitata stabilità chimico-fisica in fase di funzionamento del dispositivo, difficile trasporto di carica, scarso assorbimento nel visibile e basse efficienze di luminescenza. Al fine di migliorare le prestazioni finali dei dispositivi elettro-ottici, è stata introdotta una nuova classe di materiali che utilizza come specie attive i composti organometallici.

Nell'ambito di questo lavoro di tesi, sono stati sintetizzati nuovi complessi organometallici di Pd(II) e Ir(III) e ne sono state studiate le proprietà chimico-fisiche alla base dello sviluppo di materiali efficienti per la foto/elettro conversione.

La prima parte del lavoro di tesi ha riguardato la preparazione di complessi per la conversione dell'energia solare.

In particolare sono stati sintetizzati e caratterizzati nuovi complessi fotoconduttori ciclopalladati di Rosso Nilo, contenenti basi di Schiff opportunamente funzionalizzate come leganti ancillari. Inizialmente si è scelto di utilizzare il colorante Rosso Nilo come legante ciclo metallante per le sue ottime proprietà di assorbitore di luce visibile.

Il suo utilizzo ha inoltre comportato, nei complessi ottenuti, anche la separazione fisica su scala molecolare degli orbitali di frontiera HOMO e LUMO.

In particolare i due orbitali risultano essere prevalentemente localizzati su due diversi frammenti molecolari. Tale separazione induce un efficiente processo di fotogenerazione che è alla base delle ottime proprietà di fotoconduzione osservate per questa classe di composti in un ampio intervallo di lunghezze d'onda.

Per finalizzare l'utilizzo di complessi ciclopalladati di Rosso Nilo a specifiche applicazioni optoelettroniche, sono stati introdotti opportuni gruppi funzionali sia sul legante ciclo metallante che sul legante ancillare.

In particolare i nuovi gruppi funzionali hanno permesso di :

- i) indurre proprietà mesomorfiche caratterizzate da un ampio grado di ordine in un grande intervallo di temperature e di ottenere così una nuova classe di metallomesogeni fotoconduttori;
- ii) aumentare la solubilità dei complessi preparati rendendo possibile il loro utilizzo unitamente al PC<sub>61</sub>BM, nella costruzione di celle solari ad eterogiunzione dispersa;
- iii) preparare, tramite il processo di elettropolimerizzazione, film sottili fotoconduttori di elevata qualità su elettrodi modificati;
- iv) poter ancorare i complessi sintetizzati a substrati di TiO<sub>2</sub> e costruire celle solari di tipo *Dye Sensitized* (DSSCs).

La seconda parte del lavoro di tesi, ha invece riguardato, la sintesi e la caratterizzazione fotofisica ed elettrochimica di complessi di Ir(III) per lo sviluppo di dispositivi elettroluminescenti.

Sebbene esista in letteratura un elevato numero di esempi di complessi cationici di Ir(III) solamente pochi complessi anionici di Ir(III) sono stati descritti finora. Inoltre, i pochi esempi riportati, contengono leganti ancillari monodentati che rendono tali complessi chimicamente instabili all'interno di dispositivi elettroluminescenti.

Al fine di ampliare la classe di composti anionici di Ir(III) esistenti e di migliorarne la stabilità chimica, sono stati sintetizzati nuovi complessi anionici aventi leganti ancillari bidentati di tipo catecolato e orotato. E' stata inoltre preparata e caratterizzata una nuova serie di "soft salt" di Ir(III) contenenti i nuovi complessi anionici ottenuti accoppiati ad opportuni complessi cationici di Ir(III) già noti in letteratura.

Sono stati infine preparati e caratterizzati nuovi complessi luminescenti neutri di Ir(III) elettropolimerizzabili. Utilizzando tali complessi sono stati anche ottenuti film sottili elettrogenerati di alta qualità.

University of Calabria



Department of Chemistry

---

*Doctorate School of Science and Technique "Bernardino Telesio"*

*Mesophases and Molecular Materials - XXVI Cycle*

Ph.D. Thesis

**Novel molecular materials  
for photo/electro conversion based on  
Palladium and Iridium organometallic complexes**

Supervisors

Prof. Mauro Ghedini

Dr. Nicolas Godbert

Ph.D. Candidate

Andreea Ionescu

---

December 2013



## Table of Contents

<b>Thesis Overview</b> .....	1
------------------------------	---

### **1<sup>st</sup> Part. Novel molecular materials based on Pd(II) for photoconversion**

#### **Chapter One**

<b>Introduction to Solar Energy Conversion</b> .....	7
1.1 Inorganic Solar Cells.....	8
1.1.1 Silicon based solar cells.....	8
1.1.2 Copper indium gallium selenide (CIGS) based solar cells.....	8
1.2 Organic Solar Cells.....	11
1.2.1 Heterojunction solar cells.....	14
1.2.2 Dye Sensitized solar Cells (DSSCs).....	19
1.3 New frontiers in solar cells.....	24
1.4 Concluding remarks.....	25

#### **Chapter Two**

<b>Nile red cyclopalladated neutral and ionic metallomesogens</b> .....	27
2.1 Introduction.....	27
2.2 Nile red structure and properties.....	31
2.3 Research scopes.....	33
2.4 Photoconductive Nile red cyclopalladated metallomesogens.....	33
2.4.1 Synthesis.....	34
2.4.2 Mesomorphic properties.....	36
2.4.3 Solution electrochemistry.....	43
2.4.4 UV/Vis spectroscopy and photoconduction.....	45
2.5 Cationic cyclopalladated Nile Red metallomesogens.....	50
2.6 Using Nile red as an ancillary ligand in a cyclopalladated complex.....	52
2.6.1 Synthesis.....	52
2.6.2 Solution electrochemistry.....	54
2.6.3 UV/Vis spectroscopy.....	55
2.6.4 Photoconduction.....	55
2.7 Conclusions.....	56

## **Chapter Three**

### **Electropolymerizable Nile red cyclopalladated complexes for bulk**

<b>heterojunction solar cell application</b> .....	59
3.1 Introduction.....	59
3.2 Testing a Nile red cyclopalladated photoconductor in a bulk heterojunction solar cell.....	62
3.2.1 Synthesis.....	62
3.2.2 Electrochemistry.....	63
3.2.3 Bulk heterojunction cell.....	64
3.3 Towards high quality photoconductive thin films .....	72
3.3.1 Synthesis.....	75
3.3.2 Structural characterization.....	77
3.3.3 Electrochemistry.....	79
3.3.4 Film photoconduction.....	84
3.4 Conclusions.....	87

## **Chapter Four**

### **Synthesis and properties of new Nile red cyclopalladated dyes and their application as sensitizers in Dye Sensitised Solar Cells**.....

4.1 Introduction.....	89
4.2 Nile red functionalization for post-grafting to TiO <sub>2</sub> .....	90
4.3 Nile Red cyclopalladated complexes containing anchoring groups.....	93
4.4 Solution electrochemistry.....	96
4.5 Testing Nile red cyclopalladated complexes in DSSCs.....	99
4.6 Conclusions.....	104

## **Chapter Five**

<b>Conclusions</b> .....	107
--------------------------	-----



**2<sup>nd</sup> Part. Novel molecular materials based on Ir(III)  
for electroconversion**

**Chapter Six**

<b>Introduction to electroluminescence</b> .....	113
6.1 Inorganic LEDs.....	113
6.2 Organic Light Emitting Diodes (OLEDs) .....	113
6.3 Light Emitting Electrochemical Cells (LECs).....	117
6.4 Use of transition metal complexes in electroluminescent devices.....	118
6.4.1 Use of transition metal complexes in efficient OLEDs.....	119
6.4.2 Use of transition metal complexes in efficient LECs.....	121
6.4.3 Phosphorescent neutral and ionic cyclometallated Ir(III) complexes used in electroluminescent devices.....	125
6.4.3.1 Neutral bis- and tris-cyclometallated Ir(III) complexes.....	127
6.4.3.2 Ionic bis-cyclometallated Ir(III) complexes.....	129
6.5 Concluding remarks.....	130

**Chapter Seven**

<b>Novel anionic Ir(III) complexes and their derivatives</b> .....	131
7.1. Introduction.....	131
7.2. Anionic cyclometallated Ir(III) complexes containing substituted bivalent <i>ortho</i> -hydroquinones .....	133
7.2.1 Synthesis.....	134
7.2.2 Electrochemistry.....	136
7.2.3 Photophysical properties.....	138
7.3 Luminescent anionic cyclometallated Ir(III) complexes containing an orotate ancillary ligand.....	141
7.3.1 Synthesis.....	142
7.3.2 Solution electrochemical studies.....	143
7.3.3 Photophysical properties.....	145
7.4 Ir(III) luminescent homometallic soft salts.....	147
7.4.1 Synthesis.....	147
7.4.2 Solution electrochemical studies.....	151
7.4.3 Photophysical properties.....	152
7.5 Conclusions.....	157

## **Chapter Eight**

Electropolymerizable Ir(III) cyclometallated complex.....	159
8.1. Introduction.....	155
8.2. Research scopes.....	161
8.3 Synthesis of novel bis-cyclometallated Ir(III) model complexes with Schiff bases as ancillary ligands.....	163
8.4 Electrochemical studies.....	165
8.5 Preliminary photophysical studies.....	168
8.6 Conclusions.....	169

## **Chapter Nine**

Conclusions.....	171
------------------	-----

## **Chapter Ten**

Experimental details.....	173
10.1 General equipment and procedures.....	173
10.2 Synthesis procedures.....	181
10.2.1 Synthesis of novel Pd(II) complexes and of their precursors.....	181
10.2.2 Synthesis of novel Ir(III) complexes and of their precursors.....	198

## **Appendix I**

<b>X-Ray single crystal diffraction data</b> .....	207
--	-----

## **Appendix II**

<b>Indexation of PXRD pattern of columnar liquid crystals</b> .....	209
---	-----

<b>References</b> .....	213
-------------------------	-----

<b>Acknowledgments</b> .....	231
------------------------------	-----

## Thesis Overview

Nowadays, research on functional materials represents one of the most important development areas in science and technology. Among the wide variety of possible functions to be introduced, those which permit the interaction with light of the obtained materials generating photoresponsive or light driven properties have been the most intensively investigated.

Furthermore, the comprehensive study of the processes involved, such as the energy flow through an organic-inorganic interface and the voltage control at a molecular level have permitted the fabrication of new efficient and sophisticated optoelectronic devices. The upcoming depletion of fossil fuels, the energy crisis and the urgent need for clean and renewable sources of energy has directed optoelectronic industry's steps towards solar energy conversion technologies and electroluminescent devices.

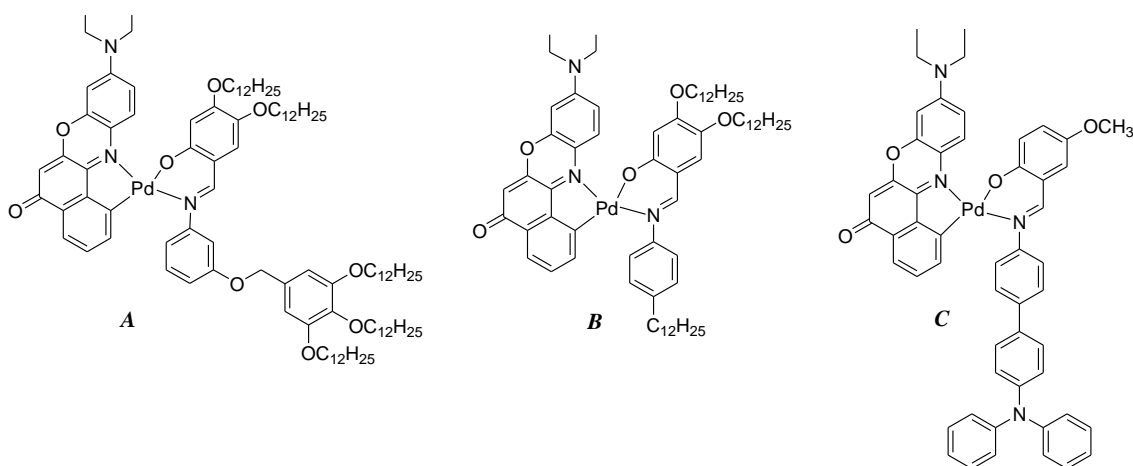
In this context, an important role is played by transition metal complexes since recent advances in their exploitation has managed to take advantage from their photo-induced functions allowing their successful use in energy conversion. In particular, organometallic complexes have received a fast growing attention since their first successful use in solar cells and as molecular emitters for light-emitting devices. In this research work, appropriate functions have been introduced onto novel transition metal complexes to allow their potential use in photo/electron energy conversion.

This thesis is divided in two main parts, dedicated to the synthesis of two different series of organometallic complexes, namely:

- a) Pd(II) square planar cyclometallated complexes and
- b) Ir(III) octahedral organometallic compounds.

a) Pd(II) complexes

The first part is dedicated to the study of new Palladium organometallic based molecular materials, a new class of photoconductive complexes. Preliminary studies have been performed to propose their use in solar energy conversion in different types of solar cells.



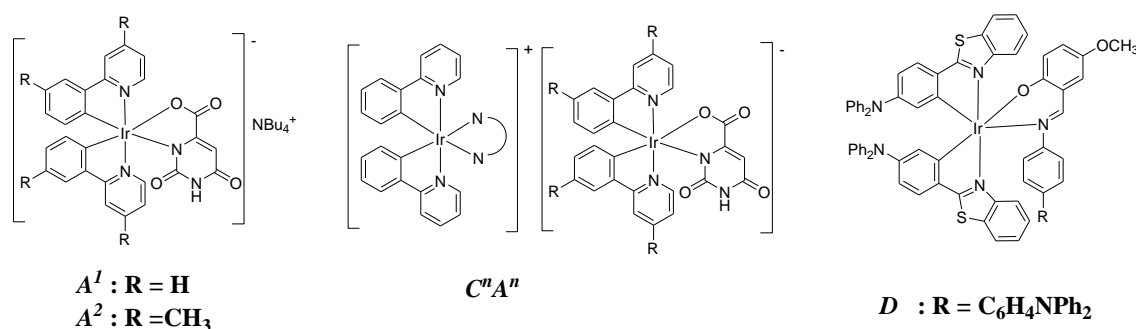
In particular, photoconductivity measurements have been performed on the discotic metallomesogen complex **A** and have shown high photoconductivity values, three orders of magnitude higher than the reported values for parent cyclopalladated complexes.

Furthermore, the low molecular weight photoconductive complex **B** has been tested as a donor in a bulk heterojunction solar cell using PC<sub>61</sub>BM as an acceptor. Even though the obtained device efficiency was scarce, the advantages of using an intrinsic photoconductor have been evidenced.

The availability of photoconductors with electropolymerizable fragments or mesogenic properties represents a starting key point for the development of new hybrid organic/inorganic optoelectronic devices based on molecular assembling. In this context, the electropolymerizable complex **C** has been synthesized and thin films have been electrogenerated.

b) Ir(III) complexes

Iridium organometallic emitters have been investigated for their potential use in electroluminescent devices. To this end, novel anionic complexes, forming ionic pairs when coupled with cationic Ir(III) complexes and neutral electropolymerizable species have been studied.



In particular, orotic acid has been successfully incorporated as a dianionic bidentate ligand to obtain the anionic high luminescent Ir(III) complexes *A* and *A'*. The introduction of this ancillary ligand might be a step toward the stabilisation of anionic Ir(III) complexes in LECs which until now have shown emission quenching and fast device degradation when monodentate ligand bearing complexes have been used as emitting species.

Furthermore, we have demonstrated the possibility of using such anionic complexes in the formation of Ir(III) homometallic soft salts *C<sup>n</sup>A<sup>n</sup>* showing enhanced photoluminescent quantum yields.

Eventually, a novel bis-cyclometallated Ir(III) neutral complex *D* bearing a benzothiazole-triphenylamine derivative as a cyclometallated ligand and a triphenylamine electropolymerizable Schiff base has been synthesized and electrogenerated polymeric thin films have been obtained.



## **First part**

Novel molecular materials  
based on Pd(II)  
for photoconversion





## **Chapter One**

### **Introduction to solar energy conversion**

Photovoltaic devices represent one of the most efficient methods of obtaining clean energy. Their working mechanism which promotes the conversion of solar radiation in electricity is based on the photovoltaic effect, discovered by Alexandre Becquerel back in 1839. This effect is defined as the potential difference between two electrodes, across a liquid or solid system, under sunlight.

The first process in the photovoltaic conversion of energy (sunlight absorption) induces an electronic transition into the absorbing material from the ground state to an excited level with subsequent formation of an opposite charged electric couple (electron-hole). In a second step, the charge separation occurs and imposes the negative charges to migrate in a preferred direction towards a specific electrode (conventionally called cathode) and the positive charges to migrate in the opposite direction, towards the anode. When the two electrodes are connected by a conductor, the photogenerated negative charges flow through the external circuit losing their energy and being collected at the cell's anode. At the anode, each electron completes its photovoltaic process, it combines with a hole and regenerates the absorbing specie in its electronic ground state.<sup>1</sup>

The photovoltaic effect remained a laboratory curiosity from 1839 until 1959 when the first solar cell based on silicon was realized by the Bell Laboratories (1954, Chapin *et al.*<sup>2</sup>) presenting a 6% efficiency. Among the great number of advantages of the photovoltaic applications there are: direct sunlight conversion to electricity (from micro to megawatts), long device lifetime, zero cost of the energy source (the sun), and zero noise and pollution.

## **1.1 Inorganic solar cells**

### **1.1.1 Silicon based solar cells**

The solar cell technology has emerged on the basis of silicon technology, based on the already developed technology of transistors and integrated circuits and on the availability of single crystal silicon.<sup>3</sup>

Apart from the efforts invested in the optimization of the production process, attention has been given to improving efficiencies in order to reduce the cost. Yet, a series of loss processes limits the efficiency of devices; each semiconductor in fact can absorb only a specific part of the whole available radiation spectrum. Even more, a part of the absorbed radiation is converted to heat rather than electric energy. Other factors contribute to diminishing the efficiency among which the reflexion of the radiation incident on the cell surface, the electric resistance within the semiconductor and the connecting leads, materials purity, surface effects, and crystal defects. Moreover, the solar cells efficiency depends on temperature. In particular, for silicon based devices, the efficiency decreases with temperature.

Due to the indirect band gap semiconductor nature of silicon, rather thick layers of silicon are needed for the efficient absorption in order to compensate the low molar extinction coefficient of silicon. Taking into account the solar radiation distribution and the value of silicon band gap, for silicon solar cells a maximum efficiency of 28% can be estimated theoretically.<sup>4</sup> However, the research is now concentrated on materials with direct band nature presenting high absorption coefficients which can be used even as very thin films. Despite the high cost and its theoretical intrinsic efficiency limit, silicon is still today the commercially dominant material for solar cells. Also considering that the silicon solar cells have a lifetime of about 20 years and that they have been already in use for almost 18 years, quite soon, the problem of their disposal will have to be faced.

### **1.1.2 Copper indium gallium selenide (CIGS) based solar cells**

Possible inorganic alternatives to the use of silicon in solar cells have been reported.<sup>5</sup> By using a direct band semiconductor thin layer that can show a large absorption of solar photons, devices with a thinner active layer (of ca. 1 micron order, with respect to about 100 micron in traditional Si cells<sup>6</sup>) can be realized. Even if a wide

variety of metallic (Fe, Ni, Cu, Pb, Bi) binary sulphides and multi component materials like  $\text{Cu}_2\text{ZnSnS}_4$  have been proposed,<sup>7</sup> the two main technologies based on direct semiconductor thin layers make use of CdTe and  $\text{CuIn}_{1-x}\text{Ga}_x\text{Se}_{2-y}\text{S}_y$  (CIGS:  $0 \leq x \leq 1$ ,  $0 \leq y \leq 2$ ).<sup>8</sup> Nevertheless, due to their high efficiencies - close to 20%<sup>9</sup> -, to the facility of depositing thin films, to their stability and to the possibility of getting rid of toxic cadmium, the interest of the researcher in this field has been mainly concentrated on CIGS devices. The deposition of thin layers of CIGS may be performed under atmospheric pressure or under vacuum, either on economic substrates as glass or flexible polymer substrates. Moreover, the CIGS characteristics can be controlled by varying the stoichiometric ratio between the component elements.

In Figure 1.1 a typical structure of a CIGS based solar cell is presented. Generally, the cell is realized from a molybdenum layer on top of a glass surface, followed by a p type active CIGS layer, and an n type CdS (or another semiconductor that do not contain Cd) layer, a non doped ZnO layer, an n type transparent conductor (mainly doped with ZnO or  $\text{In}_2\text{O}_3$ ), two metallic grids, and an anti-reflective coating. Then the entire device is encapsulated in such a way as to protect it from the external ambient.

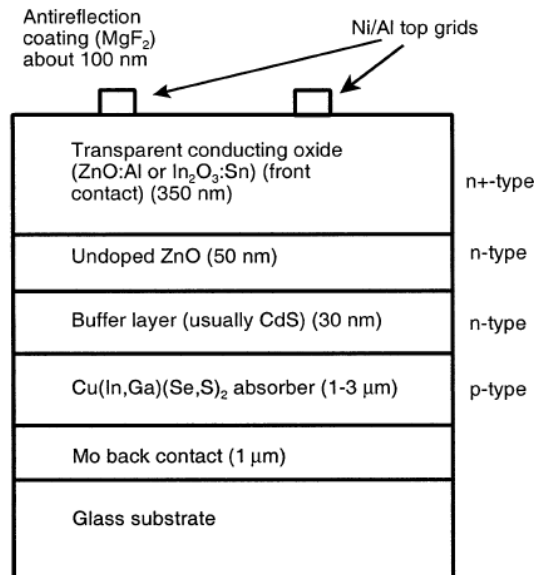


**Figure 1.1.** Structure of a CIGS based solar cell<sup>10</sup>

The operation of CIGS cells, similar to the one described above for silicon cells, is based on a p-n junction. As far as the nature of the active semiconductor layer is concerned, in order to estimate the band gap, it is necessary to consider the crystalline structure of CIGS. The ternary copper chalcogenides (CGS) normally crystallizes in the tetragonal structure of the calpocrite (Figure 1.2)<sup>11</sup>

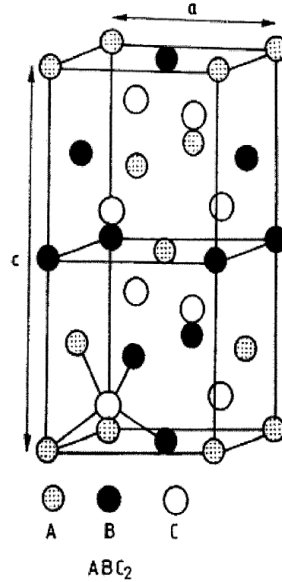


**Figure 1.2.** The crystalline structure of CGS (A=Cu, B=In, C=Se)<sup>10</sup>

The band gap in CuInSe<sub>2</sub> is rather small (1.04 eV), but it may be modulated in such a way to make it compatible to the energies associated to the solar spectrum, substituting part of the indium with gallium and part of the selenium with sulphur in the crystalline structure. The strength point of such systems is in principle the capability of tuning the band gap from 1.04 eV in CuInSe<sub>2</sub>, 1.53 eV in CuInS<sub>2</sub>, 1.7 eV in CuGaSe<sub>2</sub> (CGS) up to 2.5 eV of CuGaS<sub>2</sub>.<sup>12</sup>

Despite their multiple advantages CIGS devices are rather complex material and the efficiency of the device is determined by the absorbent layer morphology. Besides, as the domain boundaries act as recombination centres for charges generated during the photon absorption, the deposited films must necessarily have uniform domains on micrometric scale and controlled stoichiometry, in order for the device to reach acceptable efficiencies. Generally, the techniques used to deposit these films are based on multistep processes performed in vacuum.<sup>13</sup> Yet, solution deposition techniques have also been reported.<sup>14</sup>

## 1.2 Organic solar cells

In order for solar cells to become the main energy source, their cost should be lowered. Nowadays, the main drawback is represented by the excessive cost of crystalline silicon production and its future disposal after use that still has to be economically evaluated properly. A potential alternative to the silicon cells is represented by organic photovoltaic devices able to produce low cost energy, providing that reasonable efficiencies and lifetimes are reached. For these reasons and also to allow a more flexible and easier architecture for solar cells, intensive researches have been dedicated in the last years to photovoltaic cells that use other materials than silicon.<sup>15</sup> The alternative consist in using organic semiconductors since they represent a less costly alternative to inorganic semiconductors. Organic compounds were among the first to show the photovoltaic effect, successively reported in many other biologic molecules like carotene, chlorophyll, porphyrin, and phthalocyanine.<sup>16</sup> Organic materials (conjugated polymers and dyes), may present p or n type conducting properties like “classical” semiconductors. For instance, they have high absorption coefficients that allow the construction of much thinner solar cells (thicknesses much less than a micron) and thus requiring smaller amounts of active material. Moreover, the variety of organic materials potentially obtained by an appropriate chemical design is practically infinite. With the further progress in efficiency and lifetime, organic solar cells are supposed to give strong competition to silicon solar cells in the near future. By the use of advanced materials with high charge carrier mobilities and optimized nanoscale morphology, the efficiencies of the devices are expected to increase further. The typical configuration of an organic solar cell present a sandwich planar structure where the absorbing layer stays between two different electrodes. One of the two electrodes has to be (semi)transparent to allow light to reach the photoactive layer; indium tin oxide (ITO) or an ultra thin metallic layer are commonly used, whereas the other electrode is, depending on the necessary work function, made by aluminium (or calcium, magnesium, gold etc.) (Figure 1.3).

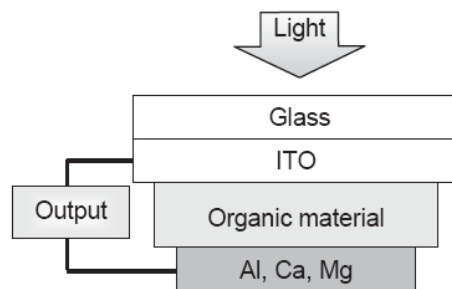


**Figure 1.3.** General scheme of an organic photovoltaic device

In an organic photovoltaic device (Figure 1.4), photon absorption leads to the promotion of one electron from the highest occupied molecular orbital (HOMO) to the lowest unoccupied molecular orbital (LUMO) forming an exciton (a pair of hole – conduction electron). In a photovoltaic device this process must be associated by subsequent dissociation followed by the migration of the electron and the hole to the appropriate electrodes. In order to separate the opposite photogenerated charges an electric field is necessary and is generated by the difference between the redox/work potentials of the two electrodes and to complete the cell. Due to this difference the electric current flows from the electrode with the lower work function to the electrode with the higher work function.

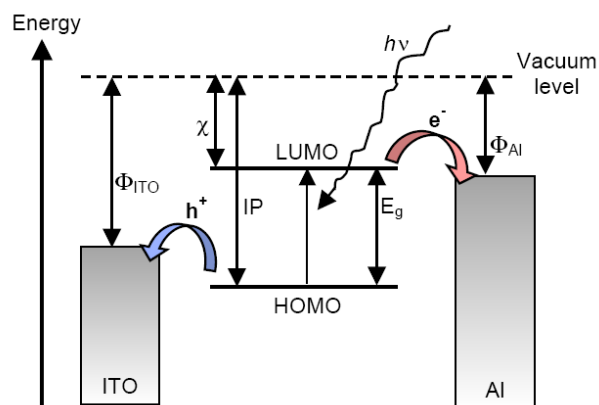


**Figure 1.4.** Solar radiation absorption process and the relative position of the energy levels in an organic photovoltaic device. The electrons are captured by the aluminium electrode and the holes by the ITO electrode.  $\Phi$  represents the work function,  $\chi$  the electronic affinity, IP the ionization potential and  $E_g$  the energy difference between the HOMO-LUMO orbitals<sup>16b</sup>

An important factor concerning the active layer in an organic solar cell is to insure absorbance in the largest possible interval of the solar spectrum. (Figure 1.5).

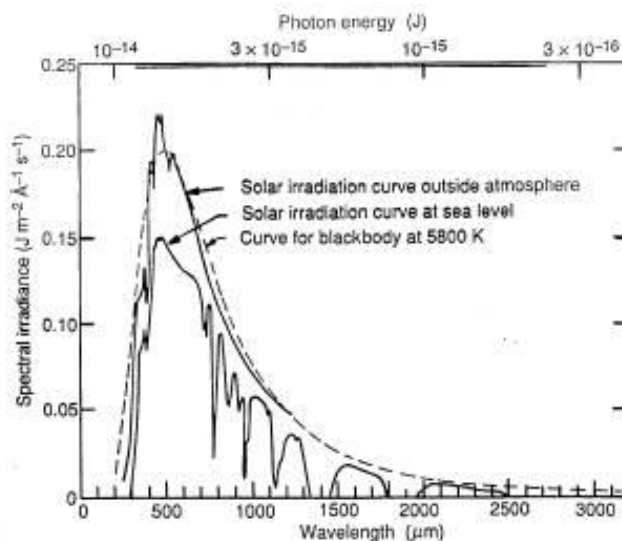


**Figure 1.5.** Solar radiation spectrum

Conjugated polymers present absorption all over the UV spectrum. Besides, whereas for crystalline silicon a 100  $\mu\text{m}$  or more thick film is needed in order to efficiently absorb the incident radiation, in organic semiconductors, due to their direct band-gap nature the efficient absorption makes possible the use of only 100-500nm thick layers.

In a crystalline inorganic semiconductor characterized by a 3D lattice, the individual HOMO and LUMO orbitals form the valence and conduction bands of the material. However, in the great part of organic semiconductors the very weak intermolecular forces are not able to generate a 3D crystalline lattice and, consequently, the frontier molecular orbitals do not mix so strongly to form bands. Therefore, the charge transport occurs by a hopping process between localized states, rather than through the energy bands.<sup>17</sup> This implies that the mobility of charges in organic semiconductors is rather low with respect to the inorganic ones. Besides, due to the low value of the dielectric constant in organic semiconductors, the charge separation results more difficult. In many inorganic semiconductors the absorption of a photon generates a not connected electron-hole pair, while in the organic ones, even at room temperature, the excited electron remains linked to the hole. Conjugated polymers present intermediate characteristics between inorganic semiconductors and organic dyes and, generally, it is considered that the excitons are localized on well determined molecular fragments.<sup>18</sup>

### 1.2.1 Heterojunction solar cells

As already mentioned, excitons do not separate easily in organic semiconductors. To favour excitons dissociation, the heterojunction concept has been introduced and is based on using two materials with different electronic affinity and different ionization potentials. Subsequently, the electrons are accepted by the material with the largest electron affinity and the holes are collected by the material with the smallest ionization potential (Figure 1.6).<sup>19</sup>

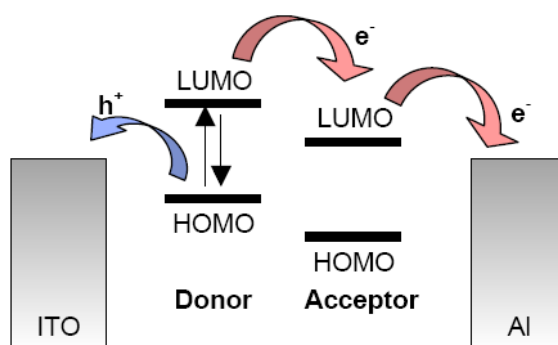


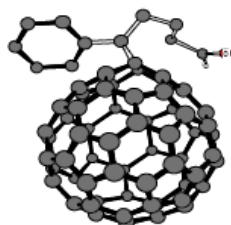
**Figure 1.6.** Relative positions of LUMO and HOMO levels of donors and acceptors in heterojunction photovoltaic cells<sup>16b</sup>

Upon illumination, the electron is promoted from the donor's HOMO to its LUMO leaving back a hole. The electron and the hole may recombine, or may dissociate. If the accepting LUMO has a sufficiently lower energy with respect to the LUMO energy level of the donor, the excited electron is injected into the acceptor's LUMO and thus separated from the hole.

One of the acceptors most commonly used in heterojunction cells is the (buckminster) fullerenes  $C_{60}$  which is quite transparent at low concentrations in polymeric matrices and shows a high electronic conductivity ( $10^{-4} \text{ S cm}^{-1}$ ). The first heterojunction photovoltaic cell was based on a MEH-PPV (poly[2-methyloxi-5-((2-ethylhexyl)oxy)-1,4-phenylenvinylene) spin coated film on a ITO coated glass and a gold counter electrode. This device showed a 0.04% efficiency under monochromatic radiation illumination.<sup>20</sup> Lately, it has been proved that the photocurrent increases after insertion of a double film of  $C_{60}$ , thus showing that the fullerene plays an essential role in charge separation. Since then, the improved processing conditions,<sup>21</sup> the pre- and post-fabrication treatments<sup>22</sup> and the application of new advanced materials with new device design<sup>23</sup> have allowed to reach efficiencies up to 8%.<sup>24</sup>



As an alternative to C<sub>60</sub> it has been proved that mixing MEH-PPV with a soluble derivative of C<sub>60</sub> 6,6-phenyl-C<sub>61</sub>-butyric acid methyl ester (PCBM) (Figure 1.7), the charge transport considerably improves and, as a consequence, there is a drastic increase of the device efficiency.<sup>25</sup>



PCBM

**Figure 1.7.** The molecular structure of methyl ester of the butyric acid of [6,6]-phenyl-C<sub>61</sub> (PCMB)<sup>26</sup>

The most frequently used donor-acceptor combinations tested are poly(3-hexylthiophene) (P3HT) or poly(2-methoxy-5-(3,7-dimethyloctyloxy)-1,4-phenylvinylene) (MDMO-PPV) as donors (Figure 1.8) and PCBM or mixtures as copper phthalocyanine-C<sub>60</sub> as acceptors.<sup>27</sup>

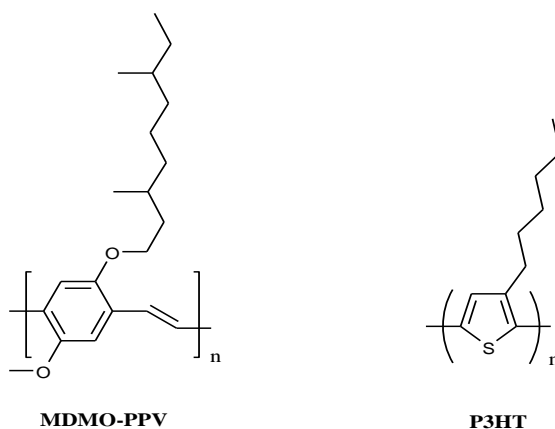


**Figure 1.8.** Molecular structure of some conjugated polymers used as donors in kulk heterojunction cells

Studies have shown that excitons dissociation in heterojunction cells is more efficient at the donor/acceptor interface rather than at the electrode. Therefore, in order to reach high efficiencies, the excitons should be formed within the diffusing length from the interface (typically of the order of 10 nm) limiting the region where the absorption is useful. On the other hand, for the majority of the organic semiconductors, film thicknesses over 100 nm are needed to efficiently absorb the light. This drawback

might be overcome by mixing the donor and the acceptor in a single phase, thus generating a dispersed (or bulk) heterojunction cell (Figure 1.9).<sup>28</sup>

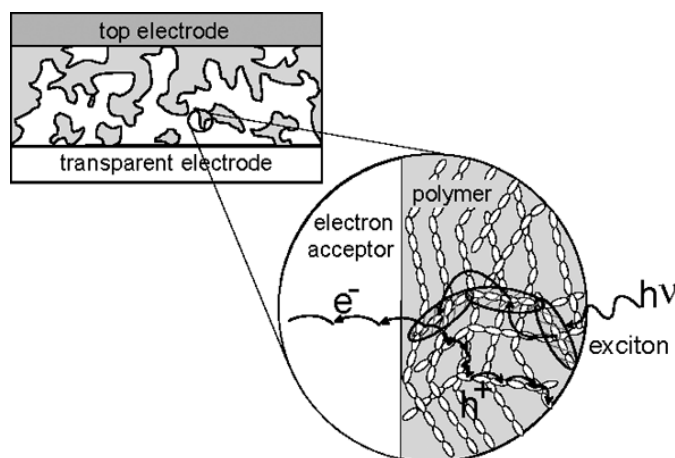


**Figure 1.9.** The dispersed heterojunction cell

Even if bulk heterojunction solar cells are fabricated with both polymers and small molecules, there is a head-to-head race going on in between these materials towards being technologically more important. A problem inherent to this type of cell is represented by the low miscibility of the components in the solid state. In fact, in order to have a homogeneous dispersion, a rapid evaporation of the solvent is necessary before the system reaches the equilibrium is necessary. To be used in heterojunction photovoltaic cells, the organic semiconductors must necessarily be soluble in most organic solvents. From this point of view, polymers present an advantage due to the possibility to be easier processed from solution by low cost wet technologies (spin casting, dip coating, etc.).

In these solar cells either the electron-acceptor PCBM and the hole carrier conjugated polymer are in contact with both electrodes. Despite the fact that the electrons and the holes may reach both electrodes of the system, it is generally true that the electrons go to the metallic electrode, whereas the holes are captured by the transparent electrode. It is therefore necessary to have a good compatibility between the relative positions of HOMO and LUMO of both polymer/small molecule donor and the PCMB acceptor.

An important issue to overcome in the cell stability is the phase separation which induces a discontinuity in the hopping process and thus a poor charge transport allowing a fast intramolecular recombination. Therefore, controlling the morphology of the

dispersive heterojunction cells represents a critical aspect. The degree of the phase separation and the dimensions of the domains depend on the choice of the solvent, the evaporation velocity, the solubility of the mixture of donors and acceptors.<sup>29</sup>

The operative mode of a bulk heterojunction solar cell is represented in Figure 1.10, which shows into details the elementary processes subsequent to the absorption of the solar radiation.

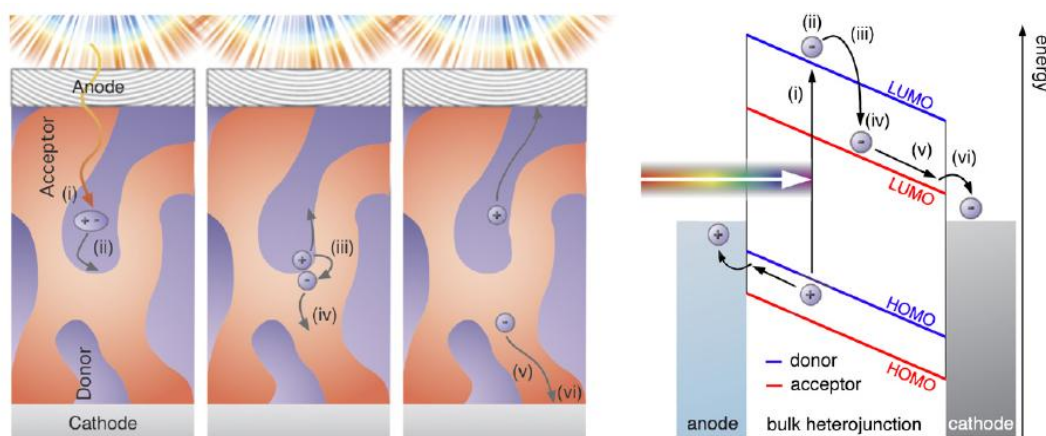


**Figure 1.10.** The operation principle of bulk heterojunction photovoltaic cell<sup>30</sup>

Upon light absorption mainly from the donor material (Figure 1.10 (i)) an electron-hole pair is generated in the semiconductor (ii), followed by the exciton diffusion (iii) and dissociation at the donor-acceptor interface with the consequent charge transfer from the donor to the acceptor. The mechanism (iv) represents the separation (photogeneration) due to the electric field or to the disorder within the material of the still bound exciton (also called polaron). Then the charges thus formed migrate to the respective electrodes (v). After being separated the photogenerated charges extracted from the electrodes constitute the photocurrent (vi).

The conversion of the solar light in energy is based on the set of just described mechanisms and is thus evident that in order to increase the efficiency of the entire device, improvements of any single process are needed. The mechanisms that determine the efficiency, as well as their respective improvement margins are summarized in Table 1.1.

<b>Limiting factors</b>	<b>Potential solutions</b>
Absorption of solar light	New materials with smaller band gap and greater absorption range
Dissociation of excitons	New organic materials with high dielectric constants to reduce the exciton binding energy Device architecture such as to promote a good separation of donor-accepter domains
Dissociation of polarons	New materials with: -high dielectric constants -good phase separation -nanocrystallinity of donor and acceptor domains
Charge transport and recombination	New materials with enhanced charge mobility
Charge extraction to the electrodes	Optimization of device engineering

**Table 1.1.** Factors that determine the efficiency of bulk heterojunction cells

Further improvements in the efficiencies of bulk heterojunction solar cells may be obtained increasing the charge mobility. According to theoretical models, ideal mobilities which makes possible the use of thicker active films are of the order of  $10^{-1}\text{cm}^2\text{V}^{-1}\text{s}^{-1}$ .<sup>31</sup> Moreover, compensating the different mobilities of electrons and holes prevents the presence of free charges that distort the electric field. Among the novel materials with similar mobilities for electrons and holes are a variety of polymers with higher hole mobilities,<sup>32</sup> discotic liquid crystals featuring high mobilities and supra molecular self-organization,<sup>33</sup> or carbon nanotubes that show high mobilities but challenging synthetic procedures.<sup>34</sup>

### 1.2.2 Dye sensitized solar cells (DSSCs)

The idea of the sensitization of semiconductors to light of wavelength longer than that corresponding to the band gap is an interesting convergence of photography and photoelectrochemistry, both of which rely on photoinduced charge separation at a liquid-solid interface.<sup>35</sup> In the 60ies, dyes were chemisorbed on the semiconductor's surface and the operating mechanism of such systems was elucidated.<sup>36</sup> In such systems, electrons are injected from the photoexcited dye molecules into the conduction band of n-type semiconductor surfaces. When the dyes are used as dispersed particles adsorbed onto a semiconducting surface, photoelectrodes are obtained.<sup>37</sup> Due to its characteristics: low cost, high availability, non-toxicity and biocompatibility, TiO<sub>2</sub> (especially in its polymorphic anatase phase) has become the mostly used material for photoelectrodes. Nevertheless, other oxide such as ZnO, SnO<sub>2</sub> and Nb<sub>2</sub>O<sub>5</sub> semiconductors have been also used.<sup>38</sup>

Furthermore, introducing dye-sensitized photoelectrodes in heterojunction based devices and replacing the solid junction with an electrolyte, photoelectrochemical solar cells have been obtained. The prototype of this new class of devices is the dye sensitized solar cell (DSSC), also called Grätzel cell (after its inventor name) in which both the absorption process and the charge separation occur by means of a semiconductor with crystalline morphology and large band gap doped with a dye.<sup>39</sup> The DSSC technology has evolved up to efficiency over 11%.<sup>40</sup>

A typical DSSC (Figure 1.11) is made up of a mesoporous oxide film obtained from nanometric sintered particles deposited on a glass conducting surface. The semiconductor is sensitized with a dye monolayer. The cell is filled up with a liquid electrolyte based on usually an iodide/triiodide solution and covered with a Platinum counter electrode.

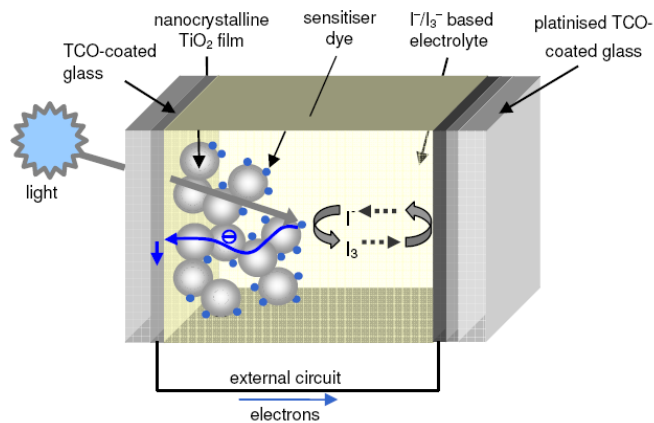


**Figure 1.11.** Outline of the dye sensitized solar cell<sup>41</sup>

The working principle of an iodide/triiodide using DSSC (Figure 1.12) is based on the absorption of a photon from the dye molecule resulting in a dye cation with promotion of an electron to the conduction band of the semiconducting oxide. The ground state of the chromophore is regenerated by accepting an electron from the reduced electrolyte, whereas the redox is regenerated by the reduction of the triiodide at the counter electrode. The electric circuit is being closed by the migration of electrons across the external load. The potential difference generated under illumination corresponds to the difference between the Fermi level of the semiconducting oxide and the redox potential of the electrolyte. On the whole, the device transforms the light into electric current without suffering irreversible chemical transformations.

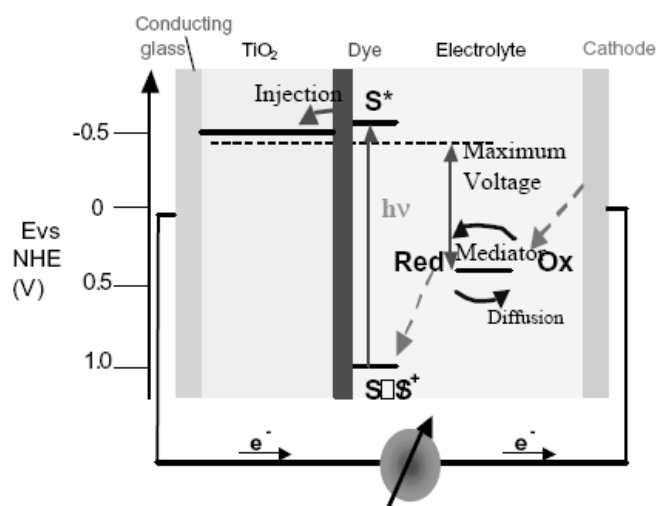


**Figure 1.12.** Operation mechanism of a dye sensitized solar cell<sup>42</sup>

Differently from silicon devices or organic cells, the concentration of mobile ions in the electrolyte is high enough to screen any macroscopic electric field. The charge transport mechanism is mainly diffusive, generated by concentration gradients induced by charge separation. Photoinduced charge separation is verified at the sensitized TiO<sub>2</sub>/electrolyte interface. In order to have the promotion of electrons from the excited state of the dye to the conduction band of the semiconductor, a more reducing redox potential than the conduction band of TiO<sub>2</sub> is required for the dye excited state. In other words, the LUMO of the dye should have a minor electronic affinity with respect to the lowest level of the conduction band of the electrode. Analogously, for the regeneration of the dye ground state, the dye cation needs to be more oxidant than the iodide/triiodide redox pair. Then, the charges thus photogenerated migrate to the respective electrodes and enter the external circuit.

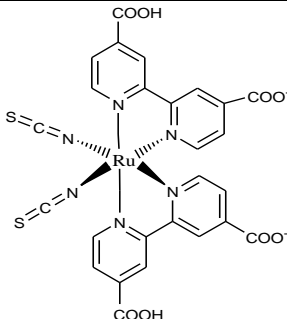
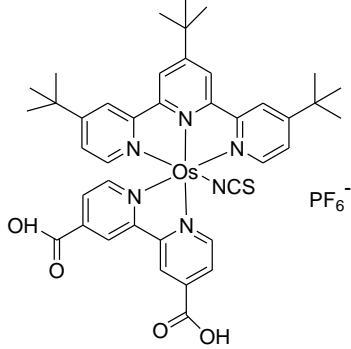
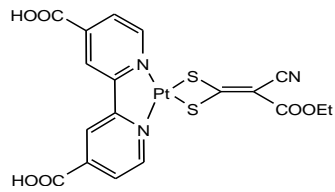
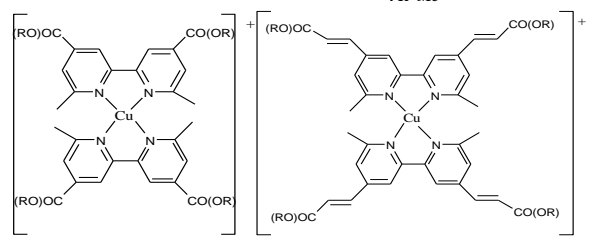
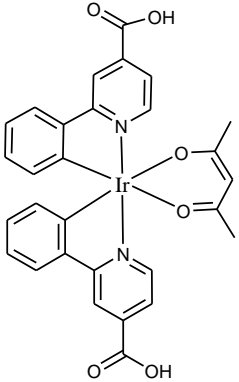
The basic functioning processes of DSSC are in equilibrium with other competitive mechanisms: the decay of the excited state of the chromophore to the ground state and the recombination of the electrons injected into the conduction band with the dye cations or the oxidized form of the electrolyte. In order for the electronic injection to be faster than the decay, the electronic coupling between the dye's LUMO and the semiconductor should be strong enough. Then, to have an efficient regeneration of the dye, it is necessary that the kinetics of the cation reduction by the electrolyte are faster than the kinetics relative to charge recombination. This happens when the dye's HOMO is situated far from the interface with the photoelectrode. Moreover, an ideal chromophore should absorb all the spectral wavelengths from UV up to about 920 nm and present specific anchoring groups toward TiO<sub>2</sub> to insure intimate contact between the dye and the semiconductor.<sup>43</sup>

Taking into consideration the above mentioned requirements, in the last two decades a wide variety of DSSCs sensitizers have been developed, either as organometallic complexes based on porphyrins or phthalocyanines, or other organic dyes.<sup>44</sup> Nevertheless, the best photovoltaic efficiencies (either in terms of conversion yield or the long term stability) have been obtained with Ru(II) polypyridil complexes (Table 1.2) of the general formula RuL<sub>2</sub>X<sub>2</sub> where L= 2,2'-bipyridil-4,4'-dicarboxylic acid and X=halide, cyanide, thiocyanide, acetyl acetate or thiocarbamate.<sup>45</sup> Reported in 1993,<sup>46</sup> the cis-RuL<sub>2</sub>(NCS)<sub>2</sub> complex, called "N3" (Table 1.2) or "N719" in its partial deprotonated form (as a di-tetrabutyl ammonium salt) has become the prototype of the sensitizer used in DSSC. The N3 complex, completely protonated, presents absorption

maxima at 518 nm and 380 nm and emission at 750 nm. The transition is of MLCT type: after the excitation, an electron is promoted to the from the  $\pi$  to the  $\pi^*$  orbital, associated to the carboxylate groups responsible of the anchorage to titania, and is afterwards injected into the conduction band of the semiconductor, generating the charge separation with unit quantum yield.<sup>47</sup> The role of the NCS groups is to increase the absorption of solar light. Therefore in this type of complexes the frontier orbitals are localized on diverse molecular moieties, with the HOMO localized on the NCS ligands and the LUMO on the anchoring groups close to the conduction band of TiO<sub>2</sub>.

In 2001<sup>48</sup> another Ru(II) complex has been synthesized and characterized, the “black dye” (tri(cianato)-2,2',2''-terpyridil-4,4',4''-tricarboxylate) Ru(II) and represented a milestone in the field of the DSSCs sensitizers since it absorbs within the whole visible range and near infrared up to 920 nm and it led to power conversion efficiency up to 10.4%. Nevertheless, other metals have been employed in organometallic DSSC sensitizers to form octahedral Os(II)<sup>49</sup> or Ir(III)<sup>50</sup> complexes, and Pt(II)<sup>51</sup> square planar complexes (Table 1.2). Due to the high cost of Ru(II), the research has been eventually directed upon studying new synthesizers based on more economic metals. Among these, it was demonstrated that Cu(I)<sup>52</sup> complexes of the type [CuL<sub>2</sub>]<sup>+</sup> with ligands 2,2'-bipyridil disubstituted or phosphonic acid derivative capable of binding to the semiconductor surface (Table 1.2) present important values of IPCE (incident-photon to current efficiencies) whereas Ferrere et al.<sup>53</sup> have synthesized Iron(II) complexes that yet have shown a non particularly high conversion efficiency.



Sensitizer	Molecular structure	Ref.
Ru (II) (N719)		48
Os (II)		49
Pt (II)		51
Cu (I)	<p>1 R=H 3 R=Me</p> <p>2 R=H 4 R=Me</p> 	52
Ir (III)		50

**Table 1.2.** Structures of some sensitizers, Ru(II), Os(II), Cu(I) and Ir(III) complexes

### 1.3 New frontiers in solar cells

In the attempt to develop new efficient solar devices, organic and inorganic materials and the respective specific technologies have been mixed. Organic sensitizers often limit light-harvesting ability because of their low absorption coefficients and narrow absorption bands. To overcome this issue, inorganic sensitizers such as quantum dots<sup>54</sup> have been introduced. Intense band-gap light absorption by these inorganic sensitizers, however, has not allowed high performance in quantum conversion and photovoltaic generation; significant losses in light utilization and/or charge separation are found at the semiconductor-sensitizer interface. In this context, organic-inorganic lead halide perovskite compounds such as  $\text{CH}_3\text{NH}_3\text{PbBr}_3$  and  $\text{CH}_3\text{NH}_3\text{PbI}_3$  have been successfully introduced as visible-light sensitizers in photoelectrochemical solar cells showing a 3.8% efficiency. In addition to being synthesized from abundant sources (Pb, C, N, and halogen), these perovskite materials present unique optical and excitonic properties, and show high electrical conductivity.<sup>55</sup>

In this context, very recently,<sup>56</sup> a perovskite based planar heterojunction solar cells has been built by vapour deposition allowing the formation of a thin nanostructured film- and showed over 15% efficiency and a 1.07 V open-circuit voltage. Figure 1.13 shows the scheme of this planar heterojunction p-n solar cell. From the bottom (the side from which the light is incident), the device is constructed on fluorine-doped tin oxide (FTO)-coated glass, coated with a compact layer of n-type  $\text{TiO}_2$  sensitized with the absorbing  $\text{CH}_3\text{NH}_3\text{PbI}_{3-2x}\text{Cl}_x$  perovskite which is then deposited on the n-type compact layer, followed by the p-type hole conductor, 2,29,7,79-tetrakis-(N,N-di-p-methoxyphenylamine)9,99-spirobifluorene (spiro-OMeTAD), which ensures the selective collection of holes at the silver cathode.

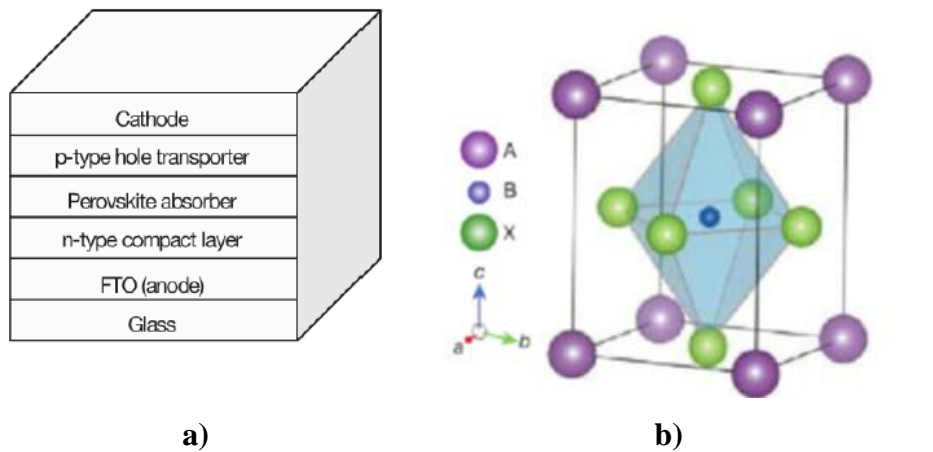


**Figure 1.13.** Generic structure of a heterojunction perovskite solar cell; crystal structure of the perovskite absorber adopting the perovskite  $ABX_3$  form, where A is methyl ammonium, B is Pb and X is I or Cl.

### 1.4 Concluding remarks

After more than two decades of research and development, organic solar cells represent nowadays a real alternative to the use of silicon based solar cells. The intensive research efforts dedicated to this field have resulted in an increase in the efficiencies from 0.001% in 1975 to 8% for bulk heterojunction solar cells and 11% for dye sensitized solar cells. The major strength points of using organic materials are: i) the expected high-efficiency per unit cost ratio, ii) the simplicity in fabrication and processing, and iii) their mechanical flexibility iv) their light weight features. The main drawbacks of using organic materials in solar cells arise instead from their short diffusion length and from low absorption of the resulting active layer.

The addition of an inorganic acceptor material to form an organic–inorganic hybrid solar cells should theoretically improve the performance of OPV, due to additional advantages such as enhanced absorption and improved charge transport characteristics. However, to date, the efficiency of hybrid solar cells have been very low, when compared to their all-organic counterparts.<sup>57</sup>

Even if, to date, silicon based solar cells are still more efficient than organic solar cells, important issues such as disposal of the used silicon and the limited theoretical efficiency need to be faced regarding inorganic solar cells. On the contrary, organic solar cells present the advantage of the non-limited efficiency and the availability of different low cost architectures.

In this context, it appears clear that further efforts need to be invested in the design and developments of novel hybrid organic/inorganic materials with high absorption properties and good charge transport leading to significant increase of efficiencies in order to allow their implementation in low cost large scale solar panels. In this context, the first part of this thesis is dedicated to the development on new absorbing species bearing functions inducing supramolecular organization and photoconductive properties.

*A selection of reviews concerning recent developments in solar energy conversion, ordered by topic, is collected in Table 1.3.*

<b>Topic</b>	<b>First author (Year)</b>	<b>Reference</b>
Silicon solar cells	A. Martin (2013)	58a
	S. Binetti (2013)	58b
CIGS	P. U. Singh (2010)	59
Organic—inorganic hybrid solar cells: a comparative review	M. Wright (2012)	57
Bulk heterojunction solar cells	K. Vandewal (2013)	60a
	Y. Lin (2012)	60b
	R. P. Singh (2013)	27b
Dye sensitized solar cells	B. Bozic-Weber (2013)	61a
	J. Gong (2012)	61b

**Table 1.3.** List of selected recent reviews

## Chapter Two

### Nile Red cyclopalladated neutral and ionic metallomesogens

#### 2.1 Introduction

In recent years, a rising interest in low-cost, flexible and easy to process electronic devices motivated the development of organic electronic technologies.<sup>62</sup> Applications of organic semiconducting materials include photodetectors, sensors, thin film transistors, lasers, and light emitting and photovoltaic devices.<sup>63</sup> Semiconductors, where charge carrier generation is promoted *in situ* by light absorption, are called photoconductors.<sup>64</sup> The photogeneration process at the origin of photoconduction can be either extrinsic<sup>65</sup> (when assisted by injection at electrodes or defect sites, or induced by doping) or intrinsic<sup>66</sup> (when a charge-pair state is formed and after its dissociation the resulting holes/electrons can drift through the bulk material). The best photoconductors present high photogeneration efficiency as well as high charge mobilities.

Over the last decade, discotic liquid crystals have received particular attention as semiconducting materials due to their columnar organisation which enhances charge mobility.<sup>67</sup> Indeed, since their discovery by Chandrasekhar in 1977,<sup>68</sup> discotic liquid crystals have attracted the attention of many research groups due to their multiple potential applications. A typical discotic mesogen generally includes a central aromatic core functionalized with flexible chains. The two main types of discotic liquid crystal mesophases forms are nematic and columnar. In the nematic phase, discs present orientational order, while in the columnar phase the discs pile into column (Figure 2.1) to form six different columnar phases: hexagonal columnar, rectangular columnar, columnar oblique, columnar plastic, helical, and columnar lamellar.<sup>69</sup>

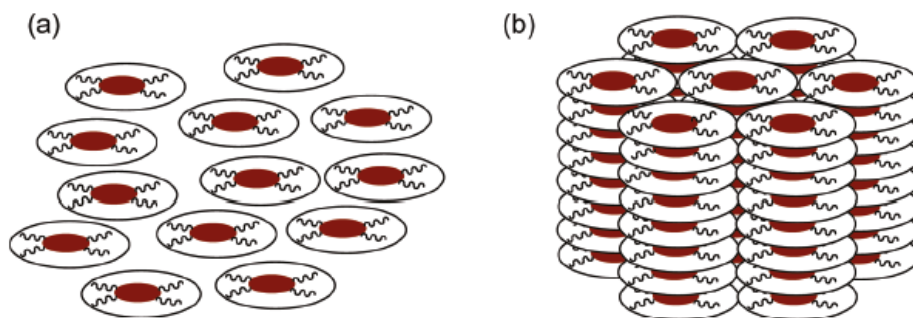


**Figure 2.1.** Schematic representation of **a)** the discotic nematic and **b)** the columnar phase<sup>70</sup>

Due to their large polyaromatic cores inducing efficient  $\pi$ - $\pi$  stacking, many triphenyl,<sup>71</sup> porphyrin<sup>72</sup> or hexa-peri-hexabenzocoronene<sup>73</sup> derivatives properly embedded with peripheral aliphatic chains (Figure 2.2) have been studied in the context of organic discotic mesogens.

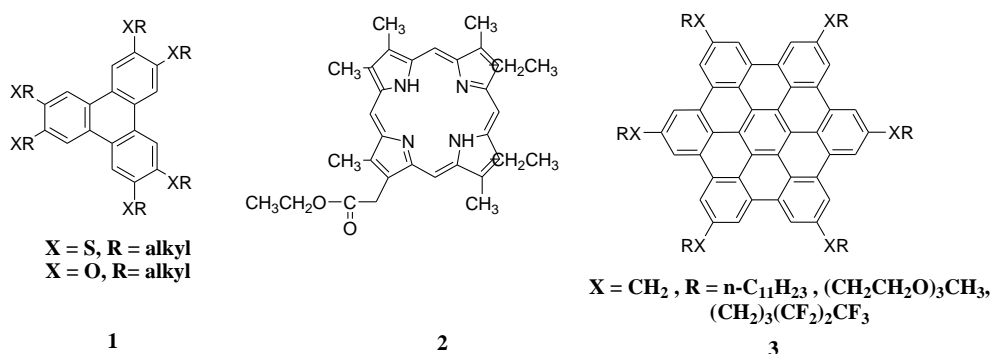


**Figure 2.2.** Triphenyl (1),<sup>71</sup> porphyrin (2)<sup>72</sup> and hexa-peri-hexabenzocoronene (3)<sup>73</sup> derivatives

Indeed, along the column stacks of discotics, for charge mobilities several orders of magnitude higher than in other directions have been measured, and a hole mobility as high as  $1.4 \text{ cm}^2 \text{ V}^{-1} \text{ s}^{-1}$  has recently been reported for tri-indole-based discotic liquid crystals. This particularly high charge mobility was obtained by reducing the stacking distance between molecules and preserving a high intramolecular order along the columns.<sup>74</sup>

For most organic compounds, the photoconduction is limited by the low photogeneration efficiency. To overcome this limitation, organic devices must often be sensitized by incorporation of pigments such as phthalocyanines, squaraines, perylenes or azopigment derivatives, or by means of a double layer architecture where the photosensitizing layer is in contact with a transport layer.<sup>64,75</sup> Another

approach, which is yet to be developed but whose preliminary results are encouraging, is the use of photoconductive metallomesogens. Metallomesogens combine the properties of transition-metal centres with the self-organisation of the liquid crystalline state, hence high absorption properties at higher wavelength are expected, in contrast to fully organic liquid crystals. In this context, a new class of photoconductive cyclometallated complexes has been synthesised and characterised in the CEMIF.Cal Laboratories. These complexes feature a 5-membered Pd(II) or Pt(II) metalocycle, obtained by using a  $H(C^{\wedge}N)$  cyclometallated ligand such as azobenzene  $H(Az)$ , benzo[h]quinoline  $H(Bq)$  or 2-phenylpyridine  $H(Pp)$ , and a 6-membered metalocycle formed by a Schiff base  $H(O^{\wedge}N)$  ancillary ligand (Figure 2.3).

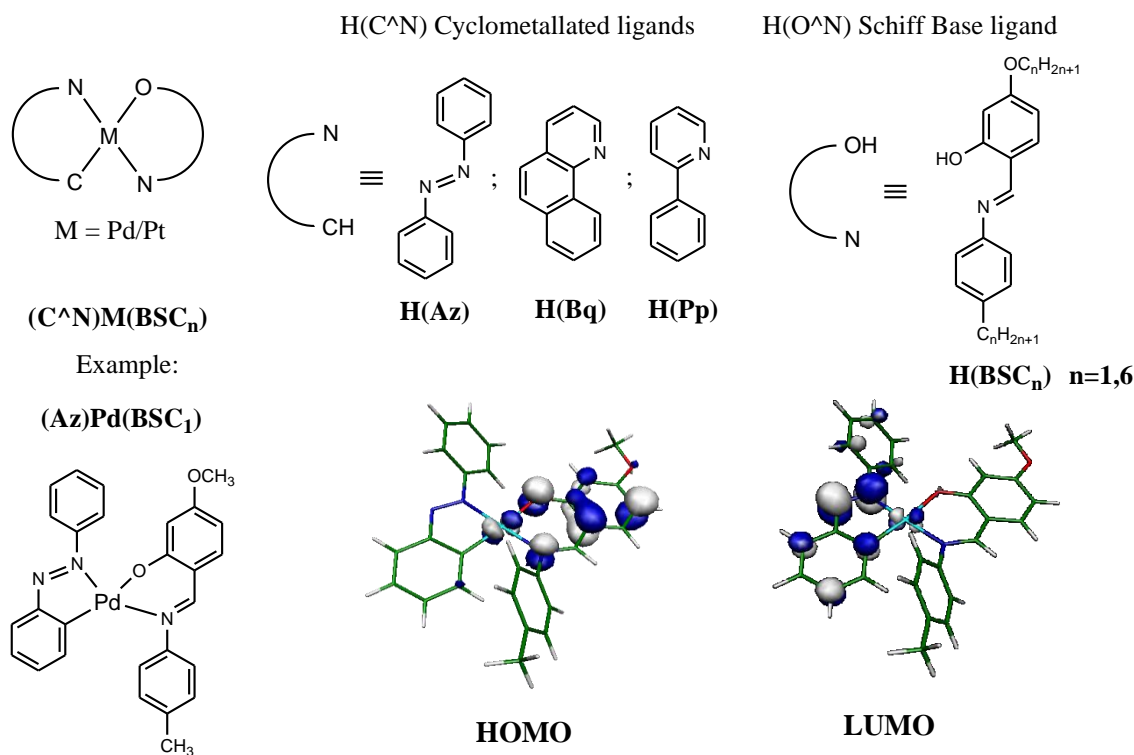


**Figure 2.3.** Photoconductive cyclometallated complexes

Some of these complexes have shown excellent photorefractive properties either dispersed into a polymeric matrix<sup>76</sup> or in their bulk amorphous state<sup>77</sup> and their excellent photogeneration–photoconduction properties were recently correlated with their chemical structure.<sup>78</sup> In fact, the HOMO and LUMO distributions are separated by the metal centre, with the HOMO mainly localised onto the Schiff base moiety while the LUMO is mainly distributed onto the cyclometallated ligand. Moreover,

theoretical computations have shown that the first singlet and triplet excited states exhibit a distorted geometry around the metal centre when compared to the ground state (Figure 2.4). Such distortion may further delay the return to the ground state of excited molecules, hence enhancing charge separation efficiency, leading to the excellent photoconductive behaviour observed for this new class of complexes.

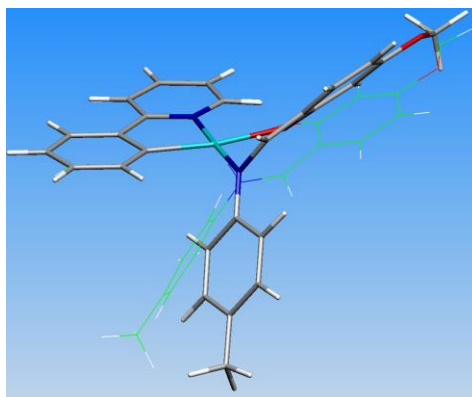


**Figure 2.4.** Comparison of the  $S_0$  (singlet) and  $T_1$  (triplet) structures (the last one is the transparent one)

Furthermore, taking advantage of this peculiar HOMO/LUMO distribution, in order to enhance the charge separation during photogeneration processes, it is expected to be useful to incorporate donor building block onto the Schiff base (ancillary ligand) and acceptor building block onto the cyclometallated ligand (Figure 2.5).

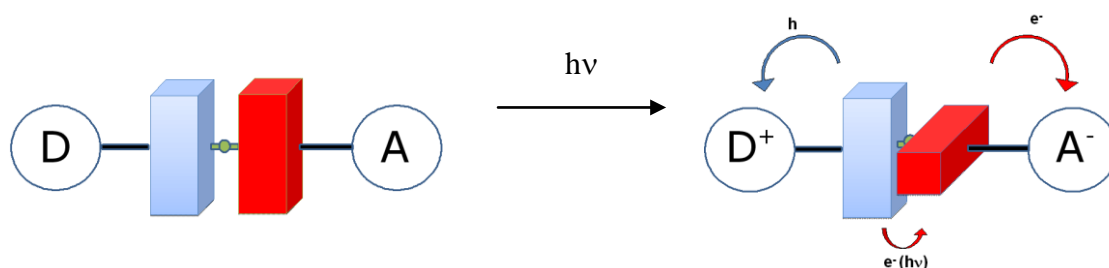


**Figure 2.5.** Schematic representation of  $(C^N)Pd(O^N)$  systems, physical separation of photogenerated charges by intramolecular charge transfer.

As illustrated in Figure 2.6 (complexes **A** and **B**), by incorporating long alkyl chains at the periphery of both ligands, discotic mesophases were obtained.<sup>79</sup> Furthermore, by changing the chemical nature of the linker between the cyclometallated core and the alkyl chains (ester for **I** vs. ether for **II**), it was possible to tune the absorption



properties of the resulting complexes and to obtain cyclopalladated liquid crystal complexes photoconductive at room temperature from UV-Vis to near IR (from 300 to 800 nm).<sup>79</sup> Due to their high viscosity, low mesophase temperature range (from room temperature to ca. 50 °C) and low degree of order of the columnar organisation, the photoconduction of these complexes could be, however, increased by only one order of magnitude upon thermal annealing, when compared to the same property in non-annealed samples.

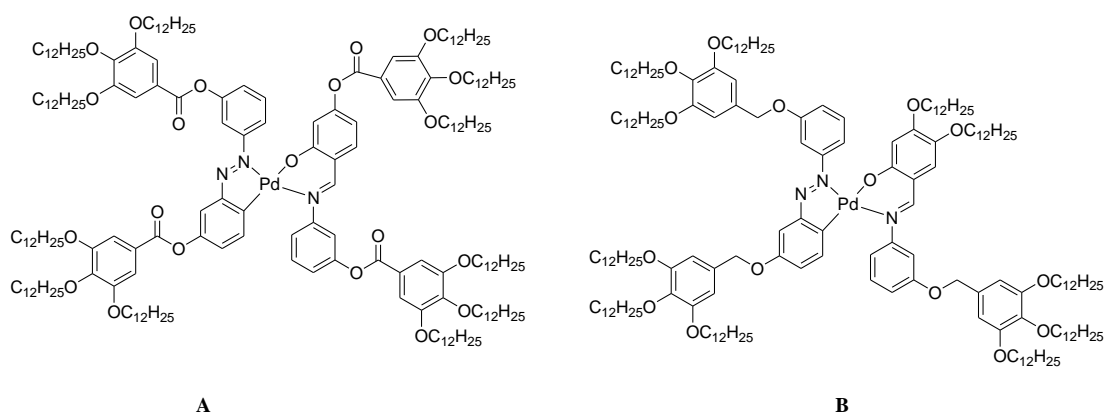


**Figure 2.6.** Photoconductive discotics (**A**, **B**)

In general, in order to improve both the stability and the degree of order of discotic mesophases, several approaches have been developed and are commonly used, such as: (i) increasing the size of the discoid core,<sup>80</sup> (ii) the introduction of secondary interactions such as hydrogen bonds,<sup>81</sup> and (iii) the generation of helicoidal conformation that induce a higher degree of order.<sup>82</sup>

## 2.2 Nile Red structure and properties

In order to increase absorption in cyclopalladated complexes like **(Az)Pd(BSC<sub>6</sub>)**, **(Bp)Pd(BSC<sub>6</sub>)** and **(Pp)Pd(BSC<sub>6</sub>)** (Figure 2.3), one possible strategy is to choose a dye with a molecular structure similar to the cyclometalating azobenzene, benzoquinoline and phenylpyridine. A rightful candidate may be 9-diethyl-amino-5H-benzo[a]fenoxazin-5-one, commonly named Nile Red (Figure 2.7).

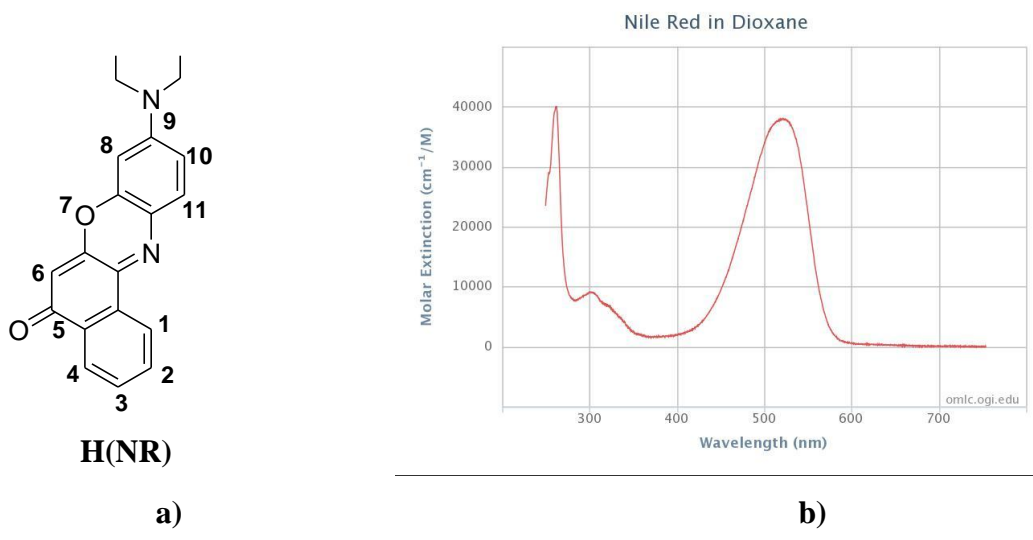


**Figure 2.7.** a) Molecular structure and b) absorption spectrum of Nile Red, **H(NR)**

While its fluorescent and solvatochromic properties have been largely employed in biological labelling applications,<sup>83</sup> Nile Red has been poorly used as organometallic ligand and only recent studies reported the possibility of cyclopalladation (Figure 2.8a).

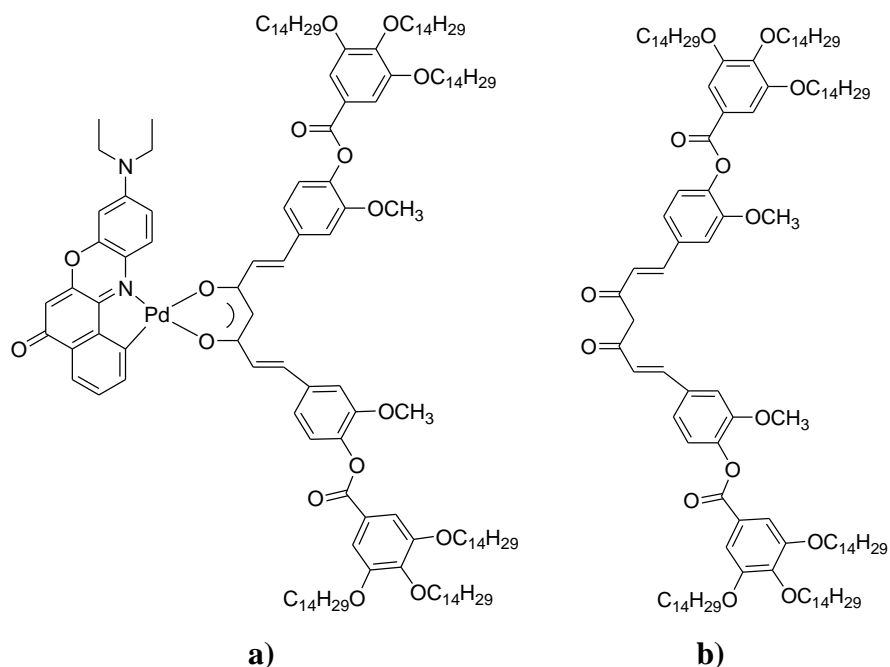


**Figure 2.8.** Nile Red cyclopalladated luminescent discotic complex **C**

Taking advantage of such tools, a red luminescent cyclopalladated complex exhibiting a columnar phase over a broad temperature range (35–173 °C) has been obtained. This discotic mesogen was synthesized by cyclopalladation of the Nile Red dye using a polyalkylated derivative of an acetylacetonone-like species, the curcumin as an ancillary ligand and represents the first example of cyclometallation of such dye molecule (Figure 2.8b).<sup>84</sup>

### 2.3 Research scopes

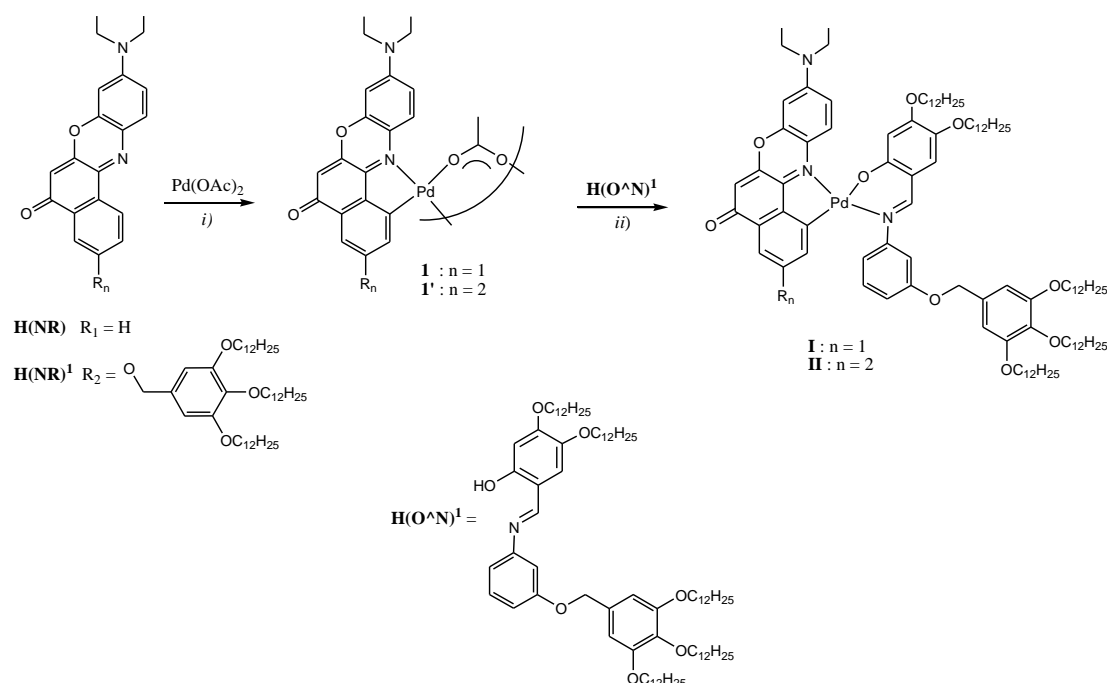
Taking advantage of the capacity of Nile Red to undergo cyclopalladation, the aim of this work is to synthesize novel complexes structurally similar to the photoconductive parent complexes **(Az)Pd(BSC<sub>6</sub>)**, **(Bp)Pd(BSC<sub>6</sub>)** and **(Pp)Pd(BSC<sub>6</sub>)** (Figure 2.3) with enhanced absorption properties. On the other hand, in the context of the design of new discotics, following the examples described above, by incorporating different functionalities into the molecular structure, the liquid crystallinity temperature range could be increased. Using such tools, novel UV-vis photoconductive discotics could be obtained.

### 2.4 Photoconductive Nile Red cyclopalladated metallomesogens

In the present work we report the synthesis and characterisation of two new room temperature photoconductive discotic liquid crystals, obtained by using either Nile Red or a polyalkylated Nile Red derivative as cyclopalladated ligands and a polyalkylated Schiff base as an ancillary ligand. The incorporation of Nile Red as a cyclometallated ligand has proven to maintain the physical separation of the frontier orbitals on their respective fragment, as shown by comparative cyclic voltametry studies, leading to efficient photoconduction over a wide wavelength window. The Nile Red fragment also induces, via formation of hydrogen bonded interactions through paired molecules, a wide temperature range of liquid-crystallinity with a high degree of order.

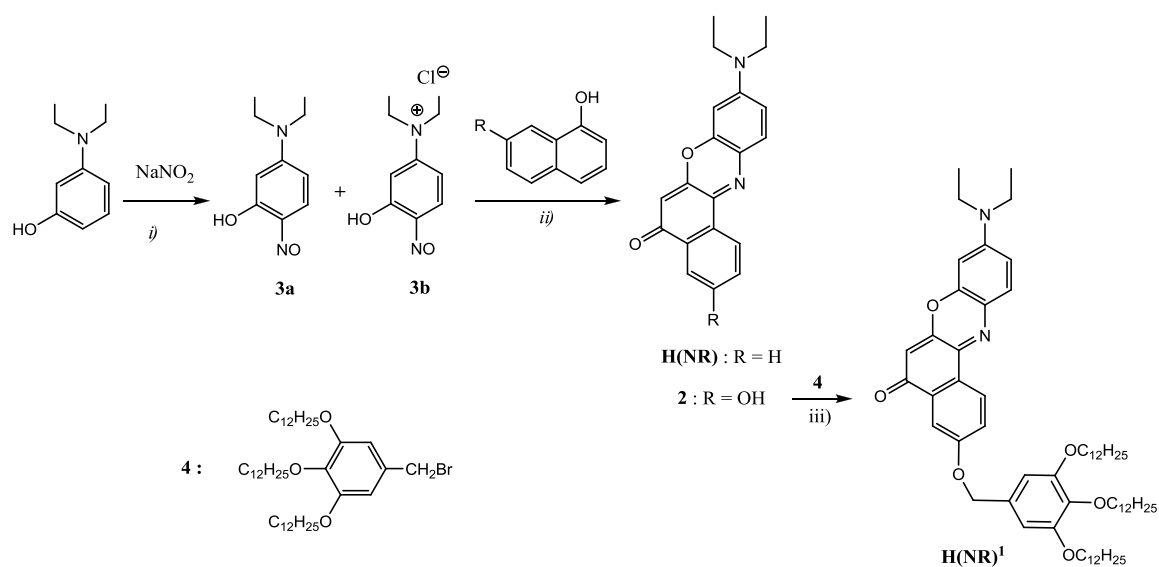
## 2.4.1 Synthesis

The synthesis of both complexes **I** and **II** (Scheme 2.1) was achieved in two steps through the formation of their corresponding Pd(II) acetato-bridged intermediates (**1** and **1'** respectively) obtained by cyclometallation of either Nile Red **H(NR)** or the Nile Red derivative **H(NR)<sup>1</sup>** with Pd(II) acetate, as previously described for the cyclometallation of **H(NR)**.<sup>85</sup> The bridge cleavage of **1** and **1'** was performed using the Schiff base **H(O<sup>^</sup>N)<sup>1</sup>**, prepared according to the previously reported procedure.<sup>79</sup>



**Scheme 2.1.** Experimental conditions: *i*) acetic acid, 55°C, 4h; *ii*) ethanol/dichloromethane, r.t., 5 d.

**H(NR)** and its hydroxy-derivative **2** (Scheme 2.2) were prepared in two steps by slight modifications of previously reported syntheses.<sup>86–88</sup> Nitrosation of 3-diethylaminophenol gave a mixture of 5-diethylamino-2-nitrosophenol (**3a**) and its hydrochloride salt (**3b**) in a 1 : 2 ratio, as determined from the <sup>1</sup>H-NMR spectrum of the mixture (Figure 2.9).



**Scheme 2.2.** Experimental conditions: *i)* HCl, H<sub>2</sub>O, 0-5 °C, 4h; *ii)* DMF, 70 °C, 8h; *iii)* K<sub>2</sub>CO<sub>3</sub>, KI cat., DMF, 130 °C, 8h.

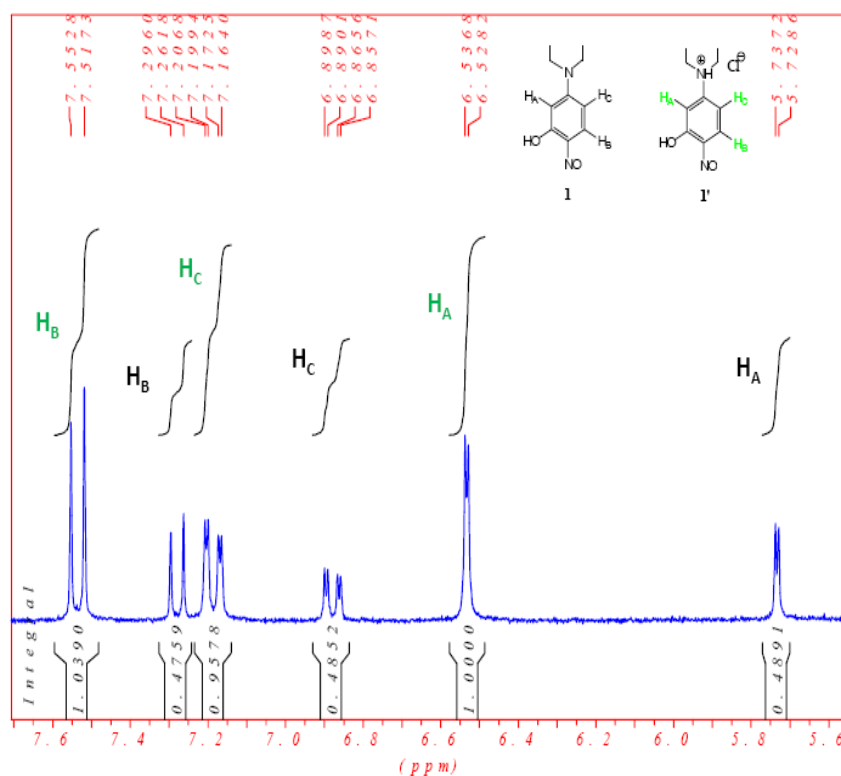


**Figure 2.9.** Aromatic region of the <sup>1</sup>H NMR spectrum of the mixture 3a and 3b showing the relative ratio of the two components

Since both **3a**<sup>81</sup> and **3b**<sup>80</sup> have been successfully used in cyclizing reactions for obtaining Nile Red derivatives, the mixture was used in the second step without any further purification. **H(NR)** and **2** were then obtained by reaction of **3a,b** with naphthol and 1,7-dihydroxynaphthalene, respectively. **H(NR)**<sup>1</sup> was finally obtained by etherification of **2** with 3,4,5-tris(dodeciloxy)bromomethylbenzene **4**.<sup>79</sup> Complex **(NR)Pd(BSC<sub>6</sub>)**, analogous to the photoconductive complexes **(C<sup>^</sup>N)Pd(BSC<sub>6</sub>)** (Figure 2.3), was synthesised with the purpose of carrying out a complete electrochemical study in order to determine the influence of the Nile Red fragment onto the frontier orbitals of the resulting cyclometallated complexes. **(NR)Pd(BSC<sub>6</sub>)** was obtained through the rupture of the bridge intermediate **1** by the Schiff base **H(BSC<sub>6</sub>)** following the pathway previously described.

#### 2.4.2 Mesomorphic properties

At room temperature, the new cyclopalladated complexes **I** and **II** (Scheme 2.1) are dark blue waxy solids. Their thermal behaviour was investigated by using polarized optical microscopy (POM), thermogravimetry (TGA) and differential scanning calorimetry (DSC). Both compounds, as observed by TGA, are thermally stable until 180 °C. While complex **I** shows typical DSC diagrams of liquid crystalline phases through repetitive scans of heating–cooling cycles (Table 2.1, DSC traces are reported in Figure 2.10), for complex **II** no thermal transitions were observed by DSC, probably due to its high viscosity and a clearing point close to its decomposition temperature. It is noteworthy that for complex **I** the DSC traces obtained on the third and successive heating/cooling cycles are identical, indicative of the high stability and reversibility of the mesophases. The mesophases of complex **I**, observed by POM upon slow cooling from the isotropic phase (Figure 2.11), show typical birefringent textures of liquid crystals but, their identification necessary in order to identify the specific mesophase was not possible for the absence of perceptible specific motifs.

Complex	DSC scan	Transitional properties, T (°C), [ $\Delta H$ in kJ mol <sup>-1</sup> ]
<b>I</b>	1 <sup>st</sup> heating	Waxy powder – 177 [72.6] - I
	1 <sup>st</sup> cooling	I-139 [29.5] – Col <sub>r</sub> ' – 62 [11.0] – Col <sub>r</sub> – 37 [3.6] – frozen
	2 <sup>nd</sup> heating	Frozen– 33 [4.0] – Col <sub>r</sub> ' – 77 [11.6] – Col <sub>r</sub> – 160 [24.4] - I
	2 <sup>nd</sup> cooling	Identical data of 1 <sup>st</sup> . cooling
	3 <sup>rd</sup> heating cycle	Identical data of 2 <sup>nd</sup> . cycle

**Table 2.1.** Thermodynamic data for all thermal transitions observed by DSC for complex **I** during 3 heating-cooling cycles (Col<sub>r</sub>: columnar rectangular, I: isotropic liquid)

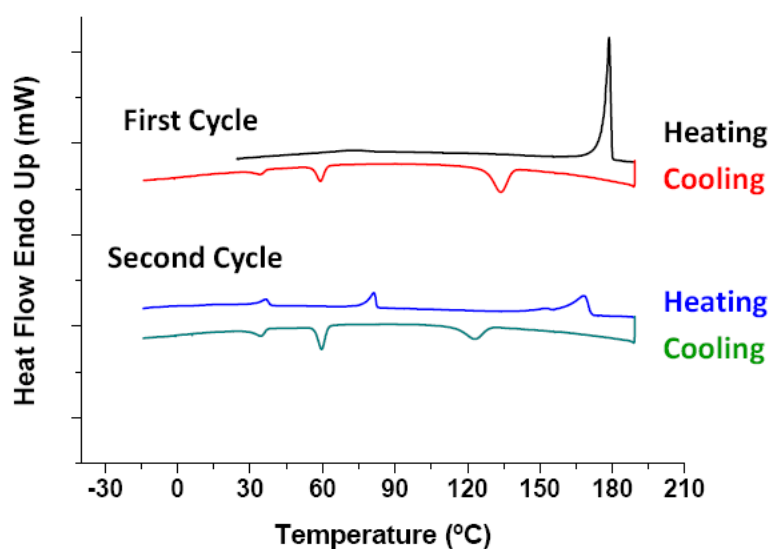


**Figure 2.10.** DSC traces for complex **I**

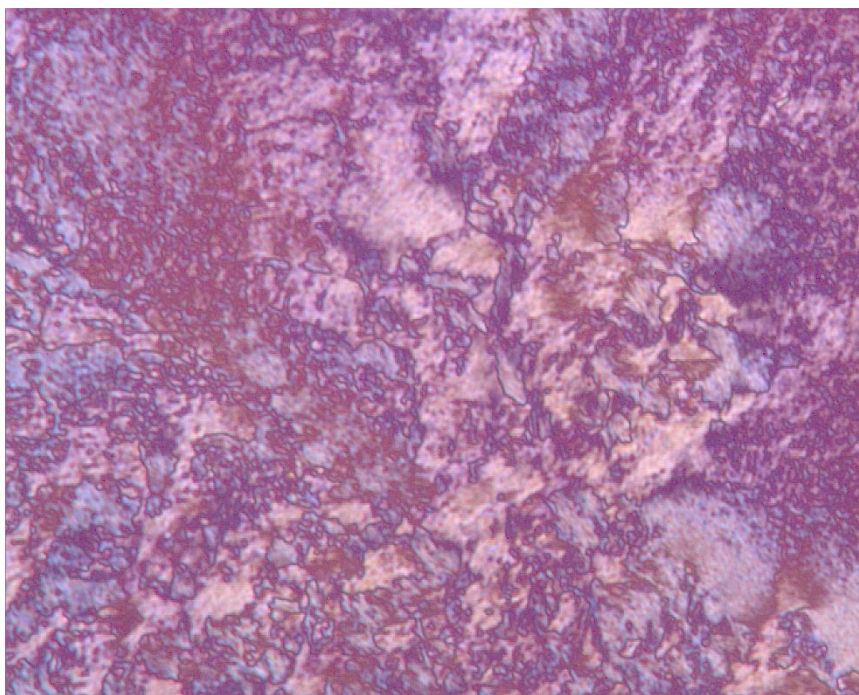


**Figure 2.11.** Birefringent textures of complex **I** observed under POM

Unequivocally, the mesophase determination was achieved by powder X-ray diffraction studies (PXRD) at variable temperatures. Both complexes **I** and **II** present a columnar rectangular organisation ( $\text{Col}_r$ ). The indexations of the PXRD patterns performed using a LCDiXRay, a newly developed program<sup>89</sup> and the cell parameters of complexes **IV** and **V** are presented in Table 2.2, together with the previously reported data of complexes **A–C**, for direct comparison.



No.	Temp.	$d_{\text{obs}}$ (Å)	$hk$	$d_{\text{calcd}}$ (Å)	Mesophase and cell parameters	Density $\rho$ (g.cm <sup>-3</sup> )	Molecules No. in Unit Cell (z)		
A <sup>[12]</sup>	r.t.	32.83	10	32.83	Col <sub>h</sub> , <i>p6mm</i> $a_h = 37.9 \text{ \AA}$ $S_r = 1245 \text{ \AA}^2$	1.2	-		
		19.32	11	18.95					
		4.47	$h_{\text{ch}}$	-					
B <sup>[12]</sup>	r.t.	31.07	10	31.07	Col <sub>h</sub> , <i>p6mm</i> $a_h = 35.9 \text{ \AA}$ $S_r = 1115 \text{ \AA}^2$	1.2	0.98		
		18.67	11	17.93					
		16.24	20	15.53					
		12.24	21	11.74					
		4.36	$h_{\text{ch}}$	-					
		3.44	$h_0$	-					
C <sup>16</sup>	140°C	46.46	20	46.46	Col <sub>r</sub> , <i>c2mm</i> $a_r = 92.9 \text{ \AA}$ $b_r = 42.4 \text{ \AA}$ $S_r = 3939 \text{ \AA}^2$	1.2	4.24		
		38.57	11	38.57					
		24.53	31	25.01					
		21.78	02	21.20					
		14.07	03	14.13					
	On second heatin g cycle	12.83	33	12.86					
		4.56	$h_{\text{ch}}$	-					
		3.39	$h_0$	-					
		I	125°C	32.52	20	32.52	Col <sub>r</sub> , <i>p2gg</i> $a_r = 65.0 \text{ \AA}$ $b_r = 37.2 \text{ \AA}$ $a_r/b_r = \sqrt{3}$ $S_r = 2421 \text{ \AA}^2$	1.2	4.08
				18.62	02	18.62			
14.14	32			14.14					
11.42	23			11.61					
9.17	14			9.22					
On cooling from 1 60°C	8.03		44	8.09					
	7.66		54	7.60					
	6.70		45	6.77					
	4.27		$h_{\text{ch}}$	-					
	3.85		$h_0$	-					
II	r.t.	35.81	20	35.81	Col <sub>r</sub> , <i>c2mm</i>	1.2	3.84		
		21.19	02	21.19					
		14.36	13	13.85					
		12.53	33	12.15					
		7.28	55	7.29					
	On cooling from 1 60°C	4.42	$h_{\text{ch}}$	-					
		4.03	$h_0$	-					
		36.74			Highly disordered L.C.				
		70 °C							
On 2 <sup>nd</sup> heatin g cycle	14.42								

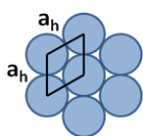
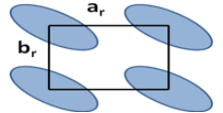
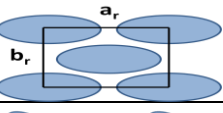
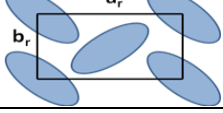
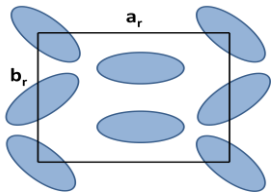
<sup>a</sup> Calculated with  $a_h = 2d_{10}/\sqrt{3}$  (Col<sub>h</sub>); and  $a_r = 2d_{20}$ ,  $b_r = 2d_{02}$  (Col<sub>r</sub>) <sup>b</sup> Not Calculated in absence of  $h_0$  signal.

**Table 2.2.** Indexations of PXRD spectra of complexes A, B, C, I and II

While the substituted azobenzene cyclometallated fragment induced a hexagonal columnar mesophase for complexes **A** and **B** (Figure 2.6) over a very short range of temperature (from r.t. to ca. 50 °C), complexes **C**, **I–II** (Figure 2.8, Scheme 2.1) present a rectangular mesophase over a wide range of temperature up to 160–170 °C. Furthermore, the cell parameters and hence the cross-sections ( $S_r$ ) of their mesophases are much larger than the average radius of the molecules (estimated at ca. 32 Å for **IV**, ca. 53 Å for **V**), as previously observed also for complex **C**, for which it was hypothesised on this basis the formation of a possible dimer constituting the mesophase.<sup>77</sup> To further verify this hypothesis, the number of molecules by cell unit ( $z$ ) for complexes **B**, **C**, **I** and **II** has been estimated according to equation (1),<sup>90</sup>

$$z = \frac{\rho N_A S_r h}{M} \quad (1)$$

where  $\rho$  is the density of the liquid crystal phase,  $N_A$  is Avogadro's constant,  $S_r$  is the columnar cross-section area,  $h$  is the height of the columnar unit cell and  $M$  is the molecular mass of the liquid crystal.  $S_r$  can be easily calculated from the cell parameters keeping in mind that its expression is dependent on the cell's geometry (Table 2.3).

Type	Notation	Space Group	Scheme	Cross section	N° diskoids in cross section
Columnar Hexagonal	Col <sub>h</sub>	p6mm		— —	$Z_{\text{disk}} = 1$
Columnar Rectangular	Col <sub>r</sub>	p2mm			$Z_{\text{disk}} = 1$
		c2mm			$Z_{\text{disk}} = 2$
		p2gg			$Z_{\text{disk}} = 2$
		p2mg			$Z_{\text{disk}} = 4$

**Table 2.3.** Lattice structures of hexagonal and rectangular columnar liquid crystals with corresponding cross section area and number of diskoids  $Z_{\text{disk}}$  (disk or ellipsoid) in the cross section

The height of the columnar unit cell can be extracted from the PXRD pattern as the mean distance given by the halo in the wide angle attributed to intracolumnar stacking distance ( $h=h_0$ ). For the liquid crystal density some hypothesis have to be made. It is customary to consider a standard density of  $1 \text{ g cm}^{-3}$ , a typical value for most organic phases.<sup>91</sup> However, for discotic liquid crystals, density values are expected to be slightly higher. As an example, density values of ca.  $1.1 \text{ g cm}^{-3}$  have been reported for columnar hexaalkoxytriphenylenes<sup>92</sup> and values up to  $1.2 \text{ g cm}^{-3}$  were recently adopted for some potassium salts of columnar crown ethers.<sup>93</sup> A higher density than those encountered in common organic discotics is expected for complexes **A-C** and **I-II**, which contain a Pd(II) metal centre. For this reason, a density value of  $\rho=1.2 \text{ g cm}^{-3}$  has been chosen for all complexes. Under these conditions, the unit cell of the Col<sub>h</sub> mesophase of complex **B** turns out to be constituted of only one molecule. For complex **A** the number of molecules by cell unit cannot be determined, due to the higher disorder of its mesophase, resulting in the absence of the halo peak  $h_0$  in the wide angle region of its PXRD pattern. For all

Nile Red metallomesogens, complexes **C**, **I–II**, Col<sub>r</sub> mesophases have been obtained with a number of molecules by a unit cell of  $Z=4$ . Considering the estimated indexations of their PXRD patterns (Table 2.2) together with the extinction rules,<sup>82c,94</sup> the space groups of the mesophases have been determined to be  $c2mm$  for **C** and **II** and  $p2gg$  for **I**. As evidenced in Table 2.3, for both these space groups the number of diskoids present in the cross-section is  $Z_{\text{disk}}=2$ , which unequivocally implies that each disk is formed by two molecules, forming a dimer-like discoid since  $\text{no molecules} = Z/Z_{\text{disk}} = 4/2 = 2$ . In order to gain a deeper insight into the possible structure of these dimers, we have performed theoretical calculations on **H(NR)** molecules by molecular mechanics (Chapter Ten). The energy-minimised conformation of two drawn up **H(NR)** molecules converged to the geometrically highly stable optimized structure of a dimer presenting a 6-hydrogen-bond network, established between two side-by-side molecules placed in a head-to-tail arrangement, which involves oxygen atoms and aromatic hydrogen atoms of the **H(NR)** molecules, as well as hydrogen atoms of the amino-alkyl chains, as shown in Figure 2.12a. Consequently, the mesophases of the new complexes **I** and **II** are constituted of full-disk shaped dimer structures, as represented in Figure 2.12b. The formation of this dimer structure can explain the high thermal stability of the Col<sub>r</sub> mesophase, which is maintained over a wide temperature range, as well as its higher degree of order when compared to the Col<sub>h</sub> mesophases formed by complexes **A** and **B** (Table 2.2). Another important feature evidenced by the PXRD pattern is the higher order of the columnar mesophase of complex **I** even at high temperatures, when compared with the rather disordered mesophase displayed by complex **II**, for which the indexation of the PXRD pattern was only possible at room temperature, in a frozen state. This drastic increment of disorder can easily be attributed to the additional alkyl-chains on the NR fragment, which probably sterically hinder the  $\pi$ – $\pi$  stacking of adjacent disks that would promote a long-range order within the columns. It is noteworthy that this steric hindrance does not prevent the formation of the highly stable dimeric form of the complex through the hydrogen bonded network.

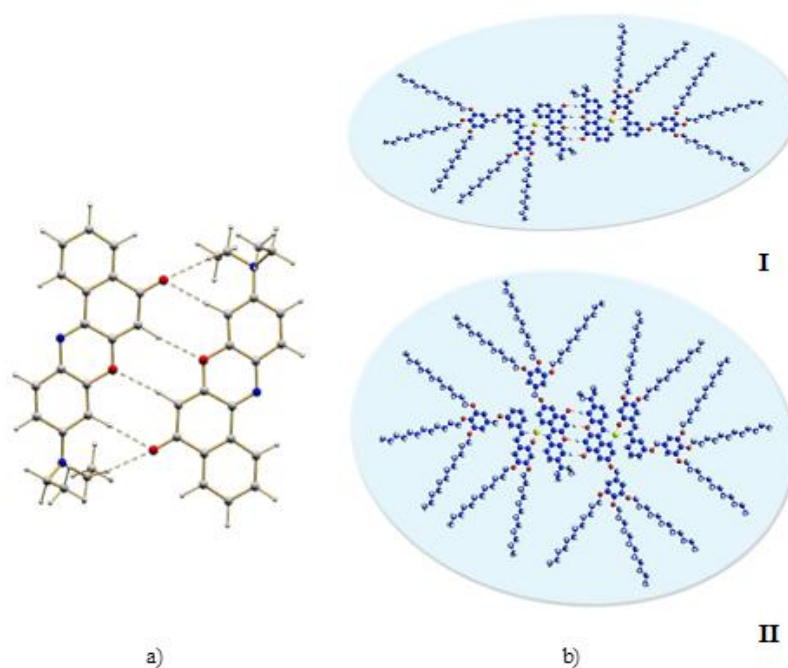


**Figure 2.12.** a) Geometrically optimised structure of **H(NR)** dimer. Hydrogen bonds are represented by dashed lines (from 2.33 to 2.37 Å). b) Scheme of resulting ellipsoid dimers **IV** and **V**

### 2.4.3 Solution electrochemistry

Solution electrochemical data for complexes **I** and **II**, obtained by cyclic voltametry, are collected in Table 2.4, together with the data of parent complexes **(C<sup>^</sup>N)Pd(BSC6)**, **C<sup>^</sup>N = Az, Bq, Pp** (Figure 2.3) for direct comparisons. Within the **(C<sup>^</sup>N)Pd(BSC6)** series, it can easily be noticed that regardless of the nature of the cyclometallated ligand (**H(Az)**, **H(Bq)**, **H(Pp)** or **H(NR)**), the HOMO energy value is maintained at *ca.* 5.4 eV. In contrast, the LUMO energy is highly dependent on the cyclometallated ligand, varying from 2.6 to 3.6 eV. This observation is consistent with the separation between HOMO and LUMO, the HOMO being localised onto the Schiff base fragment while the LUMO is mainly localised onto the cyclometallated fragment, as previously described and confirmed in the case of complexes **(Az)Pd(O<sup>^</sup>N)**, **(Bq)Pd(O<sup>^</sup>N)** and **(Pp)Pd(O<sup>^</sup>N)** by theoretical calculations.<sup>78</sup>



slightly decreased (by ca. 300 mV). This suggests that the addition of supplementary alkyl chains onto the Schiff base ligand allows a fine tuning of the HOMO energy level, lowering it, while the introduction of alkyl chains through an ether linkage onto the Nile Red fragment does not modify the LUMO energy. Furthermore, while the first oxidation for complexes **I** and **II** occurs at the same potential (+300 mV vs. Fc/Fc<sup>+</sup>), the second oxidation for complex **V** occurs at a lower potential, reducing the gap between the two oxidation waves ( $E_{2ox} - E_{1ox} = 300$  mV for **I**,  $E_{2ox} - E_{1ox} = 200$  mV for **II**). This oxidation behaviour suggests that the HOMO+1 might be localised onto the NR fragment and that its energy is stabilised by the ether-linked alkyl chains. It is noteworthy that all redox processes for complexes **I** and **II** are fully reversible, indicative of their high electrochemical stabilities.

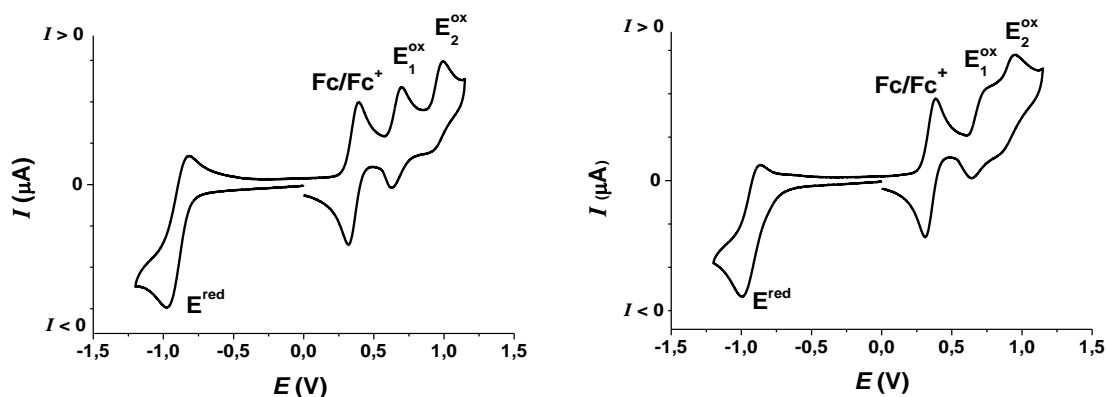


**Figure 2.14.** Cyclic voltammograms of complexes **I** (a) and **V** (b) in the presence of ca. 1eq. of Ferrocene as internal reference (Fc/Fc<sup>+</sup>)  
Scan rate:  $100 \text{ mV}\cdot\text{s}^{-1}$ , DCM,  $\text{Bu}_4\text{NPF}_6$  (0.1M)

#### 2.4.4 UV/Vis spectroscopy and photoconduction

UV-Vis spectra of metallomesogens **I** and **II** were obtained in dichloromethane solution, and data are reported in Table 2.5. The absorption properties of both complexes **I** and **II** are spread on a wide wavelength window. In contrast to complex **C**,<sup>95</sup> no emission was observed, and both complexes do not show the solvatochromic properties of **H(NR)**.<sup>96</sup>

Complex	$\lambda/\text{nm}$ ( $\log \epsilon$ )
<b>I</b>	259 (3.79), 306 (3.45), 334*, 373*, 437 (3.01), 570*, 608 (3.59)
<b>II</b>	254 (3.81), 302*, 352 (3.39), 377*, 573*, 609 (3.44)

**Table 2.5.** Absorption maxima recorded in dichloromethane solution at room temperature.

Both complexes **I** and **II**, however, show photoconductive properties, *i.e.* an increase in electrical conductivity when exposed to light. A typical current increase under light irradiation is shown in Figure 2.15 for complex **I**, where the light was turned on at  $t=2.5$  s and turned off at  $t=17.5$  s.

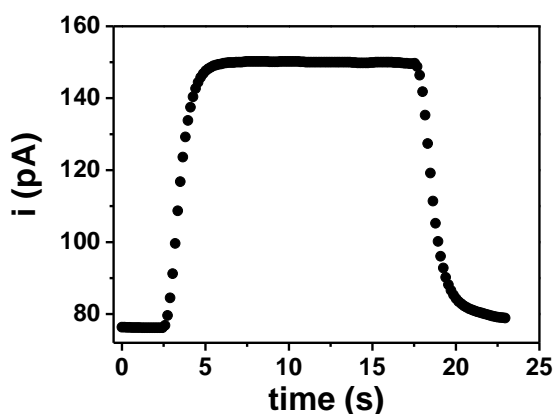


**Figure 2.15.** Current measured on a sample of **I** exposed to light at  $\lambda = 560$  nm under an applied electric field  $E = 23$  V/ $\mu\text{m}$

Figure 2.16 shows the photoconductivity of complexes **I** and **II** versus the applied electric field  $E$ , normalized over the absorption coefficient  $\alpha$  and the light intensity  $I$ . For complex **II**, it was not possible to acquire data with an applied field higher than 7-8 V/ $\mu\text{m}$  because of dielectric breakdown at higher fields. It is clear that the photoconductivity of **I** is about 1 order of magnitude higher than in **II**. This difference could be explained by considering that the stacking distance of **I** is shorter than in **II** (3.85 Å vs. 4.03 Å). In addition, and perhaps more importantly, **I** exhibits a higher long range order within the columns. It is well known that in discotic liquid crystals both a long range order and a short stacking distance increase the  $\pi$ -orbitals overlap between neighbouring molecules in the columns, favouring one-directional charge transport. This can increase charge mobility and photoconductivity even by several orders of magnitude.<sup>97</sup>



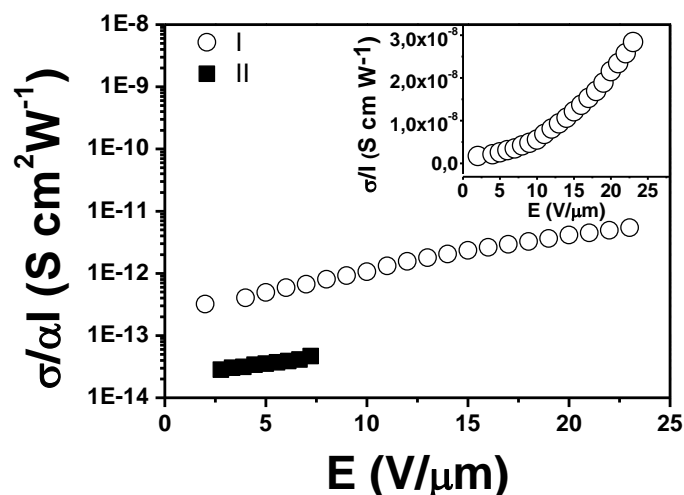


**Figure 2.16.** Photoconductivities normalized over the absorption coefficient  $\alpha$  and the light intensity  $I$  are reported for **I** and **II**. The experiments were performed at  $\lambda=520$  nm and  $I=5 \cdot 10^{-3}$  W/cm<sup>2</sup> for **I** and at  $\lambda=633$  nm and  $I = 2$  W/cm<sup>2</sup> for **II**, while the absorption coefficients were 5213 cm<sup>-1</sup> for **I** and 112 cm<sup>-1</sup> for **V**. The inset shows the photoconductivity of **I** normalized over light intensity only

The data reported in the inset of Figure 2.16 show that the  $\sigma/I$  value for **I** is in the order of  $3 \cdot 10^{-8}$  S cm W<sup>-1</sup> at 25 V/ $\mu$ m, which is a very high value when compared to the photoconductivity of other organic photoconductors,<sup>98</sup> especially because this result is obtained without addition of dopants and without any annealing process to increase the order. This result represents a tremendous step forward in the development of this class of photoconductors since in previously analysed cyclopalladated complexes, at the same applied electric field, the  $\sigma/I$  value was of the order of  $10^{-12}$  S cm W<sup>-1</sup> for annealed cyclopalladated discotics (complexes **A** and **B**),<sup>79</sup> while it was of ca.  $10^{-9}$  S cm W<sup>-1</sup> for crystalline samples of the (C<sup>^N</sup>)Pd(O<sup>^N</sup>) series reported in Figure 2.1 and of the order of  $10^{-12}$  S cm W<sup>-1</sup> for amorphous samples (Figure 2.17).<sup>78</sup>

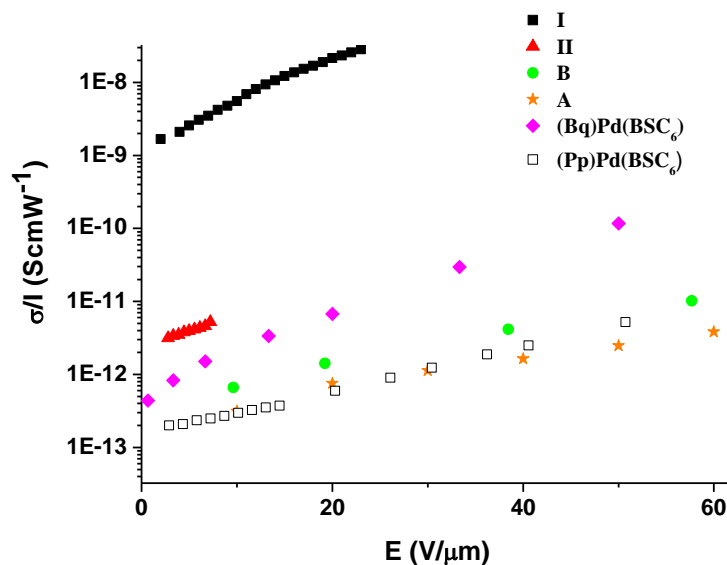


**Figure 2.17.** Comparison between photoconductivities measured for cyclopalladated complexes **A-B**, **I-II**, **(Bq)Pd(BSC<sub>6</sub>)** and **(Pp)Pd(BSC<sub>6</sub>)**

From Figure 2.17 it is clearly seen that complex **I** presents the highest photoconductive response of all until now studied cyclopalladated complexes. Noteworthy, the photoconduction of **I** is even higher than those of crystalline samples of **(Bq)Pd(BSC<sub>6</sub>)** or annealed discotics **A** and **B**. This should be the result of the high order of the LC mesophase of **I**, which significantly increase the charge transport properties.

The wavelength dependence of the normalized photocurrent and of the absorption coefficient of complex **I** is reported in Figure 2.18. For photoconduction measurements, a particular cell geometry (Chapter Ten) has been used, allowing the observation of the photocurrent even for high values of absorption coefficients and for wavelengths well below the absorption limit of the ITO covered glass substrates. The observed photocurrent is proportional to the absorption of the material. In particular, it is noteworthy that how even a little decrease in the absorption between 300 nm and 330 nm results in a corresponding decrease in the photocurrent. Such behaviour was also observed for complex **II**. These new complexes show, therefore, photoconductive properties on a quite wide range of wavelength from below 200 nm up to 800 nm.

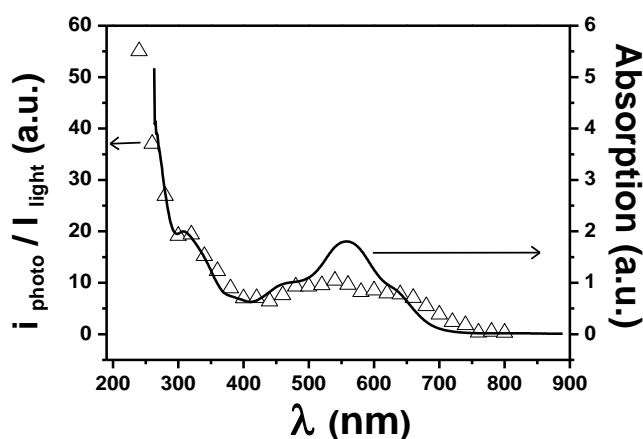


**Figure 2.18.** Normalized photocurrent and absorption, measured on film, versus the wavelength for compound **I**. Photoconductivity measurements were performed with an applied field  $E = 16 \text{ V}/\mu\text{m}$

Photoconductivity was also measured as a function of the intensity of light. As shown in Figure 2.19, it can clearly be deduced that the photocurrent varies with the square root of the light intensity. This can be explained by assuming that the carrier kinetics is controlled by a bi-molecular recombination process.<sup>99</sup>

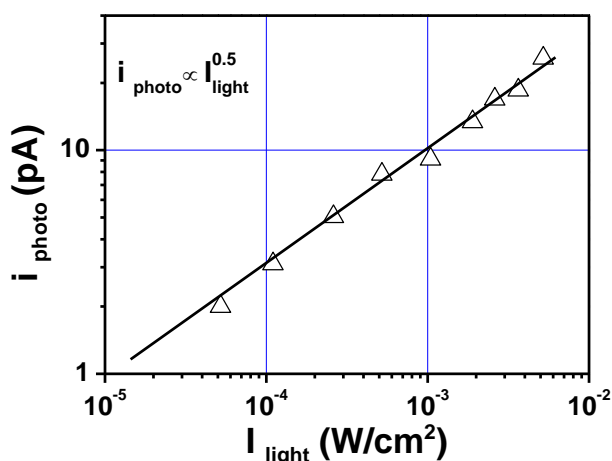
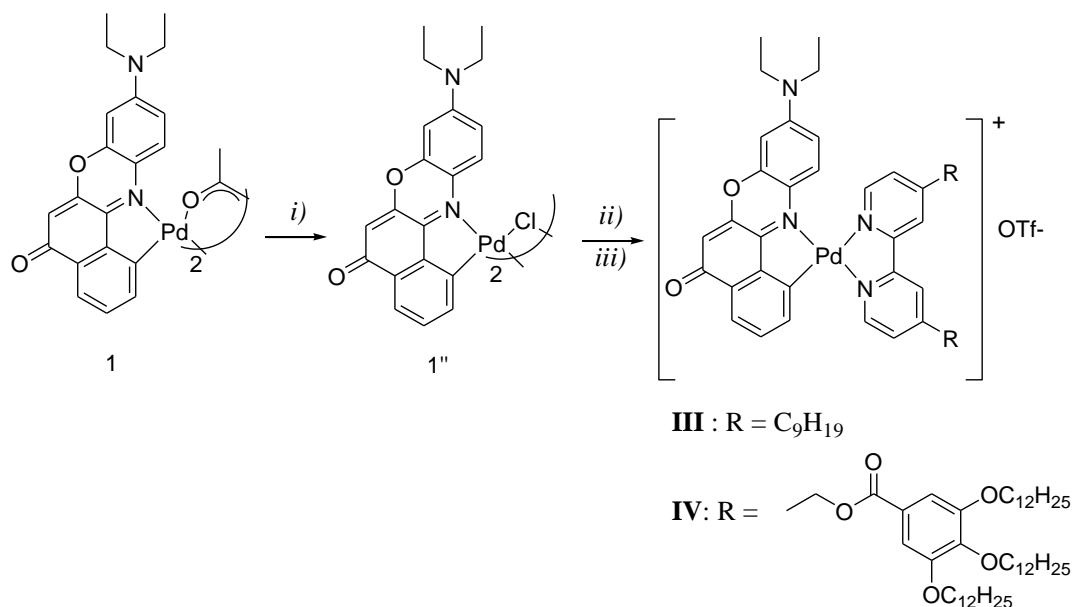


**Figure 2.19.** Photocurrent versus light intensity for **I**. Measurements were performed at  $\lambda = 520 \text{ nm}$  with an applied field  $E = 16 \text{ V}/\mu\text{m}$

The extended absorption window coupled with their photoconductive properties render such Nile Red metallomesogens potential candidates for many optoelectronic applications, particularly in photovoltaics where such features are important, a field in which organic discotics have recently proven to boost the power conversion efficiencies of devices.<sup>100</sup>

## 2.5 Cationic cyclopalladated Nile Red metallomesogens

Taking advantage from the well known chemistry of the cyclopalladated compounds,<sup>101</sup> and in order to study the possible effects of charges and the presence of the counter anions onto the supramolecular organisation, we have synthesised cationic cyclopalladated complexes of comparable structure with those already described in this Chapter. Two differently polyalkylated 2,2'-bipyridines H(C<sub>n,m</sub>-bpy) were used as ancillary ligands to afford complexes **III** and **IV** of general formula: [NRPd(C<sub>n,m</sub>bpy)]<sup>+</sup>[OTf]<sup>-</sup> where C<sub>n,m</sub> represents the number and the length of the substituted alkyl chains as illustrated in Scheme 2.4 (for complex **III**: n = 2, m = 9; for complex **IV**: n = 6, m = 12).



**Scheme 2.4.** Reagents and conditions:

- i) LiCl, ethanol/water, r.t., 5 d.;
- ii) AgCF<sub>3</sub>SO<sub>3</sub>, acetone, reflux, 2h, r.t., 12h;
- iii) H(C<sub>n,m</sub>-bpy), acetone, reflux for 6h., r.t. for 12 h.

While H(C<sub>2,9</sub>-bpy) is commercially available, H(C<sub>6,12</sub>-bpy) was synthesised following the previously reported procedure.<sup>102</sup> Complexes **III** and **IV** were synthesised from the previously obtained acetato-bridge dimer **1** (Scheme 2.4) which was engaged in a metathesis reaction in excess of lithium chloride in ethanol/water to afford in quantitative yield the corresponding chloro-bridge dimer intermediate **1''**. Bridge splitting reaction of **1''** with the formation of the new ionic species were

effectuated in acetone solution in the presence of quantitative amount of silver triflate, followed by addition of the corresponding H(C<sub>n,m</sub>-bpy) 2,2'-bipyridine ligand after filtration of the silver chloride precipitate.

Both complexes **III** and **IV** were obtained as intense dark blue waxy solids, highly soluble in most organic solvents. IR spectra shown the characteristic stretching bands of the triflate (OTf) ion observed at 1257, 1030 and 638 cm<sup>-1</sup> as well as the intense stretching band at 1635 cm<sup>-1</sup> characteristic of NR fragment carbonyl group. The intensity of the dark colour of both complexes and the high viscosity of the samples prevented a constructive observation through POM microscopy and lead to a high difficulty in the phase transition temperature determination. Nonetheless, on the basis of the increased fluidity observed during heating, a melting temperature of ca. 180 °C and ca. 160 °C for complexes **III** and **IV** respectively can be attributed. The thermal behaviour of these complexes was investigated by thermogravimetric analysis (TGA) showing that both complexes are stable up to ca. 200 °C. Differential scanning calorimetry (DSC) runed at 5 °C/min and 2 °C/min scan rates did not present for both complexes any visible thermal transitions indicating a complete amorphous/glassy state. However, under PXRD analysis, while complex **III** showed the typical broad patterns of a glassy state morphology independently on the temperature/time chosen, complex **IV** upon annealing from the melt (160 °C) at 100 °C for 24 h and further 5 h at 50 °C presented a PXRD pattern characteristic of a columnar organization, which indexation is reported in Table 2.6.

T (°C)	d <sub>obs</sub> (Å)	hk	d <sub>clcd</sub> (Å)	Mesophase and cell parameters
50 °C	36.48	20	36.48	Col <sub>r</sub>
	21.22	11	21.22	a <sub>r</sub> =72.96 Å
After annealing at 100 °C for 24 h and at 50 °C for 5h	18.94	21	18.95	b <sub>r</sub> =22.18 Å
	16.67	31	16.39	
	4.46	h <sub>ch</sub>	-	

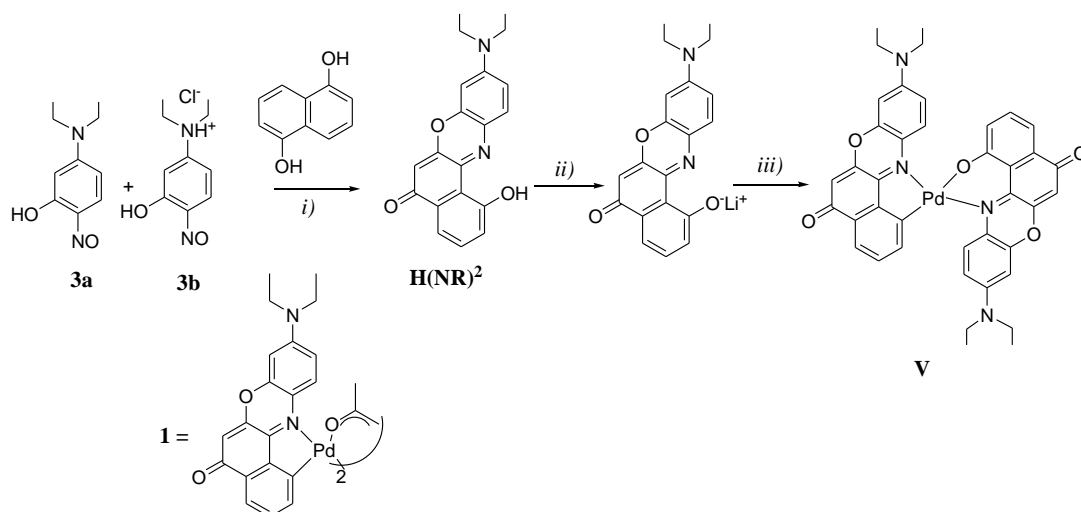
**Table 2.6.** Detailed indexation of the PXRD spectra of complex **IV** obtained by annealing from the melt (160 °C) for 24 h at 100 °C followed by 5 h at 50 °C

As for its parent neutral complexes **I** and **II**, the high cell parameter obtained for complex **IV** ( $a = 72.96 \text{ \AA}$ ) is indicative of the presence of a similar dimeric association of molecules, leading to a full disk-shape like structure. The long time required for the development of the columnar texture of complex **IV** and the low resolution of its PXRD spectrum (in terms of peak numbers and intensity) compared with the PXRD spectrum obtained for complex **IV** is indicative of a higher disorder. This latter could be easily attributed to both the presence of the triflate counter ion as well as the electrostatic repulsions that seem to hinder the stacking efficiency within the columns more than the formation of the hydrogen bonding network within the dimer. The lower number of alkyl chains results in absence of thermotropic behaviour for complex **III** which remains in its glassy state until its thermal decomposition at ca. 200 °C. Unfortunately for both complexes, light emission was not observed in solution nor in the solid state most likely due to the quenching of the 2,2'-bipyridine ancillary ligands by electronic effects.

## 2.6 Using Nile Red as an ancillary ligand in a cyclopalladated complex

### 2.6.1 Synthesis

In the attempt to further study the chemistry and the interesting electrochemical properties of the Nile Red cyclopalladated compounds, a new complex bearing a hydroxy Nile Red derivative as ancillary ligand was synthesized (Scheme 2.3). The coordination sphere of the Nile Red cyclopalladated complex **V** is completed by a 1-hydroxy Nile Red derivative,  $\text{H}(\text{NR})^2$  acting as an  $\text{H}(\text{O}^-\text{N})$  Schiff base, which was obtained following the same procedure described earlier in this Chapter (section 2.2.1), by reaction of the mixture **3a,b** (Scheme 2.2) with 1,5-dihydroxynaphthalene.<sup>86-88</sup>



**Scheme 2.3.** Synthesis of complex **V**. Experimental conditions: *i*) HCl, H<sub>2</sub>O, 0-5 °C, 4h; *ii*) BuLi, dry THF, -78 °C, 15 min.; *iii*) **1**, dry THF, r.t., overnight

As reported in literature,<sup>103</sup> **H(NR)**<sup>2</sup> forms a hydrogen bond between the acidic proton and the electron donating pyridinic nitrogen atom which prevents the deprotonation in normal reaction conditions (Figure 2.20) and require more drastic conditions *i.e.* anhydrous solvent and strong base.

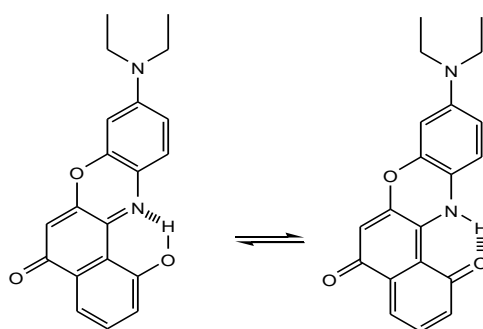


**Figure 2.20.** Intramolecular hydrogen bond induced tautomeric forms of **H(NR)**<sup>2</sup><sup>104</sup>

In fact, the attempts to deprotonate **H(NR)**<sup>2</sup> with common protic bases like NaOH and NaOCH<sub>3</sub> resulted unsuccessful due to the instability of its conjugated anion which tends to rapid capture protons from the environment. Therefore, the deprotonation of **H(NR)**<sup>2</sup> was directly *in situ* under rough conditions (buthyl lithium, dry tetrahydrofuran). A novel cyclopalladated complex was thus obtained by adding, to the preformed lithium salt, the Nile Red acetato bridged dimer **1** (Scheme 2.3). This is the first example of using a Nile Red derivative as an ancillary ligand. The complex was characterised by <sup>1</sup>H NMR, FT IR, UV-vis, elemental analysis (Chapter Ten) and electrochemistry.

## 2.6.2 Solution electrochemistry

Solution electrochemical data was obtained for complex **V** by cyclic voltametry and the cyclic voltamogram (comprising the oxidation of the internal standard couple  $\text{Fc}/\text{Fc}^+$ ) is presented in Figure 2.21. The redox behaviour of complex **V** is very similar to the ones reported for the parent complexes **I** and **II** (Figure 2.17). The data relative to complex **V** is reported in Table 2.6, together with the data of the already discussed complexes **I** and **II** for direct comparisons. Two one-electron reversible oxidations occur for **V**, the first reasonably attributed to the ancillary O<sup>^</sup>N Nile Red derivative, while the second is presumably attributed, taking into account the already observed redox behaviour of **I** and **II**, to the cyclometallated Nile Red fragment. The reduction behaviour of complexes **I**, **II** and **V** is identical and accounts for a reversible one-electron reduction wave attributed to the reduction of the cyclometallated Nile Red fragment. It is noteworthy that the oxidation of the ancillary Nile Red ligand occurs at nearly the same potential as the Schiff base in **I** and **II** ( $E_{\text{ox}}^{\text{NR}}=0.36$  mV vs.  $\text{Fc}/\text{Fc}^+$  with respect to  $E_{\text{ox}}=0.3$  mV vs.  $\text{Fc}/\text{Fc}^+$ ). The frontier orbitals HOMO/LUMO separation must be consequently maintained as in the parent complexes,<sup>78</sup> with the LUMO level located on the cyclometallated ligand, while the HOMO is prevalently situated on the ancillary Nile Red fragment. The HOMO+1 level seems to be associated with the cyclometallated molecular fragment, as in **I** and **II** (Section 2.2.3). The HOMO and LUMO estimated positions remain practically unchanged with respect with IV and V (Table 2.6).

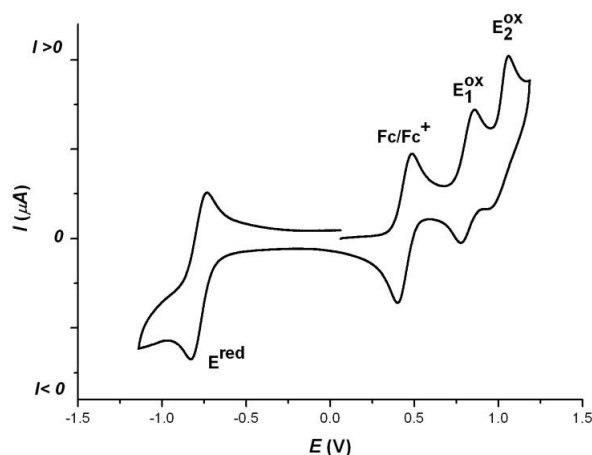


**Figure 2.21.** Cyclic voltamogram of **V**.  $\text{Fc}/\text{Fc}^+$  is used as an internal standard



No.	$E^{\text{red}}$ (V) vs. Fc/Fc <sup>+</sup>	$E^{\text{ox}}_1$ (V) vs. Fc/Fc	$E^{\text{ox}}_2$ (V) vs. Fc/Fc	Estimated LUMO (eV)	Estimated HOMO (eV)
<b>I</b>	-1.20 (Rev.)	+ 0.30 (Rev.)	+0.60 (Rev.)	- 3.6	- 5.1
<b>II</b>	-1.20 (Rev.)	+ 0.30 (Rev.)	+0.55 (Rev.)	- 3.6	- 5.1
<b>V</b>	-1.23 (Rev.)	+0.36 (Rev.)	+0.56 (Rev.)	-3.5	-5.2

Rev.=Reversible wave, Irr.=Irreversible wave

**Table 2.6.** Cyclic voltametry data. Potentials are given versus ferrocene/ferrocinium (Fc/Fc<sup>+</sup>)

### 2.6.3 UV/Vis spectroscopy

UV-Vis spectra of complex **V** was obtained in dichloromethane solution, and data is reported in Table 2.7. The absorption properties of complex **V** are very similar with **I** and **II** and is spread over a wide wavelength window. As in the case of **I** and **II**, no emission nor any solvatochromism behaviour were observed.

Complex	$\lambda/\text{nm}$ ( $\log \epsilon$ )
<b>V</b>	261 (3.78), 310 (3.50), 333*, 374*, 438 (3.02), 575*, 609 (3.49)

**Table 2.5.** Absorption maxima recorded in dichloromethane solution at room temperature.

### 2.6.4 Photoconduction

In complex **V**, as suggested by the electrochemistry characterization, the HOMO/LUMO separation is reasonably maintained. This indicates, taking into account the results obtained for similar compounds, that complex **V** may behave as a photoconductor. In order to further investigate the properties of this novel Nile Red complex, photoconductivity measurements are in progress.

## 2.7 Conclusions

Through the synthesis of complexes **I-V**, we have shown the possibility of using Nile Red both as a cyclometallated and as an ancillary ligand obtaining either neutral or cationic cyclopalladated complexes. When an O<sup>N</sup> fragment (Schiff base or Nile Red derivative) is used as ancillary ligands, neutral complexes **I**, **II** and **V** are obtained.

Two of the neutral complexes, bearing an alkyl chain substituted Schiff base exhibit a columnar rectangular mesophase in a wide temperature range were, while complex **V** represents the first example of using a monoanionic Nile Red derivative as an ancillary ligand. The mesophases were obtained by the self-assembly of ellipsoidal dimeric pairs kept together by a hydrogen bonding network. This particular dimer interaction lends a high stability to the mesophase and, in the case of complex **I**, also a high order. The additional introduction of alkyl chains onto the Nile Red fragment (complex **II**) does not prevent the formation of these dimeric pairs but dramatically increases the columnar disorder by steric hindrance. All the three complexes have shown an amphoteric similar redox behaviour with fully reversible oxidation and reduction processes, showing their high electrochemical stabilities. Through the electrochemical estimation of the energy levels of their frontier orbitals, we have shown that HOMO and LUMO are physically separated by the Pd(II) metal centre, the HOMO being mainly distributed onto the ancillary ligand regardless of the fact of being a Schiff base or a Nile Red derivative, while the LUMO is mainly localized onto the cyclometallated Nile Red fragment. A band-gap of ca. 1.5 eV imparts to these complexes a wide range window of absorption from the UV-Vis up to the near IR region, while the HOMO/LUMO physical separation probably originates the excellent photoconduction properties of **I** and **II**. Indeed, photoconductivity measurements, performed with a cell geometry that allows the observation of photocurrent even at low wavelengths, have been performed on **I** and **II**. These measurements have shown the correlation between the absorption of the complexes and its photocurrent, with normalized photocurrent values reaching  $3 \cdot 10^{-8}$  S cm W<sup>-1</sup> at an applied electric field  $E = 25$  V/ $\mu$ m. The photoconductivity behaviour of **V** is still to be investigated, in order to better elucidate the role of the ancillary ligand. All together, the features displayed by these new complexes constitute highly

significant improvements towards the use of such complexes in optoelectronic devices.

Furthermore, cationic cyclopalladated complexes **III** and **IV** have been obtained presenting, in the case of 12 alkyl chains, a disordered columnar liquid crystal organisation. As a result of the structural similarities between metallomesogens **I** and **IV**, it has been possible to observe the influence of charges onto the columnar supramolecular organisation of the mesophase. Electrostatic interactions generated by the ionic nature of complex **IV** do not prevent the formation of the dimers that constitute the building blocks of the mesophase, but increase the intracolumnar disorder, hindering the mesophase induction upon cooling.



## Chapter Three

### Electropolymerizable Nile Red cyclopalladated complexes for bulk heterojunction solar cell application

#### 3.1 Introduction

As previously discussed in Chapter 1, polymers have often been used in bulk heterojunction solar cells, reaching efficiencies up to 8%,<sup>24</sup> while low molecular weight donors based heterojunction cells reached only very recently an efficiency of 7.3%.<sup>105</sup> The higher interest showed so far for polymer solar cells with respect to low molecular weight devices is probably due to the higher charge mobilities presented by most polymeric materials and to the higher versatility for controlling their morphology in devices (choice of solvents, annealing temperature, concentration of the components in the absorbing solution).<sup>106</sup> Nevertheless, despite of their high performances, polymers present some drawbacks related to the high molecular weight dispersity, the batch to batch reproducibility etc.<sup>27a</sup> On the contrary, low molecular weight donors do not show the same problems since they are high purity materials with well defined molecular structures, definite molecular weights and recently demonstrated high charge carrier mobility.<sup>107</sup>

The recently used low molecular weight donor in bulk heterojunction solar cells are: i) electron donating containing fragments or ii) conjugated dyes derivatives. Among the first category, triarylamine derivatives, showing strong electron donating and good hole transport properties (**A**,<sup>108</sup> **B**<sup>109</sup> in Figure 3.1) and sulphur containing electron donating heterocycles such as oligothiophenes, fused thiophenes or benzo[1,2-4b,5b']dithiophene (**C**,<sup>110</sup> **D**<sup>111</sup>) have been successfully used in solar cells. Dyes like porphyrins, with their extensively conjugated  $\pi$  system inducing fast electron transport, high absorption properties and tuneable photochemical properties have been functionalized (**E**<sup>112</sup>) and used in bulk heterojunction solar cells, so as squaraine dyes, especially 2,4-bis[4-(N,N-diisobutylamino)-2,6-dihydroxyphenyl] squaraine (**F**<sup>113</sup>) or merocyanine (**G**<sup>114</sup>). These donor low molecular materials have been used with fullerene C<sub>70</sub>, PC<sub>61</sub>BM or PC<sub>71</sub>BM as acceptors.

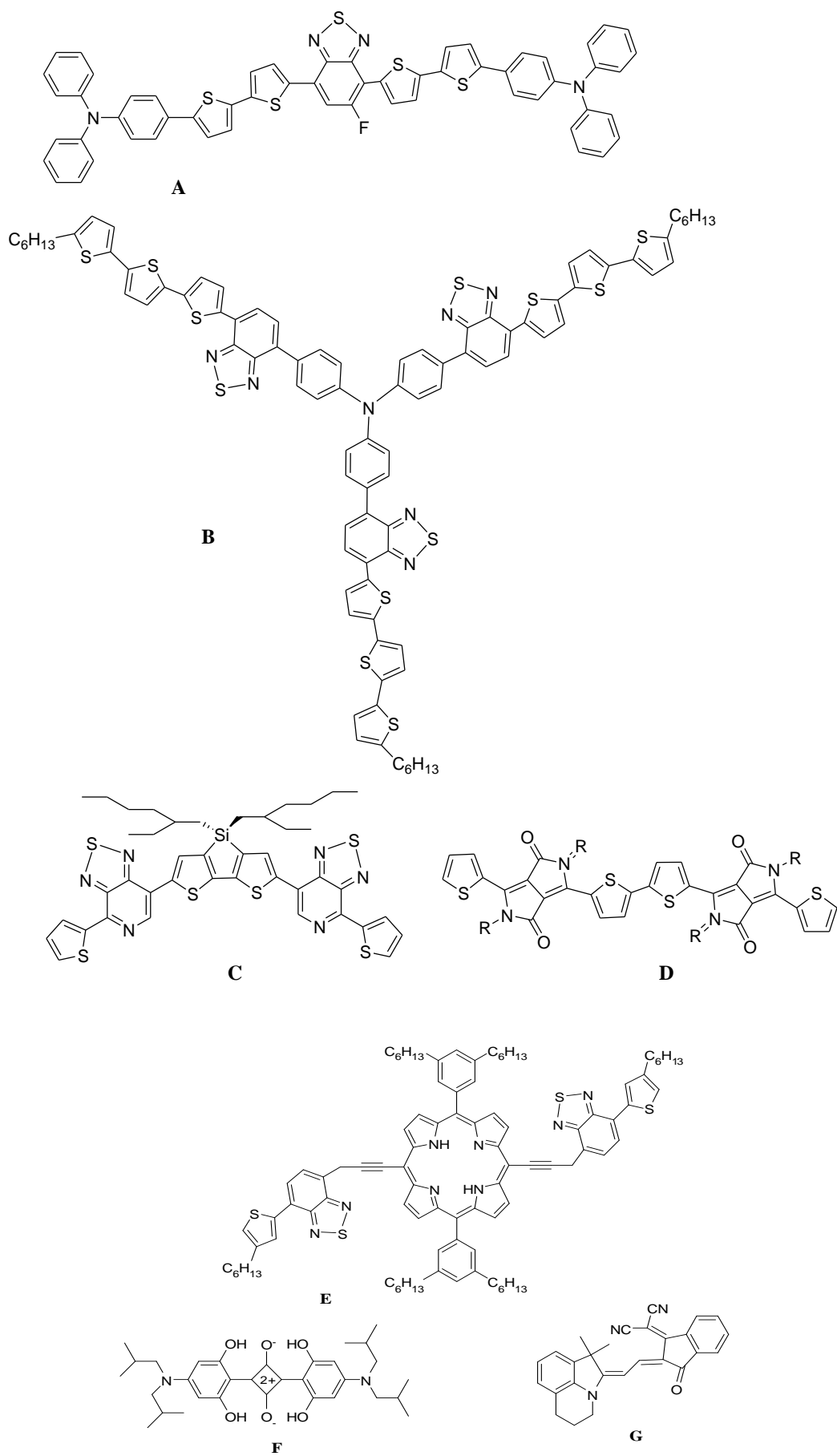


**Figure 3.1.** Low molecular weight donors used in bulk heterojunction solar cells<sup>27a</sup>

In the synthesis of low molecular weight donors in bulk heterojunction solar cells, in order to further improve efficiencies, several parameters need to be considered: i) electron donating/withdrawing abilities of the molecular fragments, ii) frontier orbitals energy levels, iii) molecular material charge mobility, iv) molecular self assemble behaviour and dipole-dipole interactions.<sup>27a</sup>

Another versatile alternative to organic polymers in solar cells is represented by metal containing polymers.<sup>115</sup> The introduction of transition metal ions into conjugated polymers offers strength points as: i) the central metal ion can act as architectural template in the assembly of the organic subunits; ii) they may provide redox-active or paramagnetic centres to generate active species for charge transport and may influence the optoelectronic properties of conjugated systems; iii) they allow fine tuning of HOMO/LUMO energies (affording values compatible with those of the electrodes used in the fabrication of devices) through the interaction of the metal *d* orbitals with the ligand orbitals; iv) provide a wide variety of possible frameworks based on different coordination numbers and molecular geometries. Moreover, due to spin-orbit coupling, efficient intersystem crossing is verified in such organometallic species, leading to the formation of longer lifetime triplet excitons allowing longer diffusion length.<sup>115</sup> Among these, polyplatinyne<sup>116</sup> and Zn(porphyrin)-dithiophene polymers with acetylene linkage<sup>117</sup> have demonstrated their efficiency (Figure 3.2).

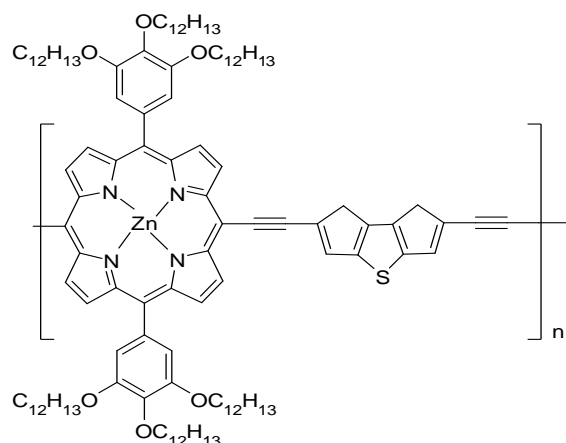


**Figure 3.2.** Zn(porphyrin)-dithienothiophene polymer

However, whether polymeric or low molecular weight materials are used, the performance of bulk heterojunction solar cells depends mainly on the same factors: light absorption, exciton diffusion, efficiency of exciton dissociation at the heterojunction and charge mobility.

In this context, considering the good absorption properties of Nile Red cyclopalladated complexes, the separation HOMO/LUMO which induces high photogeneration and their photoconduction properties, the scope of this project is to test a cyclopalladated Nile Red complex as a low molecular weight donor in a bulk heterojunction solar cell.

### **3.2 Testing a Nile Red cyclopalladated photoconductor in a bulk heterojunction solar cell**

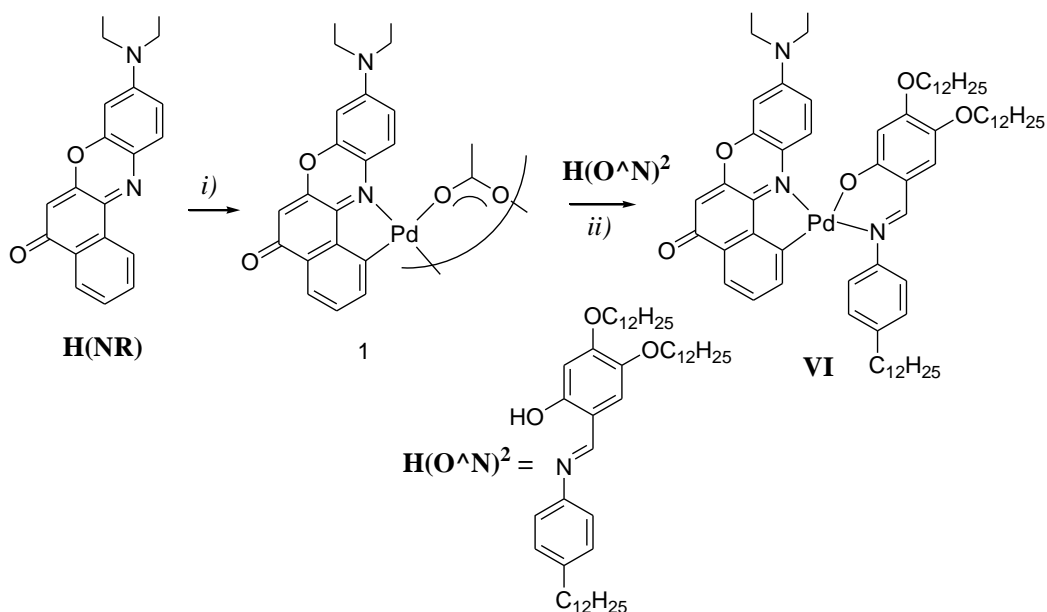
We present herein the results obtained on a bulk heterojunction cell formed by PC<sub>61</sub>BM and a cyclopalladated Nile Red complex (Scheme 3.1). This compound belongs to the new class of photoconductors presented in Chapter 2 and has been chosen as a representative model to test the feasibility of using such photoconducting low molecular materials in bulk heterojunction solar cells. The work has been also aimed at establishing the possible improvement in exciton dissociation that can be achieved if the materials used are intrinsic photogenerators.

The photoconducting properties of this complex make it a good candidate for testing the effect of intrinsic charge photogeneration on exciton dissociation.

#### **3.2.1 Synthesis**

The cyclopalladated complex **VI** was synthesised through the two steps procedure which involves the formation, by reaction of Nile Red with Pd(OAc)<sub>2</sub>, of the acetato-bridged dimer **1**,<sup>85</sup> followed by its rupture upon addition of the Schiff base ligand, as illustrated in Scheme 3.1.





**Scheme 3.1.** Reagents and conditions: i) Pd(OAc)<sub>2</sub>, acetic acid, 55 °C, 4h; ii) **H(O<sup>^</sup>N)<sup>2</sup>**, ethanol, reflux, 2d.

The required Schiff base **H(O<sup>^</sup>N)<sup>2</sup>** was quantitatively obtained by condensation of 4-dodecylaniline with 4,5-bis(dodecyloxy)-2-hydroxybenzaldehyde in refluxed ethanol, following previously reported procedures.<sup>79</sup>

### 3.2.2 Electrochemistry

The cyclic voltametry of complex **VI** is reported in Figure 3.3 and presents the typical redox behaviour observed for cyclopalladated complexes with a cyclometallated Nile Red ligand and an ancillary Schiff base with the LUMO situated on the cyclometallated fragment and the HOMO onto the Schiff base ligand.

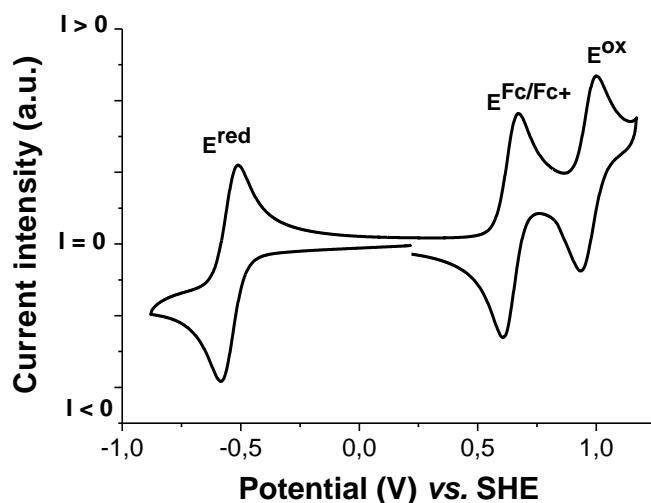


**Figure 3.3.** Cyclic voltametry of complex **VI**

A reversible one-electron oxidation attributed to the Schiff base and a reversible one-electron reduction of the Nile Red fragment are observed. The redox potentials vs.  $\text{Fc}/\text{Fc}^+$  as well as the estimated HOMO and LUMO energies are listed in Table 3.1.

Complex No.	$E^{\text{red}}_{\text{NR}} (\text{V})^a$	$E^{\text{ox}}_1 (\text{V})^a$	HOMO (eV)	LUMO (eV)
<b>VI</b>	-1.19 (R)	+0.33 (R)	-5.13	-3.61
<sup>a</sup> Potentials expressed in volts vs. $\text{Fc}/\text{Fc}^+$ ; R=reversible				

**Table 3.1.** Cyclic voltametry data relative to complex **VI**

### 3.2.3 Bulk heterojunction cell

Complex **VI** was chosen not only for the separation HOMO/LUMO, but also because it exhibits an extended absorption range, from 250 nm up to  $\lambda \sim 650$  nm, which is desirable for photovoltaic applications. In addition, the presence of long alkyl chains improves processability during spin coating.

As in the case of other complexes of the same class, complex **VI** is also a photoconductor. Photoconductivity measurements were carried out both on pure **VI** and on samples doped with less than 1% of  $\text{C}_{60}$ . As it is evident from the results illustrated in Figure 3.4, the photoconductivity increases by two orders of magnitude in the presence of  $\text{C}_{60}$ , without a measurable increase in absorption. Since  $\text{C}_{60}$  is a well known electron acceptor, such increase in photoconductivity shows that i) there is a significant

electron transfer from the excited state of **VI** to C<sub>60</sub> and ii) complex **VI** is a hole conductor, as already known for the other complexes of the class (C<sup>^</sup>N)Pd(O<sup>^</sup>N) (Chapter 2).

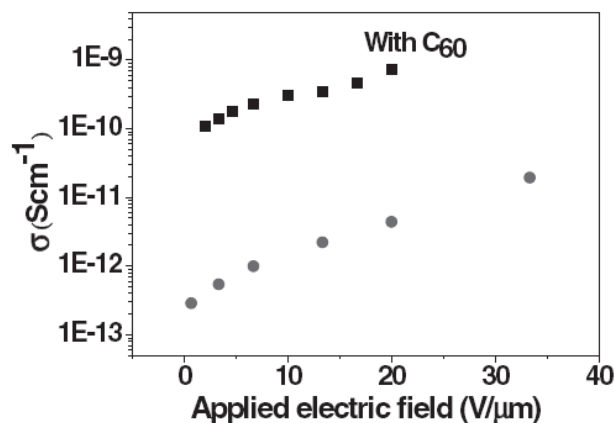


**Figure 3.4.** Photoconductivity of pure complex **VI** and of complex **VI** doped with C<sub>60</sub> as a function of the applied electric field. The measurements were carried out at  $\lambda=633$  nm, with a light intensity of  $I=0.65$  W/cm<sup>2</sup>

On the basis of these observations, the use of **VI** in bulk heterojunction solar devices, in combination with soluble derivatives of C<sub>60</sub>, seemed possible. **VI** was also chosen for its potential compatibility (see HOMO/LUMO values in Table 3.1) with the energy levels of the components of a typical bulk heterojunction cell (Figure 3.5) The most common soluble commercial C<sub>60</sub> compound that plays the role of acceptor in bulk heterojunction cells is PC<sub>61</sub>BM, which was used, in combination with **VI**, to obtain photovoltaic cells, as described in Chapter Ten. The chemical structure of PC<sub>61</sub>BM is shown in Figure 3.5, together with a schematic diagram of the energy level alignment of frontier orbitals for the donor **VI**, the acceptor (PC<sub>61</sub>BM), the PEDOT:PSS hole injection layer and the work functions of the electrodes within the cells.

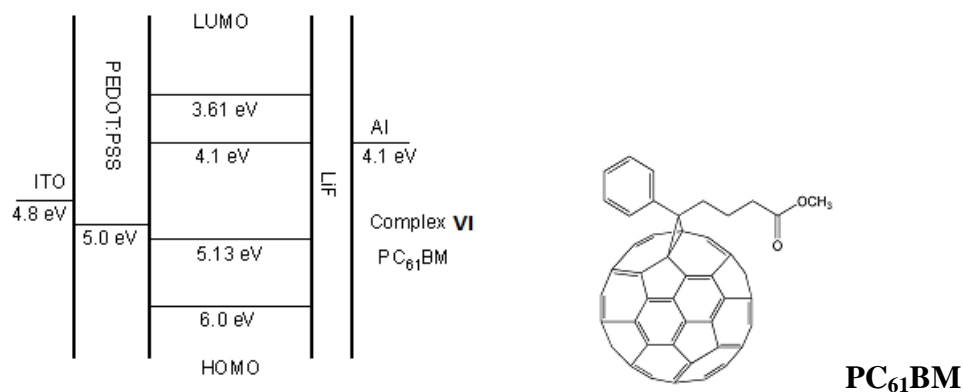


**Figure 3.5.** Schematic illustration of the energy levels alignment of the materials used in the device. The chemical structure of PC<sub>61</sub>BM is also shown

It is well known that in bulk heterojunction solar cells, performance is strongly affected by the morphology of the interpenetrating phases, which, in turn, depends on both the solvent and the molar ratio of the active components (acceptor/donor).<sup>118</sup> Bulk heterojunction cells were prepared as mentioned in Chapter Ten by using different solvents, such as dichloromethane, chloroform and chlorobenzene. The best performing solvent was chlorobenzene and only results obtained by using such solvent will be illustrated in the following. Typical J-V curves in the dark and under illumination are shown in Figure 3.6 for a VI:PC<sub>61</sub>BM weight ratio of 1:4, which gave the best results.

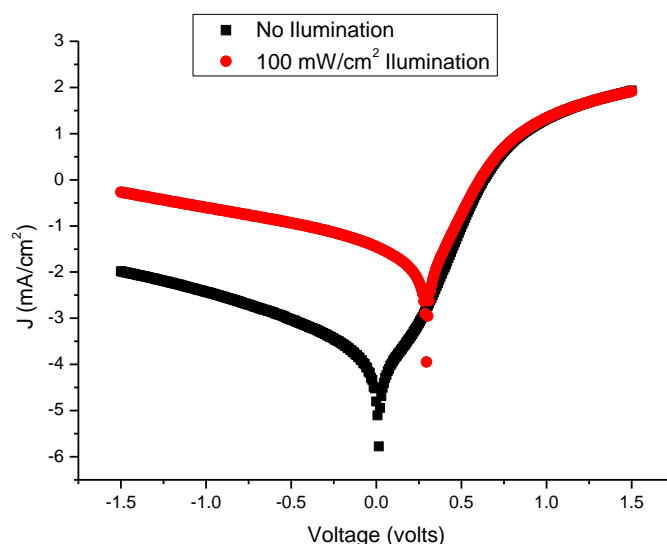


**Figure 3.6.** Typical J-V curves for the VI:PC<sub>61</sub>BM system with a 1:4 weight ratio, under 100 mW/cm<sup>2</sup> light illumination (AM 1.5) and in the dark

From the J/V curves it is possible to extract the efficiency of devices. The power conversion efficiency  $\eta$  is defined by:

---

Where  $I$  is light intensity,  $J_{sc}$  is the measured short circuit current density,  $V_{oc}$  is the open circuit voltage and FF is the fill factor. FF is defined considering the maximum power  $P_{max}$  (obtained from characteristic curves) as:

---

The external quantum efficiency (EQE) is defined by the ratio between the number of charges  $N_e$  extracted at the electrode and the total number of photons  $N_{ph}$  incident on the device at a particular wavelength as:

---

In the experiment, the  $EQE(\lambda)$  was obtained by first measuring the photocurrent density of a calibrated Si photodiode  $J_{Si}$  and then the photocurrent density of the device  $J_D$ . EQE was calculated as:

---

where  $QE_{Si}$  is the quantum efficiency of the calibrated Si photodiode. The internal quantum efficiency IQE was obtained as:

---

where  $\alpha$  is the extinction coefficient of a device of thickness  $d$ .

The various parameters of the devices with different compositions are summarized in Table 3.1. With a 1:1 composition, cells were shorted and it was not possible to perform measurements. It is evident from Table 3.2 that as the concentration of PC<sub>61</sub>BM is increased  $J_{sc}$  increases, which is the main reason leading to a higher efficiency, whereas all the other parameters remains almost constant and independent from composition. However, when the content of complex VI becomes too low (1:5 composition) the efficiency decreases.

<b>VI:PC<sub>61</sub>BM</b> <b>Weight ratio</b>	<b>J<sub>sc</sub></b> <b>(mA/cm<sup>2</sup>)</b>	<b>V<sub>oc</sub></b> <b>(Volts)</b>	<b>Efficiency</b> <b>η</b>	<b>Fill Factor</b>
<b>1:2</b>	0.017	0.24	0.001	0.25
<b>1:3</b>	0.035	0.34	0.003	0.26
<b>1:4</b>	0.195	0.30	0.014	0.24
<b>1:5</b>	0.06	0.35	0.005	0.25

**Table 3.2.** Typical parameters of devices at different compositions of the active layer

An explanation for the improved performance at higher PC<sub>61</sub>BM concentration can be found by considering the atomic force microscopy (AFM) images obtained in the phase mode and shown in Figure 3.7.

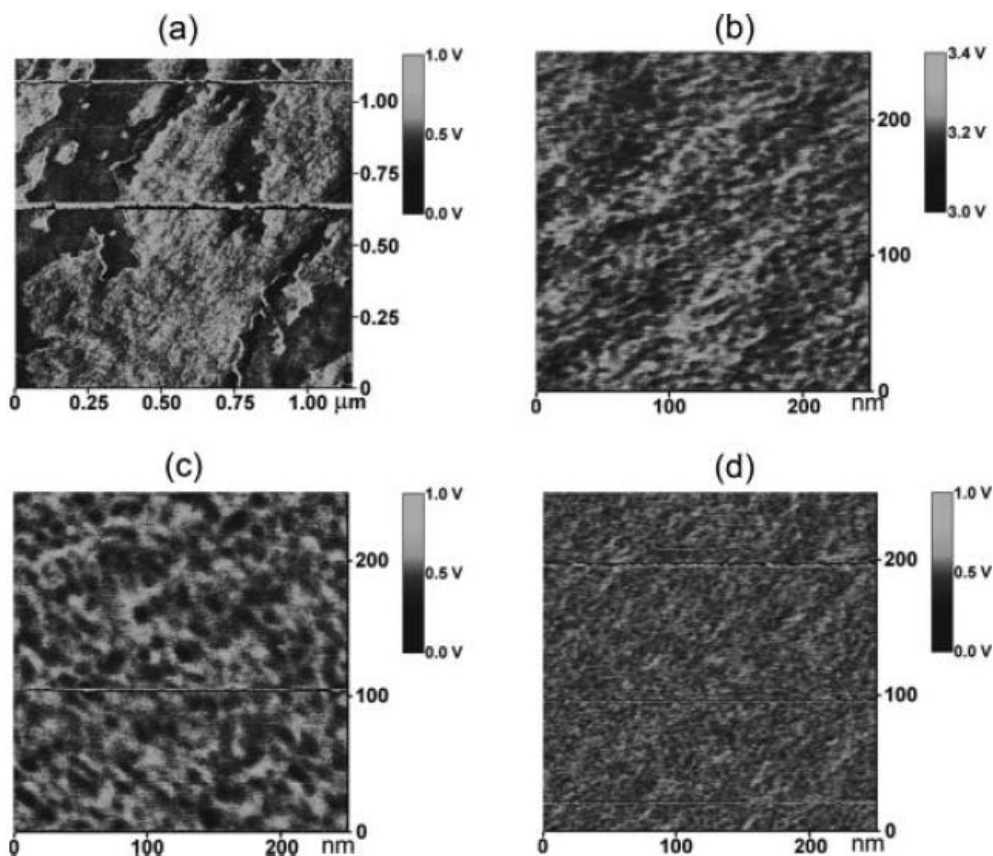


**Figure 3.7.** AFM phase images of the VI:PC<sub>61</sub>BM active blend with weight ratios 1:1 (a), 1:2 (b), 1:3 (c) and 1:4 (d)

For a 1:1 composition, large patches of the two phases with dimensions of several hundred nanometers can be observed. As the PC<sub>61</sub>BM concentration is increased, the morphology evolves towards an interpenetrated network, with typical dimensions of the domains ~25 nm for the 1:3 composition and ~10 nm for the 1:4 composition. A better performance in bulk heterojunction cells with well connected domains in this size range is expected, because it induces a higher current photogeneration and reduces the series resistance.<sup>119</sup> However, even for the best samples, efficiency is rather low, by roughly two orders of magnitude when compared to the best performing materials in bulk heterojunction solar cells.<sup>120</sup> One of the possible reasons for this low performance can be found in the difficulty in obtaining a good morphology of the interpenetrating phases in the bulk heterojunction devices, which is typical in devices using low molecular materials.

Thermal annealing, often used in order to improve morphology,<sup>121</sup> was also performed on our samples, at 70 °C and 120 °C, but it did not lead to an improvement of the efficiency, that actually decreased, indicating that the morphology of the active layer becomes worse after thermal treatments.

Despite the low performance, a deeper level of analysis of the data can be interesting in assessing the importance of using a photoconducting component in organic photovoltaic devices. The external and internal quantum efficiencies of a device with a 1:4 composition is shown in Figure 3.8.

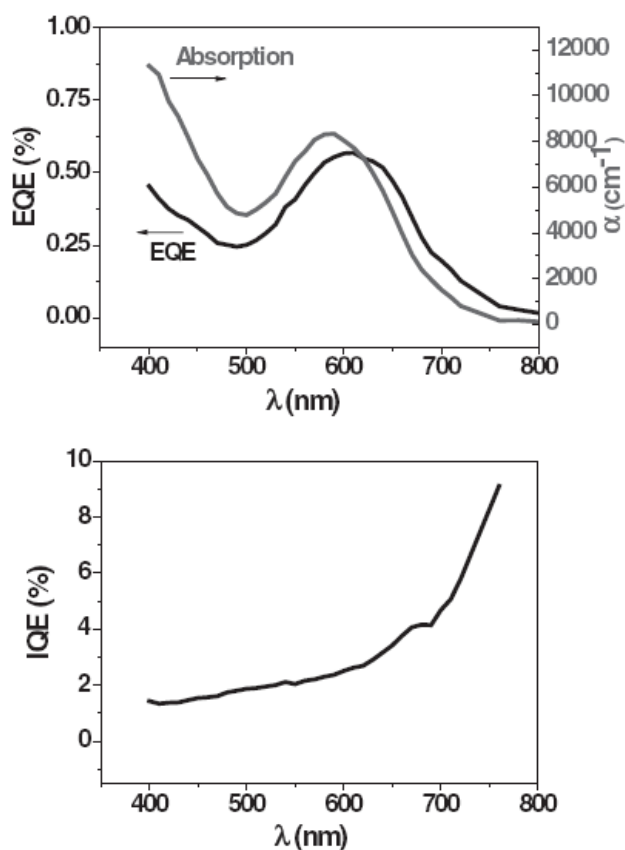


**Figure 3.8.** a) Wavelength dependence of external quantum efficiency and absorption in a film of VI:PC<sub>61</sub>BM with a 1:4 composition; b) Internal quantum efficiency of the same film

As expected, EQE follows absorption rather well, except for a shift of the efficiency towards higher wavelengths, but what is more revealing is the wavelength dependence of IQE. It is evident that at higher wavelengths, where the contribution of VI to absorption is higher, higher values of IQE are observed. There is a monotonic decrease of IQE throughout the visible region (data below 750 nm, where the absorption of the devices is very low, are greatly affected by error and are not shown). In other words, light absorbed at higher wavelengths is more effective in generating photocurrent. Although IQE dependences on wavelength reported in the literature are never flat, in this case the behaviour is rather unusual, with IQE varying by a factor 6 between  $\lambda \sim 400$  nm and  $\lambda \sim 750$  nm. In order to rationalize this observation it is necessary to consider the relative contribution to light absorption of the two components of the active layer, as shown in Figure 3.9.



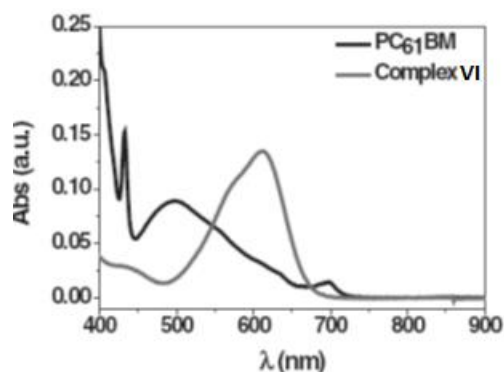


**Figure 3.9.** Absorption in solution of complex **VI** and of PC<sub>61</sub>BM

Complex **VI** exhibits an absorption maximum at  $\lambda \sim 600$  nm, with an absorption edge at  $\lambda \sim 700$  nm and residual absorption up to  $\lambda \sim 800$  nm. Absorption decreases at wavelengths below  $\lambda \sim 600$  nm, but not dramatically. PC<sub>61</sub>BM instead shows very little light absorption at high wavelengths, with an extinction coefficient almost monotonically increasing as the wavelength decreases. Simplifying, and considering that PC<sub>61</sub>BM is much more abundant in the films, we can say that at high wavelengths the contribution to absorption is due mainly to complex **VI** and, as the wavelength is decreased, the contribution of PC<sub>61</sub>BM becomes more and more important. The IQE curve is roughly shaped like the mirror image of the absorption curve for PC<sub>61</sub>BM.

It is clear from the wavelength dependence of quantum efficiency that light absorption by complex **VI** leads to a much higher photon-to-collected-charge conversion than absorption by PC<sub>61</sub>BM. The comparison between experiments carried out with different relative concentrations of the components do not show a decrease of the effect when the size of the domains decreases, ruling out the hypothesis that the different performance of the two components could be due to different exciton diffusion lengths of the two materials. Similarly, the contribution of “hot excitons”,<sup>122</sup> can be excluded, as the higher conversions are obtained for higher wavelengths. Results can instead be explained by considering the intrinsic photogeneration properties of complex **VI**. The tendency of **VI** towards charge photogeneration even in the bulk, could be the explanation for the easy charge transfer to PC<sub>61</sub>BM, when compared to other donors. In contrast, absorption by PC<sub>61</sub>BM is less efficient. In addition, given the fact that complex **VI** is an intrinsic photoconductor, a contribution to charge photogeneration far from the interface could also be important. In other words, the thickness of the interface which is

relevant for exciton dissociation might not be reduced to a single layer of molecules when the exciton is produced in the complex **VI** side of the heterojunction.

Further studies are needed in order to better understand the process and to clarify the underlying mechanisms. However, the data presented clearly show an unusual behaviour that, at least in the case of the compounds studied, indicates that the use of a photoconductor as a component of exciton solar cells can dramatically affect exciton dissociation efficiency.

### 3.3 Towards high quality photoconductive thin films

Even though the efficiency of the bulk heterojunction cell obtained with the Nile Red cyclopalladated complex was very scarce, the advantages of using an intrinsic photoconductor have emerged. It seems to us opportune at this point to investigate the formation and properties of high quality photoconductive thin films of cyclometallated complexes.

Thin films exhibiting high photoconductivity that are fabricated through the electropolymerization of electroactive monomers are potential alternative to the use of low molecular weight materials for efficient devices. The use of electrogenerated films allows high purity, fine control of the film thickness which is a determining issue in the fabrication of the active layers in devices. Electropolymerized films have been obtained using specific functions like triphenylamine or carbazole moieties.<sup>123</sup>

In particular, the efficient electron donating properties of triphenylamine and its capacity to electropolymerize have been investigated in the fabrication of electrochemical devices.<sup>124</sup> In the study of Huang et al.,<sup>125</sup> triphenylamine (TPA) moieties, through their strong electron donating ability, introduced into zinc porphyrins have the effect of modulating their electronic properties. Under oxidation, triphenylamine (TPA) forms an unstable radical monocation  $\text{TPA}^{\bullet+}$  which undergoes a dimerisation process associated with the loss of two protons, to form tetraphenylbenzidine (TPB) (Figure 3.10). Since TPB is easier to oxidize than TPA,<sup>126</sup> upon further cycling potentials scans TPB undergoes subsequent oxidations at lower potential. This occurs as a two step process: 1) radical monocation  $\text{TPB}^{\bullet+}$  formation; 2) dication  $\text{TPB}^{2+}$  formation.<sup>127</sup>

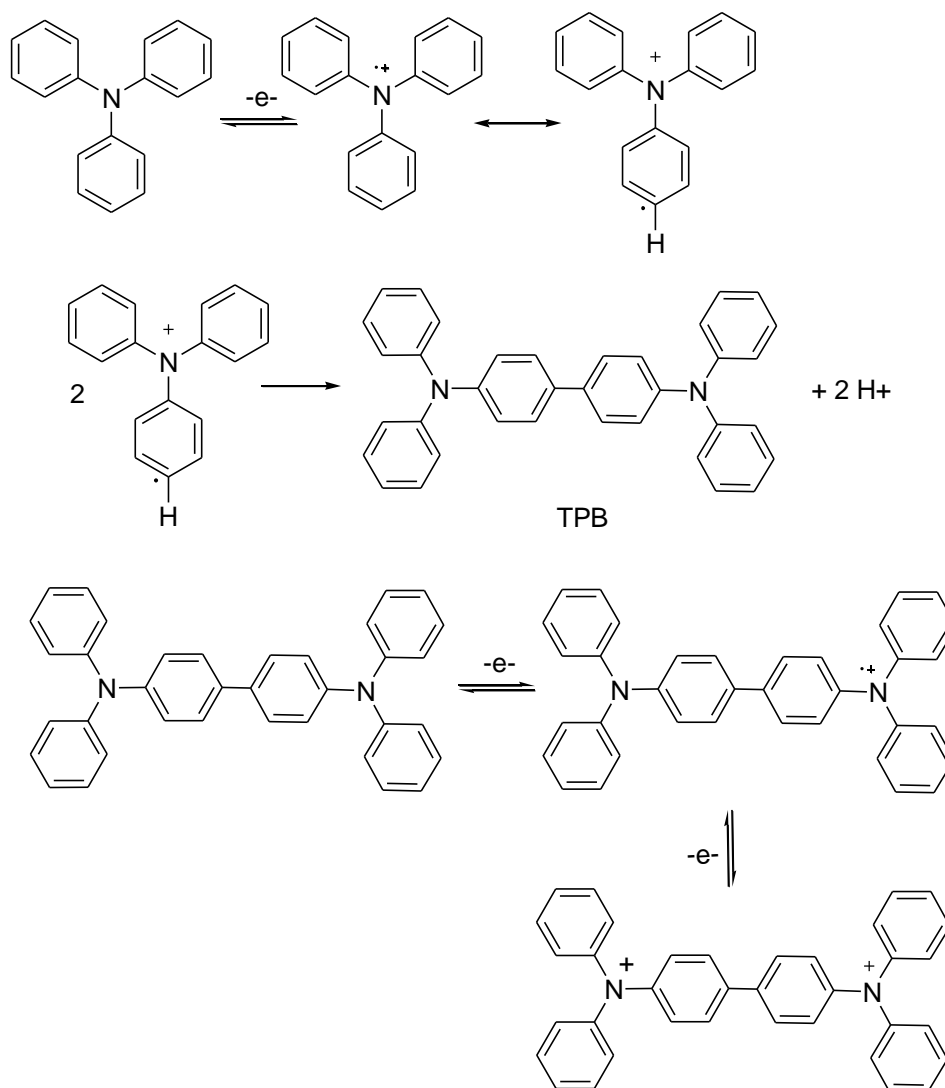


**Figure 3.10.** Mechanism of the dimerisation process of TPA

Usually, the TPA dimerisation reaction doesn't extend to polymerization due to the high stability of the radical cation  $\text{TPB}^{\bullet+}$ . Nevertheless, it has been shown that the introduction, in *para* position with respect to the nitrogen atom of TPA, of an electron deficient group such as 1,3,4-oxadiazole (Figure 3.11) prevents the dimerisation process of  $\text{TPA}^{\bullet+}$  by reducing the electron delocalisation and therefore favouring the polymerisation process.<sup>128</sup>

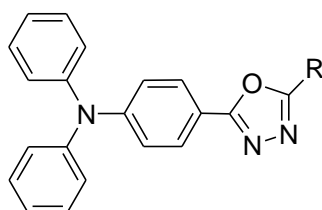


**Figure 3.11.** Molecular structure of a substituted electropolymerizable triphenylamine

Taking into account that for our developed photoconductive cyclometallated complexes (Chapter 2) the HOMO energy level is mainly localized onto the ancillary ligand, the grafting of a triphenylamine fragment onto the Schiff base should have a two-fold purpose:

i) introducing an electron donor fragment onto the Schiff base ancillary ligand to further separate the photogenerated charges within the excited state, hence boosting the photogeneration efficiency,

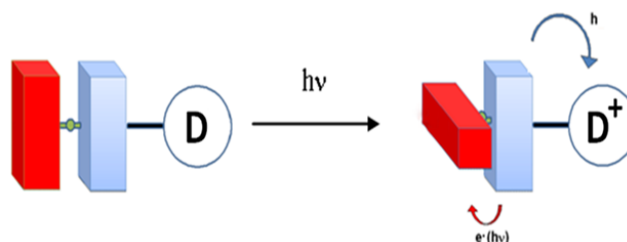


**Figure 3.12** Advantages of a donor fragment onto the Schiff base ancillary ligand

ii) allowing the possible electropolymerization of the resulting complex. The advantages of having a photoconductive polymeric network include:

- the increased stability of the amorphous state of the photoconductive material thanks to the formation of a cross-linked polymer;
- an enhanced mobility of the photogenerated charges along the polymeric chains;
- the possibility to obtain high quality ultra-thin films for using as modified electrodes in optoelectronic devices.

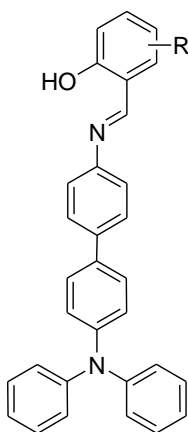


**Figure 3.13.** A possible electropolymerizable Schiff base

### 3.3.1 Synthesis

Two new Nile Red cyclopalladated complexes (Figure 3.14) were synthesised in this work. Both **VII** and **VIII** are cyclopalladated Nile Red complexes with a Schiff base ligand (Scheme 3.2). While **VII** bears a triphenylamine electropolymerizable fragment grafted on the Schiff base, the model complex **VII** differs from **VIII** by substitution of the triphenylamine fragment by a simple alkyl chain.

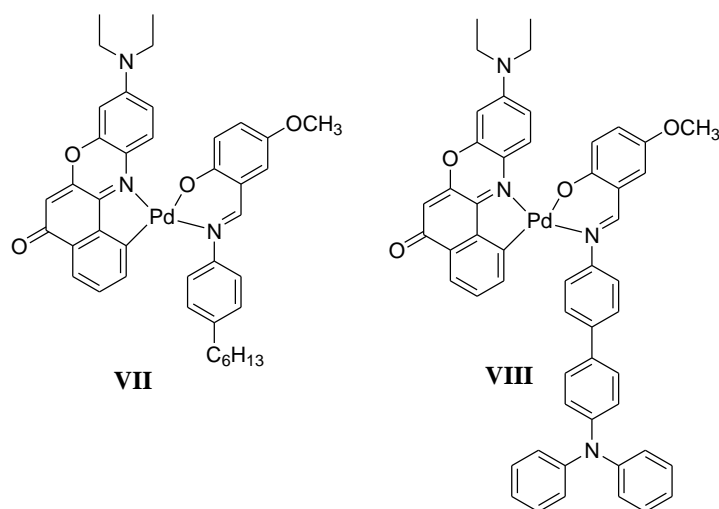
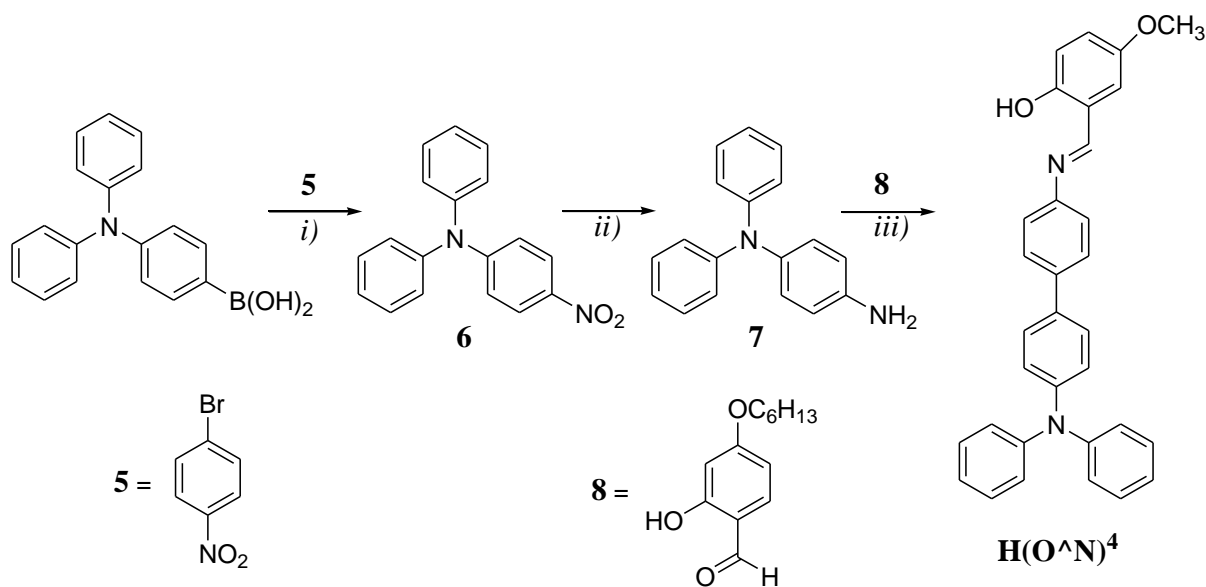
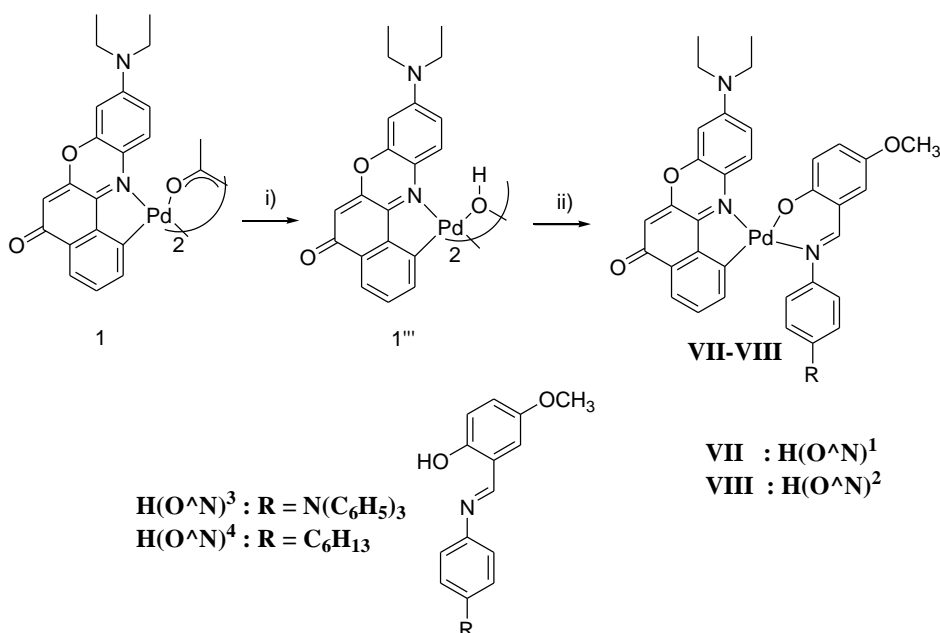


**Figure 3.14.** Molecular structure of the complexes **VII** and **VIII**



**Scheme 3.2.** Reagents and conditions: i) Pd(PPh<sub>3</sub>)<sub>4</sub> cat., Na<sub>2</sub>CO<sub>3</sub> (2M), ethanol/toluene, 36 h, N<sub>2</sub>, ii) NaBH<sub>4</sub>, NiCl<sub>2</sub>, methanol/dichloromethane, overnight, iii) ethanol, reflux, 3h.

The synthesis of complexes **VII** and **VIII** was achieved following the previously described procedure (Chapter 2). Direct cleavage of the acetato-bridged dimer **1** (Scheme 3.3) with the Schiff base afforded complex **VIII** in very scarce yield. Moreover, difficulties in the purification of **VIII** have been encountered. The synthetic strategy has been hence modified and through a metathetical reaction with NaOH, the acetato bridge was substituted with a hydroxy bridge, leading to the formation, here reported for the first time, of a more reactive dimeric Nile Red cyclopalladated intermediate **1'''**. In fact, as reported by Serrano *et al.*,<sup>129</sup> cyclometallated hydroxy-bridged complexes show enhanced reactivity with respect to their corresponding acetato-bridged complexes in reactions involving deprotonation of ancillary ligands, such as Schiff bases. In these reactions, elimination of a water molecule represents the driving force for the formation of the final complex. Indeed, this was the case for the hydroxy-bridged Nile Red derivative which showed increased reactivity towards cleavage and complexation with Schiff bases  $\text{H}(\text{O}^{\wedge}\text{N})^2$  and  $\text{H}(\text{O}^{\wedge}\text{N})^4$ . Final complexes **VII** and **VIII** were obtained in good yield and high purity. Intermediate **1'''** and complexes **VII** and **VIII** were fully characterised via  $^1\text{H}$  NMR, FT IR and elemental analysis (Chapter Ten).



**Scheme 3.3.** Reaction conditions for the synthesis of complexes 1 and 2: *i*) NaOH, water/acetone, r.t., 24h; *ii*) for **VII**:  $\text{H}(\text{O}^{\wedge}\text{N})^3$ , dichloromethane/ethanol, r.t., 7d., for **VIII**:  $\text{H}(\text{O}^{\wedge}\text{N})^4$ , dichloromethane/ethanol, r.t., 5d.

### 3.3.2 Structural characterization

Crystals of complex **VIII** were obtained from dichloromethane/n-hexane. The structure obtained by X-ray diffraction is shown in Figure 3.15, while bond lengths and angles are listed in Chapter Ten. **VIII** crystallizes in a monoclinic system, P2(1)/c space group.

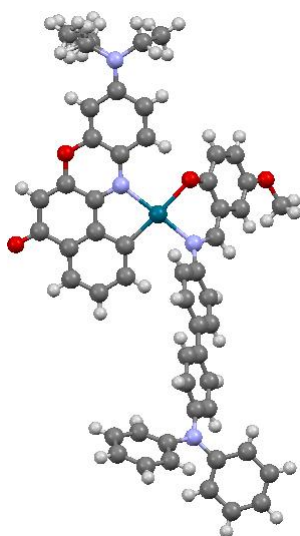


**Figure 3.15.** Molecular structure of complex **VIII**

As in the case of complexes **I** and **II** (Chapter 2), dimers are formed by hydrogen bonds between two complexes. The resulting unit cell contains four molecules (Figure 3.16).

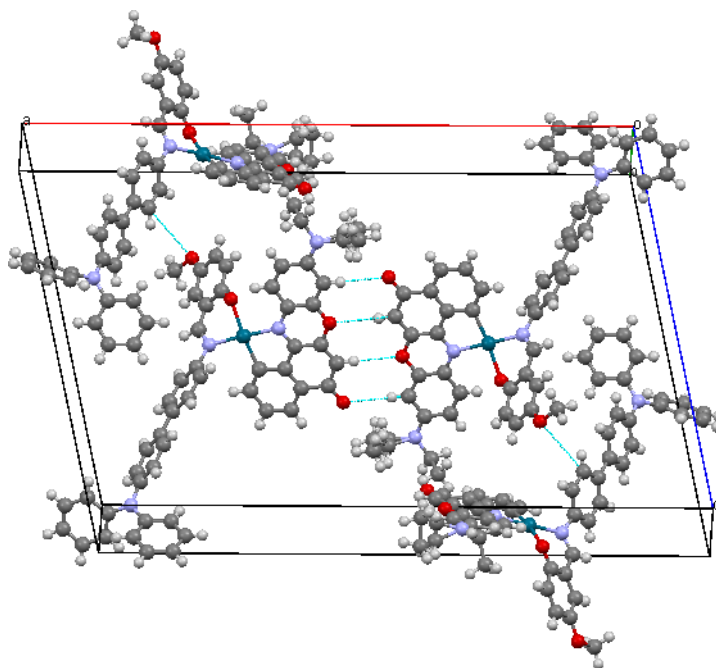


**Figure 3.16.** Unit cell composed of four molecules of **VIII**

A striking feature is the supramolecular architecture of the crystalline state of **VIII** which is governed by the formation of dimeric forms of complexes (Figure 3.16). These dimers are formed by the head to tail disposition of the Nile Red fragments of two adjacent molecules strongly interacting through a 4 hydrogen-bonds network identical to the network observed in complexes **I** and **II** (Chapter 2) and responsible for the discoidal organization of these metallomesogens. Noteworthy, the presence of the sterically hindered triphenyl fragment do not prevent the formation of the dimeric form. Instead, the triphenylamine moieties are disposed in such a way to create a unidirectional chain as shown in Figure 3.17.



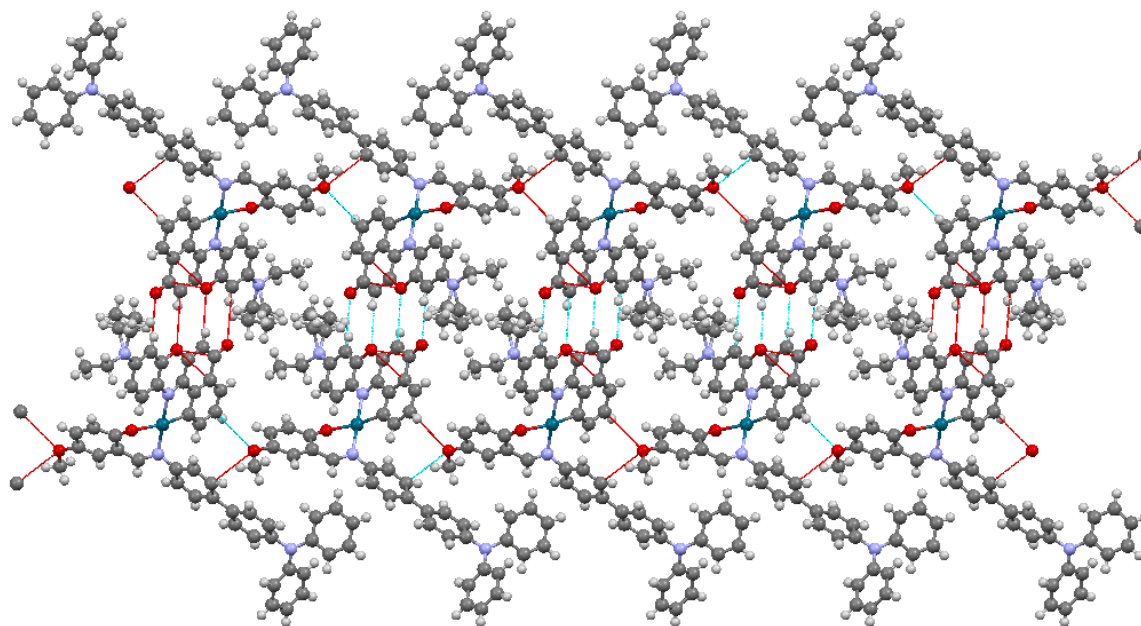


**Figure 3.17.** Crystalline packing of complex **VIII** showing the unidirectional chain formed by the triphenylamine moieties

### 3.3.3 Electrochemistry

The redox behaviours of the two compounds are typical for cyclopalladated complexes with a cyclometallated Nile Red ligand and an ancillary Schiff base with the LUMO situated on the cyclometallated fragment and the HOMO onto the Schiff base ligand. Figure 3.14 shows the cyclic voltamograms of **VII** and **VIII**. The redox potentials vs.  $\text{Fc}/\text{Fc}^+$  as well as the estimated HOMO and LUMO energies are collated in Table 3.3.

Complex No.	$E^{\text{red}}_{\text{NR}} (\text{V})^a$	$E^{\text{ox}}_1 (\text{V})^a$	$E^{\text{ox}}_2 (\text{V})^a$	HOMO (eV)	LUMO (eV)
<b>VII</b>	-1.27 (QR)	+0.37 (I)	/	-5.3	-3.7
<b>VIII</b>	-1.23 (QR)	+0.34 (R)	+0.54 (R)	-5.1	-3.6

<sup>a</sup> Potentials expressed in volts vs.  $\text{Fc}/\text{Fc}^+$ ; R=reversible, QR=quasi reversible, I=irreversible

**Table 3.3.** Cyclic voltametry data relative to complexes **VII** and **VIII**

The reduction behaviours of **VII** and **VIII** are identical, with one quasi-reversible reduction (at *ca.* -1.2 V vs. Fc/Fc<sup>+</sup>) typical of the Nile Red fragment of cyclopalladated complexes (**NR**)Pd(O<sup>^</sup>N) (Chapter 2). On the contrary, in oxidation the two complexes present rather different behaviours. The model complex **VII** is characterised by an irreversible oxidation process. However, the previously studied cyclopalladated Nile Red complexes (**I-II** (Chapter 2) and **VI**) presented two successive fully reversible oxidation waves. This main difference can be attributed to the monoalkylation of the Schiff base for **VI** while all previously studied complexes presented a double alkylation on the salicylic ring of the Schiff base. Instead, complex **VIII** presents the two consecutive fully reversible oxidation waves characteristic of the triphenylamine fragment (0.34 mV and respectively 0.54 mV vs. Fc/Fc<sup>+</sup>).<sup>130</sup> The estimated HOMO and LUMO energies (-5.1/-3.6 eV) of complex **VIII** are identical to those of complex **VI**, which proves that the compatibility of the energetic levels with the bulk heterojunction cell isn't lost when the triphenylamine is introduced onto the ancillary ligand.

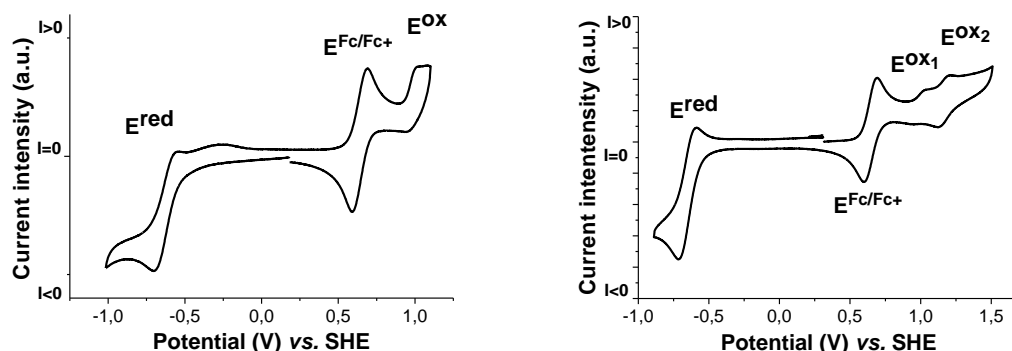


**Figure 3.18.** Cyclic voltammograms of complexes **VII** and **VIII** in the presence of Ferrocene as internal reference (Fc/Fc<sup>+</sup>).  
Scan rate: 100 mV.s<sup>-1</sup>, DCM, Bu<sub>4</sub>NPF<sub>6</sub> (0.1M)

Upon repetitive oxidation scans for complex **VIII** (-0.2V - 1.4 V), an increase in current is observed which is typical of the electropolymerization of the substituted triphenylamine fragment (Figure 3.19 a).<sup>130</sup> No such behaviour was registered for model **VI**, which is a further proof of the electropolymerization process induced by the triphenylamine fragment of **VIII**. Once the polymer formed, the modified Pt disk working electrode covered with the electropolymerized film of **VIII** was immersed in a fresh distilled dichloromethane solution (0.1 M electrolytic solution) and a cyclic

voltamogram was recorded (Figure 3.19b) and the high electrochemical stability of the thus obtained film is shown in Figure 3.19c registered upon repetitive oxidation scans on the modified Pt electrode.

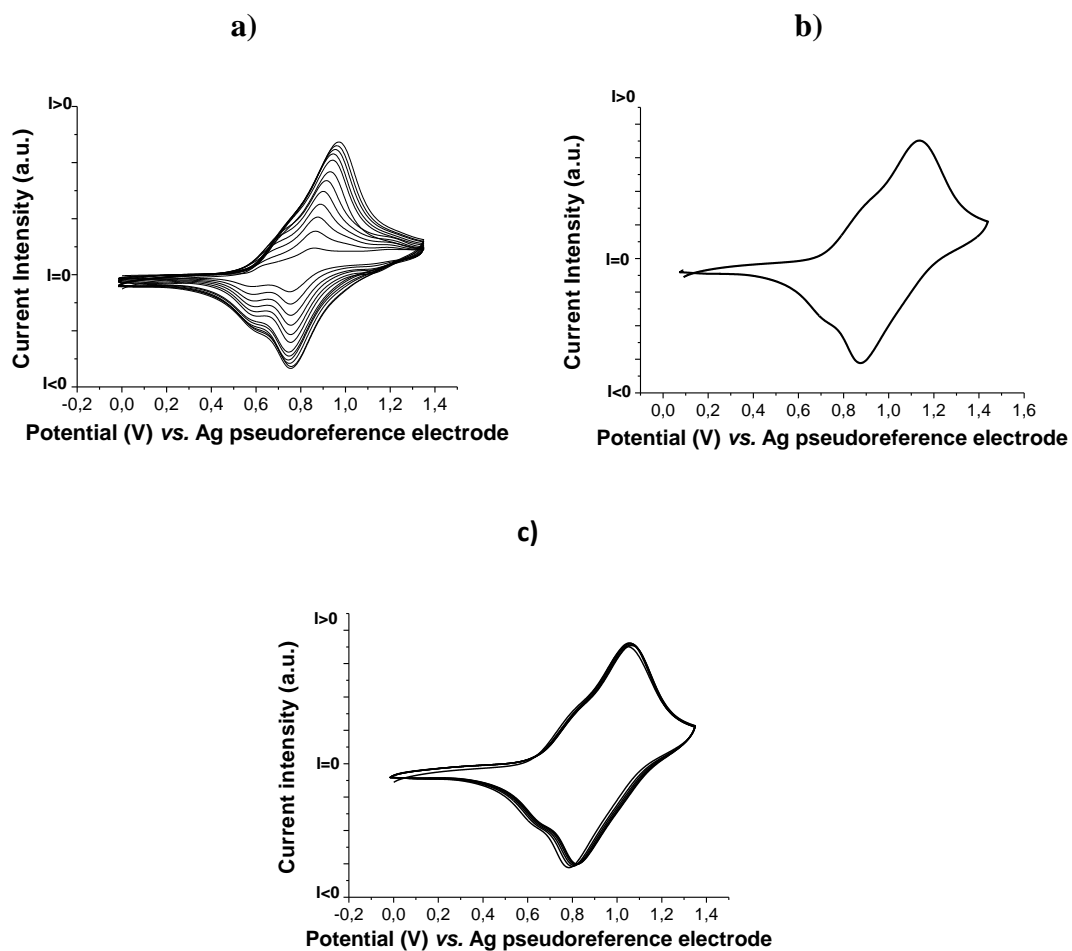


**Figure 3.19.** a) Cyclic voltamograms of **VIII** obtained from 12 consecutive oxidation scans; b) Cyclic voltamogram of the obtained modified Pt electrode.

On the other hand, no electropolymerization process is observed for **VIII** in reduction. Upon cycling onto the reduction wave, no increase of current was observed as shown in Figure 3.20.

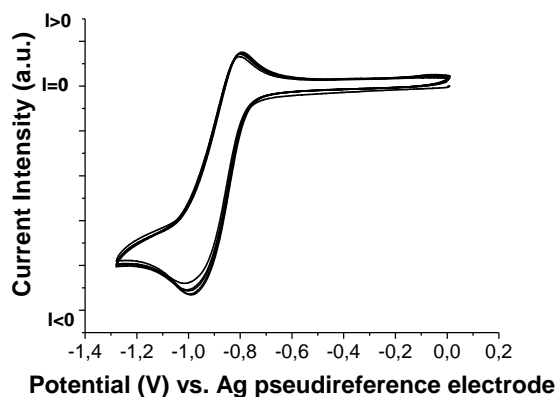


**Figure 3.20.** Repetitive scans of the reduction wave of complex **VIII**

However, a striking feature in the redox properties of **VIII** can be observed when the electropolymerization process is performed on a wider potential range window i.e. observing both oxidation and reduction during cycling. Indeed in these conditions, the decrease of the reduction wave associated to the Nile Red fragment is observed during cycling as well as the appearance of a new irreversible oxidation wave at a lower potential compared to the double-oxidation wave of the triphenylamine fragment (Figure 3.21a)

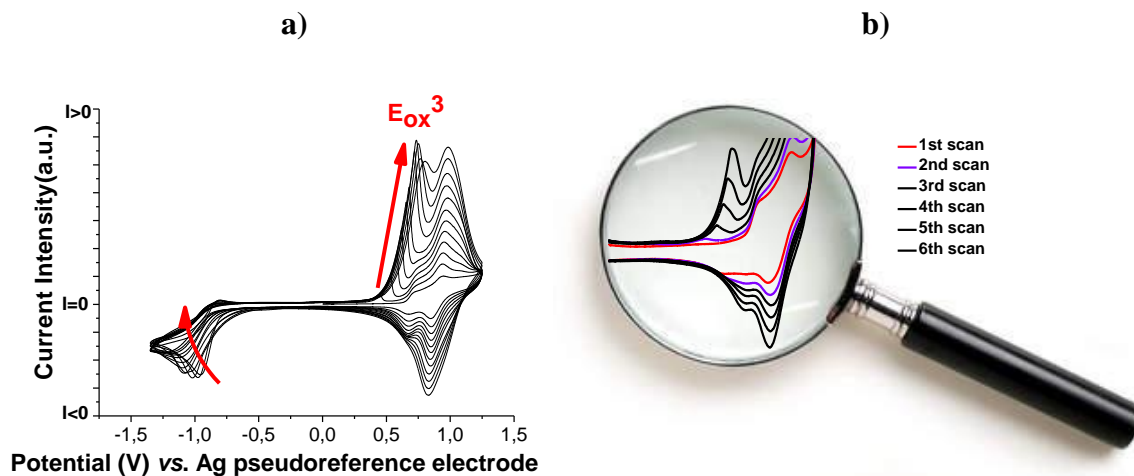


**Figure 3.21.** a) Electropolymerization of **VIII** on repetitive scans with appearance of  $E_{ox}^3$ ; b) magnified view showing the increase in intensity of  $E_{ox}^3$  in function of the number of performed scans

Noteworthy, the appearance of this new oxidation peak ( $E_{ox}^3$ ) can be observed already on the second scan (Figure 3.21b), once a first oxidation and a first reduction of complex **VIII** have been performed. However, a single scan starting towards reduction potentials followed by oxidation does not present the appearance of such peak (Figure 3.22).

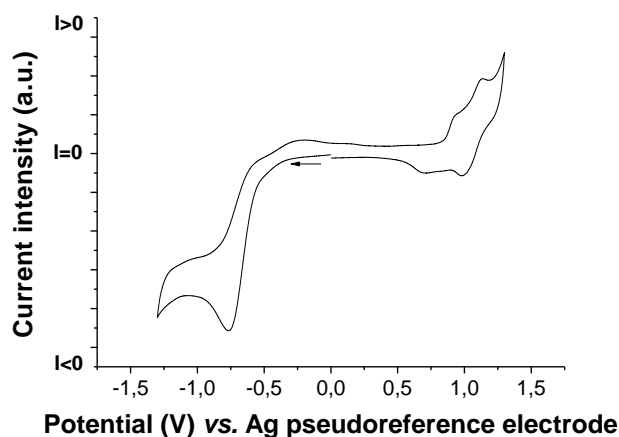


**Figure 3.22.** Redox behaviour of **VIII** starting from reduction

Therefore to witness this new oxidation peak ( $E_{ox}^3$ ), the oxidation of **VIII** must have been performed. During oxidation of **VIII**, TPB (see figure 3.10) is formed and since its oxidation potential is lower than TPA, at high voltage  $TPB^{2+}$  is present. Reducing the potential to 0 V, TPB is generated. Once TPB is present, the reduced form of **VIII** i.e. the reduced form of the Nile Red fragment of **VIII** must react with TPB to give rise to a new redox active specie whose oxidation is observed at  $E = E_{ox}^3$ . Repetitive cycles show consequently the disappearance of the Nile Red fragment reduction wave and the increase of the oxidation  $E_{ox}^3$  peak (Figures 3.21), whose increase in current intensity is congruent with an electropolymerization process. Interestingly, a preformed electropolymerised thin film of **VIII** obtained by cycling repetitively in oxidation (as presented in Figure 3.19a) shows an atypical behaviour when reduction of the Nile Red fragments is performed but consistent with the previous observations. Indeed, a modified Pt electrode recovered by a thin electropolymerised film of **VIII** obtained by cycling from 0 to 1.2 V has been exposed to reduction. Once the Nile Red fragments are reduced, the oxidation peak of  $E = E_{ox}^3$  is observed on the second oxidation scan. Following scans show the decrease of current intensity of the reduction wave relative to the Nile Red fragments contained within the polymer. All TPB motifs present in the preformed polymer seem to react with the reduced forms of the Nile Red fragments to generate new redox active centres within the polymer chains, suggesting the creation of a new reticulation. The thus modified new cross-linked polymer is still redox active and presents high electrochemical stability as suggested by the repetitive scans effectuated and presented in Figure 3.23.

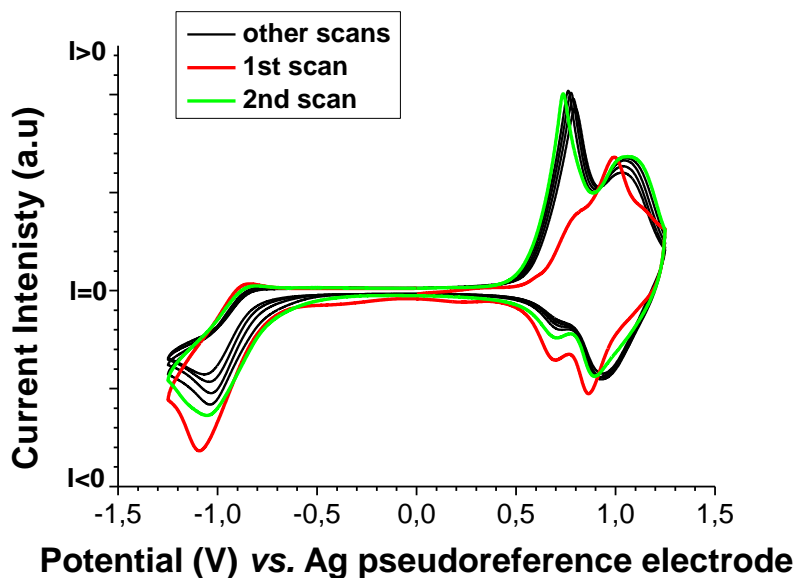


**Figure 3.23.** Cyclic voltammogram showing 6 redox scans performed on an electropolymerized thin film of **VIII** deposited on Pt disk electrode. The film was previously obtained such as described in Figures 3.19

### 3.3.4 Film photoconduction

Preliminary studies on the formation of electropolymerised thin films of **VIII** deposited on ITO etched glass substrates have been performed in order to evaluate and identify all the best experimental working conditions (solvent, temperature, concentration, scan rate, washing procedures...) to obtain high quality thin films suitable for device construction.

The ideal conditions for the film growth were established. It was observed that using diluted ( $10^{-5}$ - $5 \cdot 10^{-5}$  M) dichloromethane complex solutions with a concentration of 0.1 M  $\text{NBu}_4\text{BF}_4$  electrolyte and scan rates between 50 and  $200 \text{ mVs}^{-1}$ , films with thicknesses from 10 nm to *ca.* 600 nm were obtained. Once electrogenerated, in order to avoid film cracking, the films were not washed, but introduced overnight in a dichloromethane saturated chamber. Afterwards, the films were washed with a small volume (*ca.* 1mL) of fresh dichloromethane. The film thickness was measured with a surface profiler and the profiles registered for the obtained films are shown in Figure 3.24. However, it was observed that thinner films are more homogeneous.

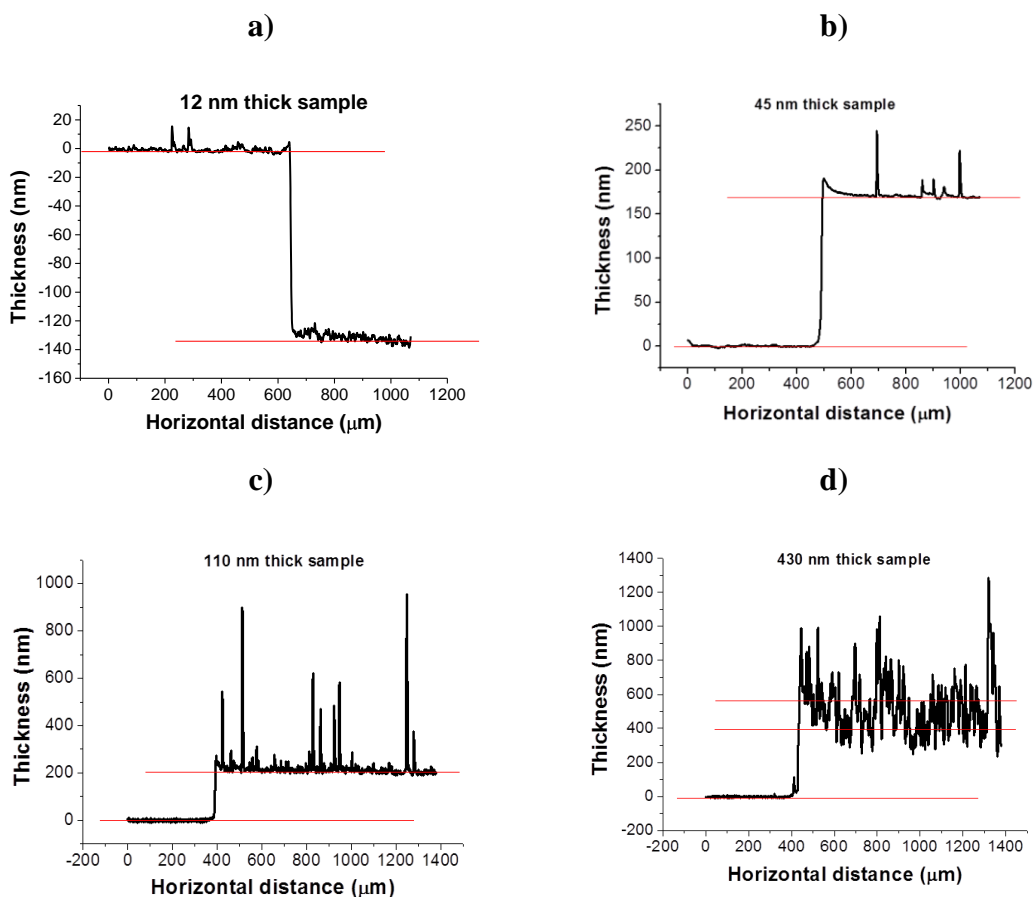


**Figure 3.24.** Surface profile thickness measurements on 120 nm thick films of ITO

Presence of spikes on the film surfaces are probably due to impurities accumulated during handling of substrates. Further experiments would have to be performed in clean room to avoid such contaminations.

Preliminary photoconductive measurements have been performed on an electrogenerated film (430 nm thickness) of **VIII** obtained by scanning 30 consecutive cycles at 50 mV/sec (Figure 3.25) from 0 to 1.3V (*vs.* Ag pseudoreference electrode) from a  $5 \cdot 10^{-5}$  M solution of complex **XII** in dry dichloromethane (0.1M NBu<sub>4</sub>PF<sub>6</sub>).

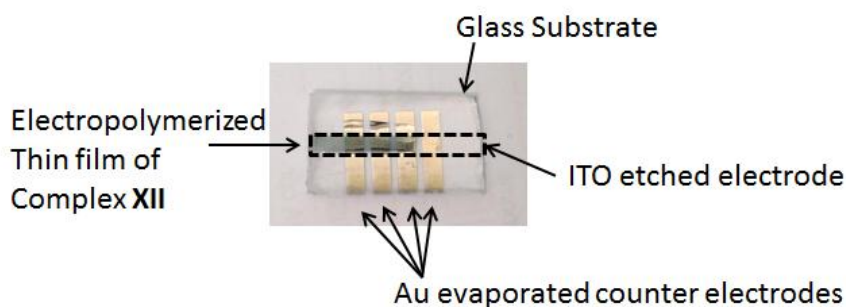


**Figure 3.25.** Experimental set-up used for measuring photoconduction of a electrogenerated film of complex **VIII**

Once the film electrogenerated and washed, an Au counter electrode has been added through chemical vapour deposition technique. The resulting device is presented in Figure 3.25.

The typical current increase under light irradiation and the photoconduction in function of wavelength are shown in Figure 3.26. Even if the photoconduction values are of the order of  $10^{-13} \Omega^{-1} \text{ W}^{-1} \text{ cm}$ , lower than for the photoconductive (C<sup>N</sup>)Pd(O<sup>N</sup>) complexes reported in Chapter 2, the feasibility of electrogenerating Nile Red films has been demonstrated. By optimizing the parameters (such as: concentration of the solution, number of scans or scan rate, post-treatments of the obtained film etc.) during the film deposition, potential further improvements in photoconduction could be obtained and measurements are in progress. Furthermore, photoconductive measurements need to be performed on films obtained from complete redox scans containing the new generated active specie described in the previous section in order to perform a comprehensive study of the effects of the cross linking in the electrogenerated film.



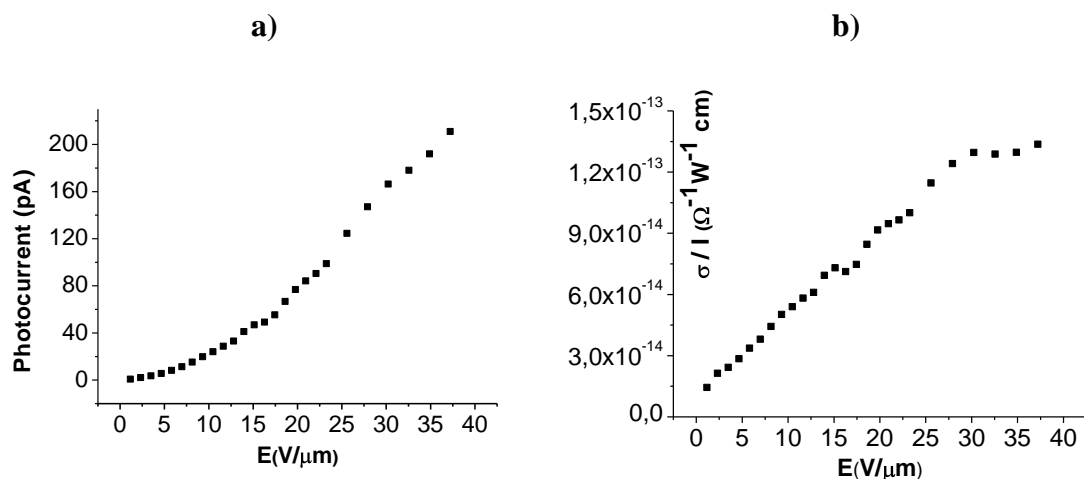


**Figure 3.26.** a) Photocurrent and b) photoconduction of an electropolymerized film of **VIII**

### 3.4 Conclusions

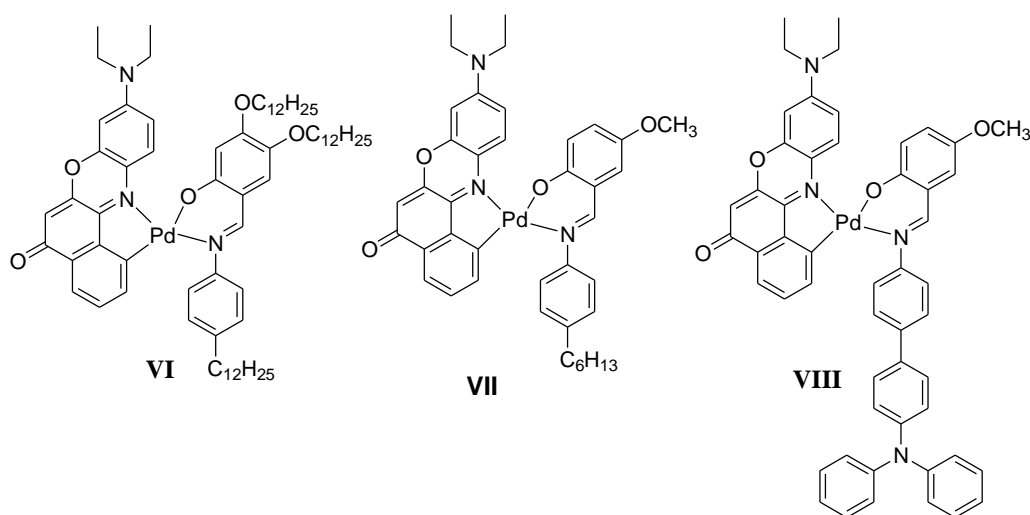


**Figure 3.27.** Synthesised and studied Nile Red cyclometallated complexes **VI-VIII**

Three novel Nile Red cyclopalladated complexes **VI-VIII** (Figure 3.27) have been synthesized and characterized. Photoconduction measurements on complex **VI** have shown values of *ca.*  $10^{-10}$  S W<sup>-1</sup> cm. Furthermore, solution electrochemical studies on all the three complexes have demonstrated the potential use in bulk heterojunction solar cells, since the positions of their frontier orbitals HOMO and LUMO match the energy levels of the typical components of an organic solar cell. The low molecular

weight photoconductive complex **VI** has been actually tested as a donator in a bulk heterojunction solar cell using PC<sub>61</sub>BM as an acceptor. Even though the obtained device efficiency was very scarce, the advantages of using an intrinsic photoconductor have emerged. Indeed, an increasing of the exciton diffusion length has been observed when using such photoconductors. By the other hand, considering that the low molecular weight of the Nile Red donor seem to represent an important drawback due to poor quality of the heterojunction, we have incorporated an electropolymerizable triphenylamine fragment in the Nile Red cyclopalladated complex **VII**. X-ray diffraction analysis of a single crystal of **VIII** has evidenced the formation of a dimeric pair formed by two identical molecules kept together by a hydrogen-bond network. This intermolecular dimeric assembling presents in the solid state confirms the hypothesised structure of the liquid crystalline state proposed for mesogenic complexes **I-II** (Chapter 2) which was at the origin of the columnar organisation. The HOMO and LUMO levels were estimated for the model complex **VII** and for complex **VIII**. A comparison between the two complexes, have demonstrated that the introduction of the triphenylamine fragment onto the molecular skeleton of **VIII** doesn't influence neither the frontier orbitals energies nor their physical separation.

A comprehensive electrochemical study of complex **VIII** has evidenced the effectiveness of the polymerization and the possibility of electrodeposition. Furthermore, a new redox active centre has been detected upon reduction of the electropolymerised film, showing the occurrence of a specific chemical reaction between the TPB and reduced Nile Red fragments. Ideal experimental conditions for obtaining homogeneous thin films of **VIII** on ITO etched substrates have been determined. An electrochemically oxidative generated film has been grown on the surface of the working electrode and preliminary photoconductive measurements have shown photoconduction values of the order of  $10^{-13} \text{ S W}^{-1}\text{cm}^{-1}$ . Further investigations are needed in order to elucidate the exact mechanism of the electropolymerization of **VIII** and to measure photoconductivity on films electrogenerated at different potentials.

## Chapter Four

### Synthesis and properties of new Nile Red cyclopalladated dyes and their application as sensitizers in Dye Sensitized Solar Cells

#### 4.1 Introduction

In order to insure the contact with the titania photoelectrode, specific anchoring groups have to be included into the molecular structure of the sensitizers projected for Dye Sensitized Solar Cells DSSCs.<sup>131</sup> The established covalent bond between the dye and the TiO<sub>2</sub> semiconductor enhances the electronic coupling between the excited LUMO orbital of the dye and the electronic levels of the titania. A rapid electronic transfer is reached under this conditions.

Since the titania surface is covered by hydroxy groups, functional groups like carboxylic acids and derivatives (esters, acid chlorides, anhydrides, carboxylates, amides),<sup>132</sup> sulphonates (-SO<sub>3</sub><sup>-</sup>), silanes (SiX<sub>3</sub>, Si(OX)<sub>3</sub>)<sup>133</sup> or phosphonic acid derivatives<sup>134</sup> will be able to bind to the photoelectrode. However, recently, the efficiency of anchoring of nitro groups was demonstrated.<sup>135</sup> Comparative studies between the device efficiency reached using polipyridine Ruthenium dyes with carboxylic and ester anchoring groups<sup>135</sup> have demonstrated that the carboxylic group shows an enhancement of the efficiency.<sup>43,49,51,52</sup> However, it is noteworthy that, in the case of the ester groups, the dye adsorption to the titania support improves when a hot dye bath is used, leading to higher efficiencies. This is an important result since from a practical point of view the synthesis of ester derivatives is more straightforward than the preparation of corresponding carboxylic acids.

Different types of binding modes of the dye to the titania by means of carboxylic groups have been modelled (Figure 4.1). These depend upon the dye molecular structure, the pH of the dying bath and upon how the semiconductor had been prepared.<sup>137</sup> Furthermore, it has been demonstrated that the number of the anchoring groups included in the dye molecular structure has an important influence on the adsorption and electronic transfer efficiency. Indeed, Hara *et al.*<sup>138</sup> have demonstrated that the phenantroline substituted Ru(II) dyes bearing one single carboxylic anchoring group induced a lower device efficiency than the ones with two or three groups (two groups were more efficient than three).

In conclusion, the molecular structure of an organometallic dye has to include, as an anchoring group at least one carboxylic functionality necessarily situated onto the LUMO bearing molecular fragment, in order to favour the electronic transfer toward the photoelectrode.

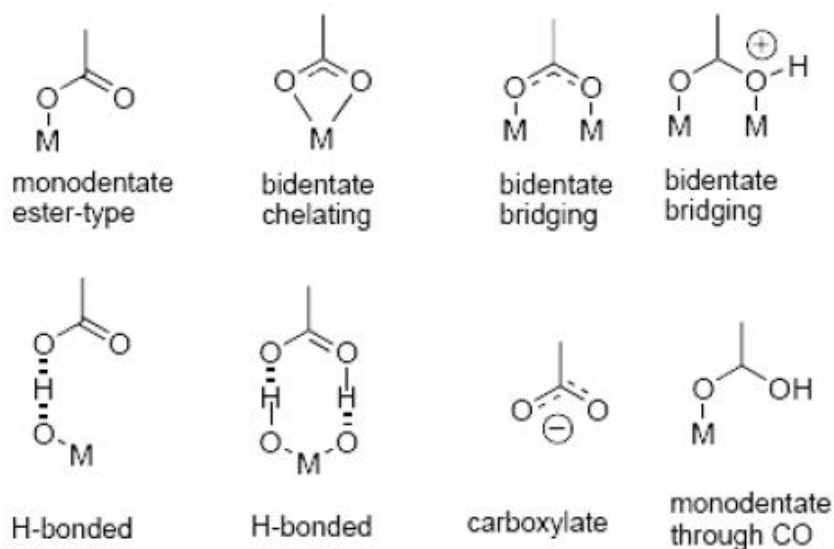


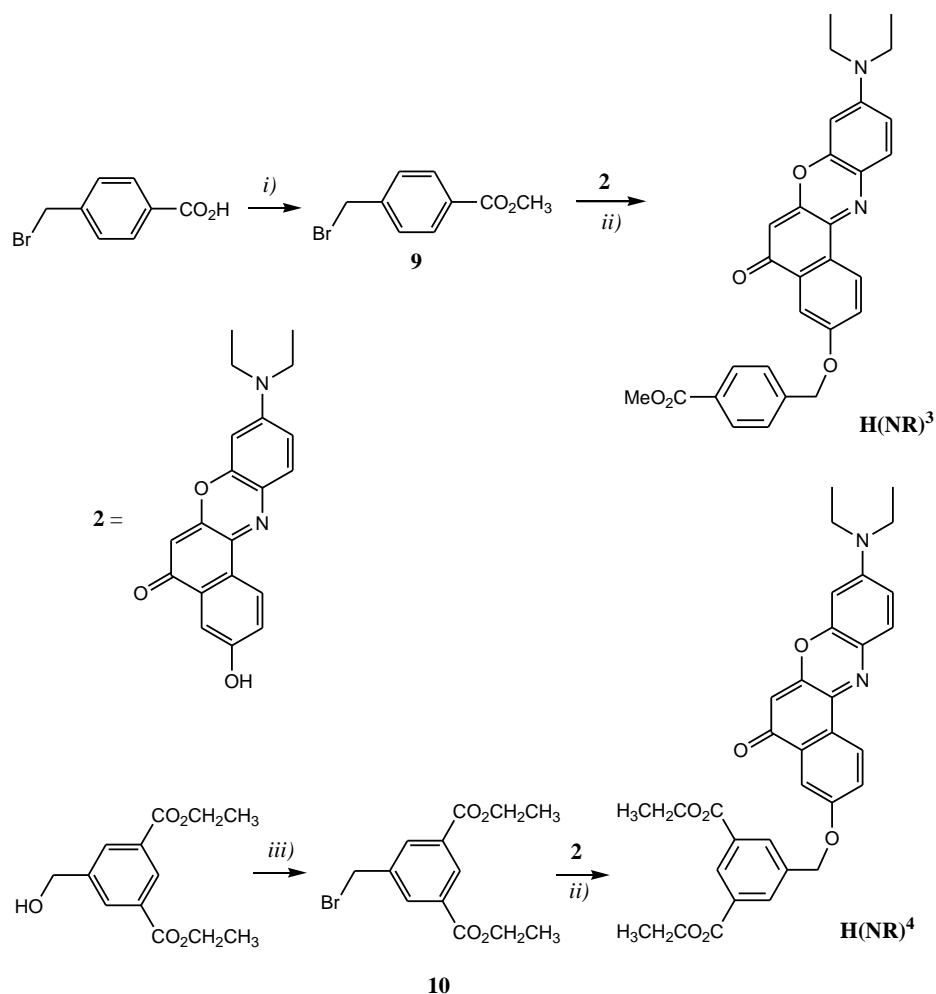
**Figure 4.1.** Model binding modes of anchoring groups to the titania semiconductor

## 4.2 Nile Red functionalization for post-grafting to TiO<sub>2</sub>

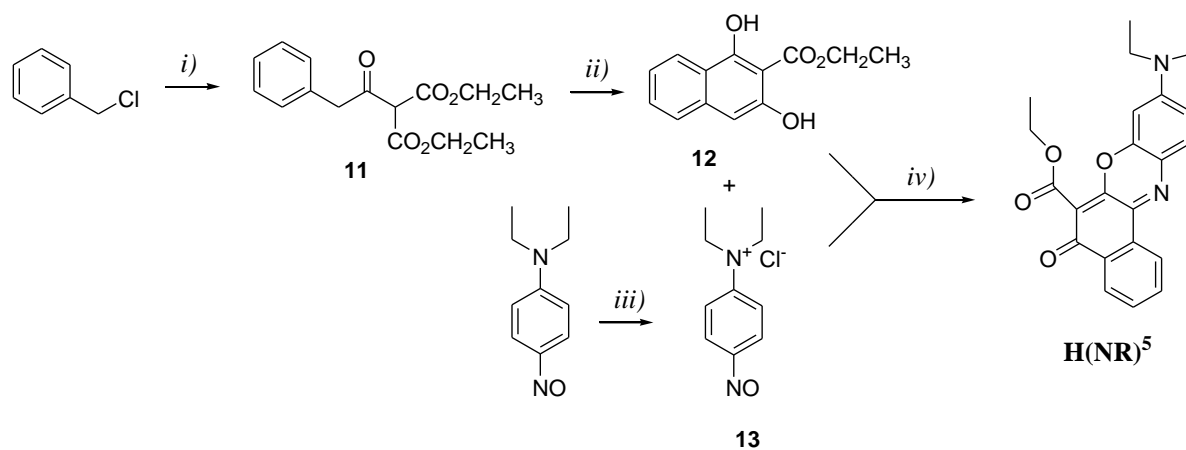
Taking advantage of the already demonstrated fact that the cyclopalladation of Nile Red in complexes bearing a Schiff base as ancillary ligands affords species in which the separation HOMO/LUMO is maintained (see Chapter 2), in this work, ester and carboxylic anchoring groups have been introduced onto the Nile Red fragment in order to obtain potentially DSSCs suitable dyes.

Starting from the same hydroxy Nile Red derivative **2** described in Chapter 2, two novel Nile Red derivatives **H(NR)<sup>3</sup>** and **H(NR)<sup>4</sup>** were obtained (Scheme 4.1), by means of a Williamson etherification reaction between the ester substituted brominated precursors **8** and **9**. Furthermore, by changing the synthetic pathway, a novel different Nile Red ester derivative **H(NR)<sup>5</sup>** was obtained (Scheme 4.2). Differently from **H(NR)<sup>3,4</sup>**, this derivative includes an ester group bonded directly to the aromatic core of

the LUMO bearing molecular fragment. In a DSSC, this should favour the electronic injection from the dye to the titania photoelectrode. **H(NR)**<sup>5</sup> was obtained by reaction under microwave radiation of the **11** precursor with the *p*-nitroso,N,N-diethylaniline hydrochloride intermediate **12**. It is noteworthy that the use of a positively charged amine is necessary in order to obtain the final product, differently from the case of **H(NR)** when either the neutral or the cationic nitroso aniline derivatives were successfully used (see Chapter 2). Under normal reflux conditions, the same reaction mixture afforded a crude product which resulted impossible to purify, probably due to the formation of two different very similar isomers. The same didn't happen under microwave radiation, in which case the harsh reaction conditions and the brief reaction time yielded a single presumably kinetic isomer. Intermediate **11** was obtained from the cyclisation reaction of **10** with *Eaton's reagent*<sup>139</sup> (MeSO<sub>2</sub>OH and catalytic P<sub>2</sub>O<sub>5</sub>) differently from the procedure reported in literature<sup>140</sup> which involves the use of dangerous H<sub>2</sub>SO<sub>4</sub> conc. and a week reaction time, still affording lower yields.



**Scheme 4.1.** Reagents and conditions: i)  $\text{H}_2\text{SO}_4$ , methanol, overnight, r.t., ii)  $\text{K}_2\text{CO}_3$ , KI cat., dimethylformamide, 5h at reflux,  $55^\circ\text{C}$  for 5. d, iii)  $\text{PBr}_3$ , dichloromethane,  $100^\circ\text{C}$  for 1h, overnight at r.t..



**Scheme 4.2.** Reagents and conditions: i) ethyl malonate,  $\text{MgCl}_2$ , triethylamine, dry acetonitrile, overnight, r.t.; ii)  $\text{MeSO}_2\text{OH}/\text{P}_2\text{O}_5$ ,  $30^\circ\text{C}$ , 4 h,  $\text{N}_2$ ; iii)  $\text{HCl}$ , methanol, r.t.; iv) MW, ethoxyethanol, 25 min., 250 W,  $200^\circ\text{C}$

### 4.3 Nile Red cyclopalladated complexes containing anchoring groups

Cyclometallation of the novel derivatives  $\mathbf{H(NR)^{3-5}}$  occurred successfully (Figure 4.2) via the already described cyclometallation reaction with  $\text{Pd(OAc)}_2$  (Scheme 4.3).<sup>85</sup> A substituted common to all the complexes **XIII-XIV** Schiff base  $\mathbf{H(BSC}_6)$  completes the coordination sphere of the metallic centre (Figure 4.2). The use of a Schiff base as an ancillary ligand was chosen in order to maintain the separation of the frontier molecular orbitals HOMO/LUMO and the photogeneration and photoconduction properties observed for this type of complexes. Furthermore, the presence of alkyl chains into the molecular structure should, as reported in literature,<sup>141</sup> prevent the molecular aggregation which favours the recombination and lowers the efficiency.

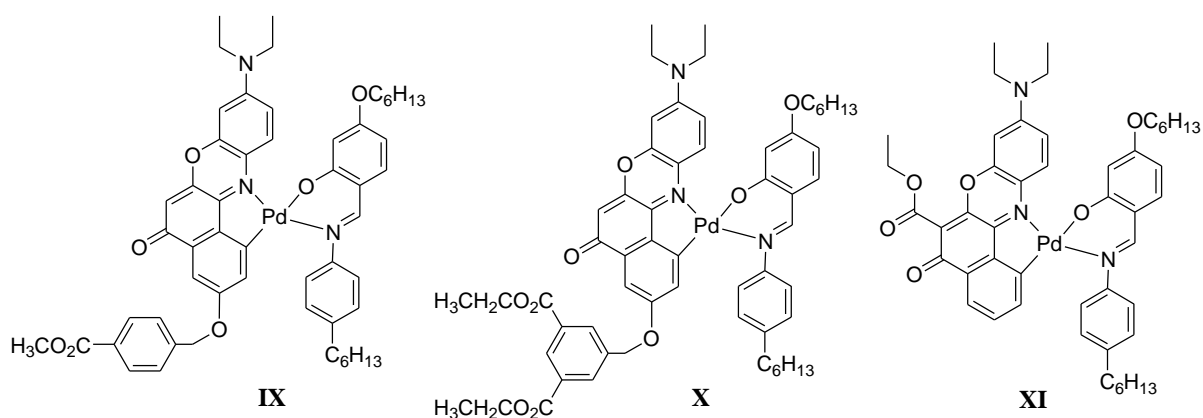
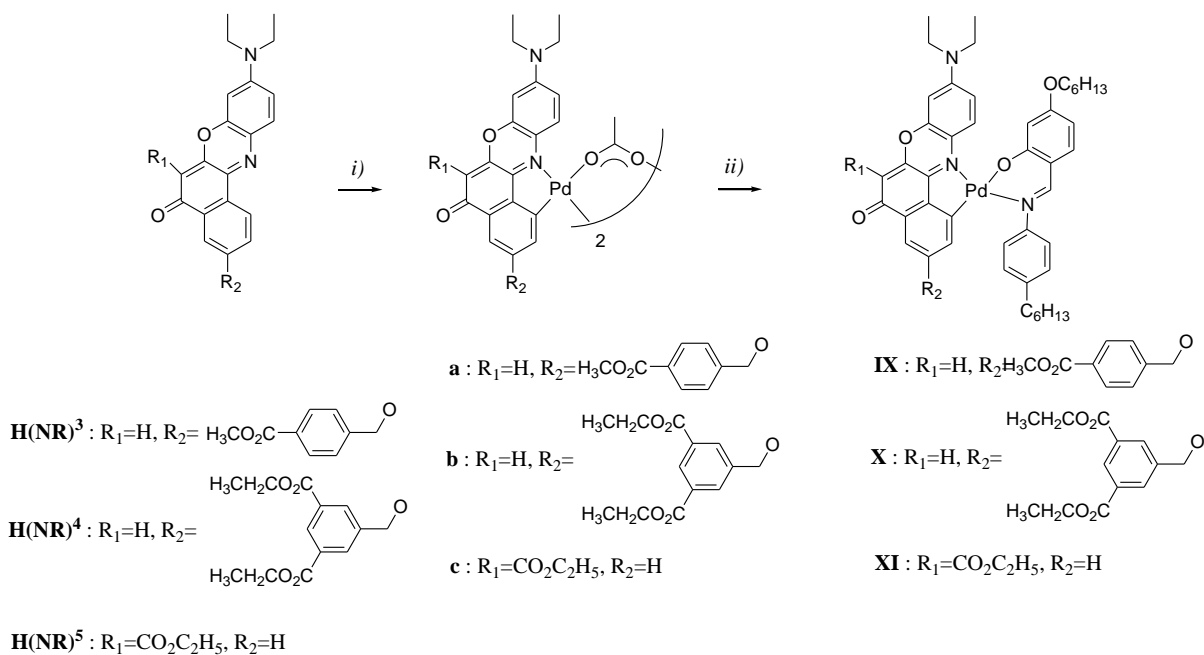
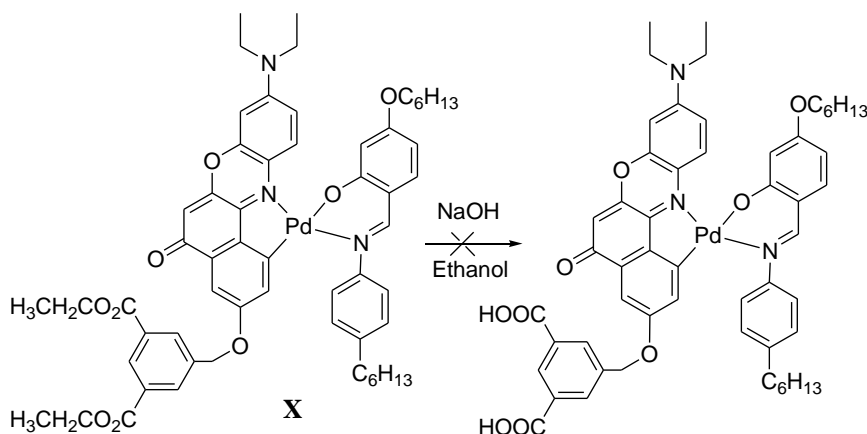


**Figure 4.2.** Molecular structures of complexes **IX-XI**



**Scheme 4.3.** Reagents and conditions: i) acetic acid, 55 °C, 5 d. for  $\mathbf{H(NR)^{3-5}}$  and 3 d. for  $\mathbf{H(NR)^5}$ , ii)  $\mathbf{H(BSC_6)}$ , dichloromethane/ethanol, r.t., 5 d.

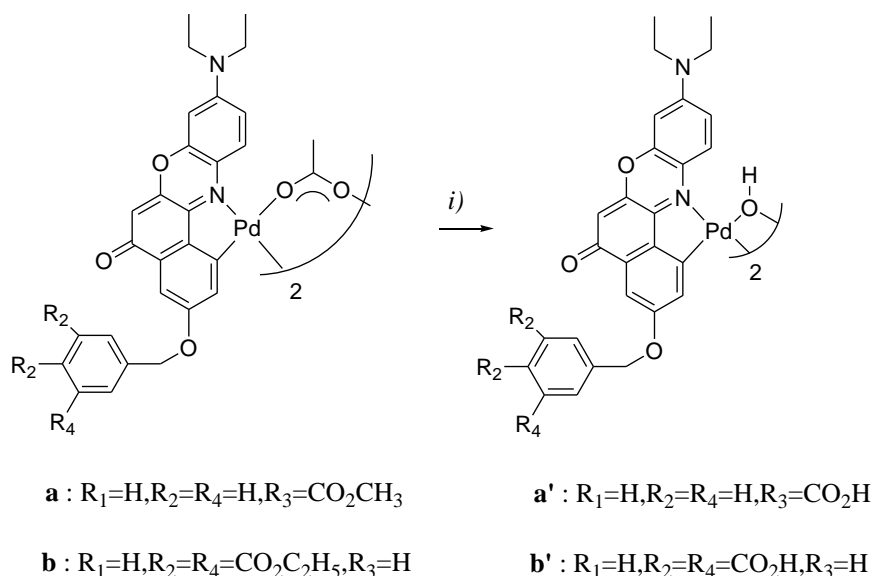
As already mentioned in the introduction, it has been demonstrated that the carboxylic functionality represents the ideal anchoring group. Unfortunately, the attempt to obtain the carboxylic analogues of complexes **IX-XI** by direct hydrolysis (Scheme 4.3) wasn't successful.



**Scheme 4.3.** Failed attempt to hydrolyse complex **X**.  
Identical results were obtained for **IX** and **XI**.

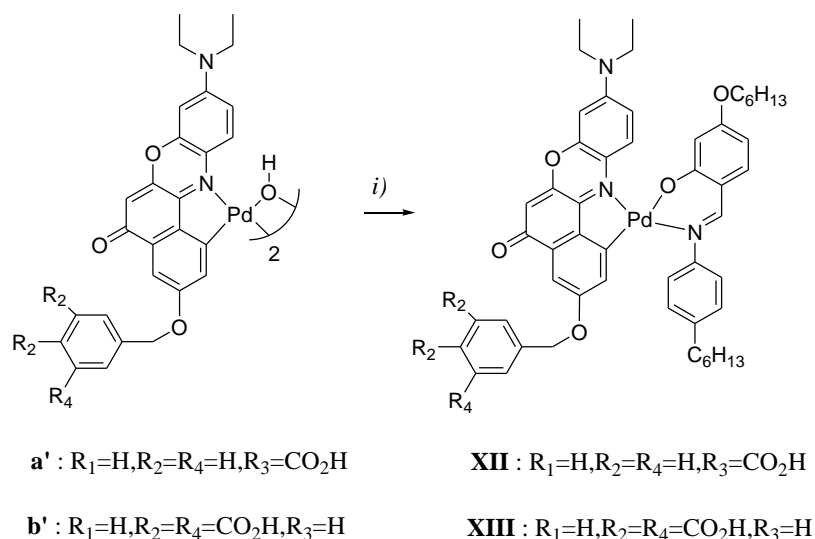


A different synthetic strategy was chosen in order to restore the carboxyl groups. The acetate bridged cyclopalladated intermediates **a** and **b** were treated with NaOH in acetone and water<sup>129</sup> affording the hydroxy bridged intermediates concomitantly with the hydrolysis of the ester group(s) of **IX** and **X** to free acid(s) (Scheme 4.4). Unfortunately, complex **XI** resulted unstable in such an alkaline medium which presumably favours an intramolecular decarboxylation reaction.



**Scheme 4.4.** Reagents and conditions: i) NaOH, acetone/water, r.t., overnight

The hydroxy-bridged cyclopalladated intermediates **1a'**-**b'** were treated with the same alkyl substituted Schiff base **H(BSC<sub>6</sub>)**<sup>78</sup> to yield the final acid complexes (Scheme 4.5). Due to the presence of the free carboxylic acid groups, the two complexes showed low solubility in common organic solvents, especially complex **XII**, which was soluble only in pyridine.



**Scheme 4.5.** Reagents and conditions: i) for **XII**: pyridine, r.t., 24 h; for **XIII**: dimethylformamide, r.t., 48 h

#### 4.4 Solution electrochemistry

The redox behaviour of the three ester derivatives complexes **IX-XI** was investigated, while, unfortunately the poor solubility of complexes **XII-XIII** prevented the obtaining of resolved cyclic voltamograms. Figure 4.2 shows the cyclic voltamograms of complexes **IX-XI**. The redox potentials vs.  $Fc/Fc^+$ , as well as the estimated HOMO and LUMO energies are listed in Table 4.1.

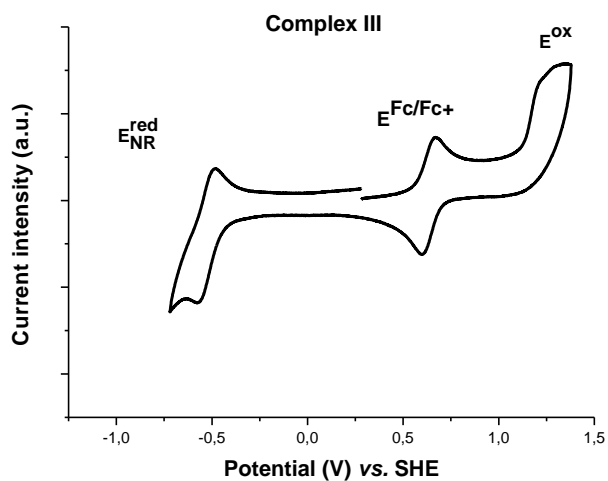
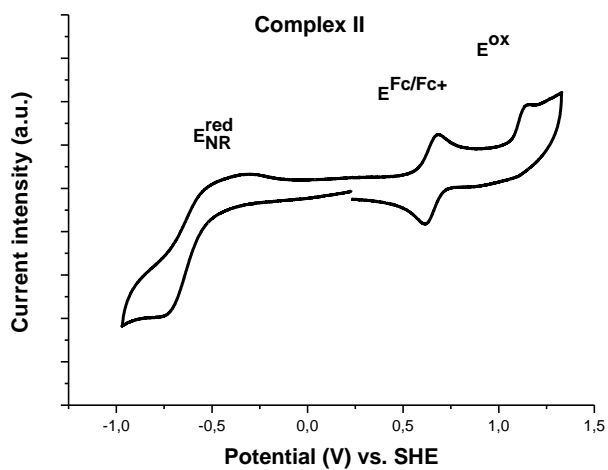
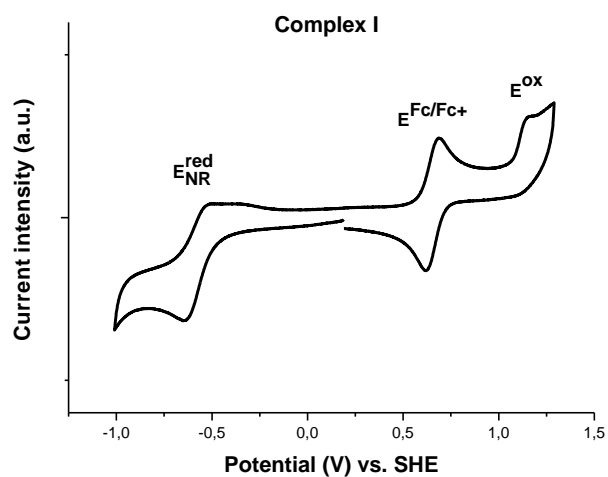


**Figure 4.2.** Cyclic voltammograms of complexes IX-XI

The redox behaviours of **IX-XI** are identical, with one quasi-reversible reduction (at *ca.* -1.2 V vs. Fc/Fc<sup>+</sup>) typical for cyclometallated Nile Red and a irreversible oxidation attributed to the Schiff base. Noteworthy, the incorporation of ester groups in different number and position onto the Nile Red backbone doesn't influence the reduction potentials of the resulting complexes even for complex **XI** for which a stronger electronic effect was expected due to the proximity of the ester group with the aromatic core of the Nile Red fragment. The estimated HOMO and LUMO energies (-5.1/-3.6 eV) of complex **IX-XI** are identical with those of the Nile Red complexes previously described in the thesis.

Complex no.	E <sup>red</sup> <sub>NR</sub> (V) <sup>a</sup>	E <sup>ox</sup> <sub>BS</sub> (V) <sup>a</sup>	HOMO	LUMO
<b>IX</b>	-1.24	+0.51	-5.3	-3.6
<b>X</b>	-1.23	+0.54	-5.3	-3.6
<b>XI</b>	-1.17	+0.56	-5.3	-3.6
<sup>a</sup> Potentials expressed in volts vs. Fc/Fc <sup>+</sup> ; R=reversible				

**Table 4.1.** Cyclic voltametry data relative to complexes **IX-XI**

These properties suggest that the separation HOMO/LUMO is maintained as observed for the class of complexes (NR)Pd(O<sup>^</sup>N) (see previous Chapters) with the HOMO situated on the ancillary Schiff base and the LUMO on the cyclometallated Nile Red fragment. Moreover, the estimated energy levels HOMO and LUMO could be suitable for the use in DSSCs (Figure 4.3).

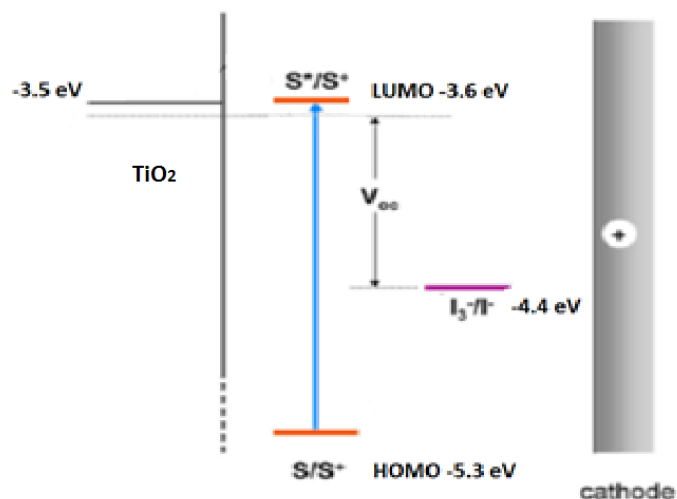


**Figure 4.3.** Schematic diagram comprising the TiO<sub>2</sub>, I/I<sup>3-</sup> energy levels and the HOMO and LUMO energy levels of the dyes IX-XI

#### 4.5 Testing Nile Red cyclopalladated complexes in DSSCs

In collaboration with the University of Bath, the synthesised complexes **X**, **XIII**, which include two anchoring groups on the molecular structure and **XI** whose unique anchoring group is directly grafted onto the aromatic core, have been tested as sensitizers in DSSC devices. The cells were prepared according to the procedure described in Chapter Ten. Preliminary adsorption tests of the complexes to nanostructured single layer titania films prepared by *doctor blading* (*ca.* 10 μm thickness) were conducted. The films were dyed from a 3·10<sup>-4</sup> M MeCN/*t*-BuOH solution, which is the commonly used dye bath for the standard Ruthenium-based DSSCs.<sup>143</sup> Figure 4.3 shows the absorption tests conducted on complex **X**. The absorbance follows an increasing trend with dye immersion time until reaching a maximum and a subsequent decrease probably due to decomposition. The immersion time correspondent to the maximum adsorption is of *ca.* 50 h, which represents a quite high value comparative with the standard Ruthenium based dyes.<sup>143,52</sup> This is in agreement with the fact that the anchoring process for complex **X** occurs via a more slow transesterification process.

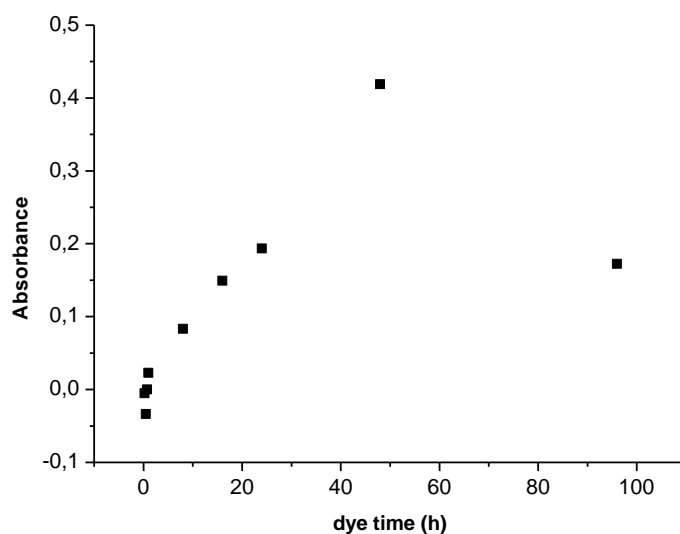


**Figure 4.3.** Absorbance of a titania film dyed with complex **X** in function of the immersion time

In the attempt to enhance the adsorption of complex **X** to titania, a basic dye bath was used by adding 4% (v/v)  $10^{-4}$  KOH solution to the  $3 \cdot 10^{-4}$  M MeCN/t-BuOH dye bath, in order to favour the grafting of the anchoring groups presumably, by an *in situ* hydrolysis mechanism. Note in Figure 4.4 the comparison of the adsorption of complex **X** (two days dying time) in the absence (a) and the presence (b) of KOH. Indeed, the absorbance is higher in the basic medium indicating a more efficient adsorption process.

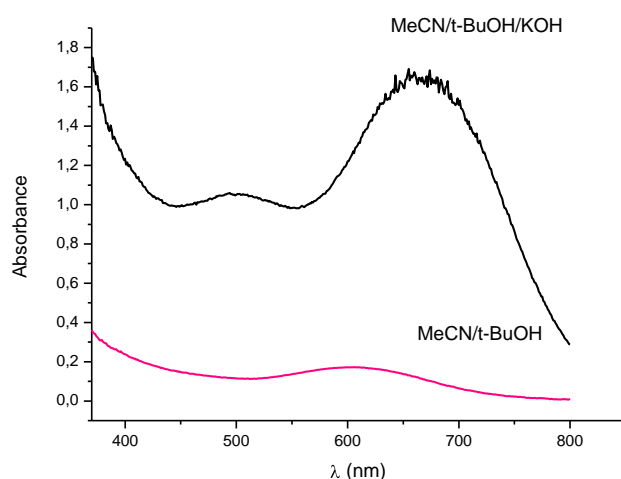


**Figure 4.4.** Absorbance of a titania film dyed with complex **X** in the absence (red curve) and in the presence (black curve) of KOH

Adsorption tests were also carried on the free acid bearing complex **XIII**. Figure 4.5 shows the comparison between the single layer titania (*ca.* 10  $\mu\text{m}$  thickness) films dyed in a DMF/*t*-BuOH/1:1 (blue) and DMF/0.05 M KOH (EtOH) (pink) solution for 24 hours. The more polar dimethylformamide was used for complex **XI** instead of acetonitrile for solubility reasons.

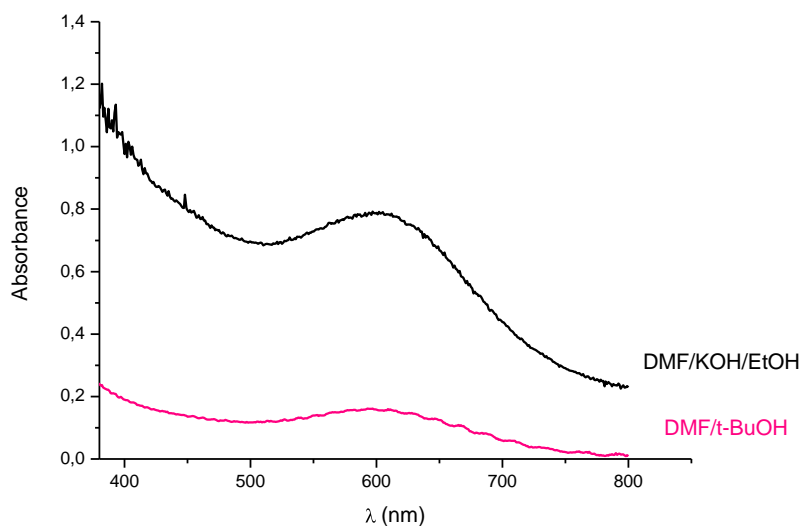


**Figure 4.5.** the titania films dyed in a DMF/*t*-BuOH/1:1 (blue) and DMF/0.05 M KOH (EtOH) (pink) solution for 24 h.

Adsorption test were carried on on complex **XI**, which presents a single ester anchoring group. The single layer titania films were dyed from a  $3 \cdot 10^{-4}$  M MeCN/*t*-BuOH solution for 3 days. The absorbance of the dyed titania films in function of dying time are reported in Figure 4.6.

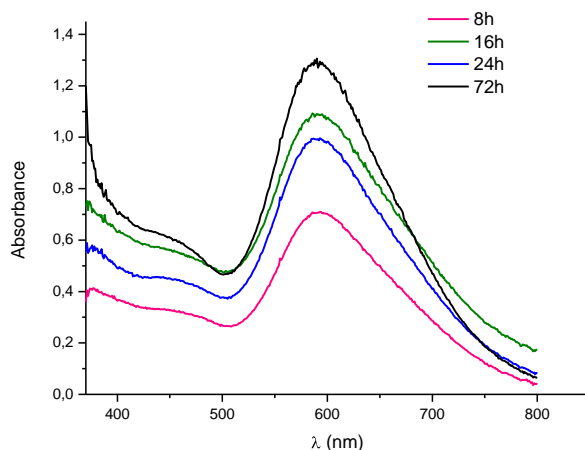


**Figure 4.6.** Absorption spectra of a) a  $3 \cdot 10^{-4}$  M MeCN/t-BuOH of **XI** and b) a titania film dyed with complex **XI**

The current-voltage performances relative to the devices realized using complexes **X** and **XI** (with two anchoring groups) and complex **XIII** (one single anchoring group) are reported in Table 4.2. The titania films were dyed from a  $3 \cdot 10^{-4}$  M MeCN/t-BuOH solution for 2 days (**X**) and for 3 days for **XI** and from a  $3 \cdot 10^{-4}$  M MeCN/t-BuOH + 4 % (v/v)  $10^{-4}$  M KOH solution (**X** basic medium).

	<b>X</b>	<b>X</b> <b>Basic medium</b>	<b>XI</b>	<b>XIII</b>
$V_{oc}$ (V)	0.59	0.42	0.38	0.64
$J_{sc}$ ( $A/cm^2$ )	0.02	0.01	0.01	0.04
<b>FF (%)</b>	57.9	49.7	44.9	64.7
$\eta$ (%)	0.009	0.003	0.003	0.017

**Table 4.2.** Characteristic parameters of the cells prepared with complexes **X**, **XI** and **XIII** as sensitizers



Even though the  $V_{oc}$  potentials are comparable with those of the standard Ru(II)-based DSSC<sup>20</sup>), a very poor electron injection was verified. Among the two dyes **X** and **XI**, the free carboxylic bearing complex **XI** showed both higher  $V_{oc}$  and  $I_{sc}$ , leading to the higher efficiency, while complex **XI** showed the comparatively lower efficiency of all, even if the adsorption tests indicated a good degree of adsorption (Figure 4.6 b)).

Considering the dyeing process, better adsorption was observed for complex **X** in basic medium, but a different  $V_{oc}$  value was reported for the cell prepared with the basic dye bath with respect to the one in which the sensitizer was adsorbed from the standard acetonitrile/*t*-butanol solution. This could presumably be attributed to a different type of interaction with the titania film. The efficiency of the DSSCs resulted dependent, as expected, of the number of the anchoring groups grafted on the sensitizer. For complexes **X** and **XI** with two anchoring groups, high  $V_{oc}$  values were measured, but low injection was observed. Considering the obtained results, we hypothesised possible reasons of the bad electron transfer from the sensitizer to the titania film which could be the lack of conjugation between the carbonylic anchoring group and the aromatic core of the cyclopalladated Nile Red ligand or the side effects exerted on the dye by the used electrolytic solution. In the attempt to deeper understand the behaviour of the dyed films in the presence of the  $I/I^{3-}$  redox couple electrolyte,  $^1H$  NMR spectra were recorded for complex **XI** (Chapter Ten) and compared with the spectrum obtained in the absence of the electrolyte in the same deuterated solvent ( $CDCl_3$ ). Indeed, different chemical shifts were observed in the  $^1H$  NMR spectrum of complex **XI** in the presence of the electrolytic couple. This fact could be attributed to the oxidative addition of  $I_2$  to the Pd(II) centre which would give rise to a new octahedral Pd (IV) complex. This hypothesis is sustained by the analysis of the  $^1H$  NMR spectra of compound **X** (Figure 4.7) before (a) and after (b) the treatment of the  $CDCl_3$  solution with the  $I_2$  containing electrolyte solution. As already described for Nile Red cycloplatinated complexes,<sup>144</sup> the oxidative addition at the square planar Pt(II) complex leads to a slight upfield shift of all the aromatic protons. Indeed, in the case of complex **X** the same trend was observed for the chemical shift of all the aromatic protons.

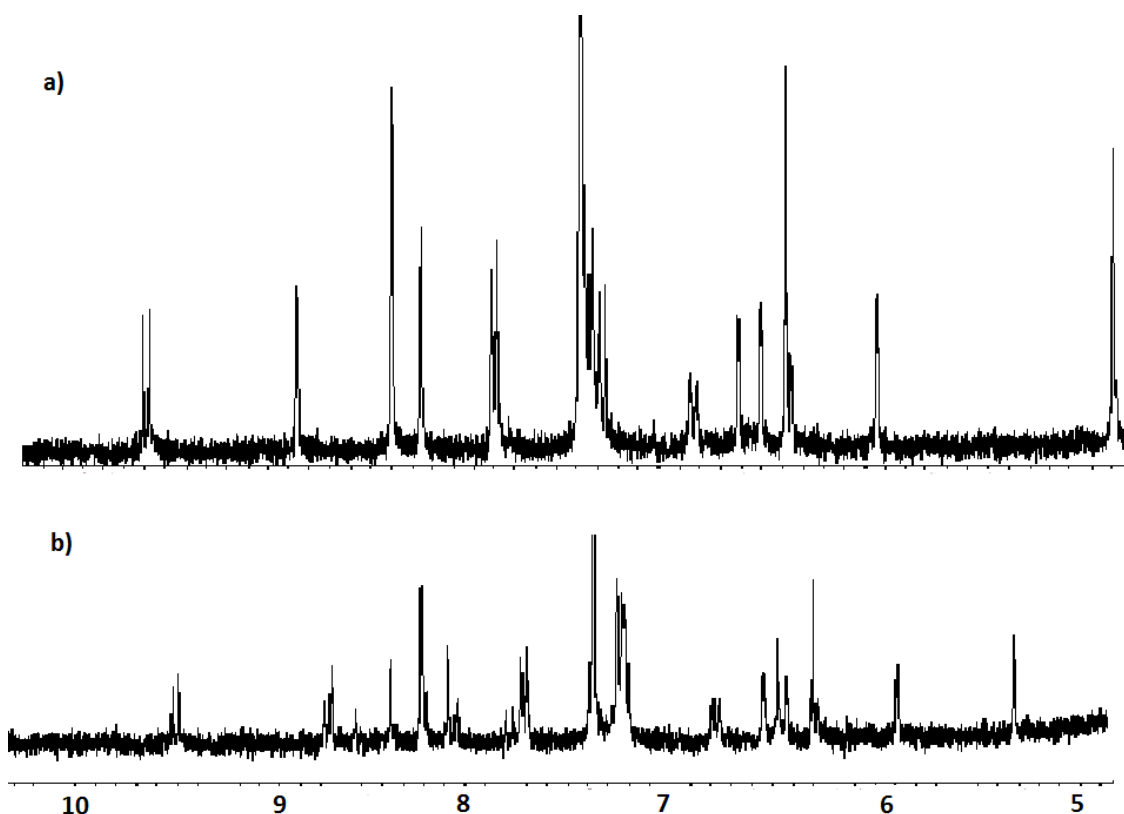


**Figure 4.7.**  $^1\text{H}$  NMR spectra of **X** a) before and b) after the treatment with  $\text{I}_2$

#### 4.6 Conclusions

Novel Nile Red complexes, bearing ester (**IX-XI**) and free carboxylic (**XII-XIII**) anchoring groups were successfully synthesized and characterized. The molecular structure of the complexes is similar to the parent photoconductive compounds already described in Chapter 2 and Chapter 3. As in that cases, the HOMO/LUMO frontier orbitals molecular separation is maintained, with the LUMO mainly situated on the cyclometallated ligand, onto which the anchoring groups are grafted and the HOMO predominantly localized on an alkyl chain substituted ancillary Schiff base.

Differently from complexes **IX-XI** which were prepared by the procedure already described in this work, to obtain complexes **XII-XIII** instead, a new synthetic pathway was followed, since direct hydrolysis of the final ester substituted complexes resulted unsuccessful. A metathetical reaction of the acetato-bridged dimers in the presence of NaOH yielded hydroxy-bridged dimers and, concomitantly, the ester groups were hydrolysed to free acids.

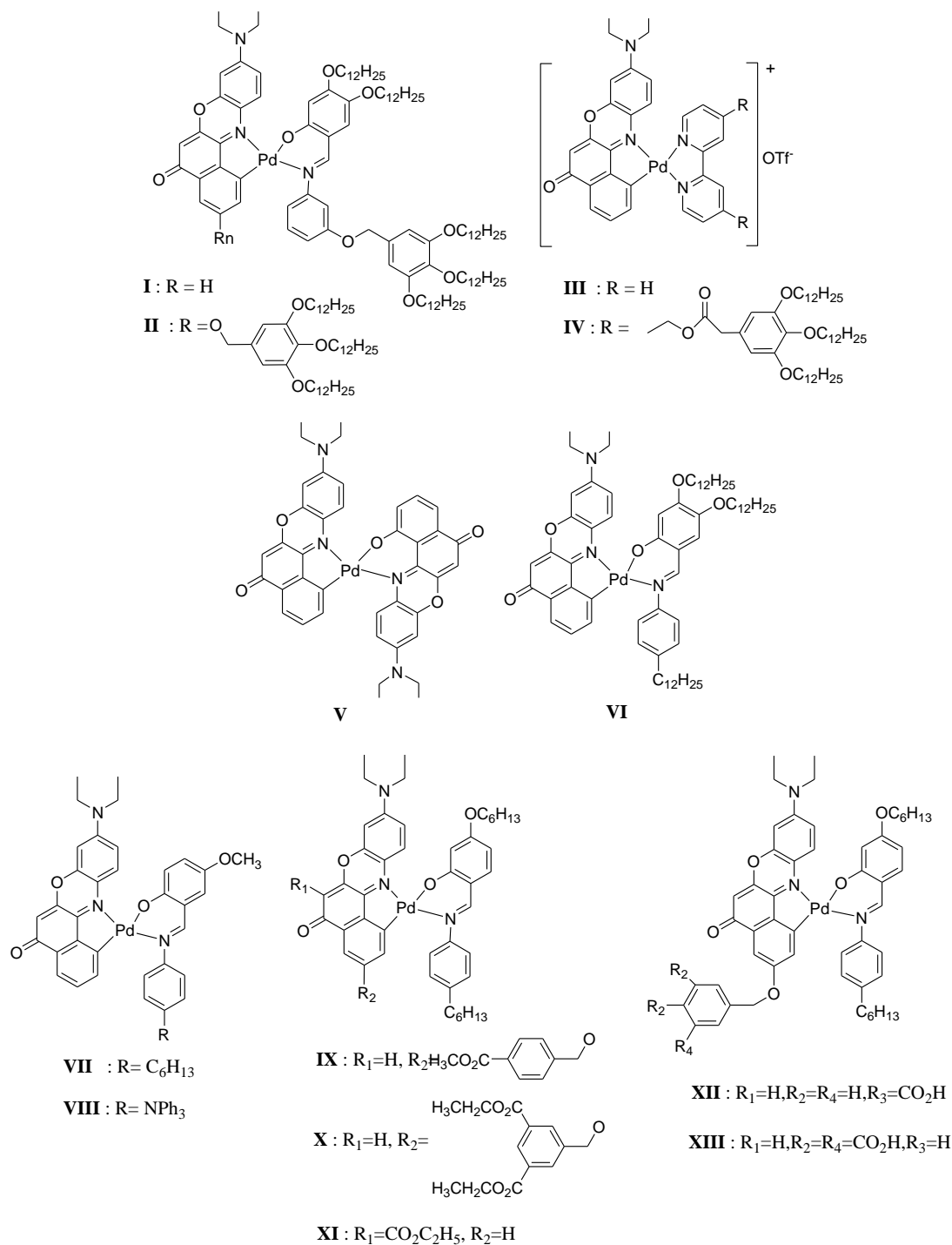
Complexes **X**, **XI** and **XIII** were tested as sensitizers in standard DSSCs during a stage at the University of Bath, after carrying on adsorption tests to titania films prepared by *doctor blading*. Complex **X** was adsorbed onto titania films in the absence and in the presence of KOH and the adsorptions were compared. Slightly better efficiencies were measured for the cells in which complex **XIII** with two free acidic anchoring groups was used as sensitizer. For all complexes, good  $V_{oc}$  values were measured, but no injection was verified, probably due to the square planar cyclopalladated complexes and a side reaction which involves with the  $I/I^{3-}$  electrolyte couple. In fact, an oxidative addition presumably occurs to the Pd(II) complexes in the presence of  $I_2$ .



## Chapter Five

### Conclusions

Through the synthesis of complexes **I-XIII**, we have shown the possibility of using Nile Red either as a cyclometallated or as an ancillary ligand, for the formation of neutral or cationic cyclopalladated complexes.



The complete characterization of these complexes have allowed us to conclude that:

i) the separation of their frontier orbitals on a molecular scale (*ca.* 1.5 eV energy gap) is maintained as in the previously reported complexes of the same class (C<sup>N</sup>)Pd(O<sup>N</sup>) with the HOMO situated mainly on the Schiff base and the LUMO on the cyclometallated ligand;

ii) by appropriate functionalization of either the Nile Red fragment and/or the ancillary ligand, neutral and cationic metallomesogens can be obtained through the self-assembly of ellipsoidal dimeric pairs kept together by a hydrogen bonding network;

iii) Nile Red cyclopalladated complexes pair as dimers in the solid state, as confirmed by X-ray diffraction analysis through identical hydrogen bonding network;

iv) by introducing an electropolymerizable triphenylamine fragment onto the ancillary ligand of Nile Red cyclopalladated complexes, electrogenerated films can be obtained and further comprehensive studies are in progress in order to investigate the properties of the obtained polymers.

Photoconductivity measurements have been performed and have shown values between  $10^{-13}$ - $10^{-8}$  SW<sup>-1</sup>cm<sup>-1</sup>, three orders of magnitude higher than the reported values for similar complexes, with the best performance obtained for the discotic metallomesogen **I**.

The availability of such photoconductors with electropolymerizable fragments or mesogenic properties represents a starting key point for the development of new hybrid organic/inorganic optoelectronic devices based on molecular assembling.

Furthermore, the low molecular weight photoconductive complex **VI** has been actually tested as a donor in a bulk heterojunction solar cell using PC<sub>61</sub>BM as an acceptor. Even though the obtained device efficiency was very low, the advantages of using an intrinsic photoconductor have been evidenced.

Eventually, complexes bearing ester and carboxylic anchoring groups have been synthesized and tested as sensitizers in standard DSSCs. Even if high  $V_{oc}$  values have been measured, no injection has been verified probably due to a chemical side reaction with supporting electrolyte ( $I/I^{3-}$ ) and possible oxidative addition of the cyclopalladated complexes. The use of a solid supporting electrolyte should be a possibility to be contemplated in further investigations.





## **Second part**

Novel molecular materials  
based on Ir(III)  
for electroconversion



## Chapter Six Introduction to electroluminescence

### 6.1 Inorganic LEDs

The operation of Light Emitting Devices (LEDs) is based on spontaneous light emission in semiconductors, when a sufficiently large forward-bias voltage is applied across a  $p$ - $n$  junction and the radiative recombination of excess electrons and holes induces luminescence. In addition to the energy savings and positive environmental effects, LEDs also offer controllability of their spectral, spatial, temporal, and polarization properties as well as their colour temperature.<sup>145</sup>

The demonstration of direct band-gap alloy semiconductor (GaAsP) visible (red) emitters by Nick Holonyak at General Electric in 1962 began the evolution of high-brightness LED technology. In 1993 Shuji Nakamura fabricated double-heterostructure InGaN/GaN blue LED chips and since then tremendous progress has been achieved in development of solid-state lighting based on InGaN semiconductors.<sup>146</sup> Currently, research is focused on white emitting LEDs, obtained by embedding blue-emitting chip LEDs with different phosphors.<sup>147</sup>

However, even if high efficiencies and long lifetimes have been reached for LEDs, important issues such as semiconductor high cost technology, the rigid architecture and the temperature dependence of the efficiency need to be overcome in order to extend the LED application area. Thus, in an attempt to develop flexible low cost devices, organic materials have been considered as emitting species in electroluminescent devices.

### 6.2 Organic Light Emitting Diodes (OLEDs)

Electroluminescence of organic materials was observed for the first time by Martin Pope *et al.* in 1963,<sup>148</sup> but only in 1987 an electroluminescent device was reported, making use of the fluorescent electron transporting tris(8-hydroxyquinoline) Aluminium (AlQ<sub>3</sub>) complex (Figure 6.1) with a 1% device efficiency.<sup>149</sup> Since then, remarkable progresses have been made in the field of Organic Light Emitting Diodes (OLEDs) by incorporating various combinations of organic polymers and organic or organometallic chromophores.<sup>150</sup>

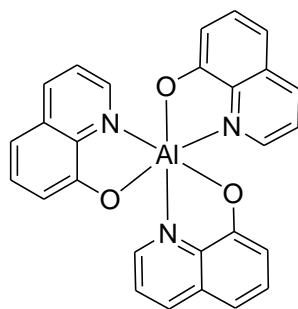


**Figure 6.1.** Molecular structure of the fluorescent emitter AlQ<sub>3</sub>

The field of OLEDs could be roughly divided into two groups, in function of the nature of the used electroluminescent materials, namely small molecules and polymeric materials<sup>151</sup> (Figure 6.2). The OLED technology has shown a fast development and dependently from the emitter nature, different architectures have been proposed for electroluminescent devices.<sup>152</sup>

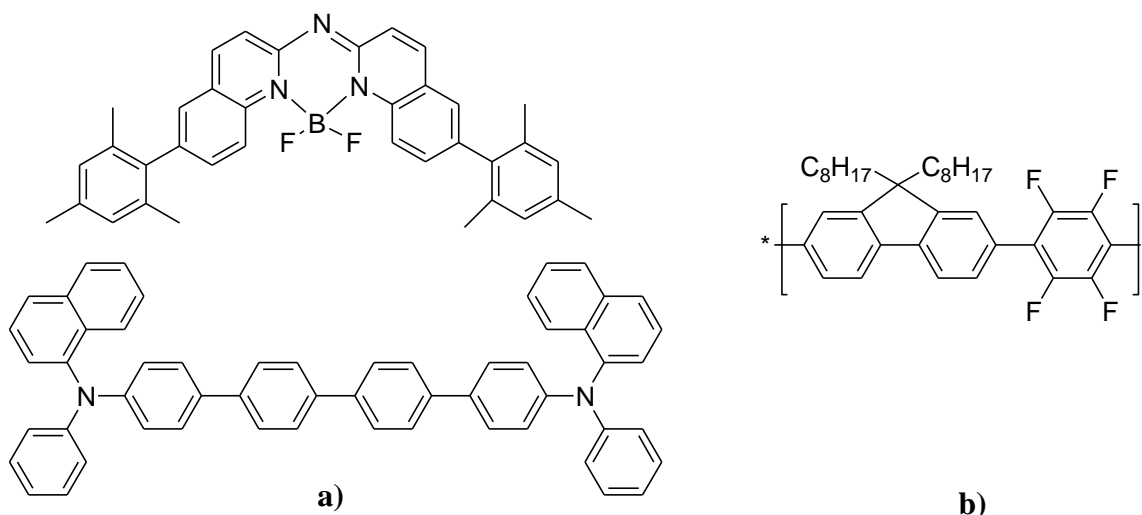


**Figure 6.2.** a) Molecular fluorescent emitters<sup>153</sup> and b) polymeric emitter<sup>154</sup> used in OLEDs

Multilayer structure in which each layer presents a specific role and cathodes made of low work function metals are generally required in order to achieve high efficiencies and low operating voltages in OLEDs. In its simplest configuration, an OLED consists of a single layer of an organic light emitting polymeric semiconductor sandwiched between two metal electrodes, the anode (positively charged) and the cathode (negatively charged). Under the application of a forward bias, holes are injected from the anode into the HOMO of the organic layer and migrate towards the cathode.

Analogously, electrons injected from the cathode into the LUMO of the organic material migrate towards the anode. When a hole and an electron meet in the bulk of the organic layer, they may combine to form an exciton. A fraction of these excitons recombine radiatively, giving rise to light emission. The basic requirements from the organic semiconductor are the ability to transport both electrons and holes and a high luminescence efficiency.<sup>155</sup>

The use of organic semiconducting polymers doped with molecular emitters in a host-guest type configuration has demonstrated good charge transport properties and formation of high efficiency emitting excitons. OLEDs (Figure 6.3) are conventionally fabricated by spin coating, inkjet printing or by vacuum deposition of organic materials on an Indium Tin Oxide (ITO) glass coated with hole-conducting polymers such as poly(3,4-ethylenedioxythiophene)/poly(styrene sulfonate) PEDOT:PSS.<sup>156</sup> On top of the ITO coated glass, an organic hole transporting layer HTL, usually composed of carbazole derivatives<sup>157</sup> is deposited, followed by the organic host (hole transporting)-guest (electron transporting) emissive layer. An electron transporting layer ETL, such as AlQ<sub>3</sub> is eventually applied. It has been shown<sup>152</sup> that OLEDs efficiency is increased when electron blocking layers EBL and hole blocking layers HBL are applied between the hole transporting layer and the emissive layer and, respectively, between the emissive layer and the electron transporting layer.

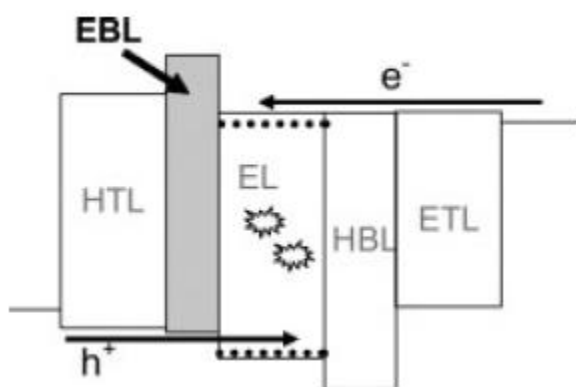


**Figure 6.3.** Schematic energy level of an OLED<sup>152</sup>

By using chromophores with different emission wavelength, OLEDs of different colours are obtained. Since one of the greatest challenges in the organic electroluminescent technology is to obtain efficient white OLEDs, intensive research have been dedicated to the development of luminescent materials showing emission at

the particular wavelengths of the primary colours red, green and blue (RGB displays). As an example, recently, a series of blue, green and red light-emitting, 9,9-bis(4-(2-ethylhexyloxy)phenyl) fluorene (PPF) based polymers containing a dibenzothiophene-*S,S*-dioxide (SO) unit (PPF-SO polymer), with an additional benzothiadiazole (BT) unit (PPF-SO-BT polymer) or a 4,7-di(4-hexylthien-2-yl)-benzothiadiazole (DHTBT) unit (PPF-SO-DHTBT polymer) were reported (Figure 6.4). Blending different ratios of blue (PPFSO), green (PPF-SO-BT) and red (PPF-SO-DHTBT) emitting polymers allowed highly efficient white polymer light-emitting diodes were realized.<sup>158</sup>

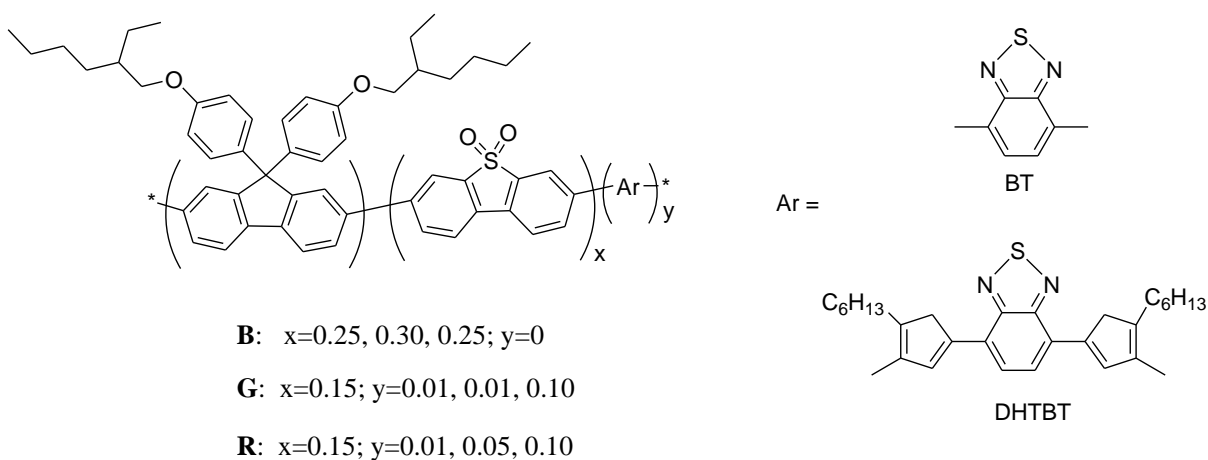


**Figure 6.4.** Molecular structures of the blue (**B**), green (**G**) and **R** (red) emitting polymers

In order for OLEDs to be used on a large scale, device lifetimes should be considered. There are two possible degradation mechanisms for OLEDs: i) the dark spot formation (induced by the penetration of moisture through defects in the cathode, causing degradation of the cathode-organic interface<sup>159</sup>) and ii) the gradual decrease of performance with current passing through the device. The former takes place independent of whether the device is operating, while the latter only takes place while the device is operating. For devices using glass substrates, the dark spots problem may be greatly resolved by encapsulating the device with a glass or metal backing, using edge seal and desiccant. For devices using plastic substrates or using thin-film encapsulation instead, adequate protection of OLEDs against moisture lasting over the expected lifetime of a lightening source has yet to be demonstrated.

However, recently reported OLED device lifetimes have reached over 125,000 hours lifetimes.<sup>160</sup>

### 6.3 Light Emitting Electrochemical Cells (LECs)

Light Electrochemical Cells (LECs) represented already since their introduction by Pei *et al.* in 1995,<sup>161</sup> a valid single layer device alternative to OLEDs. As described by Pei and co-workers, in this type of device, a p-n junction is created in situ through simultaneous p-type and n-type electrochemical doping on opposite sites of a thin film of a luminescent semiconducting polymer blended with an electrolytic salt to provide the necessary counterions for the introduced charges. Since ionic mobility is necessary in this type of device for the transport of the electrochemically generated charges, when the used polymer is not ionically conductive in nature, another ion-transporting polymer is added. When a sufficiently high bias is applied between the two metal electrodes, both p-type and n-type charge carriers start to be electrochemically injected into the active layer near the respectively oppositely charged electrodes. Under the influence of the applied field, the holes move from the anode toward the cathode and the electrons from the cathode to the anode. The propagating charges combine in the p-n junction induced region to form excitons which radiatively decay to the ground state, generating the emission of light.<sup>161</sup> Noteworthy, currently, three different models compete in describing the LECs mechanism.<sup>162</sup> However, all models recognise the key role played by the mobile counterions.

The main advantages of using LECs instead of OLEDs are: i) the possibility of using thicker single organic active layers, ii) their insensitivity to the work function of the electrodes employed, allowing the use of air-stable electrodes, such as gold, silver or aluminium which encapsulation in the device does not have to be so rigorous as in OLEDs.<sup>163</sup> Moreover, the turn-on voltages of LEC devices are generally low and approximately equal to the measured optical band gaps of the emissive materials. The principle drawback of LECs is instead the high response delay due to the time needed for electroluminescence to occur after the formation of the ionic double-layer at the electrode-interfaces.<sup>163</sup>

The first LECs used a conjugated light emitting polymers (such as poly[5-(2'-ethylhexyloxy)-2-methoxy-1,4-phenylene vinylene] MEH-PPV) in combination with inorganic salts (like trifluoromethyl sulfonate) (Figure 6.3). For example, the use of poly(*p*-phenylene vinylene) PPV blended with a solid electrolyte that provided the mobile ions was described by Yang and Pei.<sup>164</sup>

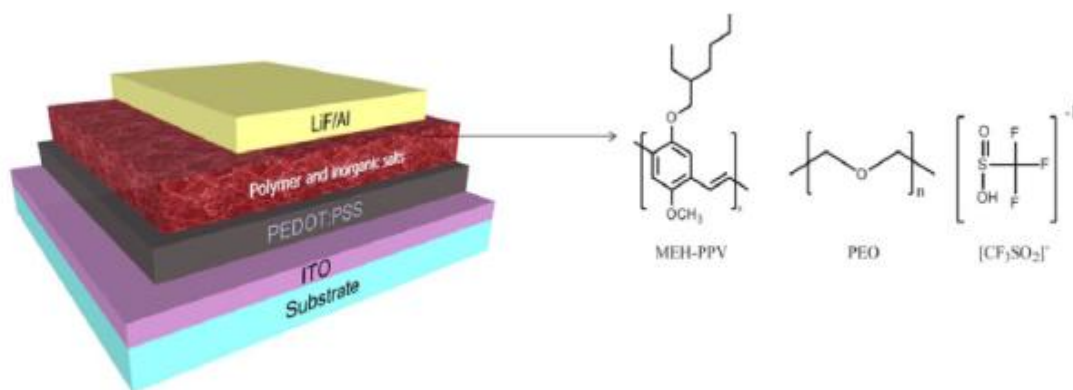


**Figure 6.3.** Schematic representation of a polymer-based LEC and the typically used materials<sup>163</sup>

#### 6.4 Use of transition metal complexes in electroluminescent devices

In purely organic OLEDs and LECs, the emission of the employed chromophores (organic small molecules, polymers or AlQ<sub>3</sub>) occurs via a fluorescence pathway. Fluorescence is limited to radiative relaxation of molecules (mainly organic) which conserve spin symmetry during the radiative transition from their excited (singlet) state to the ground state. On the contrary, phosphorescence results from spin “forbidden” transition where symmetry is not conserved, like, for instance, transitions between triplet excited states and singlet ground states.<sup>165</sup> Under electrical excitation, excitons are formed in both singlet and triplet states in a 1:3 ratio.<sup>166</sup> It follows that harvesting luminescence from both singlet and triplet excitons has the potential to lead to higher efficiencies in phosphorescent-based with respect to fluorescent-based electroluminescent devices.

In transition metal complexes, due to the spin-orbit coupling induced by the presence of the heavy metal atom, singlet and triplet states intersystem crossing occurs, leading to an efficient phosphorescent emission even at room temperature. Transition metal complexes, especially those based on Pt(II) and Ir(III)<sup>167</sup> can therefore serve as efficient phosphorescent emitters in electroluminescent devices since both singlet and triplet excited states can be trapped.



### 6.4.1 Use of transition metal complexes in efficient OLEDs

Since the report of Baldo *et al.* in 1999 on a 7.5% efficiency OLED based on electrophosphorescence of a homoleptical cyclometallated tris(2-phenylpyridine)Ir(III) organometallic complex<sup>168a</sup> (Figure 6.4), huge efforts have been made to improve phosphorescence-based OLEDs efficiency. Comprehensive studies have been carried on in the last two decades in an attempt to rationalize the working mechanism, to improve the device architectures and to design new highly phosphorescent chromophores.

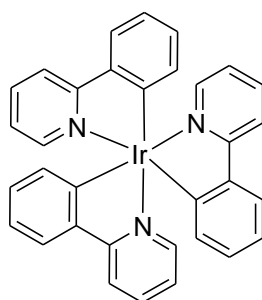


**Figure 6.4.** Molecular structure of the phosphorescent Ir(ppy)<sub>3</sub> chromophore used in an highly efficient OLED

A typical multilayer device architecture containing triplet emitters (in this case acetylacetonato-(bis(2-phenylpyridine)Ir(III))<sup>168b</sup>) is described in Figure 6.5 as an example and the resulting energy scheme is presented in Figure 6.6.

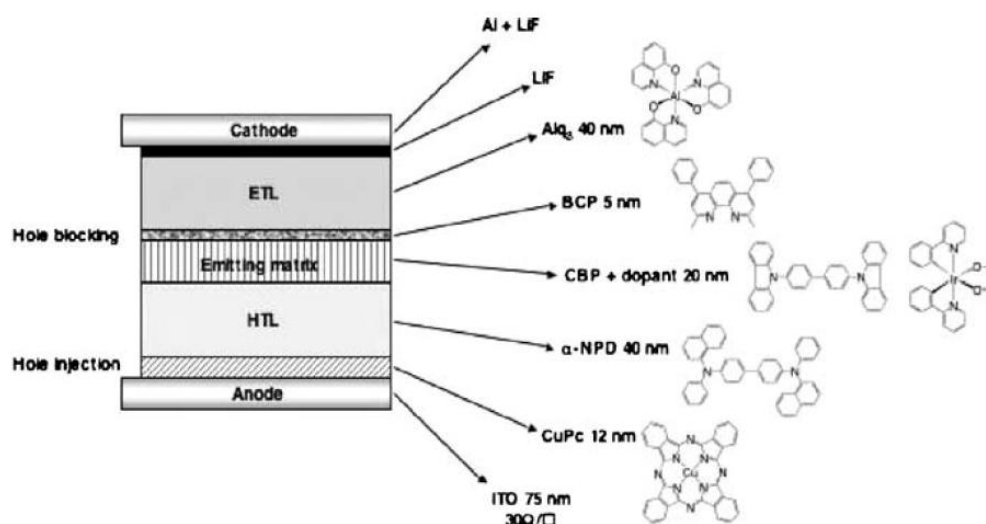


**Figure 6.5.** Cross section of an OLED device<sup>169</sup>

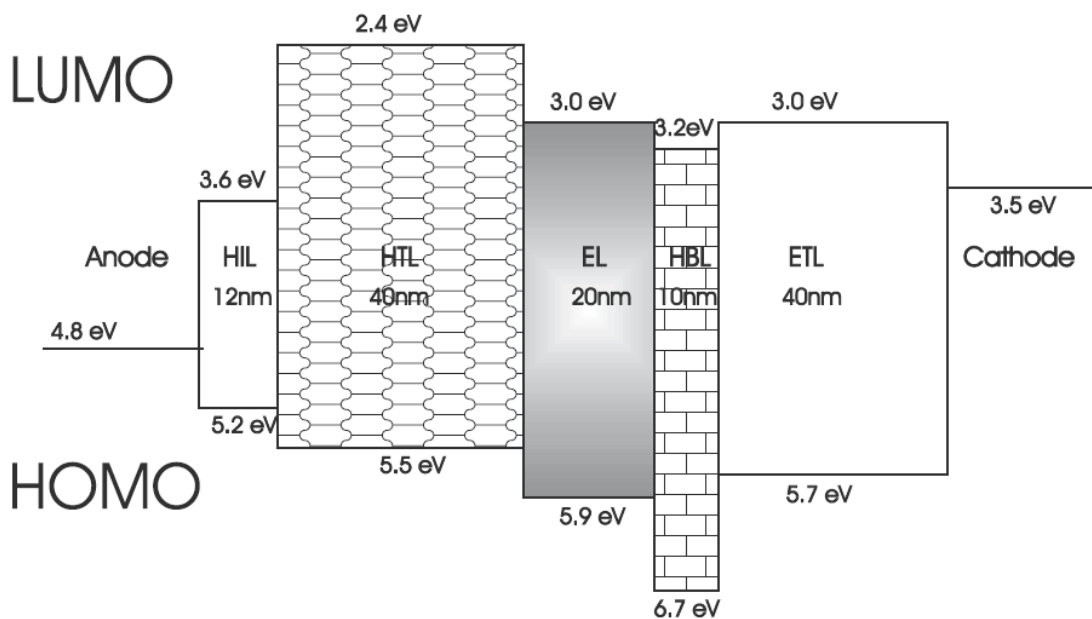


**Figure 6.6.** Typical electrophosphorescence multilayer device architecture composed of a hole injection layer (HIL), a hole transport layer (HTL), a emission layer (EL), a hole blocking layer (HBL), an electron blocking layer (EBL), and finally an electron transporting layer (ETL). The HOMO and LUMO energy levels of the corresponding molecules are shown.<sup>169</sup>

An ITO-coated glass substrate is used as anode and on top of it a CuPc hole injection layer is deposited, followed by an  $\alpha$ -NPD (N,N'-diphenyl-N,N'-bis(1-naphthyl)-1,1'-biphenyl-4,4'-diamine) hole transport layer. On top of this, a CBP (4,4'-bis(carbazol-9-yl)-biphenyl) wide energy-gap matrix is coevaporated together with the phosphorescent acetylacetonato-(bis(2-phenylpyridine)Ir(III)) emitter. A BCP (2,9-dimethyl-4,7-diphenyl-phenanthroline) hole blocking layer is deposited between the emitting layer and the electron transporting layer made of AlQ<sub>3</sub>. A LiF-Al cathode closes the device. The obtained device reaches its 13.2% maximum external quantum efficiency for an 8% molar concentration of emitter in the CBP hole conducting matrix. Important progresses have been made in increasing the OLEDs efficiencies and lowering the turn on voltages.<sup>170</sup> Recently, a series of simplified trilayer phosphorescent OLEDs based on a Ir(III)(bis(2-phenylpyridinato)-N,N-diisopropyl-diisopropylguanidinate emitter complex showed high efficiency (20%) and low driving voltage (2.2-2.7 V) depending on the concentration of the Ir(III) complex (15–30 wt%) in the host CBP matrix.<sup>171</sup>

## 6.4.2 Use of transition metal complexes in efficient LECs

Transition metal complexes have been introduced in LECs by De Cola and co-workers with a device using metal-ligand complexes as charged species. The active layer consisted of a combination of [tris(bipyridine)Ru(II)]<sup>2+</sup>X<sub>2</sub><sup>2-</sup> ([Ru(bpy)<sub>3</sub>]<sup>2+</sup>X<sub>2</sub><sup>2-</sup>) (Figure 6.5) complexes blended with poly(*p*-phenylene-vinylene) PPV. The emission colour was red to green depending on the bias of the device.<sup>172</sup> Since then, many efforts have been invested in the synthesis and device application of differently substituted Ru(II) based ionic organometallic complexes.<sup>152</sup>

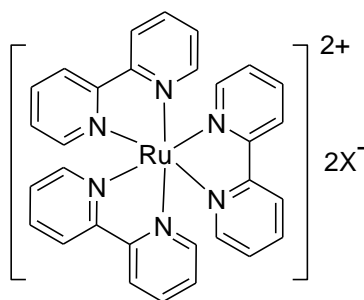


**Figure 6.5.** First organometallic ionic complex used as active species in an LEC

Transition metal complexes can support all the processes involved in luminescence. Their stability in multiple stable redox states indicates readily injection and charge transport, while the high luminescence have been already proven by their application as dyes in sensors.<sup>152</sup> In the model complex [Ru(bpy)<sub>3</sub>]<sup>2+</sup>, light emission arises from the  $\pi^*$ -t<sub>2g</sub> ligand to metal transition, where the complexes frontier orbitals HOMO and LUMO are identified with, respectively, the t<sub>2g</sub> metal orbital and the  $\pi^*$  of ligands. Electron transfer in [Ru(bpy)<sub>3</sub>]<sup>2+</sup> is described as a series of redox reactions via an electron hopping mechanism on LUMOs, while the hole transport takes place with a similar mechanism through HOMOs.<sup>173</sup> Moreover, organometallic complexes show ionic conductivity. In the same model complex [Ru(bpy)<sub>3</sub>]<sup>2+</sup>, the two positive charges are balanced by two different counterions (PF<sub>6</sub><sup>-</sup> and ClO<sub>4</sub><sup>-</sup>). Noteworthy, since the mobile ions are part of the structure, the problem of phase separation often encountered in multilayer blended OLEDs is not verified in transition metal based LECs.

Ionic transition metal complexes based LECs present only one active component, and thus, from the architecture point of view, they can be considered the simplest kind of electroluminescent device (Figure 6.6). However, if emitters of low solubility are employed, multi-layered LECs have also been reported and present the advantages to limit the presence of pinholes.<sup>174</sup>

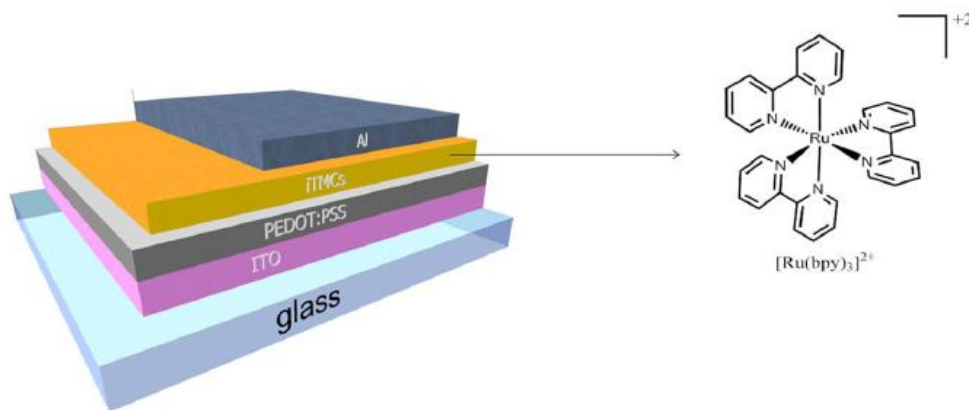


**Figure 6.6.** Typical architecture device of an LEC using  $[\text{Ru}(\text{bpy})_3]^{2+}$

An ITO-coated glass is covered by the solution-obtained film of the emissive organometallic complex. Eventually, an Al cathode is deposited on top of this layer, closing the device. After the pioneering work on Ru(II) emitters, other transition metals, such as Os(II) and Cu(I) (Figure 6.6) have been employed for the synthesis of ionic chromophores suitable for the use in LECs.<sup>175</sup>

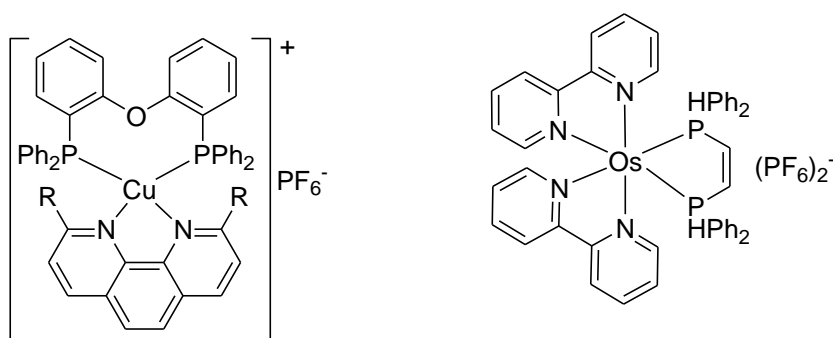


**Figure 6.6.** Molecular structures of two Cu(I) and, respectively, Os(II) organometallic complexes used as electroactive species in LECs

Nevertheless, the best LECs performances have been obtained with heteroleptic cationic bis-cyclometallated Ir(III) complexes (Figure 6.7a).<sup>176</sup> Among the reasons justifying the enhanced efficiencies of Ir(III)-based LECs with respect to devices using different transition metals, are: i) the increased photostability of Ir(III) devices, due to the lower accessibility of dissociative metal-centered excited states; ii) the higher photoluminescence quantum yields due to the larger spin-orbit coupling; iii) the straightforward synthesis of cyclometallated heteroleptic complexes; iv) the specific localisation of the frontier orbitals on a molecular scale, which makes possible the tuning of the HOMO-LUMO gap by independently modifying either the cyclometallated or/and the ancillary ligand.<sup>163</sup> However, while a very wide variety of cationic Ir(III) complexes have been successfully used in LECs, it is only recently that anionic Ir(III) complexes were incorporated in light-emitting devices, as single emitters for LECs,<sup>177</sup> but showed poor devices lifetimes, probably due to their low stability induced by the monoanionic pseudo-halogen ancillary ligands incorporated (Figure 6.7b).<sup>177a</sup>

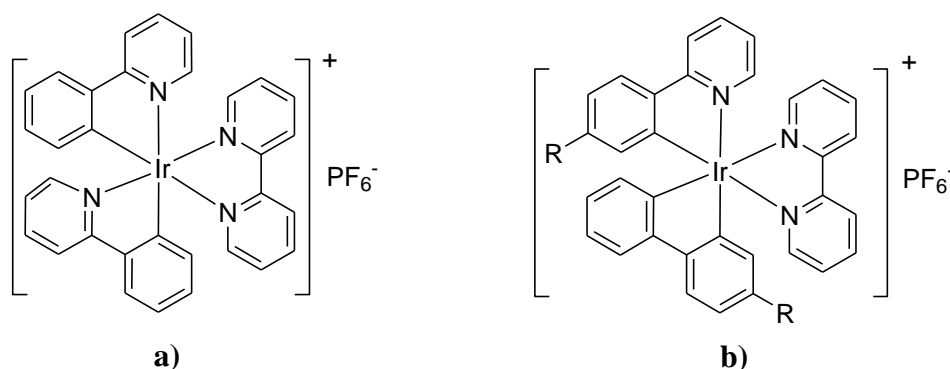


**Figure 6.7.** a) Cationic and b) anionic Ir(III) complexes used as emitters in LECs  
(R=CH<sub>3</sub>,<sup>177a</sup> R=H<sup>177b</sup>)

In fact, the poor device stability (expressed as  $t_{1/2}$ , the time for the brightness of the device to halve from its maximum value) represents one of the main drawbacks of LECs. Indeed, it has been shown from studies on Ru(II)-based LECs that the stability of such devices is determined by the emitter degradation during the working cycles.<sup>178</sup> For example, when using [Ru(bpy)<sub>3</sub>][PF<sub>6</sub>]<sub>2</sub> as active species, an oxo-bridged dimeric quencher [Ru(bpy)<sub>2</sub>(H<sub>2</sub>O)]<sub>2</sub>O[PF<sub>6</sub>]<sub>4</sub><sup>178b,c</sup> is formed, probably originated from the condensation of two units of the previously proposed quencher [Ru(bpy)<sub>2</sub>(H<sub>2</sub>O)]<sub>2</sub><sup>2+</sup>.<sup>178a</sup> The degradation mechanism is described as an exchange reaction in which the ancillary

ligand is replaced in the excited state by two nucleophilic H<sub>2</sub>O molecules.<sup>179</sup> For these reasons, protection of the coordination sphere is necessary. Furthermore, Bolink *et al.* demonstrated that the device lifetime can be significantly improved by increasing the hydrophobicity of the complex by introducing peripheral bulky aromatic. With such a molecular design, the device lifetime can significantly reach thousands of hours.<sup>180</sup> Another drawback in the use of Ir(III) emitters in LECs is the low photoluminescence of complexes in films, due to the quenching induced by the proximity of other Ir(III) species in the active layer. One possible strategy to overcome this issue is the incorporation of bulky groups<sup>181</sup> to the periphery of the ligands in order to induce separation of the centres by increasing the steric hindrance (Figure 6.8a). A second possible strategy involves the introduction of large rigid conjugated  $\pi$  spacers between the two metal centres, leading to dinuclear compounds (Figure 6.8b).<sup>182</sup>

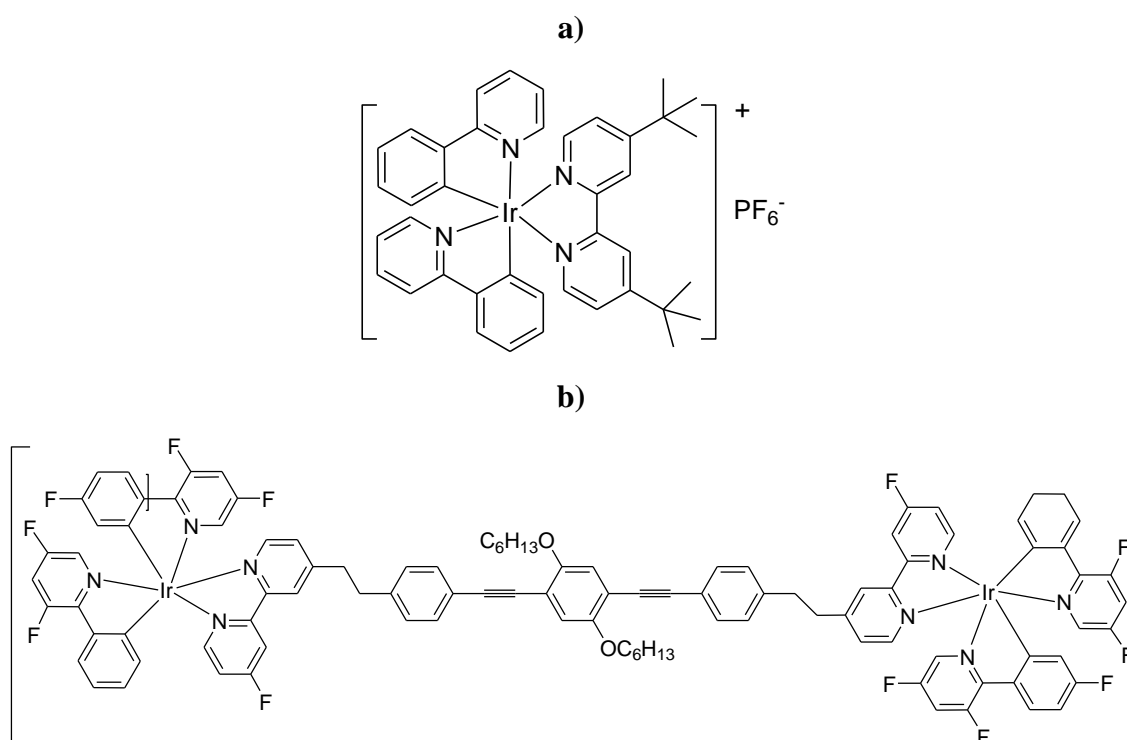


**Figure 6.8.** Ir(III) complex incorporating **a)** bulky groups onto the ancillary bipyridine fragment and **b)** a rigid  $\pi$  spacer between the two metallic centres

It is worthy of note that the Ir(III) complex depicted in Figure 6.8a represents a highlight in the pool of the promising chromophores for LECs since it showed a photoluminescence quantum yield close to unity when incorporated in a poly(methyl methacrylate)matrix to form a thin film, leading to an up to 15% device external quantum efficiency in device.

Another limitation for the practical use of transition metal based LECs, is their slow turn on time ranging from few seconds to several hours. Different strategies have been applied in order to overcome this issue. For example, the incorporation of pendant trimethylammonium groups into the ligands in Ru(II) and Ir(III) chromophores dramatically shortened the devices turn on time to 2.5 min at 3V for Ir(III) complexes and to 5 s for Ru(II) complexes.<sup>183</sup> Another strategy to decrease the turn on time is by tethering an ionic Ir(III) complex with imidazolium groups that increase the net charge per complex and the ionic conductivity in LECs.<sup>184</sup>

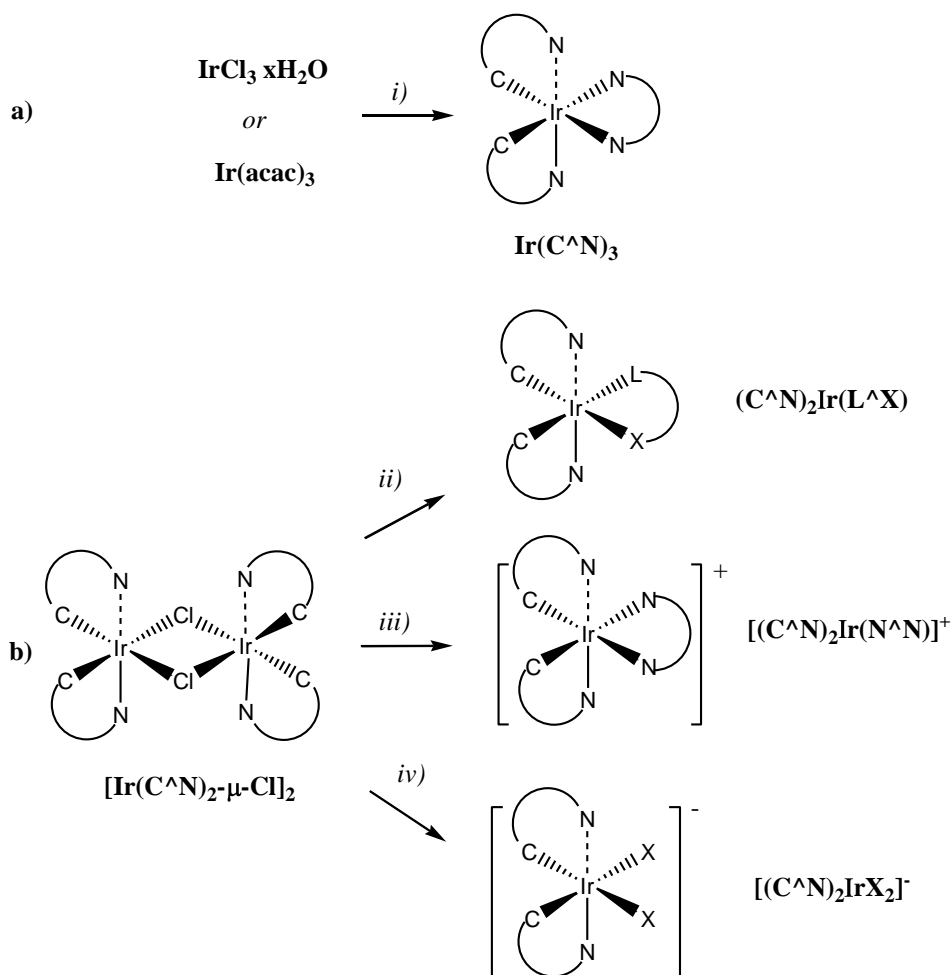
#### **6.4.3 Phosphorescent neutral and ionic cyclometallated Ir(III) complexes used in electroluminescent devices**

Today, Ir(III) complexes represent the most efficient and versatile class of phosphorescent emitters synthesized, since they show shorter triplet lifetimes and lesser triplet-triplet annihilation compared to Pt(II) species, leading to higher quantum efficiencies. Moreover, efficient colour tuning can be performed by modifying the incorporated ligands, leading to full colour applications. Nevertheless, considering also the described above drawbacks relative to the use of Ir(III) complexes in lightening devices, especially regarding anionic complexes, it is evident that there is still room for improvement. Intensive efforts have been thus invested in the recent years to rationalize the appropriate criteria for the design of efficient Ir(III) phosphorescent emitters to be applied in either OLEDs or LECs.<sup>185</sup>

Generally, Ir(III) complexes are characterized by the great inertness of their saturated coordination sphere requiring harsh reaction conditions to incorporate the ligands when the starting material is the commonly used Ir(III) chloride hydrate. However, the rich coordination chemistry of Ir(III) spans over a wide range of compounds, including mono-, bis- and tris-cyclometallated species.<sup>186</sup> A variety of cyclometallated Ir(III) complexes with a very wide pool of ancillary ligands used to complete their coordination sphere and to induce additional photophysical and/or

structural (including supramolecular) features are used as phosphorescent emitters. A strategy to tune the emission colour in Ir(III) complexes relies on the selective HOMO stabilization and/or LUMO destabilization of the complex. Mixed ligand Ir(III) complexes with C<sup>^</sup>N cyclometallating ligands, are particularly appealing in this context, since the two types of ligands can be almost independently functionalized to obtain the desired colour tuning. In particular, electron-withdrawing substituents on the C<sup>^</sup>N ligands decrease the donation to the metal and therefore stabilize the metal-based HOMO. Electron-releasing substituents on the C<sup>^</sup>N ligand, lead, on the other hand to destabilization of the ligand-based LUMO, ultimately leading to increased HOMO-LUMO gaps and emission energies.<sup>169</sup>

The general synthetic pathway leading to Ir(III) complexes is depicted in Scheme 6.1.



**Scheme 6.1.** General synthetic strategies affording **a)** tris- and **b)** bis-cyclometallated neutral and ionic complexes. Reagents and reaction conditions: *i)* H(C<sup>^</sup>N),  $\Delta$  *ii)* L<sup>^</sup>X, *iii)* N<sup>^</sup>N, *iv)* 2X<sup>-</sup>



Tris homoleptic cyclometallated Ir(III) complexes are obtained by direct reaction of  $\text{IrCl}_3 \cdot x\text{H}_2\text{O}$  in the presence of an excess of the cyclometallating ligand  $\text{H}(\text{C}^{\wedge}\text{N})$  (most commonly a 2-phenylpyridine derivative)<sup>187a</sup> (Scheme 6.1a) or by substitution of the ancillary acetoacetate in  $\text{Ir}(\text{acac})_3$ <sup>187b</sup>. The synthesis of bis-cyclometallated heteroleptic Ir(III) complexes follows instead a different synthetic pathway and involves a chloro-bridged dimeric intermediate  $[\text{Ir}(\text{C}^{\wedge}\text{N})_2-\mu\text{-Cl}]_2$ , obtained from the reaction of  $\text{IrCl}_3 \cdot x\text{H}_2\text{O}$  with two equivalents of the cyclometallating ligand.<sup>188</sup> When the chloro-bridged dimer is cleaved with a chelating monoanionic  $\text{L}^{\wedge}\text{X}$  ancillary ligand (such as  $\beta$ -diketones, picolinate etc.), neutral complexes are obtained. If the same dimer reacts with a chelating neutral  $\text{N}^{\wedge}\text{N}$  ancillary ligand (2,2'-bipyridines, 1,10-phenanthroline, diamines, etc.) in the presence of a silver salt, cationic bis-cyclometallated Ir(III) are synthesised,<sup>189a</sup> while anionic complexes are afforded by the reaction of  $[\text{Ir}(\text{C}^{\wedge}\text{N})_2-\mu\text{-Cl}]_2$  with (pseudo)halogen salts such as NaCN in the presence of an organic base such as the tetrabutylammonium salt.<sup>189b</sup>

#### 6.4.3.1 Neutral bis- and tris-cyclometallated Ir(III) complexes

Since 1985, when Watts and co-workers isolated  $\text{Ir}(\text{ppy})_3$  (**I** in Figure 6.9a) as a by-product in the synthesis of its respective chloro-bridged dimer,<sup>190</sup> numerous variations of its basic structure have been reported, leading to a wide variety of homoleptic tris-cyclometallated Ir(III) complexes: by i) introduction of electron-withdrawing or electron-donating substituents,<sup>191</sup> ii) extension of the  $\pi$ -conjugated system<sup>192</sup> (**II** in Figure 6.9a), iii) replacement of the pyridine ring by other N-heteroaromatic rings<sup>193</sup> (**III** in Figure 6.9a), iv) introduction of lateral functional groups for post-complexation modifications.<sup>194</sup>

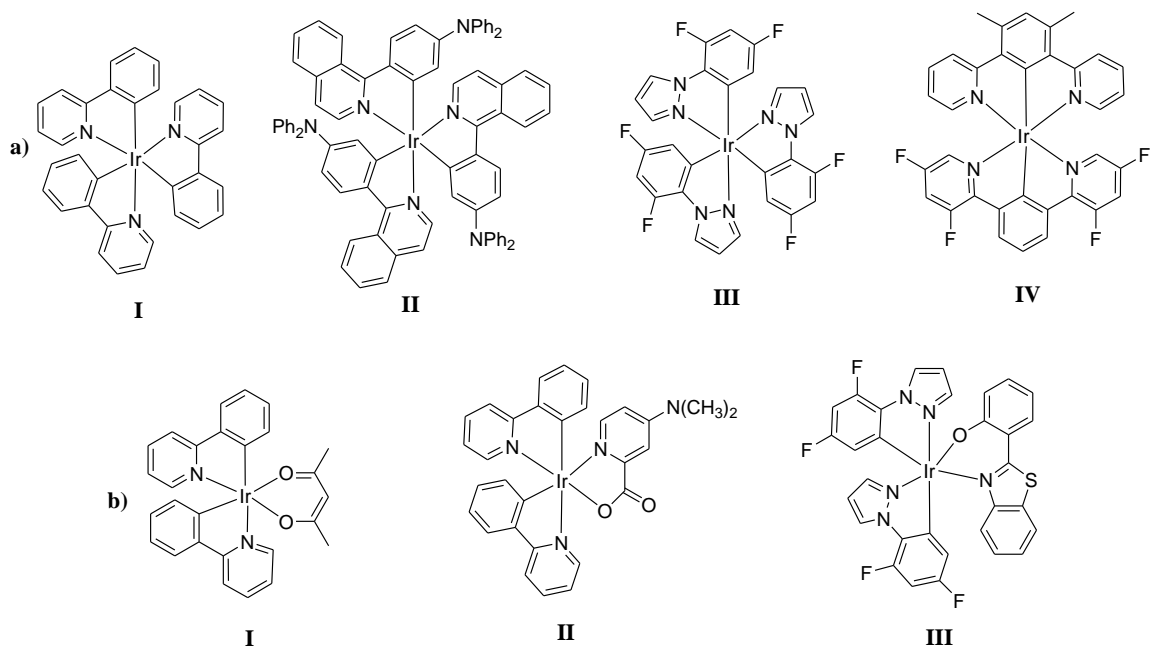


**Figure 6.9.** a) Tris- and b) bis-cyclometallated Ir(III) phosphorescent emitters

Following these strategies, a variety of emissive complexes covering the whole visible spectra from blue, green, yellow, orange to red, have been introduced, even if the synthesis of stable and efficient blue-emitters (wide HOMO-LUMO band-gap) still represents a challenging issue. By increasing the degree of fluorination and concomitantly replacing pyridine by pyrazole, a green-blue emitter was obtained (**III** in Figure 6.9a).<sup>195</sup> From a geometrical point of view, thermodynamically favoured *fac*-isomers of tris-cyclometallated Ir(III) complexes feature over an order of magnitude longer lifetimes and higher quantum efficiencies than their *mer* counterparts.<sup>196</sup> Since their synthesis require harsh conditions, alternative routes towards *fac*-tris-cyclometallated Ir(III) complexes have been proposed, including the use of microwave radiation or, as reported by Williams *et. al.*,<sup>197</sup> by substituting three bidentate C<sup>N</sup> ligands with a tridentate bis-cyclometallating ligand and another tridentate mono-cyclometallating ligand (**IV** in Figure 6.9a).

In bis-cyclometallated Ir(III) complexes, the coordination sphere of the metal centre is completed by an ancillary ligand. When monoanionic chelating ligands are used, neutral complexes are obtained. The most used ligands are acetylacetonate (**I** in Figure 6.9b), which was one of the first Ir(III) complexes to be introduced as phosphorescent emitter in OLEDs and picolinate derivatives (**II** in Figure 6.9b).<sup>198</sup>

Moreover, various pyrazole ancillary ligands have demonstrated their potential (**III** in Figure 6.9b) for the tuning of optoelectronic properties since they seem to be a promising candidate for blue-emitting complexes.

#### 6.4.3.2 Ionic bis-cyclometallated Ir(III) complexes

Due to their notable photophysical properties, ionic character and good solubility, charged Ir(III) complexes have gained much interest in recent years.<sup>199</sup> A wide variety of 2,2'-bipyridines, 1,10-phenanthrolines and 2,2',6',2''-terpyridine derivatives have been introduced as neutral chelating ancillary ligands to afford cationic Ir(III) complexes (Figure 6.10). In particular, electron-withdrawing (-F, -CF<sub>3</sub>, -C(CH<sub>3</sub>)<sub>3</sub>) or electron donating (-OR) groups have been introduced on the cyclometallating ligand (**I** in Figure 6.10a<sup>200</sup>) in combination with the incorporation of  $\pi$  conjugated lateral substituents on the pyridyl ancillary ligand (**II** and **III** in Figure 6.10a<sup>201</sup>).

The phosphorescent anionic Ir(III) complexes reported so far bear two pseudo-halogen type monoanionic ligands (CN<sup>-</sup>, SCN<sup>-</sup>, etc.) to complete their coordination sphere, while as for cationic complexes, various different groups have been incorporated onto the cyclometallated ligands.<sup>189b,202</sup>

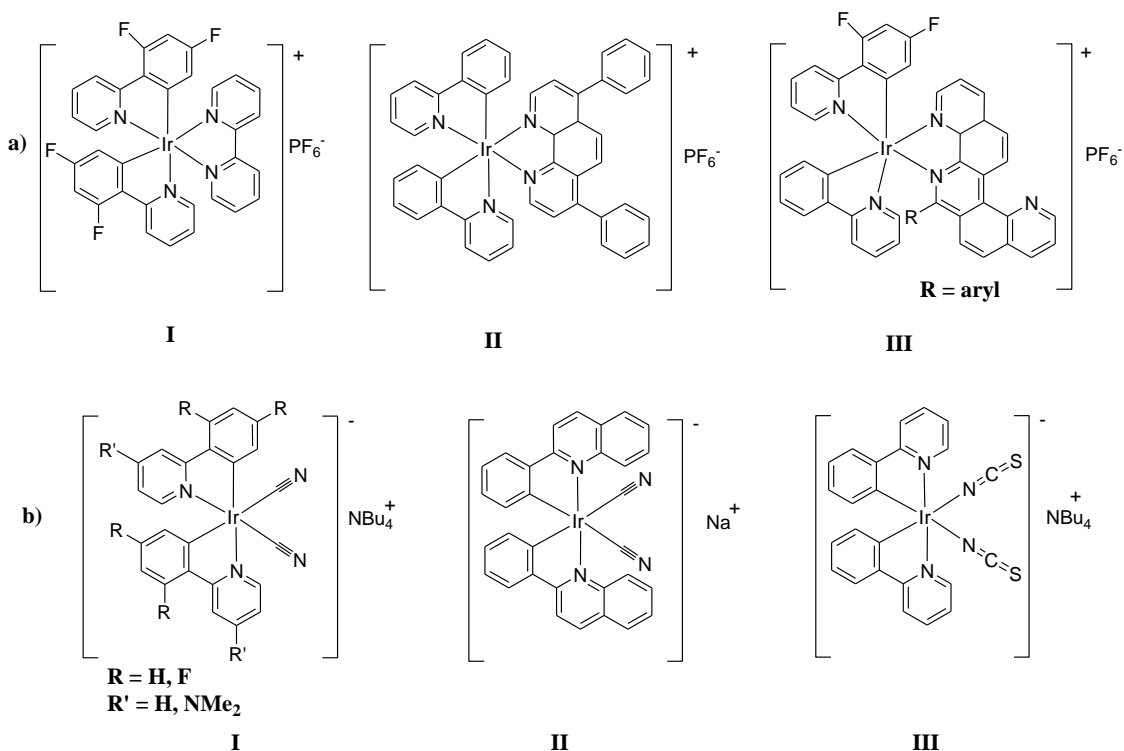


**Figure 6.10.** Charged **a)** cationic and **b)** anionic cyclometallated Ir(III) complexes

## 6.5 Concluding remarks

Since the introduction in 1987 of electroluminescent devices based on AlQ<sub>3</sub>, major improvements of the device efficiency and the development of new chromophores have been performed. LECs have arisen as a single layer-alternative to the complicated OLEDs multi-layer architectures. Still, these two types of electroluminescent devices have continued their parallel development. Nevertheless, while for OLEDs high device stabilities have been reached, the LEC technology has still to overcome the short lifetime issue. A major breakthrough was realised in 1999 with the introduction of transition metal phosphorescent chromophores, especially Ir(III) based. Since then, a wide pool of neutral and ionic Ir(III) complexes have been synthesised, characterized and part of them used as emitters in OLEDs and LECs of different colours. Even if many progresses have been realised in terms of stability, driving voltages and turn on times, transition metal based electroluminescent devices, especially LECs, still do not possess all the required characteristics for their insertion on the marketplace. Further studies need to be dedicated to the development of new materials and improved architectures in order to afford competitive lighting sources. To this regard, the second part of this thesis is dedicated to the synthesis and characterization of novel Ir(III) ionic and neutral emitters which are able to assemble in ionic pairs and, respectively to electrogenerated films.

*A selection of reviews concerning the recent developments in electroluminescent devices, ordered by topic, is collected in Table 6.1.*

<b>Topic</b>	<b>First author (Year)</b>	<b>Reference</b>
OLEDs	N. Thejo Kalyani (2012)	170
	L. Xiao (2011)	203
LECs	R. D. Costa (2012)	204
	R. D. Costa (2011)	163
Application of Ir(III) complexes in electroluminescent devices	F. Dumur (2012)	205
	C. Ulbricht (2009)	185

## Chapter Seven

### Novel anionic Ir(III) complexes and their derivatives

#### 7.1 Introduction

As already discussed in Chapter 6, the success of Ir(III) complexes is not only due to their efficient phosphorescence features, but also to the possibility of finely tune the emission colour by properly choosing the nature of the ligands included in the Ir(III) coordination sphere.<sup>185</sup> Furthermore, according to the chemical nature of the chosen ligands, neutral or ionic complexes can be obtained.<sup>206</sup> Since the pioneer work of Pei *et al* on light emitting electrochemical cells (LECs or LEECs),<sup>161</sup> ionic luminescent Ir(III) complexes have received a particular attention as well as, more recently, their corresponding ion-paired cationic and anionic complexes (or soft salts).<sup>207</sup>

The term soft salts describes a pair of complementary charged organometallic complexes lacking halide, alkali metal or other ions originally present as counterions of the single components.<sup>208</sup> Soft salts can be conveniently classified as homometallic or heterometallic. Thus, as an example, different examples of homometallic Ir(III) soft salts (Figure 7.1a), and, to the best of our knowledge, a single example of heterometallic Ir(III) soft salt are known (Figure 7.1b).

An important feature of such ionic organometallic pairs is the fact that phosphorescence is enabled from both parts of the complex salt. Thus, by choosing the two charged ions of the pair in such a way that their emission covers a large region of the visible range, white light emission can be obtained. Furthermore, in order to obtain emission of white light, the emission intensity of the single components needs to be controlled. Modulation of the single emission intensity can occur by adapting the distance between the emitting moieties induced by the steric hindrance of the incorporated ligands.<sup>207b</sup> Moreover soft salts have shown some advantages due to the intrinsic ionic nature of their components: i) a higher solubility with respect to classical neutral Iridium complexes, an important issue for device construction; ii) a higher flexibility of colour tuning due to the opportunity of chemical modifications on each component,<sup>209b</sup> and iii) the possibility of using polynuclear ionic complexes as component with control of internal electronic communication for fine colour tuning.<sup>209c</sup>

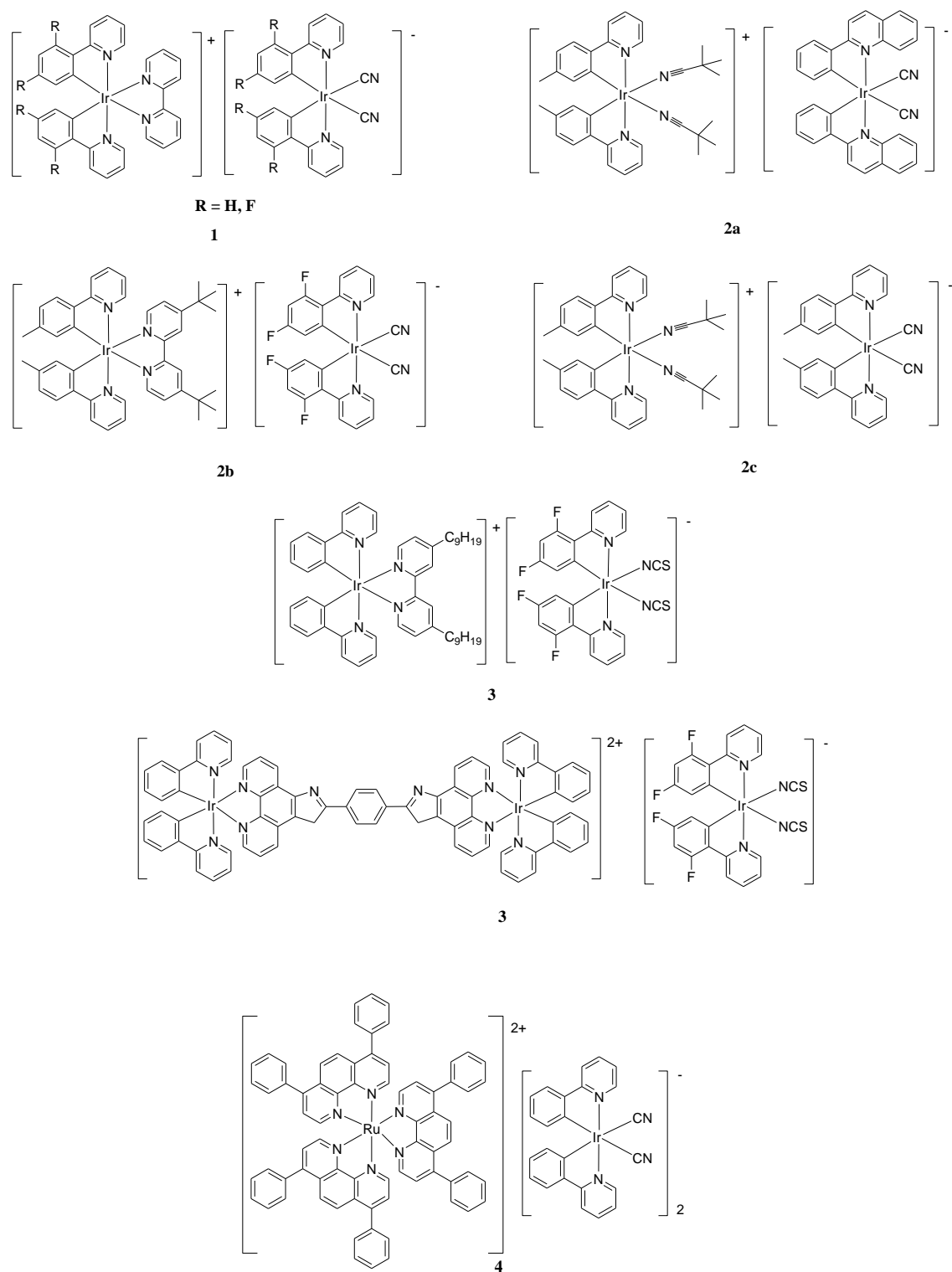


**Figure 7.1. a) Homometallic 1,<sup>207a</sup> 2,<sup>209a</sup> 3<sup>209c</sup> and 4<sup>209b</sup> Ir(III) soft salts and b) heterometallic Ir(III) soft salts 4<sup>207b</sup>**

Ir(III) based soft salts are in principle suitable for both OLEDs and LECs since these ion pairs are concomitantly overall neutral assemblies and ambipolar species with the capability of transporting both holes and electrons. However, probably due to the absence of small ions which more easily migrate under an applied field to insure ohmic contact, soft salts based LEC have still to prove their working capacity.<sup>209</sup> On the contrary, soft salts have been successfully used in OLEDs (also called PhOLEDs for Phosphorescent Organic Light Emitting Diodes) and no delay between turn-on time and light emission was reported.<sup>209a</sup>

Ir(III) soft salts either homometallic or heterometallic are synthesized via metathetical reaction starting from two conventional salts respectively containing the cation and anion of the desired soft salt. To this regard, while research on cationic Ir(III) complexes accounts already for a rather wide number of examples,<sup>185</sup> only few cyclometallated anionic Ir(III) complexes have been reported so far. The first anionic Ir(III) complex having the negative charge located on the metal centre was published in 2003 by Nazeeruddin *et al.*<sup>209d</sup> in a study of a series of highly phosphorescent anionic complexes  $[\text{Ir}(\text{ppy})_2(\text{X})_2]\text{TBA}$  with  $\text{X} = \text{CN}^-$ ,  $\text{NCS}^-$  and  $\text{NCO}^-$  and  $\text{TBA} =$  tetrabutylammonium, for application in OLEDs. By choosing appropriately functionalized 2-phenylpyridine ligands, blue emission (450-470 nm) has been observed for this class of complexes.<sup>189b</sup> Even if the first LEC device comprising a sodium salt was recently obtained, for these anionic Ir(III) complexes embedded with mono-dentate (pseudo halogen type) ligands, small molecules such as water can easily promote ligand exchange in the excited state resulting in the quenching of the emission and leading to device degradation.<sup>175d</sup>

## 7.2 Anionic cyclometallated Ir(III) complexes containing substituted bivalent *ortho*-hydroquinones

In this context, in an attempt to extend the class of anionic Ir(III) complexes available and obtaining more stable emitters, a new series of anionic Ir(III) bearing a bidentate catecholate derivative as  $\text{O}^{\wedge}\text{O}$  ancillary ligand has been synthesised.<sup>210</sup> This synthetic work has been aimed to develop the class of anionic Ir(III) complexes through a simple and versatile synthetic pathway and led by the interest of following the change in their photophysical properties by using chelating bivalent ancillary ligands. These are bis-cyclometallated Ir(III) complexes of general formula  $[(\text{ppy})\text{Ir}(\text{O}^{\wedge}\text{O})]\text{NBu}_4$  (**XIV**–**XVI**) (Figure 7.2) bearing redox switchable *ortho*-hydroquinone ancillary ligands.

Transition metal complexes containing quinone based ligands (in their three different formal oxidation states: catecholate, semiquinone or quinone) were extensively studied because of the induced delocalisation of metal-ligand charge and the generation of redox chains with complex electrochemistry processes.<sup>211</sup> Nevertheless, the coordination chemistry of Ir(III) metal with such ligands has received less attention probably because of the low stability of its diamagnetic species. However, by opportunely functionalizing the quinoid skeleton, more appealing Ir(III) neutral or ionic complexes for optoelectronic applications can be reached. In this context, and to the best of our knowledge, a single anionic Ir (III) complex embedded with a substituted *ortho*-hydroquinone ligand has been reported, unfortunately, without any specific details or description of its photophysical and electrochemical properties.<sup>212</sup>

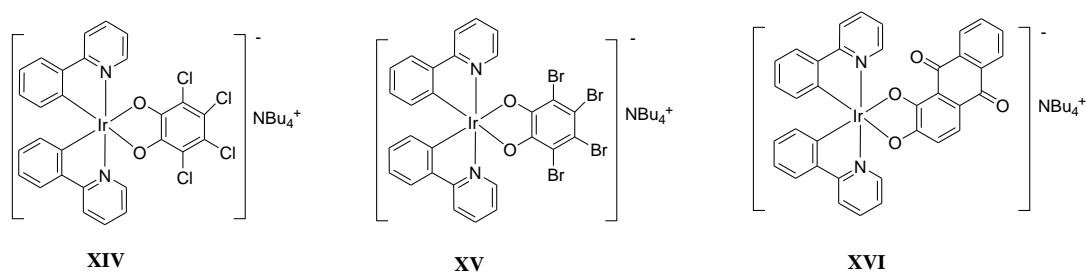


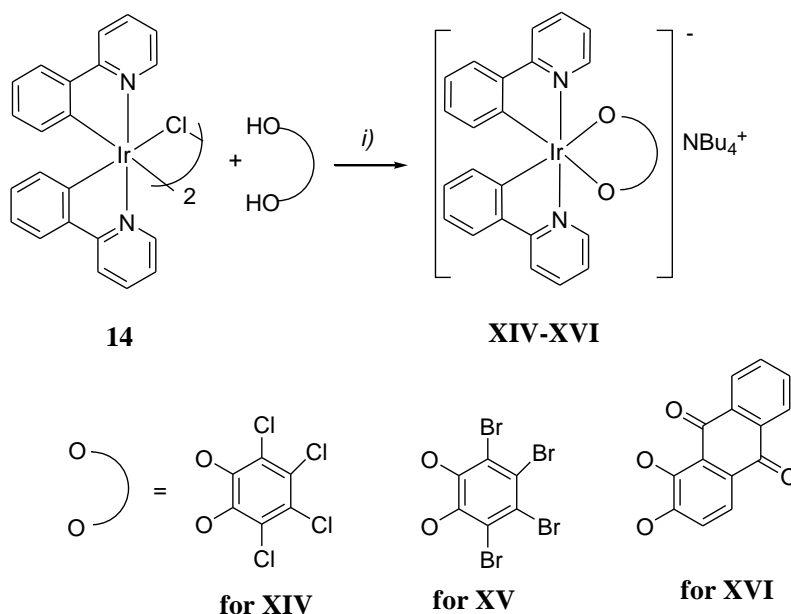
**Figure 7.2** Anionic Ir(III) cyclometallated complexes

For these reasons, we have studied the reactivity of *ortho*-quinones possessing either strong electron withdrawing groups (complexes **XVII** and **XVIII**) or a highly delocalized  $\pi$  system (complex **XIX**), with the aim of stabilising the catecholate forms and consequently obtain new anionic Ir(III) complexes that may extend their application in fields concerned with photo/electro conversion processes.

### 7.2.1 Synthesis

The synthesis of all complexes (**XIV–XVI**) was carried out starting from the previously reported dichloro-bridged dimer<sup>213</sup>  $[(ppy)_2Ir(\mu-Cl)]_2$  **14** and the appropriate substituted *ortho* hydroquinone ligand (Scheme 7.1) in presence of a slight excess of tetrabutylammonium hydroxide to ensure full deprotonation of the ancillary ligand. The pure products **XIV–XVI** were obtained in good yields (from *ca.* 70 to 98%) after recrystallization as red (**XIV**, **XV**) or blue (**XVI**) solids.





**Scheme 7.1.** Reagents and conditions: i) NBu<sub>4</sub>OH, dichloromethane/methanol, N<sub>2</sub>, r.t., 3 days.

The complexes were fully characterized by IR, <sup>1</sup>H NMR, conductivity measurements and elemental analysis (Chapter Ten), all confirming the proposed structures presented in Scheme 7.1. Noteworthy, the proton signals within the aromatic region of the <sup>1</sup>H NMR spectrum are well-resolved and showing one set of signals for complexes **XIV** and **XV**, and respectively two distinguishable sets of signals for complex **XVI**, one for each non-magnetically equivalent 2-phenylpyridine unit.

Furthermore, the ionic character of **XIV-XVI** was further confirmed by conductivity measurements in dry acetonitrile solution. Indeed, the values for both complexes are of *ca.* 120 Ω<sup>-1</sup> cm<sup>2</sup> mol<sup>-1</sup>, in agreement with a 1:1 univalent type electrolyte.<sup>214</sup> All the three complexes resulted thermally stable up to 220°C where decomposition occurred.

## 7.2.2 Electrochemistry

The redox properties of complexes **XIV-XVI** were studied by cyclic voltammetry. The redox potentials measured for all complexes are reported in Table 7.1. All the reported values are referred to the Fc/Fc<sup>+</sup> redox couple, used as internal standard reference. The three complexes present the same oxidation behaviour (Figure 7.3).

	E <sup>red</sup> (mV)*	E <sup>1/2</sup> cat/sq (mV) *	E <sup>ox</sup> <sub>1</sub> sq/q (mV) *	E <sup>ox</sup> <sub>2</sub> Ir <sup>III</sup> /Ir <sup>IV</sup> (mV)*
<b>XIV</b>	not observed	-192 (Rev.)	+536 (Irr.)	+641 (Irr.)
<b>XV</b>	not observed	-180 (Rev.)	+530 (Irr.)	+640 (Irr.)
<b>XVI</b>	-1510 (Irr, 2e-)	-163 (Rev.)	+438 (Irr.)	+640 (Irr.)

\*vs. Fc/Fc<sup>+</sup>; cat=catecholate, sq=semiquinoid, q=quinoid forms of the ancillary ligand

**Table 7.1.** Redox potentials (vs. Fc/Fc<sup>+</sup>) observed for complexes **XIV-XVI**. Irreversible wave (Irr.), Reversible wave (Rev.)

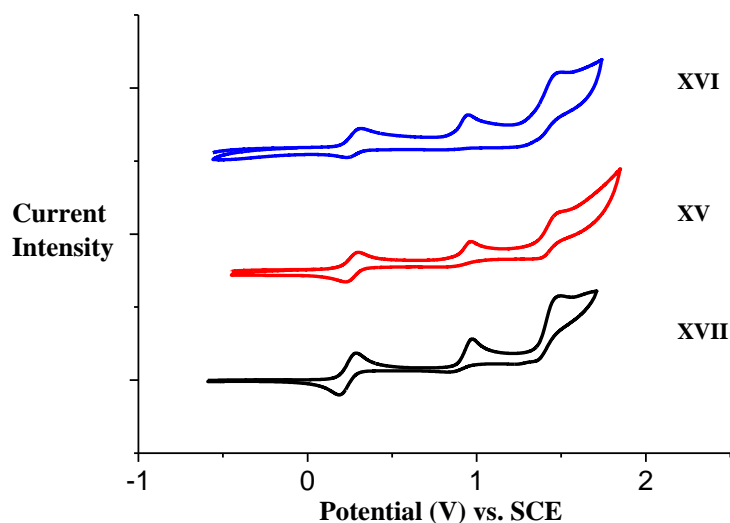


**Figure 7.3.** Cyclic voltammograms of **XIV-XVI** complexes measured in acetonitrile at room temperature. The potentials are shown relative to Fc/Fc<sup>+</sup> couple.

As previously reported for catecholato substituted cyclometallated Ir(III) complexes,<sup>215</sup> three oxidation waves are observed for **XIV-XVI**. The first reversible wave is attributed to the oxidation of the *ortho*-hydroquinone ligands from the catecholate (cat) to the sequinone (sq) state, while the second irreversible wave is related to the semiquinone (sq)/quinone (q) oxidation redox couple. While in previously reported complexes obtained using 3,5-di-*tert*-butylcatechol<sup>215</sup> the catecholate fragment

is in its semiquinone form, for complexes **XIV-XVI** the *ortho*-hydroquinone ligand is in its fully reduced catecholate oxidation state. Noteworthy, no change was observed neither in signal intensity nor in potential drift by cycling repeatedly onto the first reversible oxidation wave showing the high electrochemical stability of all complexes in their catecholate and semiquinone forms (Figure 7.4).

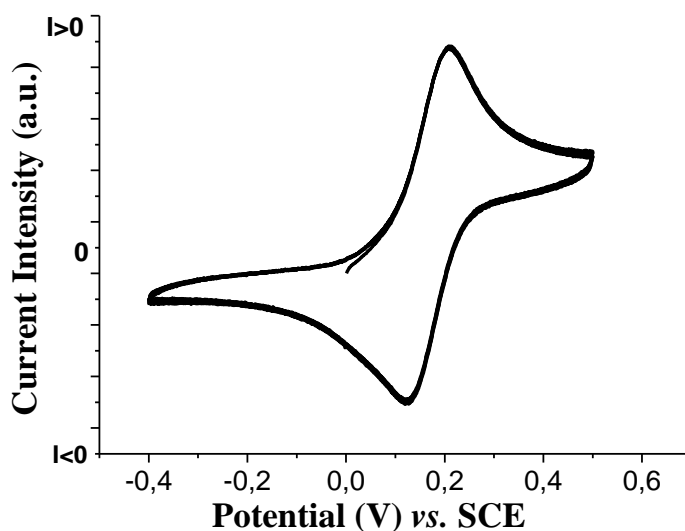


**Figure 7.4.** Cyclic voltammogram of **XV** in dry DCM repeating 6 cycles on the first oxidation wave showing the high electrochemical stability of both the catechol and semiquinone forms

The irreversibility of the second wave can be correlated to the chemical instability of the quinolate form of the complexes assisted by releasing of the free ligand in solution and the possible incorporation of two acetonitrile solvent molecules to complete the metal coordination sphere. Indeed, the third oxidation wave is related to the Ir(III)/Ir(IV) oxidation state of the  $[(ppy)_2Ir(CH_3CN)_2]^+$  ion complex,<sup>216</sup> and thus its potential (+ 640 mV) is invariant for the three complexes. As expected, on increasing the aromaticity/electronegativity of the substituents of the catecholato ligand, a slight increase of the potential of the first two oxidation peaks is observed representing the higher difficulty to oxidize the catecholate complexes whose oxidation potentials vary with the order **XIV** > **XV** > **XVI**.

Considering the reduction behaviour of complexes **XIV-XVI**, no reduction wave was observed for **XIV** and **XV**, as expected since in cyclometallated Ir(III) complexes the reduction is generally associated to the cyclometallated moiety<sup>217</sup> and the metal bound 2-phenylpyridine reduction wave probably occurs outside of the solvent

potentials window (i.e.  $< -1.8$  V vs.  $\text{Fc}/\text{Fc}^+$ ). On the contrary, complex **XVI** exhibits an irreversible 2 electrons reduction wave at *ca.*  $-1.5$  V (Figure 7.5), attributed to the reduction of the anthraquinone fragment of the alizarin moiety.<sup>218</sup>

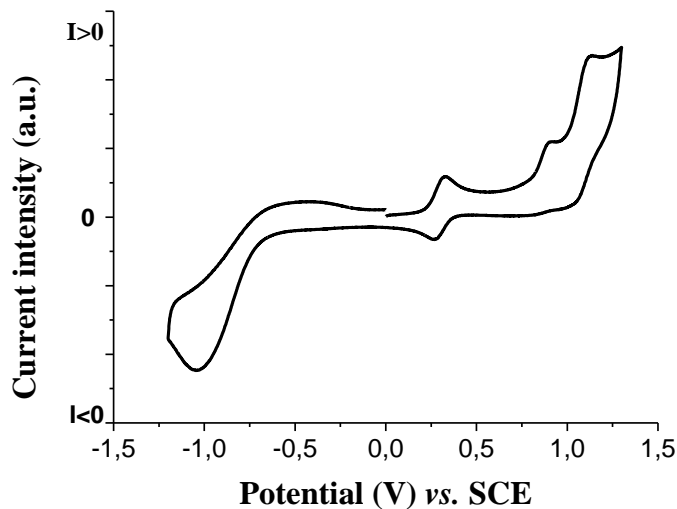


**Figure 7.5.** Cyclic voltammogram of complex **XVI**, measured in acetonitrile at room temperature

Contrary to the colour change observed upon addition of ferrocene for the previously reported 3,5- di-*tert*-butylcatechol Ir(III) neutral complex<sup>215</sup> which was attributed to the formation of a charge transfer complex, for all complexes **XIV-XVI**, no such variation was observed. This is in agreement with the ionic nature of the complexes, the *ortho*-hydroquinone ligand being present in its lowest reduced form (catecholate), no formation of such a charge-transfer complex with ferrocene can take place.

### 7.2.3 Photophysical properties

In deoxygenated acetonitrile dilute ( $8 \cdot 10^{-6}$  M) solution, complex **XIV** and **XVI** showed a scarce orange luminescence (600 nm for complex **XIV** and 590 for complex **XVI**) superimposed to a green emission component centred at 500 nm, more intense for complex **XVI** (Figure 7.6a and 7.6b).

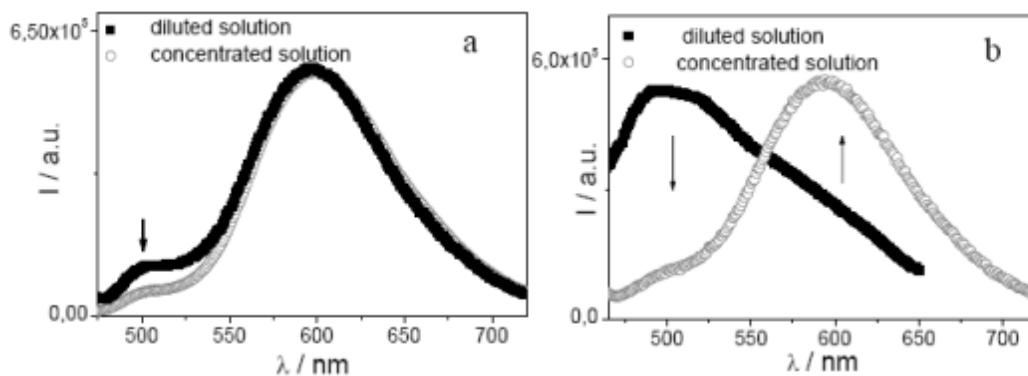


**Figure 7.6.** Emission spectra of complex **XIV** (a) and **XV** (b) in diluted and concentrated acetonitrile solutions ( $\lambda_{\text{exc}}=400$  nm).

Following dilutions processes for complex **XIV** ( $<10^{-6}$  M) no further changes in the spectroscopic features were observed whereas a significant increase in concentration (up to  $10^{-3}$  M) led to the almost sole presence of the orange component for both complexes **XIV** and **XV**. Since the orange component is, at least for complex **XIV**, always the most intense signal, independently of concentration, the monomer-excimer equilibrium<sup>219</sup> can be ruled out. Evidence of a possible hydrolysis pathway more perceptible in dilute solutions (spectroscopic concentrations) and more efficient for complex **XV** has been obtained. In particular, at spectroscopic concentrations, the solvato  $[\text{Ir}(\text{ppy})_2(\text{H}_2\text{O})_2]^+$  complex is reasonably formed as observed by time monitoring of the emission of an acetonitrile solution of complex **XV** in absence of oxygen and upon addition of water (50  $\mu\text{L}$ ), where after a short period of time, a significant increase of the green component can already be measured (Figure 7.7).

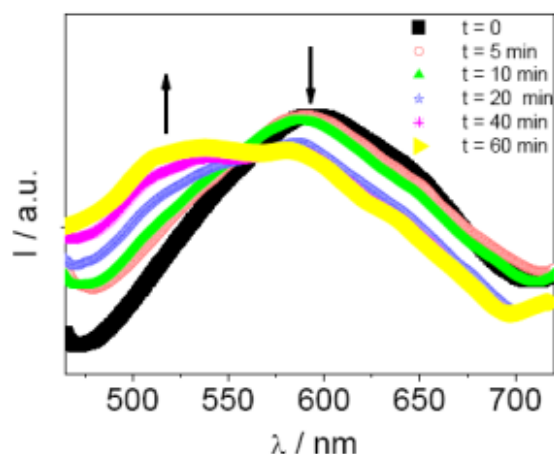


**Figure 7.7.** Emission spectra as a function of time of a concentrated deaerated acetonitrile solution of complex **XV** after the addition of a drop of water ( $\lambda_{\text{exc}}=400$  nm)

Indeed, similar green emission has been observed for related complexes  $[\text{Ir}(\text{ppy})_2(\text{solv})_2]^+$  where  $\text{solv} = \text{H}_2\text{O}$  or  $\text{CH}_3\text{CN}$ .<sup>220</sup> Additional photophysical measurements were performed in order to further investigate the observed behaviour. In particular luminescence lifetimes were measured for complexes **XIV** and **XV** by monitoring the emission decay curves both in the green and in the orange luminescence range. Nevertheless, the complicated multiexponential decays observed are hardly interpretable on the basis of the available data. No luminescence have been detected for complex **XIV** and **XV** in the solid state.

Differently from **XIV** and **XV**, complex **XVI** showed no emission at all neither in concentrated nor diluted solutions. The absorption spectra of acetonitrile diluted solutions of complexes **XIV** and **XV** display distinctive bands in the UV and the visible region due to ligand centred ( $\pi\text{-}\pi^*$ ) and MLCT transitions, respectively characteristics of cyclometallated Ir(III) complexes (Figure 7.8).<sup>210</sup>

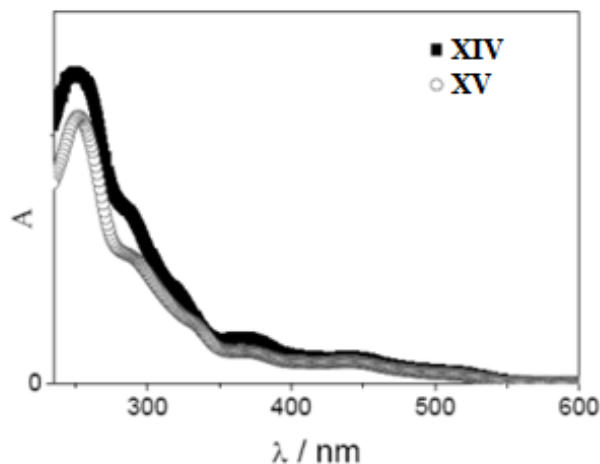


**Figure 7.8.** Absorption spectra of complexes **XIV** and **XV** in diluted acetonitrile solutions

Worthy of note, the absorption spectrum of complex **XV** shows intense bands (molar extinction coefficient  $\epsilon > 10^4 \text{ M}^{-1} \text{ cm}^{-1}$ ) in the ultraviolet part of the spectrum associated with  $\pi\text{-}\pi^*$  electronic transitions and weaker bands (with molar extinction coefficients of *ca.*  $10^3$  to  $1.5 \cdot 10^4 \text{ M}^{-1} \text{ cm}^{-1}$ ) extended from 320 to 700 nm including spin-allowed and spin-forbidden metal-to-ligand charge transfer (MLCT) transitions and  $\pi\text{-}\pi^*$  alizarinate transitions (Figure 7.9).<sup>221</sup> The stability of complex **XVI** at spectroscopic concentrations ( $10^{-6} \text{ M}$ - $10^{-5} \text{ M}$ ) was checked, indicating its effective stability also in this experimental condition.

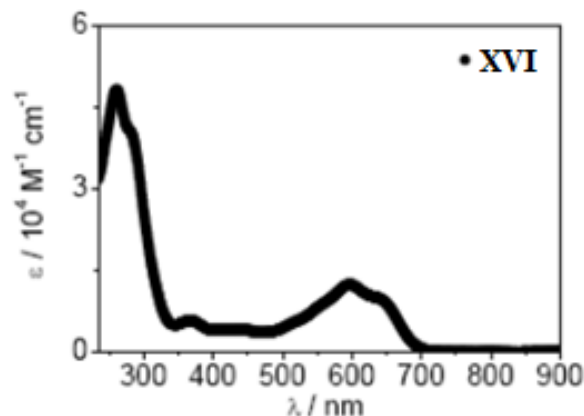


**Figure 7.9.** Absorption spectra of complex **XVI** in acetonitrile solution

Complexes **XIV-XVI** represent the first examples of anionic Ir(III) cyclometallated complexes bearing a bidentate ancillary ligand which have been characterized. Even if these compounds show poor emission, the developed synthetic procedure can be applied to other systems. A proper choice of the ancillary ligand could afford anionic luminescent Ir(III) cyclometallated complexes.

### **7.3 Luminescent anionic cyclometallated Ir(III) complexes containing an orotate ancillary ligand**

In the context of the wide variety of chelating ancillary ligands investigated in the last years in Ir(III) cyclometallated complexes, a number of efficient blue-emitting cyclometallated Ir(III) neutral complexes have been reported with monoanionic O<sup>N</sup> ligands such as picolinic acid (Figure 7.10a).<sup>222</sup> This suggest that, in principle, the use of a dianionic O<sup>N</sup> type bivalent ligand could lead to anionic Ir(III) complexes with highly interesting luminescence properties. To this regard, orotic acid (Figure 7.10b) whose coordination chemistry to a wide number of transition metals (Cu<sup>2+</sup>, Mn<sup>2+</sup>, Zn<sup>2+</sup>, Hg<sup>2+</sup>, Cd<sup>2+</sup>, Fe<sup>3+</sup>, Cr<sup>3+</sup>, Ag<sup>+</sup>, Ir<sup>+</sup>, Rh<sup>+</sup>) has already been investigated,<sup>223</sup> could be a rightful candidate.

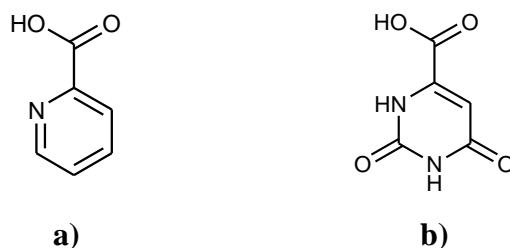
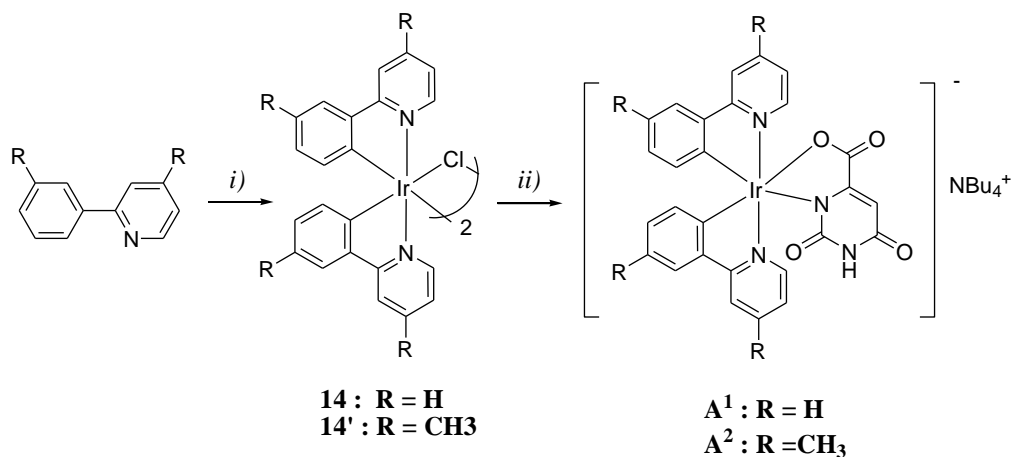


**Figure 7.10.** Molecular structure of picolinic acid (a) and orotic acid (b)

### 7.3.1 Synthesis

We have therefore proceeded to the synthesis of two new anionic bis-cyclometallated Ir(III) complexes **A**<sup>1</sup> and **A**<sup>2</sup>, of general formula [(*R*-ppy)<sub>2</sub>Ir(O<sup>-</sup>N)]TBA with *R*-ppy=2-phenylpyridine (R = H) or 4,5'-dimethyl-2-phenylpyridine (R = CH<sub>3</sub>), O<sup>-</sup>N = dianionic form of the orotic acid and TBA = tetrabutylammonium (Scheme 7.2).



**Scheme 7.2.** Reagents and conditions: i) 2-ethoxyethanol/water, reflux, 24 h., N<sub>2</sub>;  
ii) orotic acid, NBu<sub>4</sub>OH, dichloromethane/methanol, r.t., 24 h

The anionic complexes **A**<sup>1</sup> and **A**<sup>2</sup> were obtained starting from the relative dichloro bridged precursor [(*R*ppy)<sub>2</sub>Ir(μ-Cl)]<sub>2</sub> **14** and **14'** which were reacted with a slight excess of orotic acid in the presence of tetrabutylammonium hydroxide similarly to the synthesis of catecholate Ir(III) complexes in the previous section.

The IR spectra of the anionic complexes **A**<sup>1</sup> and **A**<sup>2</sup> confirm the binding of the carboxylate group and the adjacent N atom of the orotic ligand to the Ir(III) metal center.<sup>223a</sup> Indeed, the deprotonation of both groups results in the disappearance of the acidic ν(O-H) band at 2500 cm<sup>-1</sup>, and of the stretching and bending N-H vibration bands of the adjacent N situated in the free ligand at 3200 and 1430 cm<sup>-1</sup> respectively (Figure 7.11).



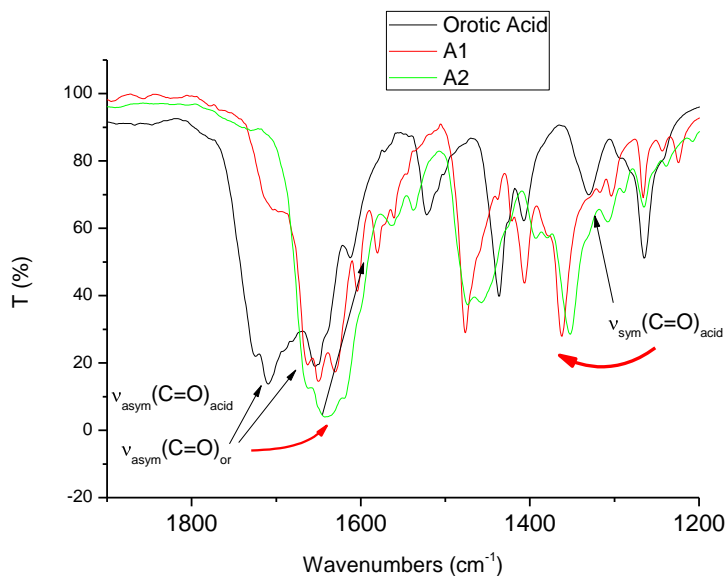


**Figure 7.11.** IR spectra of orotic acid and complexes **A**<sup>1</sup> and **A**<sup>2</sup>

Further confirmation of this coordination mode was obtained from the shift towards lower frequencies of the adjacent exocyclic  $\nu(\text{C}=\text{O})$  carboxylate band, and the corresponding shifts of the symmetric (downfield) and asymmetric (upfield) stretching bands of the carboxylate group.<sup>223b</sup>

Furthermore, the ionic character of **A**<sup>1</sup> and **A**<sup>2</sup> was confirmed by conductivity measurements in dry acetonitrile solution. Indeed, the values for both complexes are around  $120 \Omega^{-1} \cdot \text{cm}^2 \cdot \text{mol}^{-1}$ , in agreement with a 1:1 univalent electrolyte type.<sup>214</sup>

### 7.3.2 Solution electrochemical studies

The redox behaviour of **A**<sup>1</sup> and **A**<sup>2</sup> was studied by cyclic voltametry. The HOMO energy levels were estimated considering the measured redox potentials, while the LUMO levels were estimated considering spectroscopic data, taking into account -4.8 eV for  $\text{Fc}/\text{Fc}^+$ . The redox potentials measured for complexes **A**<sup>1</sup> and **A**<sup>2</sup> and the HOMO/LUMO levels estimated are reported in Table 7.2.

	$E^{\text{ox}}$ (mV)	HOMO/LUMO (eV)
$\mathbf{A}^1$	+ 319 (R)	-5.1 / - 2.4
$\mathbf{A}^2$	+ 171 (R)	-4.9 / - 2.3
All potential are given vs. $\text{Fc}/\text{Fc}^+$ .		
(R) : Reversible wave		

**Table 7.2.** Redox potential (vs.  $\text{Fc}/\text{Fc}^+$ ) observed for  $\mathbf{A}^1$  and  $\mathbf{A}^2$ . Estimation of HOMO/LUMO.

As described in a previous study,<sup>224</sup> oxidation of cyclometallated Ir(III) neutral and ionic complexes can be described as a metal-centred process which depends on the electron richness of the metal. The electron density of the metal centre is influenced, through the presence of the carbon-metal bond by the  $\sigma$ -donating capability of the cyclometallated ligands. One single-electron reversible oxidation (Figure 7.12) was observed for both the anions  $\mathbf{A}^1$  and  $\mathbf{A}^2$ . The oxidation of  $\mathbf{A}^2$  occurs at a lower potential (of *ca.* 150 mV) with respect to  $\mathbf{A}^1$  due to the different  $\sigma$ -donating effect induced by the presence of the two methyl groups on the cyclometallated ligand,<sup>225</sup> that finally results in the lowering of the HOMO energy level of  $\mathbf{A}^2$  with respect to  $\mathbf{A}^1$ .

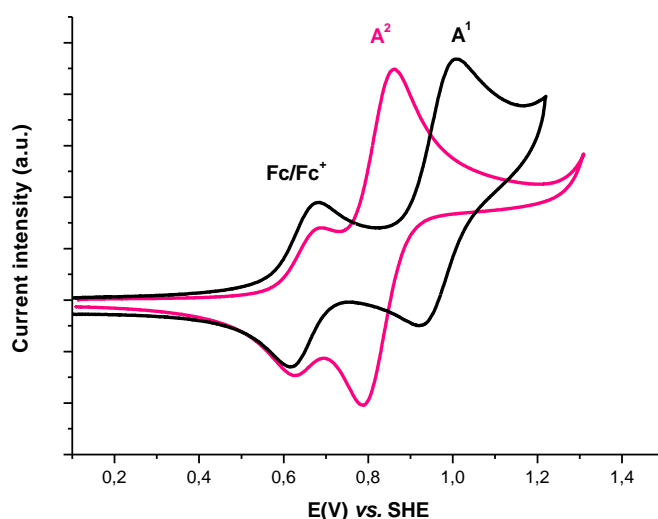


**Figure 7.12.** CV traces of  $\mathbf{A}^1$  and  $\mathbf{A}^2$  in presence of  $\text{Fc}/\text{Fc}^+$ . Scan rate  $100 \text{ mV s}^{-1}$  in dry acetonitrile

This rather high potential difference due to the dimethylation can be ascribed to the specific position of the methyl groups which are playing a crucial role onto the electronic effects on the 2-phenylpyridine ligand. Indeed, such high differences have been already observed for tris-cyclometallated homoleptic neutral Iridium complexes

bearing two methyl substituents. Depending on their position, the potential difference with respect to Ir(ppy)<sub>3</sub> can range from 170 to 240 mV without inducing any noticeable effect onto their emission energies.<sup>225</sup>

No reduction was observed for the two anionic complexes **A**<sup>1</sup> and **A**<sup>2</sup> in the solvent window used (-2.0/+1.8 V vs. SHE).

### 7.3.3 Photophysical properties

Photophysical studies were performed on deoxygenated acetonitrile solutions of the anionic complexes **A**<sup>1</sup> and **A**<sup>2</sup>. The absorption and emission data is summarized in Table 7.3.

	$\lambda_{\text{abs}}/\text{nm} (\log \epsilon)$		
<b>A</b> <sup>1</sup>	465 (3.28), 405 (3.59), 341 (4.04), 258 (4.47)		
<b>A</b> <sup>2</sup>	470 (3.56), 415 (3.74), 342 (4.17), 266 (4.57)		
	$\lambda_{\text{em}} (\text{nm})$	<sup>a</sup> $\tau (\text{nsec})$	<sup>b</sup> $\phi (\%)$
<b>A</b> <sup>1</sup>	530	1090	69
<b>A</b> <sup>2</sup>	536	1142	58
<sup>a</sup> Excited-state lifetimes.			
<sup>b</sup> Photoluminescence quantum yields obtained from degassed solutions (%)			

**Table 7.3.** Spectroscopic properties of **A**<sup>1</sup> and **A**<sup>2</sup> in deoxygenated highly diluted acetonitrile solutions ( $C \leq 5 \cdot 10^{-6}$  M). Luminescence quantum yields have been determined exciting the samples at  $\lambda = 380$  nm

In deoxygenated acetonitrile the two anionic **A**<sup>1</sup> and **A**<sup>2</sup> complexes show a structureless emission spectrum with the emission maximum centred at 530 nm and 536 nm respectively (Figure 7.13).

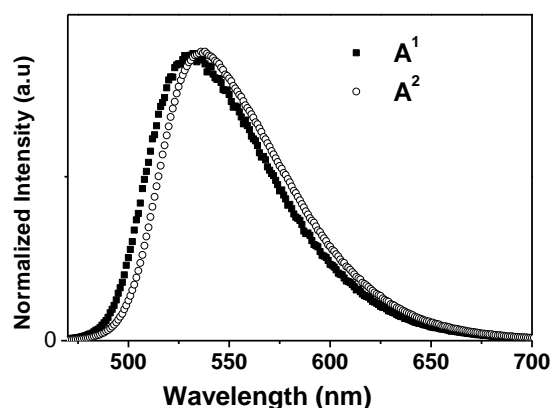


**Figure 7.13.** Emission spectra of  $A^1$  and  $A^2$  complexes in acetonitrile solutions

$A^1$  shows a luminescence quantum yield ( $\phi$ ) of 0.69 and an emission lifetime of about 1090 ns, while  $A^2$  shows a luminescence quantum yield ( $\phi$ ) of 0.58 and an emission lifetime of about 1142 ns. The broad and structureless shape of the observed emission profiles suggests an  $^3MLCT$  emission, while the small variation of the photophysical properties of the two anionic complexes can reasonably be attributed to the electronic effects exerted by the methyl substitutions on  $A^2$  C<sup>N</sup> ligand with respect to  $A^1$ .<sup>226</sup>

The two novel anionic complexes  $A^1$  and  $A^2$  bearing an orotate moiety as an ancillary ligand present high thermal stability and high luminescence. Considering that the use of anionic complexes in LECs has been so far prevented by the poor efficiency and lifetime of devices induced by the low stability in working conditions of the available ionic Ir(III) complexes embedded with monodentate pseudohalogen type ligands, complexes  $A^1$  and  $A^2$ , bearing a bidentate ancillary ligand, represent good candidates to be tested as active species in LECs. Furthermore, in the context of the synthesis of Ir(III) soft salts, such luminescent novel anionic complexes can be paired with a wide variety of cationic luminescent complexes to form homo or heterometallic soft salts.

## 7.4 Ir(III) luminescent homometallic soft salts

### 7.4.1 Synthesis

To this regard, we prepared and studied the homometallic soft salts formed by the two orotate containing anionic complexes  $A^1$  and  $A^2$  with two cationic Ir(III) previously reported complexes  $C^1$  and  $C^2$  (Figure 7.14) of general formula  $[(ppy)_2Ir(N^N)]X$ , where  $N^N = 2$ -picolylamine or  $2,2'$ -bipyridil and  $X = Cl^-$  or  $CH_3CO_2^-$  respectively.<sup>221</sup>

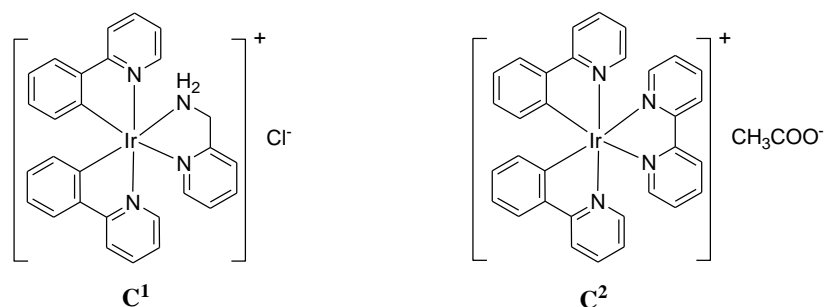


**Figure 7.14.** Molecular structures of the cationic Ir(III) complexes  $C^1$  and  $C^2$

The obtained homometallic Ir(III) soft salts, namely  $C^1A^1$ ,  $C^1A^2$ ,  $C^2A^1$ , and  $C^2A^2$  of general formula  $[(ppy)_2Ir(N^N)][(R-ppy)_2Ir(O^N)]$  are presented in Figure 7.15.

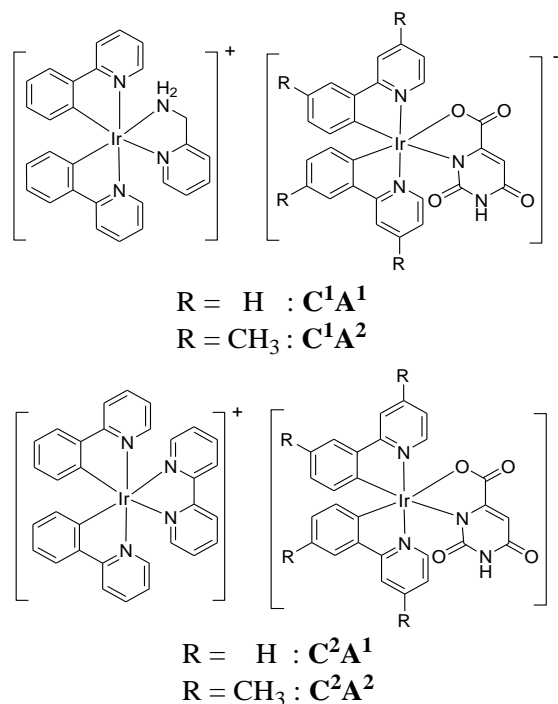
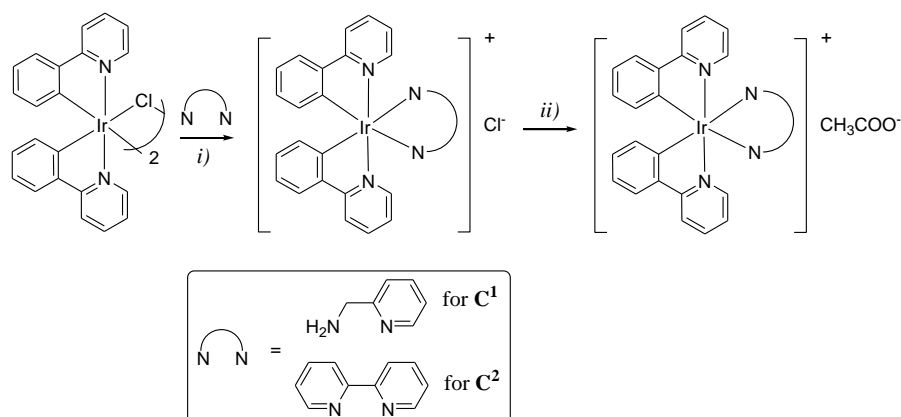


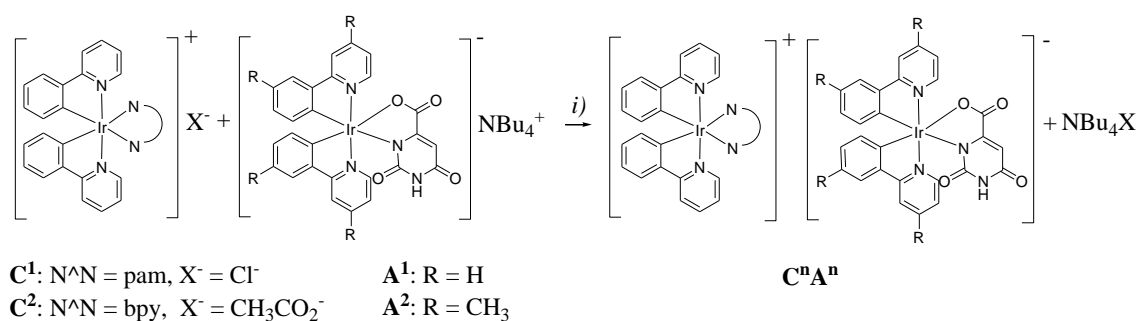
**Figure 7.15.** Molecular structures of the soft salts  $C^1A^1$ ,  $C^1A^2$ ,  $C^2A^1$  and  $C^2A^2$

Considering the choice of the cationic complexes, namely **C**<sup>2</sup> as the archetype cationic compound and **C**<sup>1</sup> because of its readiness to crystallize with a variety of counteranions (Cl<sup>-</sup>, ClO<sub>4</sub><sup>-</sup>, PF<sub>6</sub><sup>-</sup>).<sup>227a</sup> Indeed, the presence of a NH<sub>2</sub> functional group that could result in the formation of H-bond networks with the orotate ligand of the anionic Iridium complexes directed our choice of **C**<sup>1</sup> as a perfect candidate to emphasize cation/anion interactions. The cationic Ir(III) complexes **C**<sup>1</sup> and **C**<sup>2</sup> were synthesized as previously reported (Scheme 7.3).<sup>227</sup>



**Scheme 7.3.** Reagents and conditions: i) dichloromethane/methanol, reflux, N<sub>2</sub>, ii) AgCH<sub>3</sub>COO, methanol N<sub>2</sub>

The soft salts were prepared (Scheme 7.4) by dissolving the corresponding complementary charged Ir(III) complexes (1:1 molar ratio) in a mixture of methanol/water (4:1 v/v) at room temperature, and stirring the resulting mixture in open vessel to allow a slow evaporation of methanol to 1/3 of its initial volume.

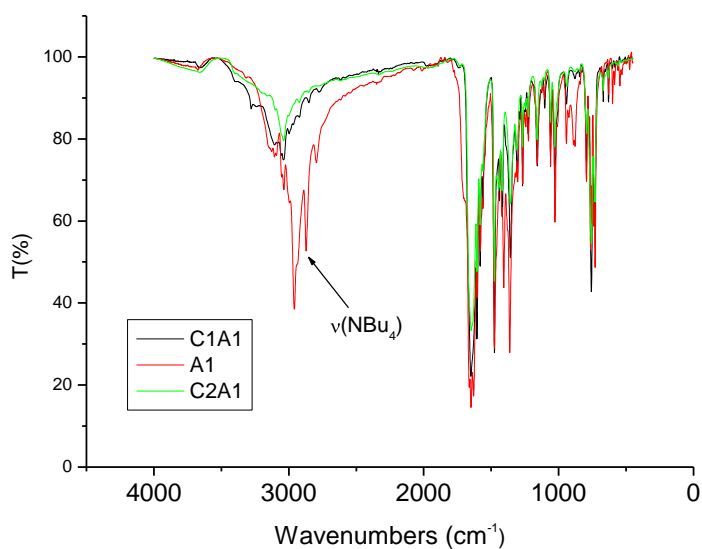


**Scheme 7.4.** Reagents and conditions: i) methanol/water, r.t.

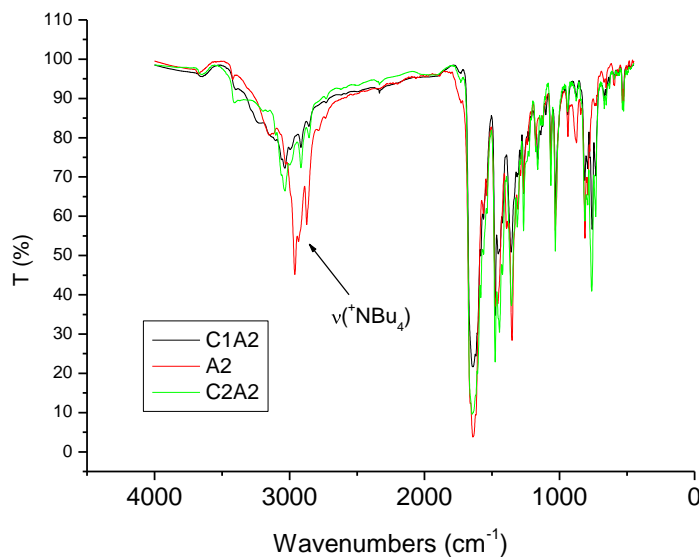
The as obtained yellowish precipitates were filtered out and washed several times with large amounts of water in order to remove the NBu<sub>4</sub>X byproduct salt formed together with the expected soft salts. The novel homometallic dinuclear ionic

species  $[(ppy)_2Ir(N^{\wedge}N)][(R-ppy)_2Ir(O^{\wedge}N)]$  were separated in moderate yields and fully characterized by FT-IR,  $^1H$  NMR and elemental analysis.

The actual formations of the soft salts were established through their relative IR spectra by the disappearance of the characteristic bands attributed to the counterions ( $\nu = 2962, 2874\text{ cm}^{-1}$  ( $NBu_4^+$ ) and  $1560, 1390\text{ cm}^{-1}$  ( $CH_3COO^-$ ) (Figures 7.16) and confirmed by  $^1H$  NMR again for the disappearance of the relative proton signals.



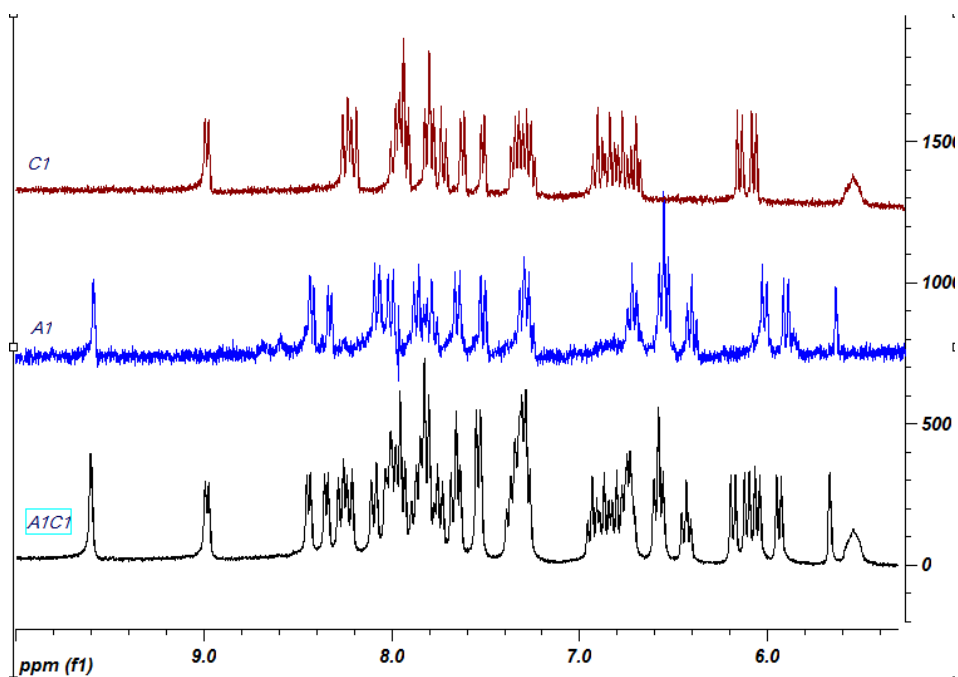
a)



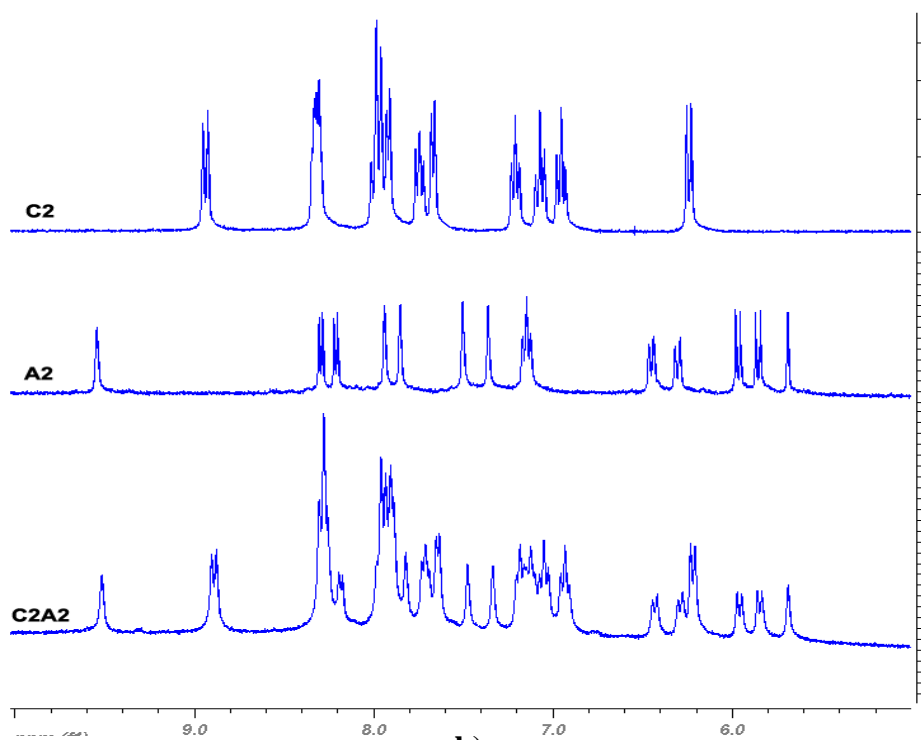
b)

**Figure 7.16.** IR spectra complexes of a)  $A^1$  and the corresponding soft salts  $C^1A^1$  and  $C^2A^1$  and b)  $A^2$  and the corresponding soft salts  $C^1A^2$  and  $C^2A^2$

For all the four  $C^nA^n$  species, it was observed that  $^1H$  NMR spectrum of the soft salts are exactly the superposition of the  $^1H$  NMR spectra of the two ionic components (Figure 7.17).



a)



b)

**Figure 7.17.**  $^1\text{H}$  NMR spectra of a) complexes  $\text{A}^1$  and  $\text{C}^1$  and their corresponding soft salt  $\text{A}^1\text{C}^1$  and b)  $\text{A}^2$  and  $\text{C}^2$  and their corresponding soft salt  $\text{A}^2\text{C}^2$

All soft salts are highly hygroscopic and the loss of water molecules has been observed on TGA traces below  $100^\circ\text{C}$ .



## 7.4.2 Solution electrochemical studies

The redox properties of all the soft salts, as well as their single cationic  $C^1$  and  $C^2$  were studied by cyclic voltametry. The HOMO/LUMO energy levels were estimated considering the measured redox potentials and the complexes spectroscopic data when reductive potentials were not available, taking into account -4.8 eV for  $Fc/Fc^+$ . The redox potentials measured for the complexes  $C^1$ ,  $C^2$  and for the soft salts are reported in Table 7.4, as well as the data relative to the anions  $A^1$  and  $A^2$  for direct comparison.

	$E^{\text{red}}_{\text{bpy}}$ (mV)	$E^{\text{ox}}_1$ (mV)	$E^{\text{ox}}_{2 \text{ pam}}$ (mV)	$E^{\text{ox}}_{2 \text{ bpy}}$ (mV)	HOMO/LUMO (eV)
$C^1$	/	/	+780 (I)	/	-5.6 / - 2.9
$C^2$	-1777 (R)	/	/	+ 852 (I)	-5.7 / - 3.0
$A^1$	/	+ 319 (R)	/	/	-5.1 / - 2.4
$A^2$	/	+ 171 (R)	/	/	- 4.9 / - 2.3
$C^1A^1$	/	+ 330 (R)	+ 801 (I)	/	- 5.1 / - 2.4
$C^1A^2$	/	+ 172 (R)	+ 762 (I)	/	- 4.9 / - 2.3
$C^2A^1$	- 1772 (R)	+ 305 (R)		+ 808 (I)	- 5.1 / - 3.0
$C^2A^2$	- 1769 (R)	+ 162 (R)		+ 774 (I)	- 4.9 / - 3.0
All potential are given vs. $Fc/Fc^+$ . (R): Reversible wave, (I): Irreversible wave. pam: picolyl amine moiety, bpy: bipyridine moiety					

**Table 7.4.** Redox potential (vs.  $Fc/Fc^+$ ) observed for all complexes and soft salts. Estimation of HOMO/LUMO.

Considering the solution electrochemistry of the single ions, it was observed that the oxidative potential of  $C^2$  ( $E^{\text{ox}}_{2 \text{ bpy}}$ ) is *ca.* 70 mV higher than the one of cation  $C^1$  ( $E^{\text{ox}}_{2 \text{ pam}}$ ).

No reduction waves were observed for the two anions neither for  $C^1$  in the solvent window used (-2.0/+1.8 V vs. SHE), while reduction of  $C^2$  occurs at -1777 mV vs.  $Fc/Fc^+$ . The process can reasonably be attributed to the reduction of the bipyridine moiety.<sup>228</sup> While the electrochemical properties of  $C^1$  have not previously been investigated, the oxidation and reduction potentials of  $C^2$  ( $E^{\text{ox}} = + 850$  mV and  $E^{\text{red}} = -1780$  mV vs.  $Fc/Fc^+$ ) are in agreement with literature reported values.<sup>229</sup>

As previously observed for Ir(III) soft salts based on monodentate anionic complexes,<sup>209a</sup> the redox properties of the soft salts are identical to their corresponding component ions. The voltamogram of  $C^2A^2$  (for which both reduction and oxidation are observed) is presented in Figure 7.18 as example.

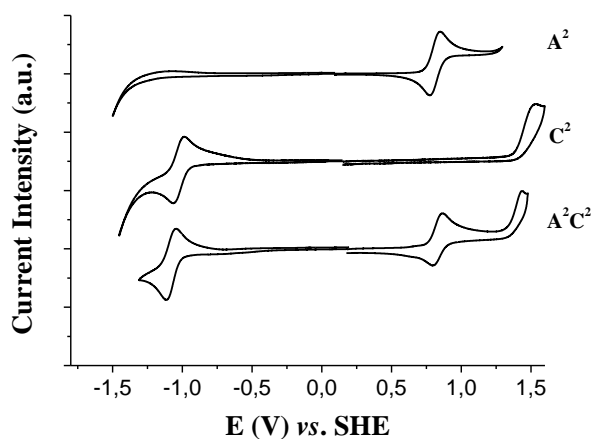


**Figure 7.18.** Comparison between the cyclic voltammograms obtained for the soft salt  $C^2A^2$  and its corresponding ion components  $A^2$  and  $C^2$

The  $C^2A^2$  voltammogram is consequently the sum of the voltammograms of  $C^2$  and  $A^2$ , the reduction and oxidations potentials of the single ions remain unchanged in the salt. The same behaviour was observed for the whole series of  $C^nA^n$  soft salts. Consequently, the HOMO and LUMO energy levels of the salt are given by the highest oxidation and the lowest reduction potentials of the couple anion/cation. In the  $C^2A^2$  example, the LUMO orbital is localized on the cation, while the HOMO is associated with the anion. This provides a straightforward way to tune the energy levels of soft salts by chemically modifying the chelating ligands of the individual ions, a way to probe the role of carrier trapping on the cationic and anionic component of soft salts in lightning devices.

### 7.4.3 Photophysical properties

A comprehensive photophysical investigation including emission spectra, luminescence quantum yield and time-resolved luminescence was performed on deoxygenated acetonitrile solutions of the cationic complexes  $C^1$  and  $C^2$  and their corresponding soft salts. The emission data of the single ions and soft salts are summarized in Table 7.5 (data relative to  $A^1$  and  $A^2$  is reported too for direct comparison).

	$\lambda_{em}$ (nm)	$^c\tau$ (nsec)	$^d\phi$ (%)	$k_{en}(s^{-1})$
<sup>a</sup> <b>C<sup>1</sup></b>	490	1200	52	
<sup>b</sup> <b>C<sup>2</sup></b>	585	310	9	
<b>A<sup>1</sup></b>	530	1090	69	
<b>A<sup>2</sup></b>	536	1142	58	
<b>C<sup>1</sup>A<sup>1</sup></b>	(480) 525	372 / 1220	83	$1.9*10^6$
<b>C<sup>1</sup>A<sup>2</sup></b>	(486) 532	560 / 1300	81	$9.5*10^5$
<b>C<sup>2</sup>A<sup>1</sup></b>	532	320 / 940	51	$1.4*10^5$
<b>C<sup>2</sup>A<sup>2</sup></b>	538	336 / 1135	48	$5.4*10^3$
<sup>a</sup> as a ClO <sub>4</sub> <sup>-</sup> salt for solubility in acetonitrile <sup>b</sup> as a Cl <sup>-</sup> salt for solubility in acetonitrile <sup>c</sup> Excited-state lifetimes. <sup>d</sup> Photoluminescence quantum yields obtained from degassed solutions (%). <sup>e</sup> rate constant for the energy-transfer process				

**Table 7.5.** Luminescence properties of soft salts and of their respective cations and anions components in deoxygenated highly diluted acetonitrile solutions ( $C \leq 5*10^{-6}$  M). Luminescence quantum yields have been determined exciting the samples at  $\lambda = 380$  nm.

The photophysical properties observed for both **C<sup>1</sup>** and **C<sup>2</sup>** cationic complexes are in good agreement with those already reported in literature.<sup>204,225,227</sup>

All soft salts displayed a broad emission band corresponding to the overlap of the emission of their respective cation and anion components. Concerning luminescence quantum yields, all the soft salts resulted to be highly luminescent with a luminescence quantum yield values ranging from 48 % to 81%. The large overlap of absorption bands of the cationic and anionic soft salts components prevents the selective excitation of each salt components. Furthermore the analogous significant emission spectra overlap made single component analysis rather difficult. Consequently, a quantitative analysis of the obtained soft salts luminescence quantum yield values not allowed.

A deeper analysis of soft salts photophysical properties was obtained by performing time-resolved luminescence measurements. In particular, all salts yield a characteristic double-exponential decay in agreement with the presence in the salt of the two different ion components. Moreover, while the lifetime of the ion component with higher triplet state energy resulted markedly shortened for  $C^1A^1$  and  $C^1A^2$  salts and only slightly shortened for the couples  $C^2A^1$  and  $C^2A^2$  with respect to the corresponding isolated components, the lifetime of the ion with lower energy in the pair resulted to be slightly longer in all cases. The shortening of the luminescence lifetime of the ion component with higher triplet state energy is probably due to the presence of an energy transfer process active within all the soft salts, analogously from what observed for related systems.<sup>207a,209</sup> The process efficiency of such a proposed energy transfer is significantly higher for the salts containing  $C^1$  complex cation acting as energy donor showing in these salts a drastic decrease of luminescence lifetime. Differently, in the soft salts comprising  $C^2$ , which would act in this case as energy acceptor, the energy transfer appears less efficient. Furthermore, the increase of the luminescence lifetime observed for all the ions with the lower energy in the pairs (energy acceptors), should derive from a partial reduction of nonradiative decays due to vibrational modes caused by the ion pair formation.

To further investigate the energy transfer process we compared the emission spectra of the salts, excited at  $\lambda_{exc} = 380$  nm (excitation wavelength used for both luminescence quantum yield and luminescent lifetimes determinations) with the emission spectra of their corresponding ion components obtained at the same excitation wavelength and controlling the experimental conditions to insure that the number of absorbed photons for each component was matching the number of photons they effectively absorbed in the salt. It is important to point out that these measurements are feasible since the absorption spectra of all soft salts (Table 7.4) result from the simple superposition of the spectra of the component units indicating a negligible electronic interaction between them as it is expected for this class of compounds.<sup>209</sup>

samples	$\lambda_{\text{abs}}/\text{nm}$ ( $\log \epsilon$ )
$\text{C}^1 \text{ClO}_4$	420 (3.57), 384 (3.68), 343 (3.87), 258 (4.63)
$\text{C}^2 \text{Cl}$	467 (3.12), 381 (3.70), 309 (4.24), 257 (4.59)
$\text{C}^1 \text{A}^1$	465 (3.46), 389 (4.01), 345 (4.30), 258 (4.86)
$\text{C}^1 \text{A}^2$	470 (3.54), 416 (3.91), 342 (4.33), 263 (4.88)
$\text{C}^2 \text{A}^1$	467 (3.41), 408 (3.83), 340 (4.24), 309 (4.45), 258 (4.83)
$\text{C}^2 \text{A}^2$	470 (3.61), 415 (3.91), 342 (4.33), 309 (4.51), 263 (4.88)

**Table 7.4.** Spectroscopic data of the samples in acetonitrile solutions

Since  $\text{A}^1$  and  $\text{A}^2$  have shown similar photophysical properties, this investigation has been only conducted for the couple  $\text{C}^1 \text{A}^1$  and  $\text{C}^2 \text{A}^2$  while analogous conclusions can be reasonably assumed for  $\text{C}^1 \text{A}^2$  and  $\text{C}^2 \text{A}^1$  soft salts. The photoluminescent spectra obtained for  $\text{C}^1 \text{A}^1$  and  $\text{C}^2 \text{A}^2$  soft salts are presented in Figures 7.19.

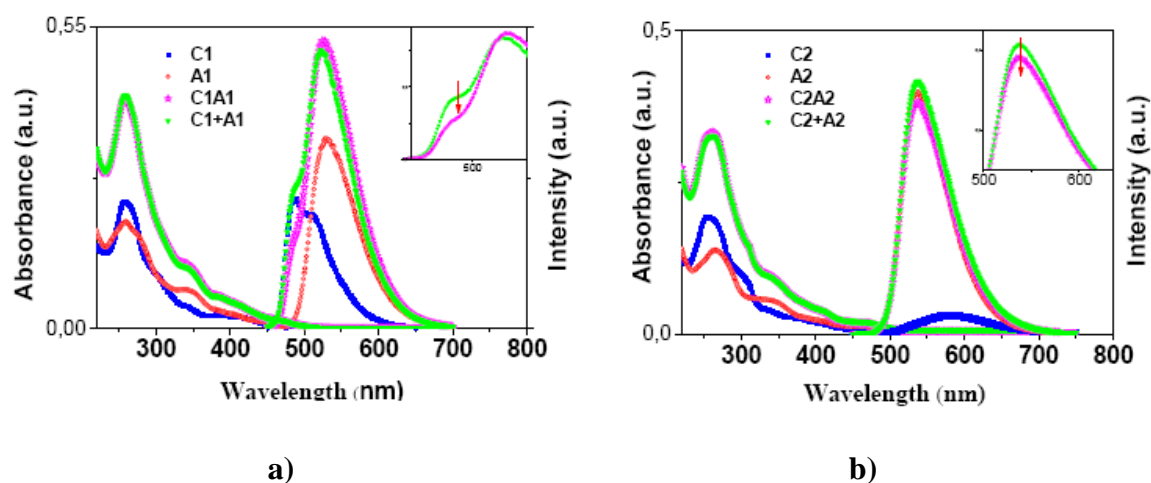


**Figure 7.19.** a) Absorption and Emission Spectra in deoxygenated acetonitrile at 298K of  $\text{C}^1 \text{A}^1$  (Abs.380nm = 13%),  $\text{C}^1$  (Abs.380nm = 5.9%) and  $\text{A}^1$  (Abs.380nm = 7.1%). In inset, a detailed around ca. 500 nm of the comparison between the emission spectrum of  $\text{C}^1 \text{A}^1$  and the sum of emission spectra  $\text{C}^1 + \text{A}^1$ , b) Absorption and Emission Spectra in deoxygenated acetonitrile at 298K of  $\text{C}^2 \text{A}^2$  (Abs.380nm = 12%),  $\text{C}^2$  (Abs.380nm = 95.6%) and  $\text{A}^2$  (Abs.380nm = 6.4%). In inset, a detailed around ca. 550 nm of the comparison between the emission spectrum of  $\text{C}^2 \text{A}^2$  and the sum of emission spectra  $\text{C}^2 + \text{A}^2$ .

All the measurements were performed in deoxygenated acetonitrile solutions. By comparing the emission spectrum of each soft salt with the sum of the emission spectrum of the corresponding ionic components absorbing the same number of photons as in the salt, it can be noticed that the sum spectrum is always higher in intensity. However, while for  $C^2A^2$  this behaviour is barely noticeable, it becomes more pronounced for  $C^1A^1$  suggesting that a different amount of emitted photons are lost in the salt.

In particular, since the luminescence spectral features relative to the energy donor ( $C^1$ ) remain partially distinguishable in  $C^1A^1$  salt this comparison ( $A^1C^1$  vs.  $A^1 + C^1$ ) immediately highlights that  $C^1$ , the ionic component with the higher triplet state energy in the salt is the quenched one, while in the case of  $C^2A^2$  such observation is prevented by a too close overlap of both emission bands of  $C^2$  and  $A^2$  together with the low emission efficiency of the energy acceptor  $C^2$ .

These experimental evidences corroborate a higher efficiency of the energy transfer process within the soft salts containing  $C^1$  as complex cation and a less important quasi negligible one within the soft salts containing  $C^2$  as complex cation. The rate constant for the energy-transfer process,  $k_{en}$ , can be obtained from the following equation:

$$k_{en} = 1/\tau - 1/\tau_0$$

where  $\tau_0$  and  $\tau$  are respectively the phosphorescence lifetimes of the un-quenched and quenched energy of the donor. The rates of the energy-transfer processes calculated for our systems are reported in Table 7.5. Noteworthy, the rates are significantly higher for the salts containing  $C^1$  as energy donor.

The energy transfer process can occur via different mechanisms: (i) the Forster mechanism, which relies on the coupling of the transition dipole moments to transfer energy and which is active over long distances ( $< 100 \text{ \AA}$ ); (ii) the Dexter mechanism, which actually involves the exchange of electrons between donor and acceptor and only occurs when their molecular orbitals overlap (interchromophoric distance  $< 10 \text{ \AA}$ ). This energy transfer efficiency drops exponentially with distance.<sup>230</sup>

Taking into account that no significant electronic interactions between the salts components resulted from both photophysical and electrochemical measurements and that in acetonitrile solution each ion forming the soft salts should be completely solvated, the Dexter mechanism could be reasonably excluded.

Since the rate of the energy transfer depends, among other factors, also on the extent of the spectral overlap of the emission spectrum of the donor with the absorption spectrum of the acceptor, the higher rates values obtained for the salts containing  $C^1$  as energy donor ( $C^1A^1$ ,  $C^1A^2$ ) should mainly result from the greater extent of the spectral overlap showed by these soft salts with respect to  $C^2A^1$  and  $C^2A^2$  for which the overlap become quasi negligible (Figure 7.20).

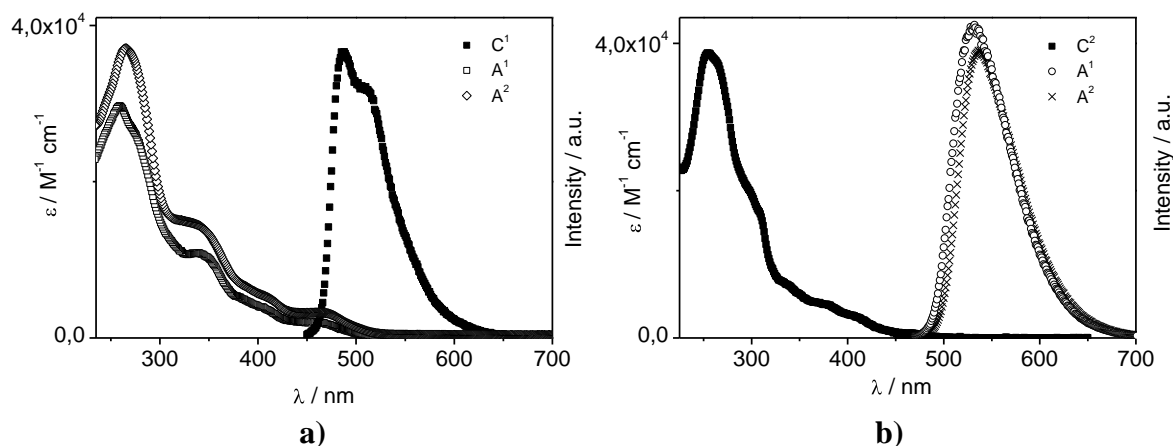


**Figure 7.20.** a) Superimposition of the emission spectrum of  $C^1$  energy donor with the absorption spectra of both  $A^1$  and  $A^2$  energy acceptors relative to the soft salts  $C^1A^1$ ,  $C^1A^2$ , b) Superimposition of the emission spectrum of  $A^1$  and  $A^2$  energy donors with the absorption spectra of  $C^2$  energy acceptor relative to the soft salts  $C^2A^1$ ,  $C^2A^2$

## 7.5 Conclusions

New anionic cyclometallated Ir(III) complexes with  $O^{\wedge}O$  and  $O^{\wedge}N$  type dianionic ancillary ligands have been successfully synthesised. The first series of anionic complexes is composed of catecholate containing Ir(III) anionic complexes with the *ortho*-hydroquinone ligands bearing strong electron withdrawing groups (complexes **XIV** and **XV**) or featuring a largely delocalized  $\pi$  system (complex **XVI**). These complexes present similar redox behaviour, showing high electrochemical stability in their catecholate and semiquinonate forms. However, photophysical characterizations have evidenced for complex **XIV** and especially for **XV** high sensitivity towards hydrolysis. Regardless of the luminescence properties that can be improved by smart ligand functionalization if desired, remarkably complex **XVI** shows strong absorption extending as far as 700 nm making this system of interest for solar energy harvesting

applications.<sup>231</sup> These synthetic results, encouraged us to go further with the investigation of anionic Ir(III) complexes.

In fact, orotic acid has been successful used as a dianionic bidentate ligand to obtain anionic green emitting with high luminescent quantum yields (60-70%,  $\lambda_{em}$  ca. 530 nm), and thermally stable (until ca. 200°C) Ir(III) complexes. The introduction of this bidentate orotic acid as an appealing ancillary ligand might be a step toward the stabilisation of anionic Ir(III) complexes which until now have both shown emission quenching and fast device degradation when used in LECs, in particular the until now commonly used monodentate anionic complexes studied. Furthermore, we have demonstrated the possibility of using such anionic complexes in the formation of homometallic soft salts with enhanced luminescent properties showing up to 81–83% photoluminescent quantum yield ( $C^1A^1$  and  $C^1A^2$ ). Finally, by adequately choosing the couple cation/anion we have shown how to modulate the possible energy transfer process within the soft salts allowing both the cation and anion to present their individual emission frequencies. This results in the enhancement of the emission. Further test of the anionic luminescent complexes  $A^1$  and  $A^2$  in LECs and of the corresponding overall neutral soft salts in OLEDs is in progress.

Moreover, since the choice of the single components can modulate the luminescence properties of the synthesised homometallic Ir(III) soft salts, the results of the above described investigations suggest that following the developed synthetic pathway, cations of different metals and/or different geometries could be introduced to form heterometallic soft salts.



## Chapter Eight

### Electropolymerizable Ir(III) cyclometallated complexes

#### 8.1 Introduction

As introduced in Chapter 6, in order to be used in OLEDs, phosphorescent emitters are commonly embedded within an appropriate (hole/electron or ambipolar) charge transporting host matrix.<sup>232</sup> It has been observed that high concentration promote aggregation of the emitters often leading to reduced emission efficiency due to concentration quenching and triplet–triplet annihilation. Furthermore, in order to have efficient charge injection, the energy barriers between the device layers should result the lowest possible.<sup>185</sup> Independently of the emitter's nature (small molecules or polymers), the host need thus to fulfil several tasks: i) separation of phosphors, ii) charge injection, iii) charge/energy-transport, and iv) charge transfer to the phosphorescent species.

Two strategies have been developed in order to successfully fabricate phosphorescent Ir(III) based OLEDs. The most widely used involves the physically blend of the emitting specie with the polymer host. Even if many efficient OLEDs have been obtained in such way,<sup>233</sup> blended systems, inherently involve the risk of phase separation, aggregation, or crystallization, leading to device degradation, colour instability and shorten of the device lifetimes.<sup>234</sup>

Therefore, in order to overcome this issues, an alternative approach was recently investigated taking advantage of the intrinsic nature of (co)polymers combining both charge transport and emission functionalities.<sup>235</sup> The advantages of such dual systems are eventually better energy transfer to the emitters leading to higher efficiencies and longer device lifetime. In addition, polymeric materials present the strength points of their specific features such as flexibility, film-forming properties, and processability from solution which allow large scale processing through for instance the inkjet printing technique.

The general synthetic strategies to design Ir(III) complexes containing polymers such as illustrated in Figure 8.1 are based on : i) the embedding of complexes within (co)polymers, ii) the complexation of (co)polymers, iii) the (co)polymerization by complexation, iv) the use of a complex as polymerization initiator, and iv) (co)polymerization/condensation of complex monomers.<sup>185</sup>

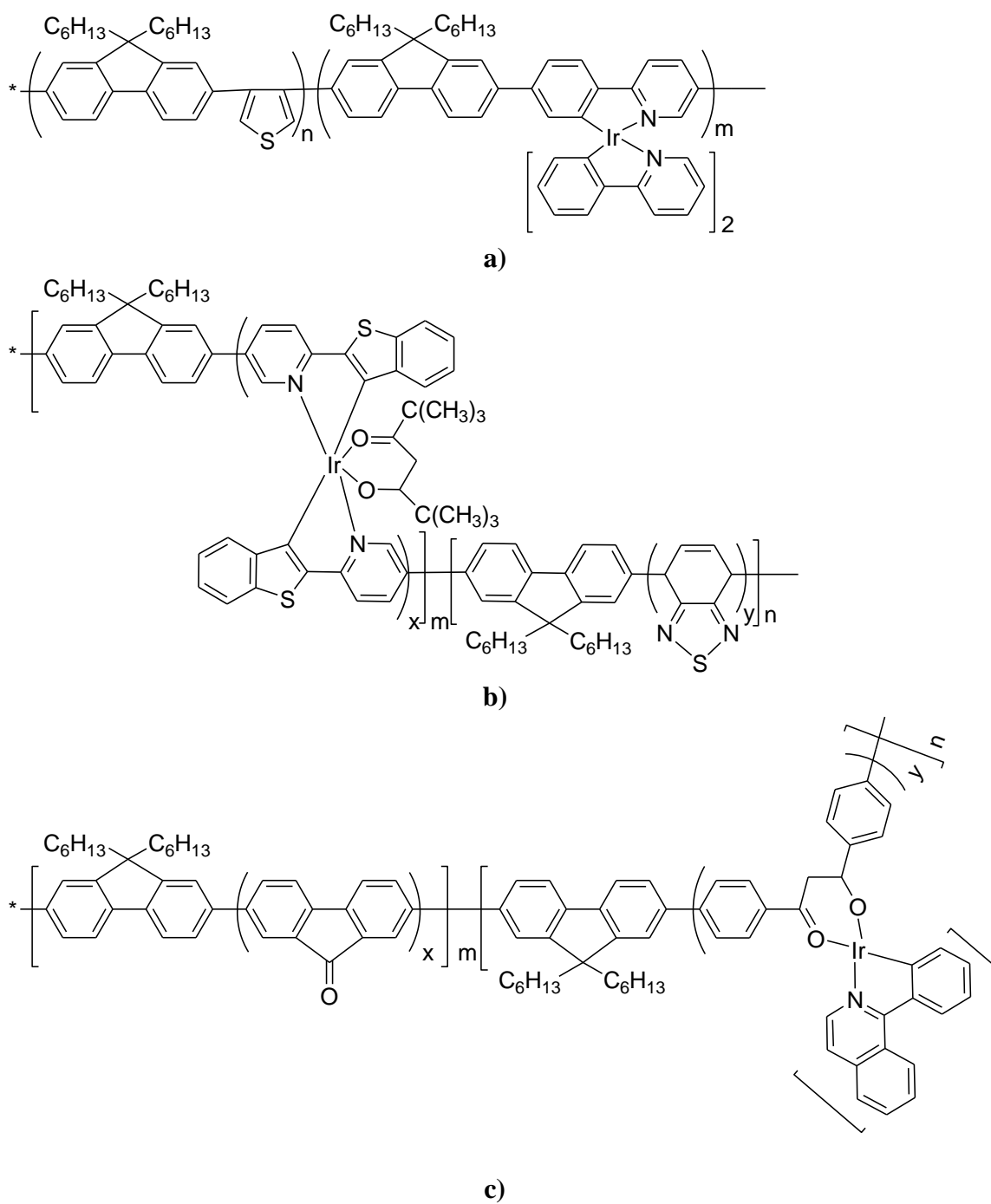


**Figure 8.1.** Examples of Ir(III) containing polymers<sup>236</sup>

Following these synthetic approaches, green,<sup>235c,237a</sup> red,<sup>237b</sup> blue<sup>237c</sup> and white<sup>237d</sup> electrophosphorescent Ir(III) copolymers have been successfully obtained and tested in OLEDs. Interestingly, white emitting OLEDs have been obtained by using a single Ir (III) containing polymer with broad emission covering the whole visible region.<sup>237d</sup>

## 8.2 Research scopes

Although the use of Ir(III) containing copolymers represent a valid alternative to the use of multilayer OLEDs architectures, long synthetic pathways involving aromatic coupling reactions need to be followed to obtain such materials. In this context, a useful synthetic tool could be represented by the electropolymerization showing the advantages of facile polymer formation with high purity and controlled thickness and direct grafting of the polymer onto the semiconducting electrode.

To this regard, in an attempt to obtain polymeric films containing cyclometallated Ir(III) complexes and, taking advantage of the synthetic tools developed for the electrogeneration of Nile red cyclopalladated thin films (Chapter 3), new cyclometallated Ir(III) complexes containing the electropolymerizable Schiff base  $\text{H}(\text{O}^{\wedge}\text{N})^4$  (Figure 8.2) have been synthesized and studied.

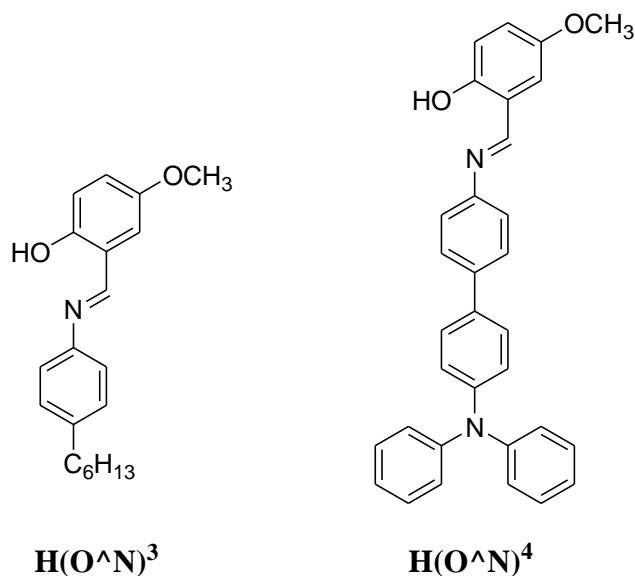


**Figure 8.2.** Molecular structure of the electropolymerizable Schiff bases  $\text{H}(\text{O}^{\wedge}\text{N})^3$  and  $\text{H}(\text{O}^{\wedge}\text{N})^4$

Considering the triphenylamine electron donating fragment, to the best of our knowledge, a single example of Ir(III) complex containing the triphenylamine fragment has been reported until now. Indeed, Zhang *et al.*<sup>238</sup> have reported on a novel emitting Ir(III) complex bearing as a cyclometallated ligand the triphenylamine-benzothiazole **btz-tpa** and acetylacetonate as ancillary ligand (Figure 8.3). This complex showed interesting solvatochromic emission from orange to blue and rather high emission quantum yields (*ca.* 50%).

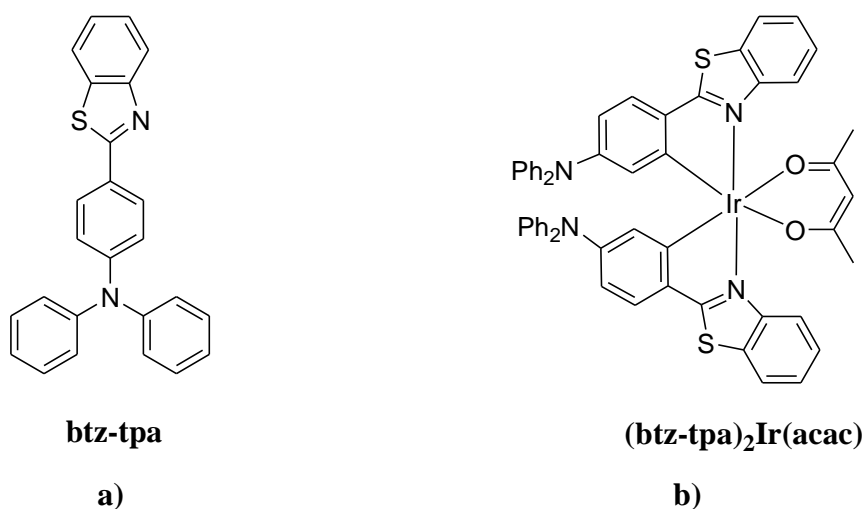


**Figure 8.3.** Molecular structure of a) **btz-tpa** and b) the luminescent Ir(III) complex **(btz-tpa)<sub>2</sub>Ir(acac)**<sup>238</sup>

However, no electrochemical studies have been performed on this emitting complex. In this context, considering the luminescence properties of complex **(btz-tpa)<sub>2</sub>Ir(acac)** and also in order to check the capability of a triphenylamine moiety bearing a phenyl ring involved into the metallacycle to undergo electropolymerization, a series of new Ir(III) cyclometallated complexes embedded with the triphenylamine fragment either on the cyclometallated ligand and/or onto the ancillary ligand have been synthesized and studied.

### 8.3 Synthesis of novel bis-cyclometallated Ir(III) model complexes with Schiff bases as ancillary ligands

The two first synthesized complexes **XVII** and **XVIII** comprise the 2-phenylpyridine fragment as archetype cyclometallated ligand and the two Schiff bases  $\text{H}(\text{O}^{\wedge}\text{N})^3$  and  $\text{H}(\text{O}^{\wedge}\text{N})^4$  were respectively used as ancillary ligands. To complete the series in order to study the influence of the triphenylamine moiety placed onto the cyclometallated ligand, two novel cyclometallated benzothiazole-triphenylamine Ir(III) complexes, **XIX** and **XX** were also synthesized respectively comprising the same Schiff bases  $\text{H}(\text{O}^{\wedge}\text{N})^3$  and  $\text{H}(\text{O}^{\wedge}\text{N})^4$ . The complete series of the new complexes is illustrated in Figure 8.4.

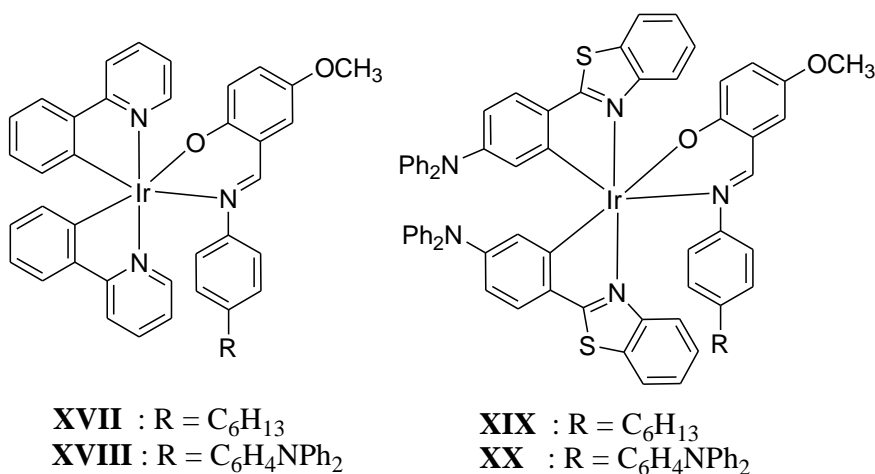
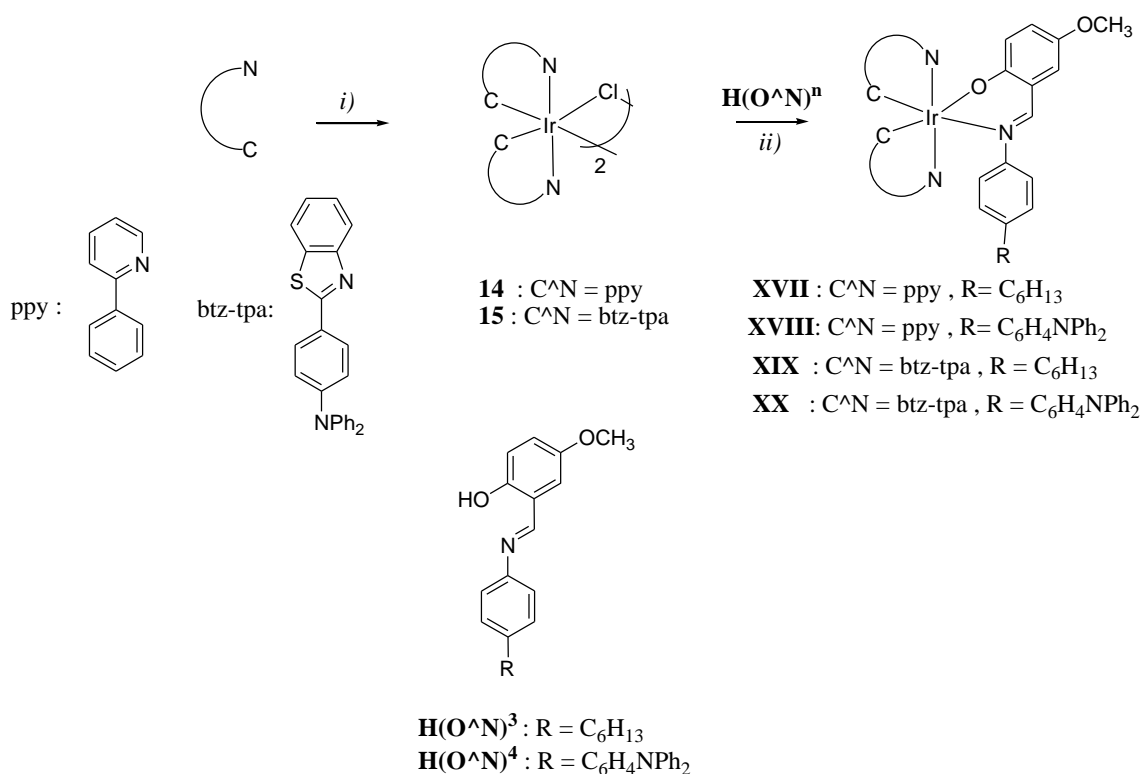


**Figure 8.4.** Comparison between the molecular structures of the synthesised complexes **XVII-XX**

The synthesis of the complexes **XVII-XX** (Scheme 8.1) was achieved starting from their respective dichloro-bridged dimer. In particular, complexes **XVII-XVIII** were obtained starting from the already described chloro-bridged dimer **14**,<sup>213</sup> while **XIX-XX** complexes were obtained starting from the synthesis of the cyclometallated ligand **btz-tpa**<sup>238</sup> and of the corresponding dichloro-bridged cyclometallated Ir(III) intermediate **15** obtained by modification of the reported procedure.<sup>238</sup> Differently from what reported the synthesis of the chloro-bridged intermediate **15**, (isolated and fully characterized), was performed using microwave radiation, preventing the possible and easy degradation of the  $\text{IrCl}_3 \cdot x\text{H}_2\text{O}$  during the first step of the reaction. Eventually, the addition of the appropriate substituted Schiff base in the presence of an excess of trimethylamine to ensure the complete deprotonation of the ancillary ligand, afforded the final complexes **XVII-XX**.



**Scheme 8.1.** Reagents and conditions: i) for **14**: 2-ethoxyethanol/water:3/1, reflux, 48 h; for **15**: ethoxyethanol/water:3/1, MW, 20 min. (250 W, 120° C), reflux, 4 d.,  $\text{N}_2$ ; ii) dichloromethane/acetone, reflux, 48 h.

## 8.4 Electrochemical studies

The redox behaviour of complexes **XVII-XX** was studied by cyclic voltametry. The HOMO energy levels were estimated considering the measured oxidation potentials, taking into account -4.8 eV for Fc/Fc<sup>+</sup>. Voltammograms were registered in ca. 3 mL degassed (Ar) fresh distilled dichloromethane solution with 0.1 M tetrabutylammonium hexafluorophosphate used as supporting electrolyte. The oxidation potentials measured for complexes **XVII-XX** and the HOMO levels estimated are reported in Table 8.1, together with the oxidation potential of the benzothiazole-triphenylamine btz-tpa ligand for direct comparison. The corresponding obtained cyclic voltammograms are presented in Figure 8.5.

	$E_{ox}^1$ (mV)	$E_{ox}^2$ (mV)	$E_{ox}^3$ (mV)	HOMO (eV)
<b>XVII</b>	+165 (R)	/	/	-4.3
<b>XVIII</b>	+ 190 (R)	+510 (R)	/	-4.3
<b>btz-tpa</b>	+ 545 (R)	/	/	-4.7
<b>XIX</b>	+150 (R)	+530 (R)	/	-4.3
<b>XX</b>	+162 (QR)	+370 (R)	+545 (R)	-4.3

All potential are given vs. Fc/Fc<sup>+</sup>.  
(R) : Reversible wave  
(QR) : Quasi-reversible

**Table 8.1.** Cyclic voltametry data relative to complexes **XVII-XVIII** and **btz-tpa**.  
Estimated HOMO

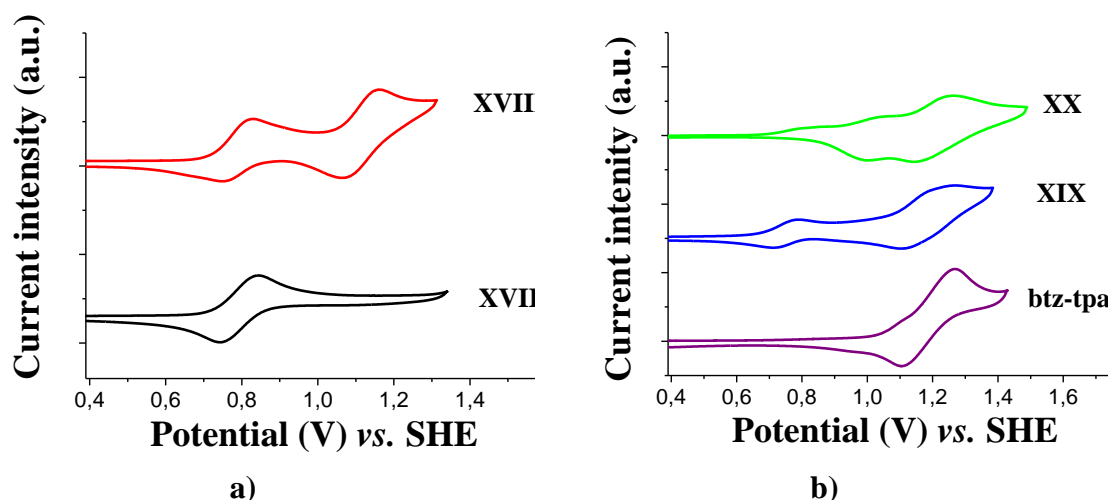


**Figure 8.5.** Cyclic voltamograms of a) complexes **XVII-XVIII** and b) ligand **btz-tpa** and complexes **XIX-XX**. Scan rate  $100 \text{ mV}\cdot\text{s}^{-1}$  in dry dichloromethane

Considering the oxidation behaviour of the model complexes **XVII-XVIII** (Figure 8.5a), a single reversible one-electron wave is present for complex **XVII** and can be attributed to the oxidation of the Schiff base  $\text{H}(\text{O}^{\wedge}\text{N})^3$ , while in the case of complex **XVIII**, the two consecutive oxidation waves observed are typical of the triphenylamine moiety of the  $\text{H}(\text{O}^{\wedge}\text{N})^4$  Schiff base (Chapter 3). The cyclometallated ligand **btz-tpa** showed in the solvent window explored (-1.2-1.45 V) a single reversible oxidation at *ca.* +545 mV *vs.*  $\text{Fc}/\text{Fc}^+$ . Complex **XIX** showed two reversible oxidation peaks, the first one probably associated (by comparison with **XVII** and **XVIII** in Chapter 3) with the Schiff base  $\text{H}(\text{O}^{\wedge}\text{N})^3$  as its potential is close to the oxidation potential of **XVII**. The second reversible wave can reasonably be attributed to the oxidation of the cyclometallated ligand.<sup>239</sup> Regarding the oxidation properties of complexes **XX**, a specific attribution of the oxidation process on a molecular scale resulted unfeasible due to the overlap of the oxidation waves of the various fragments.

For all complexes **XVII-XX**, no reduction wave was recorded in the solvent window (-1.2-1.45 V).

Neither complex **XVII** embedded with the  $(\text{O}^{\wedge}\text{N})^4$  triphenylamine substituted Schiff base nor the complex **XIX** grafted with the triphenylamine fragment onto the cyclometallated ligand showed electropolymerization upon repeated cycling potential scans (Figure 8.6). The slight increase in current intensity visible on the respective cyclic voltamograms is only due to slight accumulation of oxidized specie at the surface electrode.



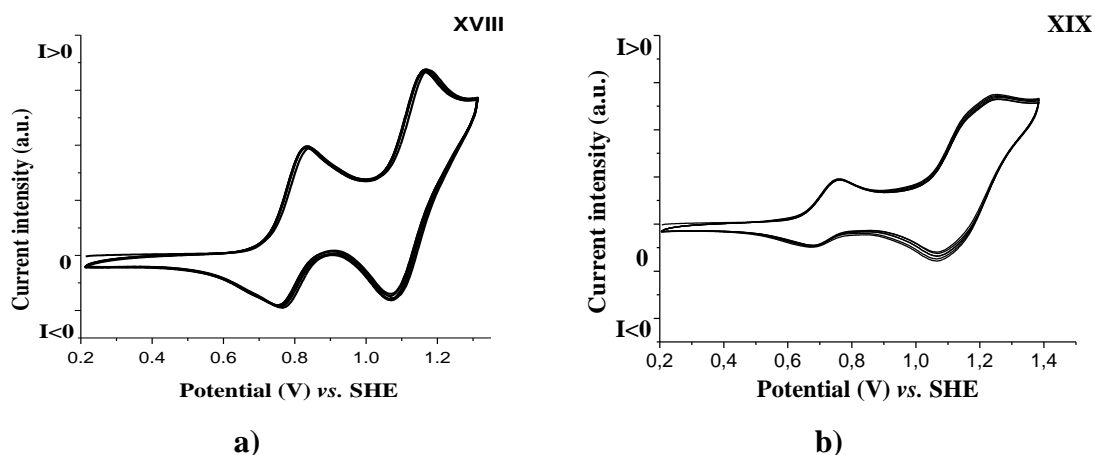


**Figure 8.6.** Cyclic voltammograms of **XVIII** (a) and **XIX** (b) obtained from six consecutive oxidation scans

We can conclude that for the triphenylamine moieties incorporated either onto the Schiff base (complex **XVIII**) or onto the cyclometallated ligand **btz-tpa** (complex **XIX**) the electropolymerization in both cases is prevented probably by the electronic factors induced by the nature of the ligands incorporated in the coordination sphere of the Ir(III) centre.

On the contrary, upon repetitive oxidation scans for complex **XX**, a distinctive increase in current is observed which is typical of the electropolymerization of the substituted triphenylamine fragment (Figure 8.7a).<sup>130</sup> Once the polymer formed, the modified Pt disk working electrode covered with the electropolymerized film of **XX** was immersed in a fresh distilled dichloromethane solution (0.1 M electrolytic solution) and a cyclic voltamogram was recorded (Figure 8.7b).

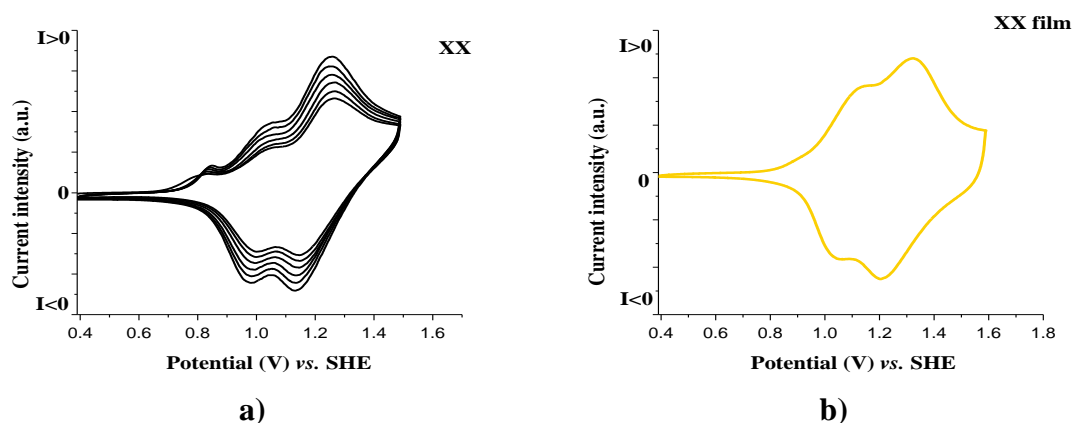


**Figure 8.7.** a) Cyclic voltammograms of **XX** obtained from six consecutive oxidation scans and b) cyclic voltammogram of the obtained modified Pt electrode

Electrogenerated thin films of **XX** were deposited on ITO etched glass substrates. Although these preliminary results sound very encouraging, further studies are necessary in order to identify the best experimental working conditions (solvent, temperature, concentration, scan rate, post treatments) in order to obtain high quality thin films. A cyclic voltamogram recorded upon electropolymerization of **XX** onto an ITO glass substrate is presented in Figure 8.8 together with the photography of the obtained deposited thin film.

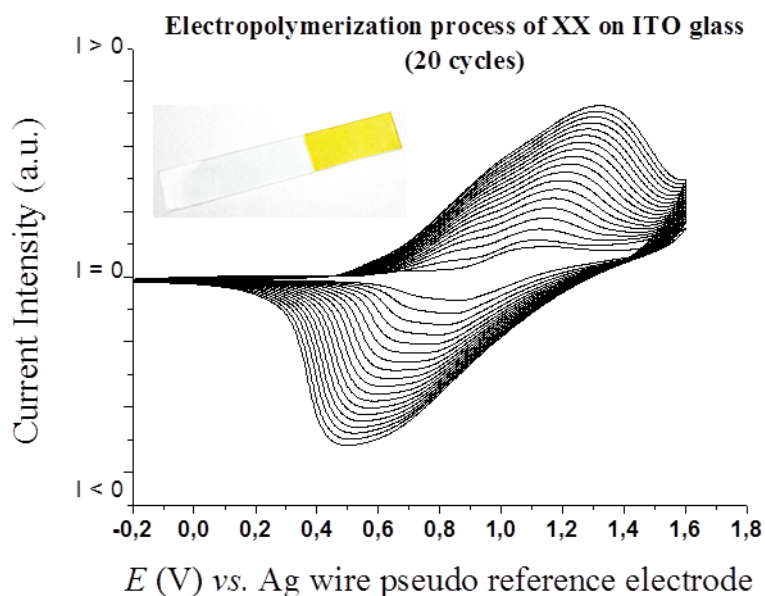
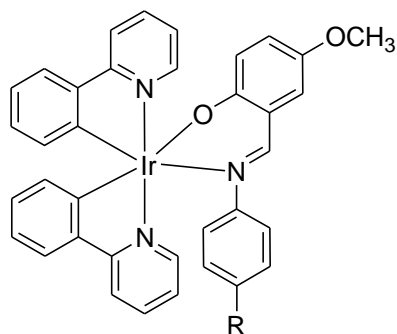


**Figure 8.8.** Electropolymerization of **XX** on ITO substrate (20 cycles)

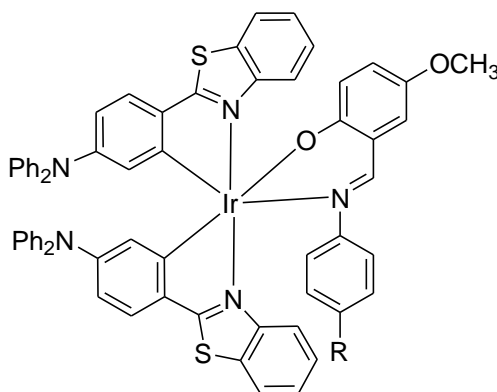
### 8.5 Preliminary photophysical studies

Photophysical investigations on the synthesised complexes **XVII-XX** in solution and of the electrogenerated thin films are in progress.

## 8.6 Conclusions



**XVII** : R = C<sub>6</sub>H<sub>13</sub>  
**XVIII** : R = C<sub>6</sub>H<sub>4</sub>NPh<sub>2</sub>



**XIX** : R = C<sub>6</sub>H<sub>13</sub>  
**XX** : R = C<sub>6</sub>H<sub>4</sub>NPh<sub>2</sub>

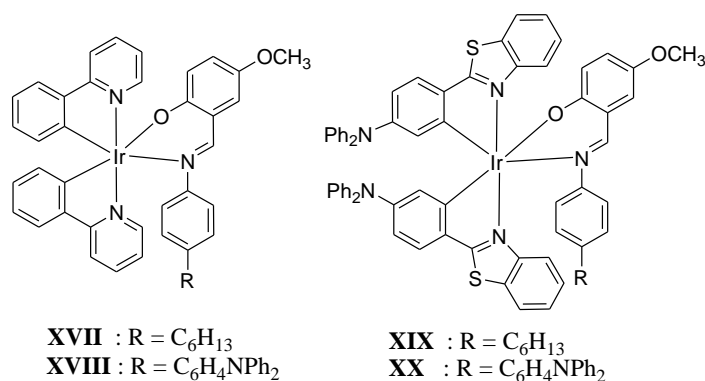
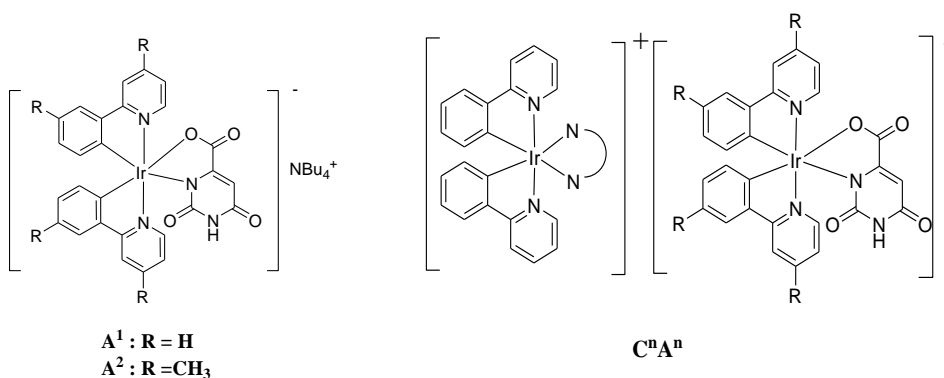
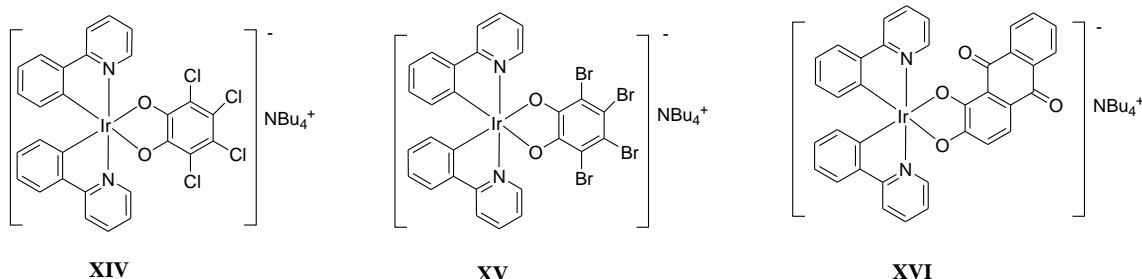
Novel bis-cyclometallated Ir(III) complexes have been synthesized by incorporating substituted Schiff bases. The model complexes **XVII-XVIII**, bear phenylpyridine as cyclometallated ligand, while a benzothiazole-triphenylamine derivative has been incorporated as a cyclometallated ligand into complexes **XIX-XX**. Furthermore, a complete electrochemical study has been performed on the complexes **XVII-XX**. It has been observed that electropolymerization of the triphenylamine fragment part of the Schiff base (complex **XVIII**) or involved into cyclometallation (complex **XIX**) is prevented by the nature of the ligands incorporated in the coordination sphere of this complexes. Instead, the introduction of the triphenylamine onto the Schiff base  $\text{H}(\text{O}^{\wedge}\text{N})^4$  moiety in the presence of the cyclometallated ligands **btz-tpa**, have favoured the electropolymerization process and have led to the electrogeneration of polymeric thin films of **XX**. The presence of the triphenylamine fragment onto the Schiff base represents thus a necessary condition in order for the electropolymerization to be verified. However, as demonstrated by the electrochemical study described, this condition is not sufficient since it did not lead to electropolymerization in the case of complexes **XVII-XVIII** bearing 2-phenylpyridine fragments as cyclometallated ligands, but only for the **btz-tpa** substituted complex **XX**. However, further studies are needed in order to evaluate the ideal electropolymerization conditions leading to high quality Ir(III) cyclometallated thin films suitable for a complete solid-state photophysical study. Moreover, photophysical investigations of the synthesized complexes in solution are in progress.



## Chapter Nine

### Conclusions

In this second part of the thesis, novel Ir(III) cyclometallated ionic and neutral complexes have been synthesized.



Anionic cyclometallated Ir(III) complexes with (O<sup>2-</sup>) and (O<sup>-</sup>N) type dianionic ancillary ligands have been successfully synthesised. The first series of anionic complexes is composed of catecholate containing Ir(III) anionic complexes with *ortho*-hydroquinone ligands (**XIV-XVI**). Photophysical characterizations have evidenced for complex **XVII** and especially for **XVIII** high sensitivity towards hydrolysis, while, noteworthy, complex **XVI** shows strong absorption extending up to 700 nm.

Furthermore, orotic acid has been successfully used as a dianionic bidentate ligand to obtain anionic green emitting complexes with high luminescent quantum yields (60-70%,  $\lambda_{em}$  ca. 530 nm), and thermally stable (until ca. 200°C) Ir(III) complexes. The introduction of this ancillary ligand might be a step toward the stabilisation of anionic Ir(III) complexes in LECs which until now have shown emission quenching and fast device degradation when monodentate ligand bearing complexes have been used as emitting species. Furthermore, we have demonstrated the possibility of using such anionic complexes in the formation of homometallic soft salts with enhanced luminescent properties showing up to 81–83% photoluminescent quantum yield ( $C^1A^1$  and  $C^1A^2$ ). Further test of the anionic luminescent complexes  $A^1$  and  $A^2$  in LECs and of the corresponding overall neutral soft salts in OLEDs is in progress.

Moreover, following the developed synthetic pathway leading to homometallic Ir(III) soft salts, cations of different metals and/or different geometries could be introduced to form heterometallic soft salts.

Furthermore, novel bis-cyclometallated Ir(III) neutral complexes have been synthesized by incorporating substituted Schiff bases. The model complexes **XVII-XVIII**, bear 2-phenylpyridine as cyclometallated ligand, while a benzothiazole-triphenylamine derivative has been incorporated as a cyclometallated ligand into complexes **XIX-XX**.

A complete electrochemical study has been performed on the complexes **XVII-XX**. The different results observed comparing **XVIII** with **XX** suggest that the capability to induce electropolymerization of the triphenylamine moiety of the Schiff base  $H(O^{\wedge}N)^4$  strongly depends on the electronic effects exerted by the cyclometallated ligands. Electrogenerated polymeric thin films of **XX** have been obtained.

However, further studies are needed in order to evaluate the ideal electropolymerization conditions leading to high quality Ir(III) cyclometallated thin films suitable for a complete solid-state photophysical study. Moreover, photophysical investigations of the synthesized complexes in solution is in progress.

## **Chapter Ten**

### **Experimental details**

#### **10.1 General equipment and procedures**

All commercially available chemicals were purchased from Aldrich Chemical Co. and were used without further purification. IR spectra (KBr pellets) were recorded on a Perkin-Elmer Spectrum One FT-IR spectrometer.  $^1\text{H-NMR}$  spectra were recorded on a Bruker WH-300 spectrometer in deuterated solvents with TMS as an internal standard. Elemental analyses were performed with a Perkin-Elmer 2400 analyzer CHNS/O. Conductivity measurements were performed in acetonitrile solutions with an InoLab Cond Level 1–720 conductometer equipped with a LR 325/001 immersion cell. The thermal stability was measured on a Perkin-Elmer Thermogravimetric Analyser Pyris 6 TGA, while phase transition temperatures and enthalpies were measured on a Perkin Elmer pyris 1 Differential Scanning Calorimeter. Melting points and mesophase textures were examined with a Leica DMLP polarising microscope equipped with a Leica DFC280 camera and a CalCTec (Italy) heating stage.

#### **X-Ray powder diffraction analysis**

The powder X-Ray diffraction patterns were obtained by using a Bruker AXS General Area Detector Diffraction System (D8Discover with GADDS) with Cu-K $\alpha$  radiation; the area detector was placed at a distance of 20 cm from the sample and at an angle  $2\theta$  of  $14^\circ$ . Measurements were performed by charging samples in Lindemann capillary tubes with inner diameters of 0.5 mm. A CalCTec (Italy) heating stage was used to heat the samples at a rate of  $5^\circ\text{C}/\text{min}$  to the appropriate temperature.

## X-ray single crystal analysis

The intensity data were collected on Bruker-Nonius X8 Apex CCD area detector single crystal diffractometer equipped with a graphite monochromator and MoK $\alpha$  radiation ( $\lambda=0.71073$  Å). Bruker SADABS software<sup>240a</sup> was used for the absorption correction. Structure was solved by Patterson methods (SHELX/L program in the SHELXTL-NT software package<sup>240b</sup>) and refined by full-matrix least-squares based on F2. All non-hydrogen atoms were refined anisotropically and hydrogen atoms were included as idealized atoms riding on the respective carbon atoms with C-H bond lengths appropriate to the characteristic of the carbon atom. The disordered carbon atoms of the alkylic chains were introduced isotropically in the refinement.

## Electrochemical studies

All potentials were measured using an Epsilon electrochemical analyser. Voltametry experiments were performed in a 3 mL cell of dry, and degassed (N<sub>2</sub>) solvent solution using tetrabutylammonium hexafluorophosphate (0.1 M) as a supporting electrolyte, a Pt disk working electrode, a Pt wire counter-electrode and an Ag wire as a pseudo-reference electrode. Voltammograms were recorded at a 100 mVs<sup>-1</sup> scan rate from *ca.* 10<sup>-3</sup> M complex solutions. Redox potentials are given relative to a ferrocene/ferrocenium (Fc/Fc<sup>+</sup>) redox couple used as an internal reference. Estimation of HOMO/LUMO energy values was performed taking into account -4.8 eV for the couple Fc/Fc<sup>+</sup>.<sup>241</sup>

## Molecular modelling

The **H(NR)** dimer structure was modelled and optimised in the gas phase using the Polak–Ribiere conjugate gradient method of the Hyperchem 7.51 programme (Hyperchem, Hypercube Inc., 1115 NW 4th street, Gainesville FL 32601, USA) following standard techniques.<sup>242</sup>



## Photoconductivity measurements

The substrates used to prepare the samples were obtained from Indium Tin Oxide (ITO) covered glass sheets (UNAXIS, 110 nm ITO thickness, sheet resistivity  $12 \Omega/\text{cm}^2$ ). A photolithographic process was applied in order to pattern the ITO in 2 mm wide stripes. Patterned glasses were again covered with positive photoresist and each ITO stripe was exposed to light through a 2 mm long slit with an opening of 5 mm or 10 mm. By choosing the right process parameters, it was possible to remove the ITO from the glass in the exposed region, obtaining two ITO electrodes with sharp edges, as shown in Figure 10.1. The span between the electrodes can be modulated by changing the slit width and the exposition time. Electrode separations in the 5–40 mm range were obtained. The last step of the process was the spin-coating of the material, dissolved in chloroform with a typical concentration of 10 mg/mL. The thickness of the materials and the spacing between the electrodes were measured by using a Dektak 8 profilometer from Veeco.



**Figure 10.1.** Side view of a sample (not in scale)

Samples were then used to perform photoconductivity measurement. Note that by using the geometry shown in Figure 10.1 and irradiating the sample from the top, light reaches the material under investigation directly, making it possible to perform photoconductivity experiments even at wavelengths below 350 nm, where ITO starts to absorb.

Photoconductivity experiments were performed by using either light from a Xe-Lamp/Monochromator system or from a He–Ne laser. To change the light intensity, a set of neutral density filters with different transmittance were used. The photocurrent  $i_{photo}$  was obtained from the difference between the dark and the light currents, measured using an electrometer (6517A from Keithley), also used to apply the electric field.

## Bulk heterojunction cell fabrication and testing

Photo-lithographically patterned ITO glasses (UNAXIS, 110 nm ITO thickness, sheet resistivity  $12 \Omega/\text{cm}^2$ ) were first cleaned in consecutive steps by using distilled water and soap, distilled water, acetone and isopropanol in an ultra-sonicator and were then dried overnight in a vacuum oven at  $90^\circ\text{C}$ . Clean substrates were exposed to air plasma (Diener Electronics, Model Femto) for 5 min. The glasses were then spin coated (CaLCTec instruments, Model Fr10KPA-HC) with a 20 nm layer of PEDOT:PSS (Clevios P VP 4081, H. C. Stark GmbH) at 5000 RPM. The PEDOT:PSS coated substrates were then heat treated at  $200^\circ\text{C}$  for 10 min on a hot plate to remove any residual solvent. The substrates were immediately transferred inside a nitrogen glove box to avoid any further absorption of water and oxygen by the PEDOT:PSS layer. Solutions of 1:PC<sub>61</sub>BM with weight ratios between 1:1 and 1:5 were prepared in chlorobenzene and mixed overnight in the dark. Active layers with thicknesses between 100 to 140 nm were spin-coated at different spinning rates. The samples were then transferred to a thermal evaporator (Kurt J. LESKER) attached to a glove box for the evaporation of the cathode, without exposing them to air. LiF and Al~1 nm and 200 nm thick, respectively, were then thermally evaporated at a base pressure of  $1.2 \times 10^{-7}$  mbar. The thicknesses of the different layers of the devices were measured by using a Dektak 8 surface profilometer. The active area of the sample was  $8.75 \text{ mm}^2$ .

Absorption measurements in solution were performed with a Perkin Elmer 900 UV-Vis spectrometer using normal incidence. Absorption on thin films were performed using a reflection technique. In this case, the incident light from a light source (Oriel, Model 66902) was first directed through a monochromator (Oriel, Model 74100) before reaching the sample at an angle of  $\sim 45^\circ$ . The reflected light was then collected using a power meter (Ophir, NOMA II). This experiment was repeated for a blank in order to calculate the absorption at different wavelengths.

Photoconductivity measurements were performed, using a He-Ne laser (Melles Griot) as a light source, with a Keithley 6517A source meter. For such measurements, two ITO substrates were glued together using spacers with thickness between 1.7 and  $5 \mu\text{m}$  and the samples were then filled by capillarity on a hot plate. Atomic Force Microscopy (AFM, Bruker Nanoscope IIIa) has been used in the tapping mode. A home-made set up allows to detect shifts in the phase angle of vibration when the

oscillating tip interacts with the sample surface. In this work, phase shift images are presented.

Current/voltage characteristics were measured (Keithley 2400 Source Meter) inside a N<sub>2</sub> glove box under simulated solar illumination (Sciencetech, Model SS150 solar simulator, AirMass 1.5G, 100 mW/cm<sup>2</sup>). The solar simulator intensity was tuned by using a calibrated Si photodiode (Hamamatsu S2386-44K).

### **Dye sensitized solar cells fabrication and testing**

Dye sensitized solar cells were produced via the following procedure. FTO glass (Hartford, TEC 15) was cleaned with Milli-RO water (In-house), DECON 90 (Decon), isopropanol (Fisher, LRG) and ethanol (Fisher, ARG). To prepare the photoanode, a blocking layer of TiO<sub>2</sub> was applied to the conducting side of the glass by spray pyrolysis on a hot plate at 400°C using a solution of 0.2M diisopropoxytitanium bis(acetylacetonate) (Aldrich) in isopropanol. A layer of TiO<sub>2</sub> nanoparticles was then deposited onto this substrate by the doctor blade technique. “Magic tape” (Scotch) was used to mark out a 1 cm wide strip on the glass, and TiO<sub>2</sub> paste (Dyesol, DSL 18NR-T) was applied. The film was then sintered at 500°C for 30 min (in air). Films were dyed by submerging in the dye solutions as described in Chapter 4.

To make the cathode, Pt metal was deposited onto clean FTO glass which had two 0.6 mm diameter holes drilled into it by dropping several drops of 5x10<sup>-3</sup>M Hexachloroplatinate (Aldrich, 99.995%) solution in isopropanol. This was then heated at 390°C for 15 mins. To assemble the cell, a hot-melt SURLYN (Solaronix, SX1170-25PF) gasket was used, and once the two sides were sealed together, a small quantity of electrolyte was introduced through the drilled holes. This consisted of 0.03 M I<sub>2</sub> (Aldrich, 99.999%), 2 M 3-propyl-1-methylimidazolium iodide (Merck), 0.1 M guanidine thiocyanate (Fluka, ≥99%) and 0.5 M tert-butylpyridine (Aldrich, 99%) in an acetonitrile:valeronitrile (Aldrich) solvent in the ratio 85:15.

Cells were then sealed under pressure on a hot plate (80 °C) with a small laboratory glass by means of a hot-melt SURLYN (Solaronix, SX1170-25PF) slide. I/V curves were measured using a TS Space Systems solar simulator equipped with a 200 W lamp and AM1.5 filter and calibrated against a Si reference cell (Fraunhofer ISE, RS-OD-4) to 1 sun illumination.

A part of the research performed at the University of Bath was effectuated onto new organic dyes in water based DSSCs.

Potential alternatives to the use of the redox couple  $\text{I}^-/\text{I}_3^-$  as an electrolyte in DSSCs have been reported.<sup>243</sup> Nevertheless, solubility is an important issue when considering the use of alternative redox mediators in DSSCs, since some redox active salts are not soluble in acetonitrile or in other organic solvents. In 2010, B. C. O'Regan *et al.*<sup>244</sup> introduced the use of water based electrolytes in DSSCs. Aqueous solutions present the advantages of non-toxicity, non-flammability, excellent solvation of many potential redox mediators and allow the use of a wider range of sealing materials otherwise non stable in the presence of organic solvents. However, the technology of the water based electrolyte DSSCs has still to be improved, since for a water based DSSC sensitized with N719 and using  $\text{I}^-/\text{I}_3^-$  as an electrolyte, a 2.4% efficiency was measured, lower than in the case of using an acetonitrile electrolyte solution.<sup>245</sup> Moreover, very few organic dyes have been used in water based electrolytes.

In this context, during the stage at the University of Bath, a new organic dye was tested in water based DSSCs. The molecular structure of **D35**, synthesised by the group of Hagfeldt is presented in Figure 10.2 and afforded a 8% efficiency in a standard DSSC cell.<sup>246</sup>

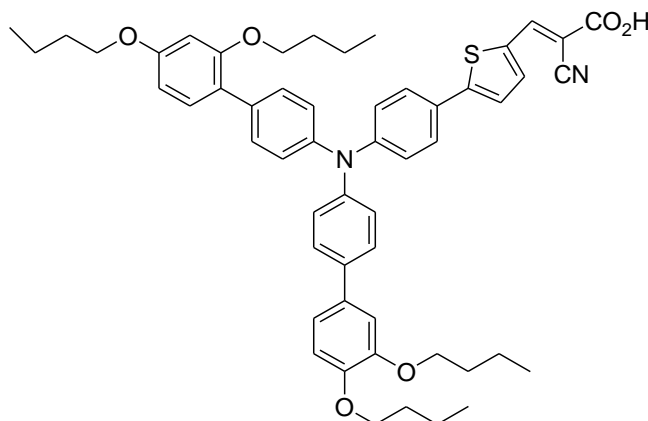


**Figure 10.2** Molecular structure of the **D35** dye

Adsorption tests were carried on the **D35** dye (Figure 10.3). Very thin (2  $\mu\text{m}$  thickness) single layer titania films were used to avoid aggregation and dyed from a  $3 \cdot 10^{-4}$  M acetonitrile/t-butanol bath. The absorbance of the dyed films is reported in function of the wavelength for different dyeing times. The results show how the adsorption increases with dyeing time, reaching very high values on such thin films for a relatively brief dyeing time (19 h.), due to the high dye absorption coefficient ( $30969 \text{ M}^{-1} \text{ cm}^{-1}$ ).

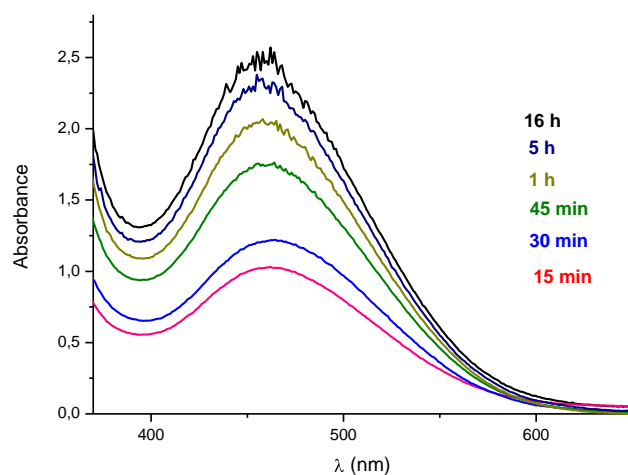


**Figure 10.3** Adsorption tests on the D35 dye

For each dyeing time, the dye adsorbed onto the film surface was desorbed in a known volume of 0.05 M KOH ethanol/acetonitrile:1/1 solution for 4 h. This experiment allowed to measure the concentration of the dye adsorbed by each film. Figure 10.4 shows the increase in adsorbed dye concentration in function of the dyeing time. The adsorbed concentration spans the range between  $10^{-6}$ - $10^5$  M.

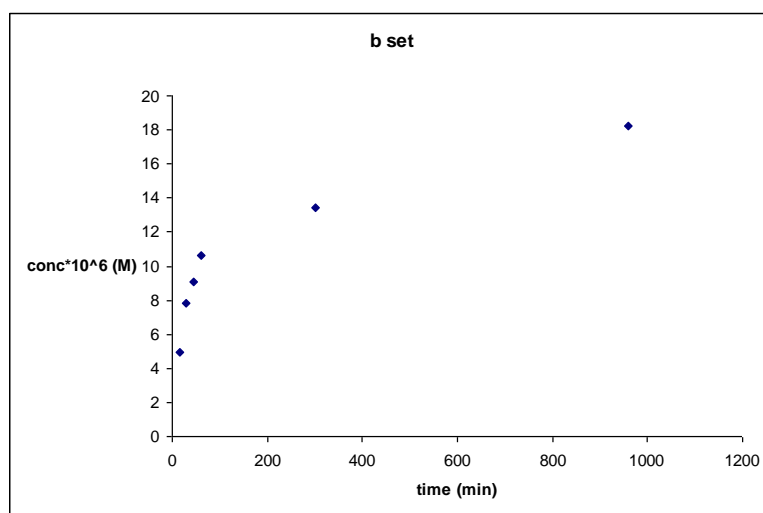


**Figure 10.4.** Concentration of the dye adsorbed by each film in function of the dyeing time

The current-voltage performances relative to the devices realized using the **D35** organic dye are reported in Table 10.1, while the I-V curves are reported in Figure 10.5. While the open circuit voltages  $V_{oc}$  are roughly constant with the dying time, the injection  $J_{sc}$  increases when going from 15 to 30 min. of dying time. Considering efficiency, the same trend is verified and relatively high efficiencies were measured for such water based cells.

	15 min	30 min	45 min	60 min	300 min	overnight
$V_{oc}$	0.72	0.77	0.77	0.80	0.80	0.76
$J_{sc}$	1.73	3.34	3.76	3.96	5.36	3.16
FF(%)	52	51	58	50	55	60
$\square$ (%)	0.64	1.22	1.18	1.22	1.26	1.24

**Table 10.1.** Characteristic performances of DSSCc based on **D35**

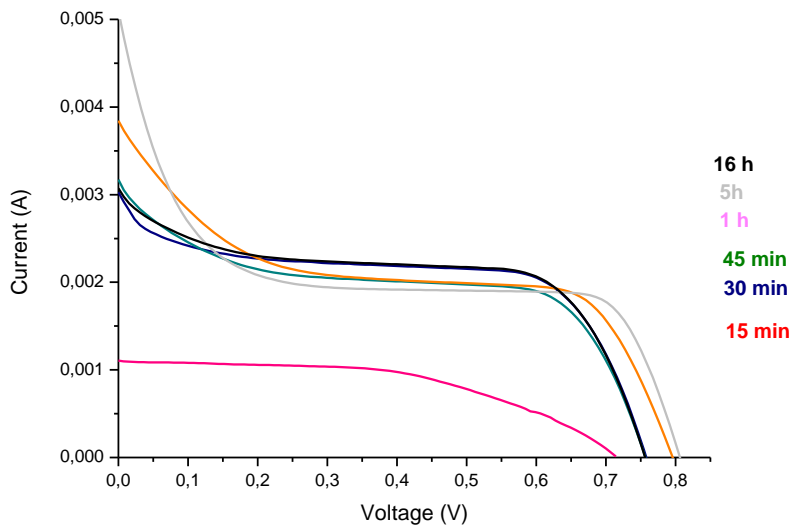


**Figure 10.5.** I-V curves of **D35** based DSSCc in function of the dying time

## Photophysical characterization

Spectrofluorimetric grade solvents (Acros Organics) were used for the photophysical investigations in solution. Absorption spectra were recorded with an UV-Vis Perkin-Elmer Lambda 900 spectrophotometer. The experimental uncertainty on the band maximum for absorption spectra is 2 nm. Steady-state emission spectra were recorded on a Horiba Jobin Yvon Fluorolog 3 spectrofluorimeter, equipped with a Hamamatsu R-928 photomultiplier tube.

## 10.2 Synthesis procedures

### 10.2.1 Synthesis of novel Pd(II) complexes and of their precursors

#### Synthesis of diethylamino-2-nitrosophenol (**3a**) and 5-diethylamino-2-nitrosophenol hydrochloride (**3b**).

3-Diethylaminophenol (12.02 g, 72.6 mmol) was dissolved in a mixture of 26 mL of HCl and 16 mL of distilled water. The obtained solution was cooled to 0 °C under stirring and an aqueous solution of NaNO<sub>2</sub> (5.01 g, 72.6 mmol) was added. The reaction mixture was stirred for 4 h at 0–5 °C. The precipitated solid was filtered, dried under vacuum and dissolved in hot ethanol (200 mL). After addition of diethylether (200 mL) and 24 h in the freezer, a mixture of **3a** and **3b** (in 1:2 molar ratio) was obtained.

Brown-yellow crystalline powder;

**3a** + **3b** <sup>1</sup>H NMR (300 MHz, DMSO, 25 °C, TMS): δ= 7.53 (d, J=10.65 Hz, 1H, 3b), 7.26 (d, J=10.3 Hz, 0.5H, 3a), 7.19 (dd, J=9.18 Hz, J=2.2 Hz, 1H, 3b), 6.83 (dd, J=10.1 Hz, J=2.4 Hz, 0.5H, 3a), 6.54 (d, J=2.6 Hz, 1H, 3b), 5.7 (d, J=2.6 Hz, 0.5H, 3a), 3.7–3.3 (m, 6H, 3a + 3b), 1.25 (t, J=7.3 Hz, 6H, 3b), 1.16 (t, J=7.4 Hz, 3H, 3a);

FT-IR (KBr, cm<sup>-1</sup>): 3424 (br), 2979, 2755, 1626, 1545, 1491, 1146, 1040, 857, 749.

#### Synthesis of H(NR).

1-Hydroxynaphthalene (1.00 g, 6.9 mmol) and the mixture **3a,b** (1.5 g, *ca.* 6.9 mmol) were dissolved in *ca.* 40 mL of dimethylformamide and the resulting solution heated at 70 °C for 8 h. The solvent was evaporated under reduced pressure and the crude solid purified by column chromatography (silica gel, dichloromethane/diethyl ether: 2/1).

Dark red solid; yield 23% (505 mg); m. p. 211°C;

$^1\text{H}$  NMR (300 MHz,  $\text{CDCl}_3$ , 25 °C, TMS):  $\delta$ = 8.66 (d,  $J$ =7.69, 1H), 8.32 (d,  $J$ =7.26, 1H), 7.74–7.59 (m, 3H), 6.66 (dd,  $J$ =5.5 Hz,  $J$ =2.15 Hz, 1H), 6.46–6.44 (m, 1H), 6.38 (s, 1H), 3.46 (q,  $J$ =6.1 Hz, 4H), 1.28 (t,  $J$ =11.9 Hz, 6H);

FT-IR (KBr,  $\text{cm}^{-1}$ ): 2964, 2935, 1624, 1584, 1555, 1403, 1306, 1255, 1111, 1020, 843, 778;

elemental analysis calculated for  $\text{C}_{20}\text{H}_{18}\text{N}_2\text{O}_2$  (318.14 g/mol): C 75.45%, H 5.70%, N 8.80%, found C 75.42%, H 5.73%, N 8.80%.

### Synthesis of **2**.

1,7-Dihydroxynaphthalene (1.243 g, 7.5 mmol) and the mixture of **3a,b** (1.580 g, ca. 7.1 mmol) were solubilized in ca. 40 mL of dimethylformamide and the resulting solution heated at 70 °C for 8 h. The solvent was evaporated under reduced pressure and the crude solid purified by column chromatography (silica gel, ethyl acetate/ethanol: 1/1).

Green solid; yield 53% (1.327 g); m. p. 250 °C;

$^1\text{H}$  NMR (300 MHz, DMSO, 25 °C, TMS):  $\delta$ = 10.38 (s, 1H), 8.57 (d,  $J$ =9 Hz, 1H), 8.40 (d,  $J$ =8.79 Hz, 1H), 7.43 (d,  $J$ =2.58 Hz, 1H), 7.21 (d,  $J$ =2.55 Hz, 1H), 7.18 (d,  $J$ =2.58 Hz, 1H), 6.51 (d,  $J$ =2.8 Hz, 1H), 6.02 (s, 1H), 3.44 (q,  $J$ =7 Hz, 4H), 1.28 (t,  $J$ =7.2 Hz, 6H);

FT-IR (KBr,  $\text{cm}^{-1}$ ): 3145 (br), 2971, 2920, 1635 (*Nile red* CO), 1584, 1559, 1328, 1114, 832, 518;

elemental analysis calculated for  $\text{C}_{20}\text{H}_{18}\text{N}_2\text{O}_3$  (334.13 g/mol): C 71.84%, H 5.43%, N 8.38%, found C 71.85%, H 5.43%, N 8.37%.

### Synthesis of **H(NR)**<sup>1</sup>.

**2** (276 mg, 0.83 mmol) was solubilized in 30 mL of dimethylformamide. To the obtained solution were added 1.5 eq. of  $\text{K}_2\text{CO}_3$  (171 mg, 1.25 mmol) and a catalytic amount of KI. The reaction mixture was stirred for 10 min and 1 eq. of **4**<sup>79</sup> (598 mg, 0.83 mmol) was added. The solution was heated at 130 °C for 8 h. The solvent was removed under reduced pressure and the product purified by column chromatography (silica gel, petroleum ether (b.p. 40–60 °C)/diethyl ether: 1/1).

Red solid; yield 53% (428 mg); m.p. 113 °C;

$^1\text{H}$  NMR (300 MHz,  $\text{CDCl}_3$ , 25 °C, TMS):  $\delta$ = 8.60 (d,  $J$ =8.8 Hz, 1H), 7.85 (d,  $J$ =2.5 Hz, 1H), 7.62 (d,  $J$ =9.1 Hz, 1H), 7.36 (dd,  $J$ =8.8 Hz,  $J$ =2.55 Hz, 1H), 6.71 (d,  $J$ =2.55 Hz,



1H), 6.67 (d, J=4.4 Hz, 2H), 6.51 (d, J=2.6 Hz, 1H), 6.42 (s, 1H), 5.11 (s, 2H), 3.97 (m, 6H), 3.48 (q, J=7 Hz, 4H), 1.82–1.47 (m, 60H), 1.20 (m, 6H), 0.9–0.85 (m, 9H);

FT-IR (KBr,  $\text{cm}^{-1}$ ): 2928, 2848, 1624 (*Nile red CO*), 1588, 1559, 1332, 1259, 1122, 844;

elemental analysis: calculated for  $\text{C}_{63}\text{H}_{96}\text{N}_2\text{O}_6$  (976.73 g/mol): C 77.41%, H 9.09%, N 2.87%, found C 77.40%, H 9.91%, N 2.90%.

### Synthesis of acetato-bridged intermediate complexes **1** and **1'**.

The intermediate complex **1'** was synthesized according to the previously reported procedure for **1**<sup>85</sup> with the following modifications:  $\text{H}(\text{NR})^1$  (187 mg, 0.2 mmol) was solubilized in 60 mL of acetic acid and 10 mL of dichloromethane. The resulting solution was heated at 55 °C for 6 d and filtered on Celite. The obtained solid was washed with acetonitrile.

Dark-blue solid; yield 75% (161 mg); m.p. 154 °C;

<sup>1</sup>H NMR (300 MHz,  $\text{CDCl}_3$ , 25 °C, TMS):  $\delta$ = 7.74 (d, J=9.5 Hz, 1H), 7.0 (d, J=2.5 Hz, 1H), 6.50 (s, 2H), 6.40 (d, J=1.8 Hz, 1H), 6.35 (dd, J=9.5 Hz, J=2.9 Hz, 1H), 6.21 (d, J=2.2 Hz, 1H), 6.03 (s, 1H), 4.69 (s, 2H), 4.1–3.8 (m, 6H), 3.3–3.1 (m, 4H), 2.31 (s, 3H), 1.9–1.6 (m, 6H), 1.5–1.4 (m, 6H), 1.4–1.1 (m, 54H), 0.9–0.8 (m, 9H);

FT-IR (KBr,  $\text{cm}^{-1}$ ): 2920, 2853, 1636 (*Nile red CO*), 1575, 1234, 1117, 1075, 720;

elemental analysis calculated for  $\text{C}_{130}\text{H}_{198}\text{N}_4\text{O}_{16}\text{Pd}_2$  (2283.29 g/mol): C 68.31%, H 8.73%, N 2.45%, found C 68.34%, H 8.70%, N 2.45%.

### Synthesis of complex **I**.

Intermediate **1** (100 mg, 0.10 mmol) and 1.5 eq. of  $\text{H}(\text{O}^{\wedge}\text{N})^1$ <sup>79</sup> (190 mg, 0.15 mmol) were solubilized in dichloromethane and ethanol and the reaction mixture was stirred at room temperature for 5 d. The solvent was removed under reduced pressure, and the resulting solid was washed with acetonitrile and precipitated from ethanol/dichloromethane, filtered and reprecipitated from diethyl ether/dichloromethane, filtered, washed with diethyl ether and with hot ethanol to yield a dark-blue solid.

Dark-blue waxy solid; yield 83% (211 mg);

<sup>1</sup>H NMR (300 MHz,  $\text{CDCl}_3$ , 25 °C, TMS):  $\delta$ = 9.35 (d, J=9.51 Hz, 1H), 7.98 (s, 1H), 7.66 (d, J=4.65 Hz, 1H), 7.41–7.39 (m, 1H), 7.38 (d, J=8.07 Hz, 1H), 6.89–6.87 (m, 1H), 6.58 (s, 2H), 6.51 (d, J=2.94 Hz, 1H), 6.36 (s, 1H), 6.28 (s, 1H), 6.23 (d, J=8.07

Hz, 1H), 4.90 (s, 1H), 4.0–3.9 (m, 10H), 3.52 (q, J= 6.72 Hz, 4H), 1.9–1.7 (m, 10H), 1.6–1.2 (m, 96H), 0.95–0.81 (m, 15H);

FT-IR (KBr,  $\text{cm}^{-1}$ ): 2920, 2853, 1635 (*Nile red CO*), 1624, 1580, 1234, 1118, 1075, 720;

elemental analysis calculated for  $\text{C}_{100}\text{H}_{153}\text{N}_3\text{O}_9\text{Pd}$  (1646.06 g/mol): C 72.89%, H 9.36%, N 2.55%, found C 72.90%, H 9.38%, N 2.56%.

### Synthesis of complex II.

Intermediate **1'** (161 mg, 0.07 mmol) and 2 eq. of  $\text{H}(\text{O}^{\wedge}\text{N})^{179}$  (176 mg, 0.14 mmol) were dissolved in 30 mL of dichloromethane and 10 mL of ethanol. The reaction mixture was stirred at r.t. for 5 d. The solvent was removed under reduced pressure and the resulting solid was filtered and washed with hot ethanol, immediately filtered on a cotton filter and dissolved in dichloromethane.

Dark-blue waxy solid; yield 67% (222 mg);

$^1\text{H}$  NMR (300 MHz,  $\text{CDCl}_3$ , 25°C, TMS):  $\delta$ = 9.28 (d, J=9.54 Hz, 1H), 7.94 (s, 1H), 7.55–7.39 (m, 2H), 7.04–6.78 (m, 4H), 6.7–6.4 (m, 6H), 6.36 (s, 1H), 6.26 (s, 1H), 5.92 (s, 1H), 4.85 (s, 2H), 4.47 (s, 2H), 4.12– 3.71 (m, 16H), 3.5–3.6 (m, 4H), 2.2–1 (m, 190H), 0.1–0.8 (m, 15H);

FT-IR (KBr,  $\text{cm}^{-1}$ ): 2913, 2852, 1624 (*Nile red CO*), 1581, 1234, 1117, 720;

elemental analysis calculated for  $\text{C}_{143}\text{H}_{231}\text{N}_3\text{O}_{13}\text{Pd}$  (2304.65 g/mol): C 74.64%, H 10.09%, N 1.82%, found C 74.61%, H 10.12%, N 1.62%.

### Synthesis of chloro-bridged intermediate complex 1''.

To a suspension of **1** (246 mg, 0.255 mmol) in 22 ml ethanol/water: (10/1 v/v) were added 20 eqs. of LiCl (216 mg, 5.096 mmol) and the obtained solution was stirred at room temperature and dark conditions for 5 d. The precipitate was filtered, washed with water and dichloromethane, and dried under vacuum.

Black solid; yield 96% (230 mg); m.p. >250°C;

FT-IR (KBr,  $\text{cm}^{-1}$ ): 2972, 2937, 2904, 2866, 2689, 1776, 1636 (*Nile red CO*), 1617, 1575, 1544, 1524, 1490, 1403, 1352, 1305, 1279, 1352, 1305, 1279, 1247, 1183, 1123, 1091, 1075, 1019, 953, 853, 797, 769, 716, 697, 650, 517, 507;

elemental analysis calculated for  $\text{C}_{40}\text{O}_4\text{N}_4\text{H}_{34}\text{PdCl}_2$  (918.48): C 52.31%, H 3.73%, N 6.10%, found C 52.33%, H 3.70%, N 6.12%.

### Synthesis of complex III.

To a suspension of **1''** (55 mg, 0.05 mmol) in 10 mL of acetone were added 2 eqs. (31 mg, 0.10 mmol) of AgOTf. The blue solution obtained was stirred at reflux for 2 h and at r. t. overnight. The AgCl precipitated was filtered off and to the resulting solution 2 eqs. (50 mg, 0.11 mmol) of H(C<sub>2,9</sub>-bipy) (Sigma Aldrich) were added. The mixture was stirred at reflux for 6 h and at room temperature overnight. The solvent was evaporated under reduced pressure and the final complex was recrystallized from dichloromethane/heptane.

Dark-blue solid; yield 40% (39 mg); m.p.: 180°C;

<sup>1</sup>H-NMR (300 MHz, CDCl<sub>3</sub>, 25°C, TMS): δ= 8.6–8.5 (m, 2H), 8.30 (s, 1H), 8.15 (s, 1H), 7.77–7.75 (m, 1H), 7.65–7.48 (m, 4H), 7.42–7.39 (m, 1H), 6.75–6.71 (m, 1H), 6.55 (s, 1H), 6.19 (s, 1H), 3.53 (q, 6.6 Hz, 4H), 2.86 (m, 4H), 1.72 (m, 4H), 1.26 (m, 30 H), 0.87 (t, 6.24 Hz, 6H);

FT-IR (KBr, cm<sup>-1</sup>): 3059, 2926 (*alkyl stretching*), 1635 (*Nile red CO*), 1615, 1581, 1493, 1462, 1409, 1379, 1355, 1276, 1257 (OTf), 1221, 1158, 1120, 1030 (OTf), 803, 716, 638 (OTf), 589, 573, 519, 491, 450;

elemental analysis calculated for C<sub>49</sub>N<sub>4</sub>O<sub>5</sub>H<sub>61</sub>PdF<sub>3</sub>S (981.63): C 59.96%, H 6.26%, N 5.71%, F 5.81%, found C 59.90%, H 6.30%, N 5.73%, F 5.78%.

### Synthesis of complex IV.

Complex **IV** was synthesised following the same procedure reported for **III**, using the corresponding **H(C<sub>6,12</sub>-bipy)** bipyridine ligand.<sup>102</sup> Purification of the crude solid was performed by successive precipitations in acetone/methanol solutions (freezer) and filtrations of the non reacted bipyridine ligand to obtain **IV** as a waxy solid.

Blue waxy solid; yield 40%; m.p. 160°C;

<sup>1</sup>H-NMR (300 MHz, CDCl<sub>3</sub>, 25°C, TMS): δ= 8.9–8.7 (m, 2H), 8.45 (s, 1H), 8.35 (s, 1H), 8.0–7.9 (m, 1H), 7.8–7.5 (m, 4H), 7.4–7.3 (m, 6H), 6.75 (s, 1H), 6.55 (s, 1H), 5.6 (s, 4H), 4.05 (m, 16H), 3.65 (m, 4H), 1.8 (m, 12H), 1.4–0.9 (m, 114 H), 0.9–0.5 (m, 18H);

FT-IR (KBr, cm<sup>-1</sup>): 2924, 2853 (*alkyl stretching*), 1718 (CO), 1635 (*Nile red CO*), 1615, 1583, 1495, 1466, 1429, 1335, 1256 (OTf), 1160, 1118, 1030 (OTf), 848, 765, 720, 638 (OTf);

elemental analysis calculated for C<sub>75</sub>N<sub>4</sub>O<sub>8</sub>H<sub>102</sub>PdF<sub>3</sub>S (1899.89 g/mol): C 47.41%, H 5.41%, N 2.95%, F 2.99%, found C 47.43%, H 5.39%, N 2.97%, F 3.0%.

### Synthesis of complex V.

**H(NR)<sup>2</sup>** (100 mg, 0.3 mmol) was solubilised in dry tetrahydrofuran under nitrogen at -78 °C and 1.2 eqs. of buthyl lithium 1.6 M hexane solution (0.36 mmol, 0.22 mL). The mixture was stirred at -78 °C for 15 min and afterwards 0.5 eqs. of precursor **1** were added (144 mg, 0.15 mmol). The solution was allowed to warm up to room temperature and stirred under nitrogen overnight. The solvent was evaporated under reduced pressure and ethanol was added. A black solid was filtered off, washed with ethanol and dried under vacuum.

Black solid; yield 30% (68 mg); m.p.>250°C

<sup>1</sup>H NMR (300 MHz, CDCl<sub>3</sub>, 25 °C, TMS): δ= 9.53 (d, J= 9.33 Hz, 1H), 8.01 (d, J=8.79 Hz, 1H), 7.66 (d, J=7.68 Hz, 1H), 7.35-7.32 (m, 2H), 7.25 (d, J=2.1 Hz, 1H), 6.98 (t, J=7.56 Hz, 1H), 6.69 (dd, J=9.27 Hz, J=2.46 Hz, 1H), 6.47 (d, J=2.61 Hz, 1H), 6.39 (d, J=8.37 Hz, 1H), 6.27 (s, 1H), 6.19-6.16 (m, 2H), 6.13 (d, J=2.5 Hz, 1H), 3.51 (q, J=6.87 Hz, 4H), 3.32 (q, J=6.99 Hz, 4H), 1.27 (t, J=7.30 Hz, 6H), 1.16 (t, J=7.14 Hz, 6H);

FT-IR (KBr, cm<sup>-1</sup>): 2966, 2919, 2849, 1692 (*Nile red CO*), 1619 (*Nile red CO*), 1581, 1549, 1352, 1116, 802;

elemental analysis calculated for C<sub>40</sub>H<sub>34</sub>N<sub>4</sub>O<sub>5</sub>Pd (757.14 g/mol): C 63.45%, H 4.53%, N 7.40%, found C 63.55%, H 4.71%, N 7.32%.

### Synthesis of the Schiff base H(O<sup>^</sup>N)<sup>2</sup>.

4,5-bis(dodecyloxy)-2-hydroxybenzaldehyde,<sup>79</sup> (1 g, 2 mmol) and 4-dodecilaniline (0.523 g, 2 mmol) were refluxed in ethanol (50 mL) for 3h. Upon cooling in an ice bath, a bright yellow precipitate was formed, which was filtered, washed with cold ethanol and dried under vacuum to afford the Schiff base.

Yellow crystalline solid; yield: 50% (741 mg); m.p. 45°C;

<sup>1</sup>H NMR (300 MHz, CDCl<sub>3</sub>, 25°C, TMS): δ= 13.67 (s,1H) 8.45 (s, Ha) 7.21–7.14 (m, 4H) 6.82 (s, 1H) 6.48 (s, 1H) 4.01 (t, J=7 Hz, 2H) 3.93 (t, J=7 Hz, 2H) 2.60 (t, J=8.5 Hz, 2H) 1.89–1.73 (m, 4H) 1.25–1.27 (m, 60H) 0.89–0.84 (m, 9H);

elemental analysis calculated for C<sub>49</sub>H<sub>83</sub>NO (702.15 g/mol): C 83.81%, H 11.91%, N 1.99%, found C 83.93%, H 11.89%, N 2.02%.

### Synthesis of complex VI.

To a solution of **1** (50 mg, 0.05 mmol) in 20 mL ethanol/dichloromethane (1/1 v/v),  $\text{H}(\text{O}^-\text{N})^2$  (70 mg, 0.1 mmol) was added. The resulting mixture was refluxed overnight and left under stirring at room temperature for 24 h. The solvent was evaporated and the resulting dark solid was recrystallized in dichloromethane/methanol to afford **VI**.

Black solid; yield 91% (102 mg); m.p. 190°C;

$^1\text{H}$  NMR (300 MHz,  $\text{CDCl}_3$ , 25°C, TMS):  $\delta$ = 9.33 (d,  $J$  = 9.6 Hz, 1H) 7.97 (s, 1H) 7.63–7.59 (m, 2H) 7.33 (s, 1H) 7.20 (s, 1H) 7.15 (s, 1H) 7.12 (s, 1H) 6.81 (t,  $J$  = 7.8 Hz, 1H) 6.67–6.69 (m, 2H) 6.50 (d,  $J$  = 2.7 Hz, 1H) 6.38 (s, 1H) 6.27 (s, 1H) 6.10 (d,  $J$  = 7.2, 1H) 4.01 (t,  $J$  = 7.5, 2H) 3.90 (t,  $J$  = 7.5 Hz, 2H) 3.55–3.48 (m, 4H) 2.62 (t,  $J$  = 7.6 Hz, 2H) 1.84–1.750 (m, 4H) 1.6–1.1 (m, 60 H) 0.88–0.87 (m, 15H);

FT-IR (KBr,  $\text{cm}^{-1}$ ): 3449, 2906, 2847, 1700, 1635, 1613, 1580, 1548, 1505, 1403, 1353, 1302, 1281, 1252, 1237, 1212, 1093, 1024, 843, 829, 800, 771, 717, 666;

Elemental analysis calculated for  $\text{C}_{69}\text{H}_{99}\text{N}_3\text{O}_3\text{Pd}$  (1124.93 g/mol): C 73.67%, H 8.87%, N 3.74%, found, C 73.81%, H 8.90%, N 3.73%.

**Synthesis of intermediate complex 1'''. 1** (123 mg, 0.12 mmol) was solubilised in 12 mL of acetone and 9 mL of water. An excess (14 eqs.) of NaOH (71 mg, 1.8 mmol) in pellets was added and the reaction mixture stirred at r.t. for 24 h. The solution was neutralised with an HCl (*ca.*  $10^{-3}$  M) aqueous solution until neutrality was verified with a pH paper. The black solid precipitated was centrifuged, washed with distilled water and acetone and dried in an oven overnight.

Black solid; yield 85% (95 mg); m.p. >250 °C;

$^1\text{H}$ -NMR (300 MHz,  $\text{CDCl}_3$ , 25 °C, TMS)  $\delta$ = 7.73 (d,  $J$ =7.68 Hz, 2H), 6.83 (m, 2H), 6.36 (m, 2H), 6.16 (m, 2H), 5.45 (s, 2H), 5.22 (s, 2H), 4.75 (s, *br.*, 2H), 3.01 (q,  $J$ =7 Hz, 8H), 1.00 (t,  $J$ = 7.2 Hz, 12H);

FT-IR (KBr,  $\text{cm}^{-1}$ ): 3436, 2963, 2925, 2855, 1637 (C=O), 1618, 1580, 1549, 1406, 1279, 1119, 1094, 1019, 978;

Elemental analysis calculated for  $\text{C}_{40}\text{H}_{36}\text{N}_4\text{O}_6\text{Pd}_2$  (881.58 g/mol): C 54.50%, H 4.12%, N 6.36%, found: C 54.20%, H 4.31%, N 6.36%.

### Synthesis of the Schiff base H(O<sup>-</sup>N)<sup>3</sup>.

To an ethanol solution of hexylaniline (425 mg, 2.40 mmol), 5-methoxy-2-hydroxybenzaldehyde **8** (372 mg, 2.40 mmol) is added and the reaction mixture is refluxed for 3 h. An orange solid precipitated after 12 h at -4 °C. The product was filtered off and washed with cold ethanol.

Orange solid; yield 70% (523 mg) ; m.p. 165-166 °C;

<sup>1</sup>H-NMR (300 MHz, CDCl<sub>3</sub>, 25 °C, TMS) δ= 12.93 (s, 1H), 8.59 (s, 1H), 7.26 (m, 3H), 6.98-6.89 (m, 3H), 3.81 (s, 3H), 2.63 (t, J=7.71 Hz, 2H), 1.63-1.57 (m, 3H), 1.31 (m, 6H), 0.89 (t, J=7.14 Hz, 3H);

FT-IR (KBr, cm<sup>-1</sup>): 3400 (*br.*), 3014 (*alkyl stretching*), 2950, 1323;

Elemental analysis calculated for C<sub>20</sub>H<sub>25</sub>NO<sub>2</sub> (311.42 g/mol): C 77.14%, H 8.09%, N 4.50%, found: C 77.20%, H 8.11%, N 4.55%.

### Synthesis of intermediate 6

N,N-diphenylphenyl boronic acid (2.01 g, 6.95 mmol) and *p*-nitrobromobenzene **5** (1.40 g, 6.93 mmol) are solubilised in 60 mL of a degassed solution of toluene/ethanol:5/1. 15 mL of a degassed 2 M aqueous solution of Na<sub>2</sub>CO<sub>3</sub> and Pd(PPh<sub>3</sub>)<sub>4</sub> (0.160 g, 0.14 mmol) are added. The reaction mixture is stirred at r.t. under N<sub>2</sub> for 24 h. The organic phase was extracted with dichloromethane, dried with MgSO<sub>4</sub>, filtered and, eventually, the solvent evaporated. The crude product was purified by column chromatography (silica gel, petroleum ether /dichloromethane :6/4).

Orange solid; yield 93% (2.350 g); m.p. 158-160 °C;

<sup>1</sup>H-NMR (300 MHz, CDCl<sub>3</sub>, 25°C, TMS): δ= 8.27(d, J=9.91 Hz, 2H), 7.69 (d, J=9.06 Hz, 2H); 7.49 (d,J=8.79 Hz, 2H), 7.32-7.27 (m, 4H), 7.15-7.12 (m, 6H), 7.06 (t, J=1.23 Hz, 2H);

FT-IR (KBr, cm<sup>-1</sup>): 3060, 1587, 1484 (*stretching NO<sub>2</sub>*), 1317;

Elemental analysis calculated for C<sub>18</sub>H<sub>14</sub>NO<sub>2</sub> (290,32 g/mol): C 74.47%, H 4.86%, N 9.65%, found: C 74.58%, H 4.91%, N 9.69%.

### Synthesis of intermediate 7

To 80 mL of a dichloromethane solution of intermediate **6** (2.2 g, 6.00 mmol), 80 mL of a methanol solution of NiCl<sub>2</sub>·6H<sub>2</sub>O (1 g, 13.2 mmol) is added. To the obtained solution, NaBH<sub>4</sub> (1.0 g, 26 mmol) is added slowly and under vigorous stirring. A black suspension is filtered off on a Celite column with ethyl acetate as an eluent. Part of the

solvent is evaporated and a saturated aqueous solution of  $\text{Na}_2\text{CO}_3$  is added. The organic phase is extracted with ethyl acetate and dried with  $\text{MgSO}_4$ . The crude product is purified by column chromatography (petroleum ether/dichloromethane:1/1).

Brown-yellow solid; yield 82% (1.659 g) ; m.p. 180-181 °C;

$^1\text{H-NMR}$  (300 MHz,  $\text{CDCl}_3$ , 25°C, TMS):  $\delta$ = 7.44 (d,  $J$ =8.79 Hz, 2H), 7.31-7.24 (m, 8H); 7.02-6.95 (m, 8H) 6.59 (d, $J$ =8.49 Hz, 2H), 5.17 (s, 2H);

FT-IR (KBr,  $\text{cm}^{-1}$ ): 3466, 1593, 1317;

Elemental analysis calculated for  $\text{C}_{18}\text{H}_{16}\text{N}_2$  (260,13 g/mol): C 83.04%, H 6.19%, N 10.76%, found: C 83.10%, H 6.39%, N 10.87%.

#### Synthesis of the Schiff base $\text{H}(\text{O}^{\wedge}\text{N})^4$ .

To a ethanol solution of intermediate **7** (806 mg, 2.40 mmol), 5-methoxy-2-hydroxybenzaldehyde **8** (372 mg, 2.40 mmol) is added and the reaction mixture is refluxed for 3 h. An orange solid precipitated after 12 h at -4 °C. The product was filtered off and washed with cold ethanol.

Orange solid; yield 94% (1.064 g) ; m.p. 165-166 °C;

$^1\text{H-NMR}$  (300 MHz,  $\text{CDCl}_3$ , 25°C, TMS):  $\delta$ =12.86 (s, 1H), 8.65 (s, 1H,  $H_i$ ), 7.63 (d,  $J$ =7.63 Hz, 1H), 7.49 (d,  $J$ =9.06 Hz, 1H), 7.35 (d,  $J$ =8.52 Hz, 2H), 7.30 (s, 1H), 7.28-7.26 (m, 5H), 7.16-7.12 (m, 6H), 7.04 (t,  $J$ =7.11 Hz, 3H), 6.99-6.95 (m, 3H), 6.91 (d,  $J$ =2.61 Hz, 2H), 3.82 (s, 3H);

FT-IR (KBr,  $\text{cm}^{-1}$ ): 3400 (*br.*), 3014 (*alkyl stretching*), 2950, 1323.

Elemental analysis calculated for  $\text{C}_{32}\text{H}_{26}\text{N}_2\text{O}_2$  (470,56 g/mol): C 81.68%, H 5.57%, N 5.95%, found: C 81.72%, H 5.60%, N 6.17%.

**Synthesis of complex VII. 1''''** (60 mg, 0.07 mmol) was solubilized in dichloromethane and ethanol (*ca.* 50 mL) and 2 eqs. of  $\text{H}(\text{O}^{\wedge}\text{N})^3$  (43 mg, 0.14 mmol) were added. The reaction mixture was stirred at r.t. for 7 d. The solution was concentrated and the final product was obtained by precipitation from ethanol.

Dark blue solid; yield 85% (85 mg); m.p. >250 °C;

$^1\text{H-NMR}$  (300 MHz,  $\text{CDCl}_3$ , 25 °C, TMS)  $\delta$ = 9.53 (d,  $J$ =9.06 Hz, 1H), 8.11 (s, 1H), 7.62 (t,  $J$ =10.11 Hz, 3 H), 7.15 (d,  $J$ =8.1 Hz, 2H), 7.10-6.89 (m, 2H), 6.85-6.66 (m, 3H), 6.48 (d,  $J$ =1.8 Hz, 1H), 6.27 (s, 1H), 6.11 (d,  $J$ =7.08 Hz, 1H), 3.77 (s, 3H), 3.50 (q,  $J$ =7.14 Hz, 4H), 2.66-2.60 (m, 2H), 1.7-1.5 (m, 6H), 1.4-1.2 (m, 8H), 0.87-0.83 (m, 3H);

FT-IR (KBr,  $\text{cm}^{-1}$ ): 3056, 2965, 2925, 2852, 1637, 1615, 1583, 1548, 1515, 1460, 1404, 1352, 1303, 1278, 1120, 815;

Elemental analysis calculated for  $\text{C}_{40}\text{H}_{41}\text{N}_3\text{O}_4\text{Pd}$  (734.19 g/mol): C 65.44%, H 5.63%, N 5.72%, found: C 65.40%, H 5.31%, N 6.00%.

**Synthesis of complex VIII.** Complex **VIII** was synthesised following the same procedure as **VII** with the subsequent modifications: **1'''** (100 mg, 0.11 mmol) was treated with  $\text{H}(\text{O}^-\text{N})^4$  (107 mg, 0.22 mmol).

Dark blue solid, yield 60 % (118 mg); m.p.  $>250\text{ }^\circ\text{C}$ ;

$^1\text{H-NMR}$  (300 MHz,  $\text{CDCl}_3$ ,  $25\text{ }^\circ\text{C}$ , TMS)  $\delta$ = 9.55 (d,  $J=9.48\text{ Hz}$ , 1H), 8.14 (s, 1H), 7.81-7.80 (m, 2 H), 7.61 (d,  $J=7.56\text{ Hz}$ , 1H), 7.56 (d,  $J=8.49\text{ Hz}$ , 2H), 7.49 (d,  $J=8.76\text{ Hz}$ , 2H), 7.31-7.28 (m, 2H), 7.27 (s, 1H), 7.16-7.14 (m, 6H), 7.08-7.02 (m, 3H), 6.94-6.91 (m, 1H), 6.82 (t,  $J=8.58\text{ Hz}$ , 1H), 6.71-6.70 (m, 2H), 6.48 (d,  $J=2.76$ , 1H), 6.27-6.24 (m, 2H), 3.79 (s, 3H), 3.51 (q,  $J=7.15\text{ Hz}$ , 4H), 1.30 (t,  $J=6.99\text{ Hz}$ , 6H);

FT-IR (KBr,  $\text{cm}^{-1}$ ): 3057, 3036, 2964, 2923, 1638, 1619, 1588, 1548, 1522, 1490, 1406, 1277, 1119, 1021, 819, 694;

Elemental analysis calculated for  $\text{C}_{52}\text{H}_{42}\text{N}_4\text{O}_4\text{Pd}$  (893.33g/mol): C 69.91%, H 4.74%, N 6.27%, found: C 69.95%, H 4.54%, N 6.30%.

### Synthesis of intermediate 9.

4-(Bromomethyl)benzoic acid (1.598 g, 7.43 mmol) was solubilized in methanol. Catalytic  $\text{H}_2\text{SO}_4$  was added and the reaction mixture was stirred at r. t. overnight. The solvent was evaporated under reduced pressure and the resulting solid was dried under vacuum.

White solid; yield 95% (1.10 g); m.p.  $50\text{-}52\text{ }^\circ\text{C}$ ;

$^1\text{H NMR}$  (300 MHz,  $\text{CDCl}_3$ ,  $25\text{ }^\circ\text{C}$ , TMS)  $\delta$ = 8.011 (d,  $J= 7.02\text{ Hz}$ , 2H), 7.459 (d,  $J= 6.73\text{ Hz}$ , 2H), 4.499 (s, 2H), 3.918 (s, 3H);

FT-IR (KBr,  $\text{cm}^{-1}$ ): 3017, 2960 (*alkyl stretching*), 1936, 1815, 1722 (*ester C=O*), 1613, 1574, 1433, 1413, 1312, 1281, 1227, 1199, 1110, 1090, 1118, 953, 857, 841, 798, 769, 703, 636, 624, 602 (C-Br), 490 472;

Elemental analysis calculated for  $\text{C}_9\text{H}_9\text{O}_2\text{Br}$  (229.06 g/mol): C 47.19%, H 3.96%, found: C 47.22%, H 3.93%.



### Synthesis of H(NR)<sup>3</sup>.

**2** (250 mg, 0.7 mmol) was solubilized in *ca.* 50 mL of dimethylformamide. K<sub>2</sub>CO<sub>3</sub> (124 mg, 0.9 mmol) and catalytic KI were added to the reaction mixture which was stirred for 10 min. Intermediate **9** (205 mg, 0.9 mmol) was added and the solution was refluxed for 5 h and subsequently stirred for 5 d. The solvent was evaporated under reduce pressure and the crude product was purified by silica chromatography (dichloromethane :diethyl etehr|1:1).

Dark red solid; yield 45% (164 mg), m.p. 175-180°C;

<sup>1</sup>H NMR (300 MHz, CDCl<sub>3</sub>, 25 °C, TMS) δ= 8.6 (d, J=8.8Hz, 1H), 8.05 (d, J=8Hz, 2H), 7.83 (d, J=2.6Hz, 1H), 7.61 (d, J=9.2Hz, 1H), 7.50 (d, J=8Hz, 2H), 7.36 (dd, J=8.8Hz, J=2.9Hz, 1H), 6.69 (dd, J=9.5Hz, J=2.55Hz, 1H), 6.50 (d, J=2.6Hz, 1H), 6.40 (s, 1H), 5.29 (s, 2H), 3.93 (s, 3H), 3.47 (q, J=7.1Hz, 4H), 1.26 (t, J=7Hz, 6H);

FT-IR (KBr, cm<sup>-1</sup>): 2926 (alkyl C-H), 1721 (ester C=O), 1622, 1493, 1406, 1342 (aromatic C-N), 1279 (eter C-O), 1119, 1068, 1017, 836, 753;

Elemental analysis calculated for C<sub>29</sub>H<sub>26</sub>N<sub>2</sub>O<sub>5</sub> (482.51 g/mol): C 72.19%, H 5.43%, N 5.80%, found: C 72.21%, H 5.46%, N 5.83%.

### Synthesis of intermediate 10.

To a dry dichloromethane solution of diethyl-5-(hydroxymethyl)-isophtalate (2,5 g; 9,9 mmol) at 0 °C, 1.5 eqs. of PBr<sub>3</sub> were added. The reaction mixture was stirred at 100 °C for 1 h and at r. t. overnight. 250 mL of a dilute solution of HCl 0.5 M was added. The organic phase was extracted with dichloromethane and dried over MgSO<sub>4</sub>. A white solid was filtered off and dried under vacuum.

White solid; yield 53% (1.7 g); m.p. 48 °C;

<sup>1</sup>H NMR (300 MHz, CDCl<sub>3</sub>, 25 °C, TMS) δ= 8,60 (s, 1H); 8,24 (s, 2H); 4,54 (s, 2H); 4,42 (q, 4H); 1,42 (t, 6H).

Elemental analysis calculated for C<sub>13</sub>H<sub>15</sub>BrO<sub>4</sub> (314.02 g/mol): C 49.54%, H 4.80%, found: C 49.60%, H 4.86%.

### Synthesis of H(NR)<sup>4</sup>.

**2** (0.8 g, 2.4 mmol) and 1.2 eqs. of intermediate **10** (0,9 g, 2.8 mmol) were solubilized in dimethylformamide. 1.3 eqs. of K<sub>2</sub>CO<sub>3</sub> (0.4 g, 3.0 mmol) and catalytic KI were added to the solution which was refluxed for 5 h and stirred at 55 °C for 3 d. The

solution was filtered on Celite and the crude product was purified by precipitation from dichloromethane/cyclohexane.

Red solid; yield 95% (1,3 g); m.p. 170 °C;

<sup>1</sup>H NMR (300 MHz, CDCl<sub>3</sub>, 25 °C, TMS) δ= 8.67 (s, 1H), 8.63 (d, 1 H), 8.37 (s, 2H), 7.84 (s,1H), 7.61 (d, 1H), 7.38 (d, 1H), 6.69 (d, 1H), 6.51 (s, 1H), 6.43 (s, 1H), 5.30 (s, 4H), 4.45 (m, 8 H), 3.50 (m, 4H), 1.45 (m, 6H), 1.25 (m, 6H).

FT-IR (KBr, cm<sup>-1</sup>): 2975, 2898, 2936 (alkyl C-H), 17200 (ester C=O), 1640, 1622, 1589, 1404, 1343, 1238, 1115, 1067, 1018, 838, 753.

Elemental analysis calculated for C<sub>33</sub>H<sub>32</sub>N<sub>2</sub>O<sub>7</sub> (568.62 g/mol): C 69.70%, H 5.67%, N 4.93%, found: C 69.75%, H 5.73%.

### Synthesis of intermediate 11.

To a mixture of MgCl<sub>2</sub> (4.16 g, 0.044 mol) and diethylmalonate (7g, 0.044 mol) in acetonitrile at 0°C under N<sub>2</sub>, 2 eqs. of trimethylamine (12.2 mL, 0.08 mol) was slowly added and the resulting mixture stirred for 30 min. Phenylacetyl chloride (6.76 g, 0.044 mol) was slowly added and the reaction mixture stirred overnight. Afterwards, 250 mL of a 2 M solution of HCl was used to acidify and the organic phase was extracted with ethyl acetate and washed with a NaCl solution and dried over MgSO<sub>4</sub>. The solvent was evaporated to afford the crude product which was used without any further purification.

### Synthesis of intermediate 12.

Intermediate **11** (8 g, 31 mmol) was solubilised in 100 mL of Eaton's reagent and the solution maintained under vigorous stir for 4 h under N<sub>2</sub> at 30 °C. The compound is added at ca. 600 mL of chopped ice. A yellow precipitate is formed, filtered off and washed with a small amount of cold water.

Yellow solid; yield 97% (6.8 g); m.p. 80 °C;

<sup>1</sup>H NMR (300 MHz, CDCl<sub>3</sub>, 25 °C, TMS) δ= 11.55 (s, 1H, OH), 9.01 (s, 1H, OH), 8.24 (d, J=8.76 Hz, 1H), 7.57-7.48 (m, 2H), 7.31-7.26 (m, 1H), 6.76 (s, 1H), 4.61 (q, J= 7.14 Hz, 2H), 1.52 (t, J=7.14 Hz, 3 H).

Elemental analysis calculated for C<sub>13</sub>H<sub>13</sub>O<sub>4</sub> (233.24 g/mol): C 66.94%, H 5.62%, N 4.93%, found: C 67.00%, H 5.73%, N 4.95.

### Synthesis of intermediate **13**.

N,N-diethyl-*p*-nitrosoaniline (10 g, 56 mmol) was solubilized in ethanol. A saturated HCl solution of ethanol/diethyl ether:1/1 solution was added until a green solid precipitated. The solid was filtered off and washed with diethyl ether.

Green solid; yield 85% (10 g);

<sup>1</sup>H NMR (300 MHz, DMSO-d<sub>6</sub>, 25 °C, TMS) δ= 8.09 (s, 1H, *HCl*), 7.26 (d, J=9.33 Hz, 2H), 3.85 (q, J=7.14 Hz, 4H), 1.27 (t, J=6.6 Hz, 3 H).

Elemental analysis calculated for C<sub>10</sub>H<sub>15</sub>ClN<sub>2</sub>O (214.69 g/mol): C 55.94%, H 7.04%, N 13.05%, found: C 56.00%, H 6.98%, N 13.10%.

### Synthesis of H(NR)<sup>5</sup>.

Intermediate **12** (300 mg, 1.29 mmol) were solubilized in ca. 25 mL of degassed 2-ethoxyethanol and 1.2 eqs. (333 mg, 1.55 mmol) of intermediate **13** were added. The reaction mixture was refluxed under microwave radiation (250 W, 200 °C) for 25 min. The crude product was purified by silica column chromatography (carbon disulphide: diethyl ether/5:1).

Green solid, yield 45% (227 mg), m.p.=115 °C;

<sup>1</sup>H NMR (300 MHz, CDCl<sub>3</sub>, 25 °C, TMS) δ= 8.67 (d, J=7.71 Hz, 1H), 8.34 (d, J=8.43 Hz, 1H), 7.82-7.58 (m, 3H), 6.75 (dd, J=9 Hz, J=2.9 Hz, 1H), 6.51 (d, J=2.58 Hz, 1H), 4.53 (q, J= 7.35 Hz, 2H), 3.49 (q, J=6.99 Hz, 4H), 1.47 (t, J=7.35 Hz, 3H), 1.28 (t, J=7.35 Hz, 6H).

FT-IR (KBr, cm<sup>-1</sup>): 2975, 2898, 2936 (alkyl C-H), 1720 (*ester C=O*), 1640 (*Nile red CO*), 1622, 1589, 1404, 1343, 1238, 1115, 1067, 1018, 838, 753.

Elemental analysis calculated for C<sub>23</sub>H<sub>22</sub>N<sub>2</sub>O<sub>4</sub> (390.43 g/mol): C 70.75%, H 5.68%, N 7.17%, found: C 70.75%, H 5.73%, N 7.20%.

### Synthesis of intermediate complex **a**.

H(NR)<sup>2</sup> (500 mg, 1.6 mmol) was suspended in an acetic acid solution and Pd(OAc)<sub>2</sub> (352 mg, 1.6 mmol) was added. The solution was heated at 55°C for 4 h. An azeotropic mixture of cyclohexane/methanol:1/1 was added and the solvent removed under reduced pressure. The crude product was filtered off and washed with diethyl ether.

Dark blue solid; yield 80% (324 mg); m.p. >250 °C;

$^1\text{H}$  NMR (300 MHz,  $\text{CDCl}_3$ , 25 °C, TMS)  $\delta$ = 8.04 (d,  $J$ =8.4Hz, 2H), 7.75 (d,  $J$ =9.2Hz, 1H), 7.37 (d,  $J$ =7.7Hz, 2H), 6.99 (d,  $J$ =1.8Hz, 1H), 6.37 (m, 2H), 6.18 (d,  $J$ =2.6Hz, 1H), 5.97 (s, 1H), 4.79 (d,  $J$ =1.8Hz, 2H), 3.94 (s, 3H), 3.13 (q,  $J$ =8Hz, 4H), 2.27 (s, 3H), 1.07 (t,  $J$ =6.8Hz, 6H);

FT-IR (KBr,  $\text{cm}^{-1}$ ): 3420, 2969 (C-H alchilico), 1776, 1720 (*ester CO*), 1636 (*Nile red CO*), 1496, 1410, 1389, 1333, 1312 (C-N aromatico), 1278 (C-O etere), 1242, 1185, 1118, 1072, 1016, 838, 755, 686, 633, 540;

Elemental analysis calculated for  $\text{C}_{62}\text{H}_{56}\text{N}_4\text{O}_{14}\text{Pd}_2$  (1293.91 g/mol): C 57.55%, H 4.36%, N 4.33%, found: C 57.57%, H 4.38%, N 4.30%.

### Synthesis of intermediate complex b.

The same procedure followed as for the synthesis of intermediate complex **a** with the subsequent modifications:  $\text{H}(\text{NR})^3$  (200 mg, 0.4 mmol) and 1 eq of  $\text{Pd}(\text{AcO})_2$  (88 mg, 0.4 mmol) were heated for 5 d.

Dark blue solid; yield 90% (230 mg); m.p. >250 °C;

$^1\text{H}$  NMR (300 MHz,  $\text{CDCl}_3$ , 25 °C, TMS)  $\delta$ = 8,63 (s, 1H); 8,34 (s, 2H); 8,17 (d, 1H); 7,68 (d,1H); 6,99 (s, 1H); 6,35 (s, 1H); 6,18 (s, 1H); 5,96 (s, 1H); 4,80 (s, 2H); 3,18(m, 4H); 2,35 (m, 3H); 1.5-0.9 (m, 12 H).

FT-IR (KBr,  $\text{cm}^{-1}$ ): 2969, 2910 (*alkyl stretching*), 1730 (*ester CO*), 1634 (*Nile red CO*), 1580, 1490, 1408, 1335, 1312, 1258 (eter C-O), 1240, 1190, 1116, 1070, 1018;

Elemental analysis calculated for  $\text{C}_{70}\text{H}_{68}\text{N}_4\text{O}_{18}\text{Pd}_2$  (1468.16 g/mol): C 57.27%, H 4.81%, N 3.82%, found: C 57.57%, H 4.85%, N 4.00%.

### Synthesis of intermediate complex c.

The same procedure followed as for the synthesis of intermediate complex **a** with the subsequent modifications:  $\text{H}(\text{NR})^4$  (333 mg, 0.85 mmol) and 1 eq. of  $\text{Pd}(\text{AcO})_2$  (191 mg, 0.86 mmol) were heated for 2 d.

Dark blue solid; yield 78% (365 mg); m.p. >250 °C

$^1\text{H}$  NMR (300 MHz,  $\text{CDCl}_3$ , 25 °C, TMS)  $\delta$ = 7.60 (d,  $J$ =9.45 Hz, 1H), 7.44 (d,  $J$ =7.56 Hz, 1H), 6.95-6.84 (m, 2H), 6.25 (d,  $J$ =2.73 Hz, 1H) 5.99 (dd,  $J$ =9 Hz,  $J$ =2.46 Hz, 1H), 4.48 (q,  $J$ =3.57 Hz, 2H), 3.42 (q,  $J$ =6.72 Hz, 4H), 2.29 (s, 3H), 1.48 (t,  $J$ =6.99 Hz, 6H), 1.25 (t,  $J$ =7.14 Hz, 6H);

FT-IR (KBr,  $\text{cm}^{-1}$ ): 2963, 2905, 2840, 1726 (*ester CO*), 1634 (*Nile red CO*), 1577, 1491, 1407, 1310, 170, 1248, 1110, 1067, 1013;

Elemental analysis calculated for  $\text{C}_{50}\text{H}_{48}\text{N}_4\text{O}_{12}\text{Pd}_2$  (1110.15 g/mol) C 54.02%, H 4.53%, N 5.04%, found: C 54.10%, H 4.60%, N 5.08%.

### Synthesis of complex IX

Intermediate complex **a** (128 mg, 0.1 mmol) was solubilized in a 2/1:dichloromethane/ethanol mixture and 1.6 eqs. (60 mg, 0.16 mmol) of  $\text{H}(\text{BSC}_6)^{78}$  were added. The reaction mixture was stirred at r.t. for 7 d. The solvent was evaporated and acetonitrile was added. The precipitated solid was filtered off and washed with acetonitrile.

Dark blu solid; yield 99%; m.p.>250 °C;

$^1\text{H}$  NMR (300 MHz,  $\text{CDCl}_3$ , 25 °C, TMS)  $\delta$ = 9.37 (d,  $J$ =9.51 Hz, 1H), 8.06 (s, 1H), 8.03 (d,  $J$ =2.31 Hz, 1H), 7.64 (d,  $J$ =8.22 Hz, 2H), 7.36 (d,  $J$ =8.55 Hz, 2H), 7.22-7.15 (m, 4H), 6.69 (d,  $J$ =9.54 Hz, 1H), 6.50 (d,  $J$ =2.97 Hz, 1H), 6.39 (d,  $J$ =2.64 Hz, 1H), 6.27 (d,  $J$ =2.31 Hz, 1H), 6.25-6.24 (m, 1H), 5.81 (d,  $J$ =2.31 Hz, 1H), 4.71 (s, 1H), 3.98 (t,  $J$ =6.6 Hz, 2H), 3.44 (s, 2H), 3.50 (q,  $J$ =7.23 Hz, 4H), 2.56 (t,  $J$ =7.29 Hz, 2H), 1.81-1.74 (m, 2H), 1.35-1.19 (m, 20H), 0.95-0.81 (m, 9H);

FT-IR (KBr,  $\text{cm}^{-1}$ ): 2956, 2925, 2852 (*alkyl stretching*), 1722 (*ester CO*), 1635 (*Nile red CO*), 1612, 1575, 1277, 1075, 1019, 835;

Elemental analysis calculated for  $\text{C}_{54}\text{H}_{59}\text{N}_3\text{O}_7\text{Pd}$  (968.48 g/mol): C 66.97%, H 6.14%, N 4.34%, found: C 66.99%, H 6.20%, N 4.40%.

### Synthesis of complex X

Intermediate complex **b** (100 mg, 0.08 mmol) was solubilized in a 2/1:dichloromethane/ethanol mixture and 1.8 eqs. (50 mg, 0.14 mmol) of  $\text{H}(\text{BSC}_6)^{78}$  were added. The reaction mixture was stirred at r.t. for 3 d. The dichloromethane was evaporated and ethanol was added. A solid precipitated in fridge and was filtered off and washed with cold ethanol.

Dark blue solid; yield 75% (120 g); m.p. 220 °C;

$^1\text{H}$  NMR (300 MHz,  $\text{CDCl}_3$ , 25 °C, TMS)  $\delta$  = 9.35 (m, 1H), 8.63 (s, 1H), 8.18 (s, 2H), 8.03 (d, 1H), 7.64 (t, 2H), 6.69 (d, 1H), 6.25 (s, 3H), 5.82 (s, 1H), 4.66 (s, 2H), 4.46 (q, 6H), 3.99 (m, 3H), 3.50 (q, 3H), 2.52 (m, 3H), 1.79-0.8 (m);

FT-IR (KBr,  $\text{cm}^{-1}$ ): 2928, 2856 (*alkyl stretching*), 1721 (*ester CO*), 1628 (*Nile red C=O*), 1573, 1500, 1428, 1303, 1240, 1192, 1121, 1077, 1019, 836;

Elemental analysis calculated for  $\text{C}_{58}\text{H}_{65}\text{N}_3\text{O}_9\text{Pd}$  (1054.57 g/mol): C 66.06%, H 6.21%, N 3.98%, found: C 66.10%, H 6.25%, N 4.00%.

### Synthesis of complex XI

Intermediate complex **c** (55 mg, 0.04 mmol) was solubilized in ethanol and 2 eqs. (38 mg, 0.08 mmol) of **H(BSC<sub>6</sub>)<sup>78</sup>** were added. The reaction mixture was stirred at r.t. for 4 d. The reaction mixture was cooled down and the precipitated solid was filtered off and washed with ethanol.

Dark blue solid; yield 65% (46 mg); m.p. >250 °C;

<sup>1</sup>H NMR (300 MHz,  $\text{CDCl}_3$ , 25 °C, TMS)  $\delta$  = 9.49 (d, J=10 Hz, 1H), 8.04 (s, 1H), 7.64 (d, J=7.83 Hz, 1H), 7.59 (d, J=7.56 Hz, 2H), 7.21-7.11 (m, 3H), 6.82-6.72 (m, 1H), 6.52 (d, J=2.88 Hz, 1H), 6.38 (s, 1H), 6.25 (d, J=8.91 Hz, 1H), 6.13 (d, J=7.95 Hz, 1H), 5.55 (s, 1H), 4.48 (q, J=7.26 Hz, 2H), 3.99 (t, J=6.57 Hz, 2H), 3.50 (q, J=7.14 Hz, 4H), 2.61 (t, J=8.1 Hz, 2H), 1.78 (t, J=7.9 Hz, 2H), 1.43 (t, J=6.87 Hz, 8H), 1.32-1.27 (m, 15 H), 0.89-0.88 (m, 6H);

FT-IR (KBr,  $\text{cm}^{-1}$ ): 2925, 2847 (*alkyl stretching*), 1728 (*ester CO*), 1627 (*Nile red CO*), 1609, 1580, 1519, 1407, 1279, 1202, 1111, 818;

Elemental analysis for  $\text{C}_{48}\text{H}_{55}\text{N}_3\text{O}_6\text{Pd}$  (876.39 g/mol): C 65.78%, H 6.33%, N 4.79%, found: C 66.00%, H 6.25%, N 4.81%.

### Synthesis of intermediate complex a'

Intermediate complex **a** (109 mg, 0.08 mmol) was solubilized in 4 mL of acetone and 3 mL of an aqueous NaOH (47 mg, 1.12 mmol) solution were added and the reaction mixture stirred at r.t. for 24 h. A dilute HCl solution was added dropwise until pH=6 was checked with a pH paper. The precipitated solid was centrifuged, washed with distilled water and ethanol and dried in oven. The compound is only soluble in pyridine.

Black solid; yield 80% (80 mg); m.p. >250 °C;

FT-IR (KBr,  $\text{cm}^{-1}$ ): >3000 (*br.*, *OH*), 2970, 2869 (*alkyl stretching*), 1698 (*carboxylic CO*), 1631 (*Nile red CO*), 1617, 1570, 1387, 1333, 1281, 1246, 1120, 1073, 1015, 844, 758;

Elemental analysis calculated for  $C_{54}H_{48}N_4O_{10}Pd_2$  (1125.82 g/mol): C 57.61%, H 4.30%, N 4.98%, found: C 57.57%, H 4.38%, N 4.91%.

### Synthesis of intermediate complex **b'**

Intermediate complex **b** (50 mg, 0.04 mmol) was solubilized in 4 mL of acetone and 3 mL of an aqueous NaOH (20 mg, 0.5 mmol) solution were added and the reaction mixture stirred at r.t. for 24 h. A dilute HCl solution was added dropwise until pH=6 was checked with a pH paper and a violet solid precipitated. The crude product was filtered off, washed with ethanol and dichloromethane. The compound is only soluble in dimethylformamide.

Violet solid; yield 81% (40 mg); m.p.>250 °C;

FT-IR (KBr,  $cm^{-1}$ ): >3079 (*br.*, OH), 2971-2920 (*alkyl stretching*), 1710 (*carboxylic CO*), 1635 (*Nile red CO*), 157, 1490, 1450, 1385, 1244, 1122, 1078, 1020, 837;

Elemental analysis calculated for  $C_{54}H_{48}N_4O_{12}Pd_2$  (1157.82 g/mol): C 56.02%, H 4.18%, N 4.84%, found: C 56.15%, H 4.20%, N 5.00%.

### Synthesis of complex XII

Intermediate complex **a'** (55 mg, 0.05 mmol) is solubilized in pyridine and stirred at r.t. at 30 °C for 5 hours. 2 eqs. (17 mg, 0.1 mmol) of  $H(BSC_6)^{78}$  were added and the reaction mixture stirred at r.t. for 24 h. The solvent was evaporated almost completely and distilled water was added. The obtained solution was acidified until pH=6 and the precipitated solid was filtered off, washed with acetone and dried.

Black solid; yield 50% (43 mg); m.p.>250 °C;

FT-IR (KBr,  $cm^{-1}$ ): >3500 (*br.* OH), 2917, 2847 (*alkyl stretchng*), 1718 (*carboxylic CO*), 1638 (*Nile red CO*), 1571, 1330, 1077, 1020, 837;

Elemental analysis for  $C_{52}H_{57}N_3O_6Pd_1$  (926.45 g/mol): C 67.41%, H 6.20%, N 4.54%, found: C 67.50%, H 6.25%, N 5.60%.

### Synthesis of complex XIII

Intermediate complex **b'** (40 mg, 0.03 mmol) is solubilized in dimethylformamide and 2 eqs. (20 mg, 0.06 mmol) of  $H(BSC_6)^{78}$  were added and the reaction mixture stirred at r.t. for 48 h. The solvent was evaporated almost completely and diethyl ether was added. The solid was filtered off and washed with diethyl ether and dichloromethane. The product is soluble in dimethylformamide.

Dark blue solid; yield 90% (51 mg); m.p.>250 °C;

FT-IR (KBr,  $\text{cm}^{-1}$ ): >3079 (*br.*, *OH*), 2971-2934 (*alkyl stretching*), 1714 (*carboxylic CO*), 1632 (*Nile red CO*), 1570, 1494, 1447, 1335, 1317, 1201, 1075, 1017, 930, 757.

Elemental analysis for  $\text{C}_{52}\text{H}_{57}\text{N}_3\text{O}_7\text{Pd}$  (942.44 g/mol): C 66.27%, H 6.10%, N 4.46%, found: C 66.30%, H 6.15%, N 4.60%.

## 10.2.2 Synthesis of novel Ir(III) complexes and of their precursors

### Synthesis of complex XIV.

The dichloro bridged precursor  $\mathbf{14}^{213}$  (100 mg, 0.093 mmol) and a small excess of tetrachlorocatechole (51 mg, 0.205 mmol) were dissolved in 25 mL mixture of dichloromethane/methanol:4/1, under purging  $\text{N}_2$ . To this clear yellow solution, 0.41 mL of  $\text{Bu}_4\text{NOH}$  (1M in MeOH) was added dropwise. The colour changed to red-orange. The reaction mixture was stirred under  $\text{N}_2$  for 3 d. Then the solvent was evaporated, and the pure product was obtained after recrystallization from chloroform/ethyl acetate.

Red solid; yield 73% (135 mg); m. p. = 220°C dec.;

$^1\text{H}$  NMR (300 MHz,  $\text{CD}_3\text{CN}$ , 25 °C, TMS)  $\delta$  = 8.75 (d,  $J$  = 5.8 Hz, 2H,  $\text{H}_a$ ), 7.95 (d,  $J$  = 8.0 Hz, 2H), 7.75 (td,  $J$  = 7.8 Hz,  $J$  = 71.6 Hz, 2H), 7.62 (d,  $J$  = 7.8 Hz, 2H), 7.19 (td,  $J$  = 6.6 Hz,  $J$  = 1.4 Hz, 2H), 6.76 (td,  $J$  = 7.5 Hz,  $J$  = 1.2 Hz, 2H), 6.61 (t,  $J$  = 7.3 Hz,  $J$  = 1.4 Hz, 2H), 6.19 (d,  $J$  = 7.6 Hz, 2H), 3.06 (m, 8 H), 1.60 (m, 8 H), 1.35 (m, 8H), 0.96 (t,  $J$  = 7.3 Hz, 12H);

FT-IR (KBr,  $\text{cm}^{-1}$ ): 3039 (*C-Ir*); 2962, 2874 (*alkyl stretching*); 1475, 1442, 1255 (*CO coordinated catecholate*);

Elemental analysis calculated for  $\text{C}_{44}\text{H}_{52}\text{Cl}_4\text{IrN}_3\text{O}_2$  (988.93 g/mol): C 53.44%, H 5.30%, N 4.25%, found: C 53.21%, H 5.5 %, N 4.48%;

$A_M$  ( $c = 3.6 \cdot 10^{-5}$  mol  $\text{L}^{-1}$  in acetonitrile) = 122  $\Omega^{-1} \text{cm}^2 \text{mol}^{-1}$ .

### Synthesis of complex XV

The dichloro bridged precursor  $\mathbf{14}^{213}$  (75 mg, 0.070 mmol) and a small excess of tetrabromocatechole (66 mg, 0.154 mmol) were dissolved in 25 mL mixture of dichloromethane/methanol:4/1, under purging  $\text{N}_2$ . To this clear yellow solution, 0.31 mL of  $\text{Bu}_4\text{NOH}$  (1M in MeOH) were added dropwise. The colour changed to red-orange. The reaction mixture was stirred under  $\text{N}_2$  for 3 d. Then the solvent was



evaporated. Subsequently to the addition of chloroform, a solid precipitated, filtered off and washed with chloroform.

Red solid; yield 97% (158 mg.); m.p. = 210°C dec.;

$^1\text{H}$  NMR (300 MHz,  $\text{CD}_3\text{CN}$ , 25 °C, TMS)  $\delta$  = 8.75 (d,  $J$  = 5.9 Hz, 2H), 7.95 (d,  $J$  = 8.0 Hz, 2H), 7.76 (t,  $J$  = 7.9 Hz, 2H), 7.61 (d,  $J$  = 7.5 Hz, 2H), 7.19 (t,  $J$  = 6.5 Hz, 2H), 6.76 (t,  $J$  = 7.5 Hz, 2H), 6.61 (t,  $J$  = 7.3 Hz, 2H), 6.16 (d,  $J$  = 8.1 Hz, 2H), 3.05 (m, 8 H), 1.68 (m, 8 H), 1.36 (m, 8H), 0.96 (t,  $J$  = 7.4 Hz, 12H);

FT-IR (KBr,  $\text{cm}^{-1}$ ): 3038 (*C-Ir*); 2962, 2873 (*alkyl stretching*), 1475, 1438, 1256 (*CO coordinated cathecolate*).

Elemental analysis calculated for  $\text{C}_{44}\text{H}_{52}\text{Br}_4\text{IrN}_3\text{O}_2$  (1166.74 g/mol): C 45.29%, H 4.49%, N 3.60%, found: C, 45.32; H, 4.36 ; N, 3.45.

$A_M$  ( $c = 3.6 \cdot 10^{-5}$  mol  $\text{L}^{-1}$  in acetonitrile) = 117  $\Omega^{-1} \text{cm}^2 \text{mol}^{-1}$ .

### Synthesis of complex XVI.

The dichloro bridged precursor **14**<sup>213</sup> (100 mg, 0.093 mmol) and a small excess of alizarin (49 mg, 0.205 mmol) were dissolved in 25 mL mixture of dichloromethane/methanol:4/1, under purging  $\text{N}_2$ . To this clear orange solution, 0.41 mL of  $\text{Bu}_4\text{NOH}$  (1M in MeOH) were added dropwise. The colour changed to dark blue. The reaction mixture was stirred under  $\text{N}_2$  for 3 d. Then the solvent was evaporated, the product was recrystallized from dichloromethane/hexane and washed with ethyl acetate.

Dark blue solid; yield 78% (157 mg.); m. p. = 215°C dec.;

$^1\text{H}$  NMR (300 MHz,  $\text{CD}_3\text{CN}$ , 25 °C, TMS)  $\delta$  = 8.74 (d,  $J$  = 6.6 Hz, 1H), 8.70 (d,  $J$  = 6.6 Hz, 1H), 8.09 (m, 2H), 7.96 (m, 2H), 7.77 – 7.55 (m, 6H), 7.43 (d,  $J$  = 8.0 Hz), 7.16 (m, 2H), 6.79 (m, 2H), 6.65 (m, 2H), 6.33 (d,  $J$  = 8.2 Hz, 1H), 6.25 (d,  $J$  = 7.7 Hz, 1H), 6.17 (d,  $J$  = 6.9 Hz, 2H), 3.06 (m, 8 H), 1.60 (m, 8 H), 1.34 (m, 8H), 0.96 (t,  $J$  = 7.2 Hz, 12H);

Elemental analysis calculated for:  $\text{C}_2\text{H}_{58}\text{IrN}_3\text{O}_4$  (981.25 g/mol): C 63.65%, H 5.96%, N 4.28%, found: C 63.49%, H 6.08%, N 4.38%;

FT-IR (KBr,  $\text{cm}^{-1}$ ): 3039 (*C-Ir*), 2962, 2873 (*alkyl stretching*), 1475, 1438, 1256 (*alizerine CO*);

$A_M$  ( $c = 3.6 \cdot 10^{-5}$  mol  $\text{L}^{-1}$  in acetonitrile) = 122  $\Omega^{-1} \text{cm}^2 \text{mol}^{-1}$ .

### Synthesis of complex A<sup>1</sup>.

To a mixture of dichloro bridged precursor **14**<sup>213</sup> (100 mg, 0.093 mmol) and a small excess of orotic acid monohydrate (36 mg, 0.205 mmol) in 15 mL of dichloromethane/methanol:4/1, 0.41 mL of Bu<sub>4</sub>NOH (1M in MeOH) were added dropwise under purging N<sub>2</sub>. The colour changed to orange. The reaction mixture was stirred under N<sub>2</sub> for 3 d. Then the solvents were evaporated, and the pure product was obtained after filtration on Celite in chloroform and recrystallization from chloroform/hexane;

Yellow solid; yield 73% (124 mg); m. p. = 200°C dec.;

<sup>1</sup>H NMR (300 MHz, DMSO-d<sub>6</sub>, 25 °C, TMS) δ = 9.59 (s, 1H), 8.45 (d, J = 6.1 Hz, 1H), 8.34 (d, 3J = 5.7 Hz, 1H), 8.10 (d, J = 8.4 Hz, 1H), 8.03 (d, J = 8.0 Hz, 1H), 7.88 (t, J = 7.7 Hz, 1H), 7.81 (t, J = 8.0 Hz, 1H), 7.67 (d, J = 7.8 Hz, 1H), 7.56 (d, J = 7.0, 1H), 6.31 (m, 2H), 6.75 (t, J = 7.8 Hz, 1H), 6.58 (m, 2H), 6.43 (d, J = 7.4 Hz, 1H), 6.05 (d, J = 7.6 Hz, 1H), 5.94 (d, J = 7.5 Hz, 1H), 5.67 (d, J = 1.9 Hz), 3.13 (m, 8 H), 1.53 (m, 8H), 1.28 (m, 8H), 0.91 (t, J = 7.3 Hz, 12H);

FT-IR (KBr, cm<sup>-1</sup>): 2962, 2874 (*alkyl stretching*), 1646, 1634, 1607, 1359;

Elemental analysis calculated for C<sub>43</sub>H<sub>54</sub>IrN<sub>5</sub>O<sub>4</sub> (897.38 g/mol): C 57.57%, H 6.07%, N 7.81%, found: C 57.37%, H 6.23%; N 7.53%.

### Synthesis of intermediate complex 14'.

IrCl<sub>3</sub>·xH<sub>2</sub>O (340 mg, 1.14 mmol) was solubilized in 5 mL of degassed distilled water under inert atmosphere (N<sub>2</sub>). 4,5'-dimethyl-2-phenylpyridine<sup>225</sup> (385 mg, 2.27 mmol) was solubilized in 15 mL of degassed 2-ethoxyethanol and added to the reaction mixture. The resulting solution was stirred at reflux. After 24 h., a precipitate was filtered off, washed with acetone and water and dried under vacuum.

Green solid; yield 80% (539 mg); m. p. >250°C;

<sup>1</sup>H NMR (300 MHz, CDCl<sub>3</sub>, 25 °C, TMS) δ = 9.04 (d, J=5.88 Hz, 4H), 7.64 (s, 4H), 7.27 (s, 4H), 6.51 (d, J=4.8 Hz, 4H), 6.38 (d, J=4.8 Hz, 4H), 5.82 (d, J=7.83 Hz, 4H), 2.61 (s, 12H), 2.09 (s, 12H);

FT-IR (KBr, cm<sup>-1</sup>): 3039, 2916 (*alkyl stretching*), 2863, 1619, 1540, 1477, 1446, 1268, 1032, 810;

Elemental analysis calculated for C<sub>52</sub>H<sub>48</sub>Cl<sub>2</sub>Ir<sub>2</sub>N<sub>4</sub> (1184.25 g/mol): C 52.74%, H 4.09%, N 4.73%, found: C 52.64%, H 4.18%, N 4.50.

### Synthesis of complex A<sup>2</sup>.

To a mixture of dichloro bridged precursor **14'** (100 mg, 0.084 mmol) and a small excess of orotic acid monohydrate (32 mg, 0.185 mmol) in 15 mL dichloromethane/methanol:4/1, 0.37 mL of Bu<sub>4</sub>NOH (1M in MeOH) were added dropwise, under purging N<sub>2</sub>. The colour changed to orange. The reaction mixture was stirred for 3 d. Then the solvents were evaporated and the pure product was obtained after filtration on Celite in dichloromethane and recrystallized from dichloromethane/diethyl ether;

Orange solid; yield 71% (117 mg); m. p. >250°C;

<sup>1</sup>H NMR (300 MHz, DMSO-d<sub>6</sub>, 25 °C, TMS) δ = 9.49 (s, 1H), 8.21 (d, J = 5.7, 1H), 8.13 (d, J = 5.9, 1H), 7.87 (s, 1H), 7.78 (s, 1H), 7.43 (s, 1H), 7.30 (s, 1H), 7.08 (m, 2H), 6.39 (d, J = 7.4, 1H), 6.24 (d, J = 8.0 Hz, 1H), 5.90 (d, J = 7.9 Hz, 1H), 5.79 (d, J = 7.6 Hz, 1H), 5.63 (d, J = 1.0 Hz), 3.13 (m, 8 H), 2.08 (d, J = 9.3 Hz, 6H), 1.53 (m, 8H), 1.28 (m, 8H), 0.91 (t, J = 7.3 Hz, 12H);

FT-IR (KBr, cm<sup>-1</sup>): 2962, 2874 (*alkyl stretching*), 1660, 1645, 1620, 1361.

Elemental analysis calculated for C<sub>47</sub>H<sub>62</sub>IrN<sub>5</sub>O<sub>4</sub> (953.44 g/mol): C 59.22%, H 6.56%, N 7.35%, found: C 58.94%, H 6.88%, N 7.15%.

### Synthesis of complex C<sup>1</sup>A<sup>1</sup>.

Complexes **A<sup>1</sup>** (50 mg, 0.0546 mmol) and **C<sup>1</sup>**,<sup>227a</sup> (35 mg, 0.0546 mmol) were dissolved in 50 mL of a mixture of methanol/water:4/1 at r. t., and the resulting mixture was stirred in an open vessel to allow a slow evaporation of methanol to 1/3 of its initial volume. The product, precipitated as crystalline yellowish solid, was filtered out and washed several times with large amounts of water.

Yellow solid; yield 81% (59 mg); m. p. = 240°C dec.;

<sup>1</sup>H NMR (300 MHz, DMSO-d<sub>6</sub>, 25 °C, TMS) δ = 9.60 (s, 1H), 8.98 (d, J = 5.7 Hz, 1H), 8.44 (d, J = 5.7 Hz, 1H), 8.35 (d, J = 5.6 Hz, 1H), 8.27 (d, J = 8.0 Hz, 1H), 8.22 (d, J = 8.0 Hz, 1H), 8.10 (d, J = 8.2 Hz, 1H), 8.04-7.64 (m, 11H), 7.54 (d, J = 6.7 Hz, 1H), 7.32 (m, 6H), 7.96-6.71 (m, 5H), 6.58 (m, 2H), 6.43 (t, J = 7.4 Hz, 1H), 6.18 (d, J = 7.7 Hz, 1H), 6.11 (d, J = 7.5 Hz, 1H), 6.05 (d, J = 7.7 Hz, 1H), 5.94 (d, J = 7.6 Hz, 1H), 5.67 (d, J = 1.1 Hz), 5.50 (m, 1H), 5.02 (m, 1H), 4.55 (m, 1H), 4.30 (m, 1H);

FT-IR (KBr, cm<sup>-1</sup>): 1619, 1640, 1610, 1364;

Elemental analysis calculated for: C<sub>55</sub>H<sub>42</sub>Ir<sub>2</sub>N<sub>8</sub>O<sub>4</sub> (1264.26 g/mol): C 52.69%, H 3.35%, N 8.87; found: C 52.67%, H 3.66%, N 8.32%.

### Synthesis of complex C<sup>2</sup>A<sup>1</sup>.

Complexes A<sup>1</sup> (50 mg, 0.0546 mmol) and C<sup>2</sup>,<sup>227b</sup> (41 mg, 0.0546 mmol) were dissolved in 50 mL of a mixture of methanol/water:4/1 at r. t., and the resulting mixture was stirred in an open vessel to allow a slow evaporation of methanol to 1/3 of its initial volume. The precipitated product was filtered out and washed with abundant water.

Orange solid; yield 75% (56 mg); m. p. = 250°C dec.;

<sup>1</sup>H NMR (300 MHz, DMSO-d<sub>6</sub>, 25 °C, TMS) δ = 9.56 (s, 1H), 8.86 (d, J = 8.3 Hz, 2H), 8.42 (d, J = 5.1 Hz, 1H), 8.33 (d, J = 5.8 Hz, 1H), 8.23 (m, 4H), 8.07 (d, J = 5.9 Hz, 1H), 8.01 (d, J = 8.6 Hz, 1H), 7.88 (m, 8H), 7.67 (m, 3H), 7.60 (d, J = 5.2 Hz, 2H), 7.52 (d, J = 7.2 Hz, 1H), 7.30 (m, 2H), 7.14 (t, J = 6.2 Hz, 2H), 7.00 (t, J = 7.1 Hz, 2H), 6.88 (t, J = 7.5 Hz, 2H), 6.72 (d, J = 7.3 Hz, 1H), 6.56 (m, 2H), 6.41 (d, J = 6.9 Hz, 1H), 6.17 (d, J = 7.1 Hz, 2H), 6.03 (d, J = 8.0 Hz, 1H), 5.92 (d, J = 7.0 Hz, 1H), 5.65 (d, J = 1.1 Hz);

FT-IR (KBr, cm<sup>-1</sup>): 1660, 1632, 1606, 1362;

Elemental analysis calculated for: C<sub>59</sub>H<sub>44</sub>Ir<sub>2</sub>N<sub>8</sub>O<sub>4</sub> (1314.27 g/mol): C 53.95%, H 3.38%, N, 8.53, found: C 53.56%, H 3.37%, N 8.30%.

### Synthesis of complex C<sup>1</sup>A<sup>2</sup>.

Complexes A<sup>2</sup> (50 mg, 0.0514 mmol) and C<sup>1</sup><sup>227a</sup> (33 mg, 0.0514 mmol) were dissolved in 50 mL of a mixture of methanol/water:4/1 at r. t., and the resulting mixture was stirred in an open vessel to allow a slow evaporation of methanol to 1/3 of its initial volume. The precipitated product was filtered out and washed with abundant water.

Yellow solid; yield 78% (55 mg); m. p. >250°C;

<sup>1</sup>H NMR (300 MHz, DMSO-d<sub>6</sub>, 25 °C, TMS) δ = 9.51 (s, 1H), 8.96 (d, J = 5.9 Hz, 1H), 8.22 (m, 3H), 8.13 (d, J = 5.9 Hz, 1H), 7.89 (m, 8H), 7.62 (d, J = 5.8 Hz, 1H), 7.52 (d, J = 5.3 Hz, 1H), 7.43 (s, 1H), 7.30 (m, 4H), 7.08 (m, 2H), 6.91 (t, J = 7.4 Hz, 1H), 6.84 (t, J = 7.5 Hz, 1H), 6.78 (t, J = 7.4 Hz, 1H), 6.71 (t, J = 7.6 Hz, 1H), 6.39 (d, J = 7.4 Hz, 1H), 6.24 (d, J = 8.0 Hz, 1H), 6.16 (d, J = 7.5 Hz, 1H), 6.09 (d, J = 7.4 Hz, 1H), 5.90 (d, J = 7.7 Hz, 1H), 5.78 (d, J = 7.6 Hz, 1H), 5.63 (d, J = 2.0 Hz, 1H), 5.50 (m, 1H), 4.99 (m, 1H), 4.54 (m, 1H), 4.30 (m, 1H), 2.07 (d, J = 9.5 Hz, 6H);

FT-IR (KBr, cm<sup>-1</sup>): 2916, 2858 (*alkyl stretching*), 1660, 1632, 1607, 1370;

Elemental analysis calculated for: C<sub>59</sub>H<sub>50</sub>Ir<sub>2</sub>N<sub>8</sub>O<sub>4</sub> (1320.32 g/mol): C 53.70%, H 3.82%, N 8.49%, found: C 53.33%, H 3.88%, N 8.28%.

### Complex C<sup>2</sup>A<sup>2</sup>.

Complexes A<sup>2</sup> (50 mg, 0.0514 mmol) and C<sup>2227b</sup> (39 mg, 0.0514 mmol) were dissolved in 50 mL of a mixture of methanol/water:4/1 at r. t., and the resulting mixture was stirred in an open vessel to allow a slow evaporation of methanol to 1/3 of its initial volume. The precipitated solid was filtered out and washed with abundant water. Orange solid; yield 80% (60 mg); m. p. = 200°C dec.;

<sup>1</sup>H NMR (300 MHz, DMSO-d<sub>6</sub>, 25 °C, TMS) δ = 9.49 (s, 1H), 8.86 (d, J = 8.0, 2H), 8.23 (m, 5H), 8.12 (d, J = 6.0 Hz, 1H), 7.88 (m, 7H), 7.78 (s, 1H), 7.67 (t, J = 6.4 Hz, 2H), 7.60 (d, J = 5.6 Hz, 2H), 7.53 (s, 1H), 7.29 (s, 1H), 7.12 (m, 4H), 7.00 (t, J = 7.2 Hz, 2H), 6.88 (t, J = 7.4 Hz, 2H), 6.39 (d, J = 7.6 Hz), 6.24 (d, J = 7.6 Hz, 1H), 6.17 (d, J = 7.4 Hz, 2H), 5.90 (d, J = 7.7 Hz, 1H), 5.79 (d, J = 7.6 Hz, 1H), 5.62 (d, J = 2.2 Hz, 1H), 2.08 (d, 6H, J=9.4 Hz);

FT-IR (KBr, cm<sup>-1</sup>): 2916, 2847 (*alkyl stretching*), 1660, 1622, 1609, 1369;

Elemental analysis calculated for: C<sub>63</sub>H<sub>52</sub>Ir<sub>2</sub>N<sub>8</sub>O<sub>4</sub> (1370.34 g/mol): C 55.25%, H 3.83%, N 8.18%, found: C 54.95%, H 3.90%, N 7.82%.

### Synthesis of complex XVII.

Intermediate complex 14<sup>213</sup> (150 mg, 0.14 mmol) was solubilised in *ca.* 50 mL of an 1:1 mixture of acetone and chloroform. 2 eqs. of H(BSC<sub>6</sub>)<sup>78</sup> (87 mg, 0.28 mmol) and 30 eqs. (0.3 mL, 4.2 mmol) of trimethylamine were added to the solution. The reaction mixture was stirred at reflux for 72 h. The solvent was evaporated and the organic phase extracted with dichloromethane/water and dried over sodium sulphate. The crude product was purified by precipitation from dichloromethane/hexane. The solid was filtered off, washed with hexane and dried under vacuum.

Red solid; yield 66% (149 mg); m.p.>250° C;

<sup>1</sup>H NMR (300 MHz, CDCl<sub>3</sub>, 25 °C, TMS) δ = 8.92 (d, J=5.49 Hz, 1H), 8.86 (d, J=5.79 Hz, 1H), 8.05 (s, 1H, *H<sub>i</sub>*), 7.88 (d, J=8.37 Hz, 1H), 7.67 (d, J=13 Hz, 1H), 7.68 (t, J=14 Hz, 1H), 7.59 (d, J=7.83 Hz, 1H), 7.51 (d, J=8.1 Hz, 1H), 7.12 (t, J=5.76 Hz, 1H), 7.06-7.00 (m, 2H), 6.95 (dd, J=9.18 Hz, J=3.3 Hz, 1H), 6.85 (t, J=7.95 Hz, 1H), 6.72 (t, J=7.26 Hz, 1H), 6.65 (d, J=9.18 Hz, 1H), 6.57 (d, J=3.3 Hz, 1H), 6.51-6.49 (m, 4H), 6.28 (d, J=7.26 Hz, 1H), 6.17 (d, J=7.69 Hz, 1H), 6.02 (d, J=8.25 Hz, 2H<sub>o-ir</sub>), 3.71 (s, 3H, -CH<sub>3</sub>), 2.35 (t, J=7.56 Hz, 2H, -CH<sub>2</sub>φ), 1.67-1.22 (m, 8H, (-CH<sub>2</sub>-)4), 0.93 (t, J=6.72 Hz, 3H, -CH<sub>3</sub>);

FT-IR (KBr,  $\text{cm}^{-1}$ ): 3041, 2996, 2925, 2853 (*alkyl stretching*), 1620 (*CN Schiff base*), 1604, 1584, 1476, 1465, 1425, 1314, 1212, 1147, 1030, 755, 729;

Elemental analysis calculated for  $\text{C}_{42}\text{H}_{40}\text{IrN}_3\text{O}_2$  (811.00 g/mol): C 62.20%, H 4.97%, N 5.18%, found C 62.50%, H 5.14%, N 5.20%.

### Synthesis of complex XVIII.

**14**<sup>210</sup> (100 mg, 0.09 mmol) was solubilised in *ca.* 50 mL of an 1:1 mixture of acetone and chloroform. 2 eqs. of **H(O<sup>^</sup>N)<sup>4</sup>** (88 mg, 0.18 mmol) and 30 eqs. (0.2 mL, 2.8 mmol) of trimethylamine were added to the solution. The reaction mixture was stirred at reflux for 72 h. The solvent was evaporated and the organic phase extracted with dichloromethane/water and dried over sodium sulphate. The crude product was purified by precipitation from dichloromethane/ hexane. The solid was filtered off, washed with hexane and dried under vacuum.

Red solid; yield 80% (145 mg); m.p.>250° C;

<sup>1</sup>H NMR (300 MHz,  $\text{CDCl}_3$ , 25 °C, TMS)  $\delta$  = 8.93 (d, J=5.34 Hz, 1H), 8.89 (d, J=5.49 Hz, 1H), 7.89 (d, J=8.1 Hz, 1H), 7.75-7.59 (m, 3H), 7.50 (d, J=8.1 Hz, 1H), 7.31-7.22 (m, 4H), 7.14-7.02 (m, 13H), 6.99-6.95 (m, 1H), 6.89-6.83 (m, 3H), 6.75-6.65 (m, 2H), 6.59 (d, J=3.18 Hz, 1H), 6.56-6.54 (m, 2H), 6.29 (d, J=7.68 Hz, 1H), 6.22-6.19 (m, 1H), 6.16 (d, J=8.25 Hz, 2H), 3.72 (s, 3H);

FT-IR (KBr,  $\text{cm}^{-1}$ ): 3030, 2920, 2833 (*alkyl stretching*), 1610 (*CN Schiff base*), 1584, 1525, 1486, 1476, 1436, 1313, 1267, 1212, 1146, 1029, 823, 753, 729, 695;

Elemental analysis calculated for  $\text{C}_{54}\text{H}_{41}\text{IrN}_4\text{O}_2$  (970.29 g/mol): C 66.85%, H 4.26%, N 5.78%, found: C 66.80%, H 4.14%, N 5.82%.

### Synthesis of intermediate complex 15.

To a degassed aqueous solution (10 mL) of  $\text{IrCl}_3 \cdot x\text{H}_2\text{O}$  (93 mg, 0.25 mmol), 2 eqs. of **btz-tpa**<sup>238</sup> (200 mg, 0.50 mmol) solubilized in 30 mL of degassed ethoxyethanol are added. The reaction mixture is irradiated with microwave radiation for 20 min. (250 W, 120° C) and stirred afterwards at reflux for 4 d in inert atmosphere ( $\text{N}_2$ ). A brown solid is filtered off and washed with distilled water and ethanol and dried under vacuum.

Brown solid; yield 40% (96 mg); m.p.>250° C;

<sup>1</sup>H NMR ( $\text{CDCl}_3$ , 300 MHz, TMS)  $\delta$  = 8.62 (d, J=6.0 Hz, 2H), 7.27 (d, J=1.23 Hz, 2H), 7.05-7.03 (m, 4H), 6.95-6.91 (m, 10H), 6.84-6.81 (m, 4H), 6.70-6.68 (m, 8H), 6.46 (dd, J=8.45 Hz, J=2.04 Hz, 2H), 5.48 (d, J=2.19 Hz, 2H);

FT-IR (KBr,  $\text{cm}^{-1}$ ): 1571, 1498, 1459, 1429, 1378, 1262, 1096, 1022, 802, 749, 694, 508;

Elemental analysis calculated for  $\text{C}_{50}\text{H}_{34}\text{Cl}_2\text{Ir}_2\text{N}_4\text{S}_2$ : C 49.54%, H 2.99%, N 4.62%, found: C 49.60%, H 3.04%, N 4.42%.

### Synthesis of complex XIX.

Intermediate complex **16** (75 mg, 0.038 mmol) was solubilised in *ca.* 50 mL of an 1:1 mixture of acetone and chloroform. 2 eqs. (24 mg, 0.076 mmol) of  $\text{H}(\text{BSC}_6)^{78}$  and 30 eqs. (0.06 mL, 0.9 mmol) of trimethylamine were added to the solution. The reaction mixture was stirred at reflux for 48 h. and at r.t. for 48 h. The solvent was evaporated and the organic phase extracted with dichloromethane/water and dried over sodium sulphate. The crude product was purified by precipitation from dichloromethane/cold ethanol. The solid was filtrated, washed with cold methanol and dried under vacuum.

Red-brown solid; yield 55% (53 mg), m.p. >250° C;

$^1\text{H}$  NMR ( $\text{CDCl}_3$ , 300 MHz, TMS)  $\delta$  = 8.43 (d,  $J=9.09$  Hz, 1H), 8.01 (d,  $J=9.24$  Hz, 1H), 7.91 (s, 1H), 7.59 (d,  $J=7.62$  Hz, 2H), 7.39 (d,  $J=8.49$  Hz, 1H), 7.20 (d,  $J=9.39$  Hz, 4H), 7.09-6.95 (m, 7H), 6.89-6.82 (m, 10H), 6.69 (d,  $J=9.3$  Hz, 3H), 6.63 (d,  $J=8.07$  Hz, 3H), 6.50 (dd,  $J=8.43$  Hz,  $J=2.2$  Hz, 1H), 6.47 (d,  $J=3.09$  Hz, 1H), 6.34 (d,  $J=8.49$  Hz, 2H), 6.16 (d,  $J=8.07$  Hz, 3H), 5.86 (d,  $J=2.05$  Hz, 1H), 5.70 (d,  $J=2.07$  Hz, 1H), 3.62 (s, 3H), 2.42 (m, 2H), 1.27 (m, 8H), 0.91 (t,  $J=6.6$  Hz, 3H);

FT IR (KBr,  $\text{cm}^{-1}$ ): 1584, 1571, 1483, 1459, 1429, 1261, 1095, 1021, 865, 801, 751, 694;

Elemental analysis calculated for  $\text{C}_{70}\text{H}_{58}\text{IrN}_5\text{O}_2\text{S}_2$  (1257.59 g/mol): C 66.85%, H 4.65%, N 5.57%, found: C 66.90%, H 4.064%, N 5.59%.

### Synthesis of complex XX.

Complex **XX** was prepared following the same procedure reported for complex **XIX** with the following modifications: intermediate **16** (96 mg, 0.048 mmol) and 2 eqs. of  $\text{H}(\text{O}^{\wedge}\text{N})^4$  (46 mg, 0.096 mmol) were treated with 30 eqs. of trimethylamine (86 mg, 1.44 mmol);

Brown solid; yield: 51% (70 mg); m.p. > 250°C;

$^1\text{H}$  NMR ( $\text{CDCl}_3$ , 300 MHz, TMS)  $\delta$  = 8.44 (d,  $J=8.37$  Hz, 1H), 8.05 (d,  $J=7.14$  Hz, 1H), 7.98 (s, 1H), 7.61 (t,  $J=6.59$  Hz, 3H), 7.41 (d,  $J=8.64$  Hz, 2H), 7.20-6.80 (m, 36H), 6.72

(d, J=9.06 Hz, 4H), 6.52 (d, J=10.83 Hz, 4H), 6.33 (t, J=9.33 Hz, 4H), 5.86 (d, J=2.19 Hz, 1H), 5.73 (d, J=1.53 Hz, 1H), 3.65 (s, 3H);

FT IR (KBr,  $\text{cm}^{-1}$ ): 1572, 1526, 1490, 1460, 1386, 1268, 1172, 1144, 1067, 822, 751, 695, 509;

Elemental analysis calculated for  $\text{C}_{82}\text{H}_{59}\text{IrN}_6\text{O}_2\text{S}_2$  (1416.73 g/mol): C 69.52%, H 4.20%, N 5.93%, found: C 69.60%, H 4.30%, N 6.01%



## References

1. A. Goetzberger, V.U. Hoffmann, Photovoltaic Solar Energy Generation, Springer-Verlag Berlin Heidelberg (2005);
2. D. M. Chapin, C. S. Fuller, G. L. Pearson., *Journal of Applied Physics.*, **25**, 676 (1954);
3. R. Brendel, Thin-Film Crystalline Silicon Solar Cells Physics and Technology WILEY-VCH GmbH & Co. KGaA (2003);
4. T. Markvart, L. Castaner, Solar Cells: Materials, Manufacture and Operation, Elsevier, Oxford, UK (2005);
5. A. Parisi, L. Curcio, V. Rocca, S. Stivala, A. C. Cino, A. C. Busacca, G. Cipriani, D. La Cascia, V. Di Dio, R. Miceli, G. R. Galluzzo, *International Journal of Photoenergy* **2013**, 1 (2013);
6. A. Goetzberger, C. Hebling, *Solar Energy Materials and Solar Cells*, **62**, 1 (2000);
7. K. Ramasamy, M. A. Malik, N. Revaprasadu, P. O'Brien, *Chemistry of Materials*, **25**, 3551 (2013); M. P. Suryawanshi, G. L. Agawane, S. M. Bhosale, S. W. Shin, P. S. Patil, J. H. Kim, A. V. Moholkar, *Materials Technology*, **28**, 98 (2013);
8. D. B. Mitzi, M. Yuan, W. Liu, A. J. Kellock, S. J. Chey, V. Deline, A. G. Schrott, *Advanced Materials*, **20**, 3657 (2008);
9. a) M. A. Green, K. Emery, D. L. King, Y. Hishikawa, W. Warta, *Progress in Photovoltaics: Research and Applications*, **15**, 35 (2007); b) Report on the Basic energy Sciences Workshop on Solar energy utilization, U.S. Dept. of Energy, April 18-21 (2005);
10. M. Kemell, M. Ritala, M. Leskelä, *Critical Review in Solid State and Materials Sciences*, **30**, 1 (2005);
11. Powder Diffraction Files, Card 40-1487, International Centre for Diffraction Data, Newton Square, Pennsylvania, PA;
12. R. W. Birkmire, *Solar Energy Materials and Solar Cells*, **65**, 17 (2001);
13. a) M. A. Contreras, K. Ramanathan, J. AbuShama, F. Hasoon, D. L. Young, B. Egaas, R. Noufi, *Progress in Photovoltaics: Research and Application.*, **13**, 209 (2005); b) M. Kaelin, D. Rudmann, A. N. Tiwari, *Solar Energy*, **77**, 749 (2004);
14. M. E. Calixto, K. D. Dobson, B. E. McCandless, R. W. Birkmire, *Journal of the Electrochemical Society*, **153**, G521 (2006);

15. O. A. Abdulrazzaq, V. Saini, S. Bourdo, E. Dervishi, A. S. Biris, *Particulate Science and Technology*, **31**, 427 (2013); S. B. Darling, F. Youc, *Royal Society of Chemistry Advances*, **3**, 17633 (2013);
16. P. Sahni, *Advanced Science Letters*, **5**, 1 (2012); L.-L. Li, E. W.-G. Diau, *Chemical Society Review*, **42**, 291 (2013); H. Spanggaard, F. C. Krebs, *Solar Energy Materials & Solar Cells*, **83**, 125 (2004);
17. H. Sirringhau, T. Sakanoue, J.-F. Chang, *Physica Status Solidi B*, **249**, 1655 (2012); P. Stallinga, *Advanced Mateials*, **23**, 3356 (2011);
18. K. Feron, W. J. Belcher, C. J. Fell, P. C. Dastoor, *International Journal of Molecular Sciences*, **13**, 17019 (2012);
19. C. W. Tang, *Applied Physics Letters*, **48**, 183 (1986);
20. N. S. Sariciftci, L. Smilowitz, A. J. Heeger, F. Wudl, *Synthetic Metals*, **59**, 333 (1993);
21. S. E. Shaheen, C. J. Brabec, N. S. Sariciftci, F. Padinger, T. Frmhert, J. C. Hummelen, *Applied Physics Letters*, **78**, 841 (2001);
22. F. Padinger, R.S. Rittberger, N. S. Sariciftci, *Advanced Functional Materials*, **13**, 85 (2003);
23. J. Drechel, B. Mannig, F. Kozlowski, M. Pfeiffer, K. Leo, H. Hoppe, *Applied Physics Letters*, **86**, 244102 (2005); Y. Shao, Y. Tang, *Advanced Materials*, **17**, 2481 (2005); P. Peumans, S. Uchida, S. R. Forrest, *Nature*, **425**, 158 (2003);
24. H.-C. Chen, Y.-H. Chen, C.- C. Liu, Y.-C. Chien, S.-W. Chou, P.-T. Chou, *Chemistry of Materials*, **24**, 4766 (2012); S. Chen, C. E. Small, C. M. Amb, J. Subbiah, T. Lai, S.-W. Tsang, J. R. Manders, J. R. Reynolds, F. So, *Advanced Energy Materials*, **2**, 1333 (2012);
25. G. Yu, J. Gao, J. C. Hummelen, F. Wudl, A. Heeger, *Science*, **270**, 1789 (1995);
26. M. D. Archer, A. J. Nozik, Nanostructured and photoelectrochemical systems for solar photon conversion, Imperial College Press, London (2008);
27. a) Q. L. Huang, H. X. Li, *Chiese Science Bulletin*, **58**, 2677 (2013); b) R. P. Singh, O. S. Kushwaha, *Macromolecular Symposia*, **327**, 128 (2013);
28. G. Yu, A. J. Heeger, *Journal of Applied Physics*, **78**, 4510 (1995);
29. S. van Bavel, S. Veenstra, J. Loos, *Macromolecular Rapid Communications*, **31**, 1835 (2010);
30. C. Deibel, V. Dyakonov, *Reports on Progress in Physics*, **73**, 096401 (2010);
31. F. Braun, *PhD thesis*, Physics Department, University of London (2007);

32. a) M. Heeney, W. Zhang, D. J. Crouch, D. Sparrowe, R. Hamilton, S. Higgins, P. Skabara, I. McCulloch, *Chemical Communications*, 5061 (2007); b) D. Mulbacher, M. Scharber, M. Morana, Z. Zhu, D. Waller, R. Gaudiana, C. Brabec, *Advanced Materials*, **18**, 2884 (2006);
33. S. Sergeev, W. Pisula, Y. H. Geerts, *Chemical Society Reviews*, **36**, 1902 (2007);
34. E. Kimakis, I. Alexandrou, G. A. J. Amaratunga, *Journal of Applied Physics*, **93**, 1764 (2003);
35. A. Hagfeldt, M. Graetzel, *Accounts of Chemical Research*, **33**, 269 (2000);
36. H. Gerischer, H. Tributsch, *Physical Chemistry*, **72**, 437 (1968); M. P. Dare-Edwards, J. B. Goodenough, A. Hamnett, K. R. Seddon, R. D. Wright, *Faraday Discussions for the Chemical Society*, **70**, 285 (1980); H. Tsubomura, M. Matsumura, Y. Nomura, T. Amamiya, *Nature*, **261**, 402 (1976);
37. D. Dunghong, N. Serpone, M. Grätzel, *Helvetica Chimica Acta*, **67**, 1012 (1984); J. Desilvestro, M. Grätzel, L. Kavan, J. Moser, J. Augustynski, *Journal of the American Chemical Society*, **107**, 2988 (1985);
39. B. O'Reagan, M. Grätzel, *Nature*, **353**, 737 (1991);
40. M. K. Nazeeruddin, Q. Wang, L. Cevey, V. Aranyos, P. Liska, E. Figgemeier, C. Klein, N. Hirata, S. Koops, S. A. Haque, J. R. Durrant, A. Hagfeldt, A. B. P. Lever, M. Grätzel, *Inorganic Chemistry*, **45**, 787 (2006);
41. M. D. Archer, A. J. Nozik (editors), *Solar Photon Conversion*, Imperial College Press, London, 2008, Cap. 8
42. M. Grätzel, *Journal of Photochemistry and Photobiology C: Photochemistry reviews*, **4**, 145 (2003);
43. a) M. K. Nazeeruddin, A. Kay, I. Rodicio, R. Humphrybacker, E. Muller, P. Liska, *Journal of the American Chemical Society*, **115**, 6382 (1993); b) H. Zabri, F. Odobel, S. Altobello, S. Caramori, C. A. Bignozzi, *Journal of Photochemistry and Photobiology A: Chemistry*, **166**, 99 (2004);
44. C.A. Bignozzia, R. Argazzib, R. Boarettoa, E. Busattoa, S. Carli, F. Ronconia, S. Caramoria, *Coordination Chemistry Reviews*, **257** 1472 (2013);
45. P. G. Bomben, K. C. D. Robson, B. D. Koivisto, C. P. Berlinguette, *Coordination Chemistry Reviews*, **256**, 1438 (2012);
46. M. K. Nazeeruddin, A. Kay, I. Rodicio, R. Humphry-Baker, E. Muller, P. Liska, N. Vlachopoulos, M. Grätzel, *Journal of the American Chemical Society*, **115**, 6382 (1993);

47. G. Benkő , J. Kallioinen, J. E. I. Korppi-Tommola, A. P. Yartsev, V. Sundström, *Journal of the American Chemical Society*, **124**, 489 (2002);
48. M. K. Nazeeruddin, P. Pechy, M. Grätzel, *Chem. Commun.* (1997) 1705; M. K. Nazeeruddin, P. Pechy, T. Renouard, S.M. Zakeeruddin, R. Humphry-Baker, P. Comte, P. Liska, L. Cevey, E. Costa, V. Shklover, L. Spiccia, G.B. Deacon, C. A. Bignozzi, M. Grätzel, *Journal of the American Chemical Society*, **123**, 1613 (2001);
49. A. C. Onicha, F. N. Castellano, *Journal of Physical Chemistry C*, 114, (2010);
50. E. Baranoff, J.-H. Yum, I. Jung, R. Vulcano, M. Grätzel, M. K. Nazeeruddin; *Chemistry An asian Journal*, **5**, 496 (2010);
51. A. Islam, H. Sugihara, K. Hara, L. P. Singh, R. Katoh, M. Yanagida, Y. Takahashi, S. Murata, H. Arakawa, G. Fujihashi, *Inorganic Chemistry*, **40**, 5371 (2001);
52. T. Bessho, E. C. Constable, M. Grätzel, A. Hernandez Redondo, C. E. Housecroft, W. Kylberg, M. K. Nazeeruddin, M. Neuburger, S. Schaffner, *Chemical Communications*, **32**, 3717 (2008);
53. S. Ferrere, B. A. Gregg, *Journal of the American Chemical Society*, **120**, 843 (1998);
54. a) Y. Tachibana, H. Y. Akiyama; Y. Ohtsuka; T. Torimoto; S. Kuwabata, *Chemistry Letters*, **36**, 88 (2007), b) I. Robel, V. Subramanian, M. Kuno, P. V. Kamat, *Journal of the American Chemical Society*, **128**, 2385 (2006); c) R. Plass, S. Pelet, J. Krueger, M. Grätzel, U. J. Bach, *Physical Chemistry B*, **106**, 7578 (2002); d) A. Zaban, O. I. Micic, B. A. Gregg, A. J. Nozik, *Langmuir*, **14**, 3153 (1998); e) P. Yu, K. Zhu, A. G. Norman, S. Ferrere, A. J. Frank, A. J. Nozik, *Journal of Physical Chemistry B*, **110**, 25451 (2006);
55. A. Kojima, K. Teshima, Y. Shirai, T. Miyasaka, *Journal of the American Chemical Society*, **131**, 6050 (2009);
56. L. Mingzhen, M. B. Johnston, H. J. Snaith, *Nature*, **501**, 395 (2013);
57. M. Wright, A. Uddin, *Solar Energy Materials & Solar Cells*, **107**, 87 (2012);
- 58.a) M. A. Green, *Philosophical Transactions of the Royal Society A*, **371**, 20110413 (2013); b) S. Binetti, M. Acciarri, A. Le Donne, M. Morgan, Y. Jestin, *International Journal of Photoenergy*, **2013**, 1 (2013);
59. U. P. Singh, S. P. Patra, *International Journal of Photoenergy*, **2010**, 1 (2010);
- 60.a) K. Vandewal, S. Himmelberger, A. Salleo, *Macromolecules*, **46**, 6379 (2013); b) Y. Lin, Y. Lia, X. Zhan, *Chemical Society Reviews*, **41**, 4245 (2012);

61. a) B. Bozic-Weber, E. C. Constable, C. E. Housecroft, *Coordination Chemistry Reviews*, **257**, 3089 (2013); b) J. Gong, J. Liang, K. Sumathy, *Renewable and Sustainable Energy Reviews*, **16**, 5848 (2012);
62. S. R. Forrest, *Nature*, **428**, 911 (2004);
63. Special Issue: Organic Electronics and Optoelectronics, *Chemical Reviews*, **107**, 923 (2007) and papers therein;
64. D. S. Weiss, M. Abkowitz, *Chemical Reviews*, **110**, 479 (2010);
65. C. Im, E. V. Emelianova, H. Bassler, H. Spreitzer, H. Beker, *Journal of Chemical Physics*, **117**, 2961 (2002);
66. N. Geacintov, M. Pope, *Journal of Chemical Physics*, **47**, 1194 (1967);
67. S. Sergeyev, W. Pisula, Y. H. Geerts, *Chemical Society Reviews*, **36**, 1902 (2007);
68. S. Chandrasekhar, B. K. Sadashiva, K. A. Suresh, *Pramana*, **9**, 471 (1977);
69. S. Kumar, *Chemical Society Reviews*, **35**, 83 (2006);
70. B. R. Kaafarani, *Chemistry of Materials*, **23**, 378 (2011);
71. A. N. Cammidge, R. J. Bushby, *Handbook of Liquid Crystals*, ed. D. Demus, J. W. Goodby, G. W. Gray, H. W. Spiess, V. Vill, Wiley-WCH, Weinheim, vol 2B, ch 7 (1998);
72. a) J. F. van der Pol, E. Neeleman, J. W. Zwikker, R. J. Nolte, W. Drenth, J. Aerts, R. Visser, S. J. Picken, *Liquid Crystals*, **6**, 577 (1989); b) K. Ohta, L. Jacquemin, C. Sirlin, L. Bosio, J. Simon, *New Journal of Chemistry*, **12**, 751 (1988); c) D. Guillon, A. Skoulis, C. Piechocki, J. Simon, P. Weber, *Molecular Crystals Liquid Crystals*, **100**, 275 (1983); d) L. Dulog, A. Gittinger, *Molecular Crystals Liquid Crystals*, **213**, 31 (1992); e) S. Sergeyev, E. Pouzet, O. Debever, J. Levin, J. Gierschner, J. Cornil, R. Gomez-Aspe, Y. H. Geets, *Journal of Materials Chemistry*, **17**, 1777 (2007);
73. P. Herwig, C. W. Kayser, K. Müllen, H. W. Spiess, *Advanced Materials*, **8**, 510 (1996);
74. E. M. Garcia-Frutos, U. K. Pandey, R. Termine, A. Omenat, J. Barbera, J. L. Serrano, A. Golemme, B. Gomez-Lor, *Angewandte Chemie International Edition*, **50**, 7399 (2011);
75. K. Y. Law, *Chemical Reviews*, **93**, 449 (1993);
76. (a) I. Aiello, D. Dattilo, M. Ghedini, A. Golemme, *Journal of the American Chemical Society*, **123**, 5598 (2001); (b) R. Termine, D. Dattilo, I. Aiello, M. Ghedini, A. Golemme, *Advanced Materials*, **15**, 723 (2003);

77. I. Aiello, D. Dattilo, M. Ghedini, A. Bruno, R. Termine, A. Golemme, *Advanced Materials*, **14**, 1233 (2002);
78. M. Ghedini, A. Golemme, I. Aiello, N. Godbert, R. Termine, A. Crispini, M. La Deda, F. Lelj, M. Amati, S. Belviso, *Journal of Materials Chemistry*, **21**, 13434 (2011);
79. N. Godbert, D. Dattilo, R. Termine, I. Aiello, A. Bellusci, A. Crispini, A. Golemme, M. Ghedini, *Chemistry—An Asian Journal*, **4**, 1141 (2009);
80. a) H. Eichhorn, *Journal of Porphyrins and Phthalocyanines*, **4**, 88 (2000); b) M. G. Debije, J. Piris, M. P. de Haas, J. M. Warman, Z. Tomovic, C. D. Simpson, M. D. Watson, K. Mullen, *Journal of the American Chemical Society*, **126**, 4641 (2004); c) A. M. van de Craats, J. M. Warman, *Advanced Materials*, **13**, 130 (2001);
81. a) T. Q. Nguyen, M. L. Bushey, L. E. Brus and C. J. Nuckolls, *Journal of the American Chemical Society*, **124**, 15051 (2002); b) T. Kato, N. Mizoshita and K. Kishimoto, *Angewandte Chemie International Edition*, **45**, 38 (2006);
82. a) J. J. van Gorp, J. A. J. M. Vekemans, E. W. Meijer, *Journal of the American Chemical Society*, **124**, 14759 (2002); b) M. L. Bushey, A. Hwang, P. W. Stephens, C. Nuckolls, *Angewandte Chemie International Edition*, **41**, 2828 (2002); c) S. Laschat, A. Baro, N. Steinke, F. Giesselmann, C. Hagele, G. Scalia, R. Judele, E. Kapatsina, S. Sauer, A. Schreivogel, M. Tosoni, *Angewandte Chemie International Edition*, **46**, 4832 (2007);
83. G. Patonay, M. D. Antoine, *Analytical Chemistry*, **63**, 321A (1991);
84. M. Ghedini, D. Pucci, A. Crispini, A. Bellusci, M. La Deda, I. Aiello, T. Pugliese, *Inorganic Chemistry Communications*, **10**, 243 (2007);
85. I. Aiello, M. Ghedini, M. La Deda, *Journal of Luminescence*, **96**, 249 (2002);
86. M. S. J. Briggs, I. Bruce, J. N. Miller, C. J. Moody, A. C. Simmonds, E. Swann, *Journal of Chemical Society, Perkin Transactions 1*, 1051 (1997);
87. S. A. Swanson, G. M. Wallraff, J. P. Chen, W. Zhang, L. D. Bozano, K. R. Carter, J. R. Salem, R. Villa and J. Campbell Scott, *Chemistry of Materials*, **15**, 2305 (2003);
88. S. A. Martin-Brown, Y. Fu, G. Saroja, M. M. Collinson, D. A. Higgins, *Analytical Chemistry*, **77**, 486 (2005);
89. N. Godbert, A. Crispini, M. Ghedini, M. Carini, F. Chiaravalloti, A. Ferrise, *J. Appl. Cryst.*, Submitted;
90. M. Lehmann, C. Koln, H. Meier, S. Renker, A. Oehlhol, *Journal of Materials Chemistry*, **16**, 441 (2006);

91. M. Kaller, S. Tussetschl, P. Fisher, C. Deck, A. Baro, F. Giesselmann, S. Laschat, *Chemistry–An European Journal*, **15**, 9530 (2009);
92. V. A. Gunyakov, N. P. Shestakov, S. M. Shibli, *Liquid Crystals*, **30**, 871 (2003);
93. M. Kaller, C. Deck, A. Meister, G. Hause, A. Baro, S. Laschat, *Chemistry–An European Journal*, **16**, 6326 (2010);
94. K. Venkatesan, P. H. J. Kouwer, S. Yagi, P. Muller, T. M. Swager, *Journal of Materials Chemistry*, **18**, 400 (2008);
95. A. Ionescu, N. Godbert, I. Aiello, A. Crispini, M. Ghedini, *Molecular Crystals Liquid Crystals*, **558**, 84 (2012);
96. C. M. Golini, B. W. Williamsand, J. B. Foresman, *Journal of Fluorescence*, **8**, 395 (1998);
97. E. M. Garcia-Frutos, U. K. Pandey, R. Termine, A. Omenat, J. Barbera, J. L. Serrano, A. Golemme, B. Gomez-Lor, *Angewandte Chemie International Edition*, **50**, 7399 (2011);
98. N. A. Davidenko, N. A. Derevyanko, A. A. Ishchenko, N. G. Kuvshinsky, A. V. Kulinich, O. Y. Neiland, M. V. Plotniece, *Russian Chemical Bulletin*, **53**, 1674 (2004);
99. J. Kalinowski and K. Szybowska, *Organic Electronics*, **9**, 1032 (2008);
100. a) H. C. Hesse, J. Weickert, M. Al-Hussein, L. Dossel, X. Feng, K. Mullen, L. Schmidt-Mende, *Solar Energy Materials & Solar Cells*, **94**, 560 (2010); b) Q. Zheng, G. Fang, W. Bai, N. Sun, P. Qin, X. Fan, F. Cheng, L. Yuan, X. Zhao, *Solar Energy Materials & Solar Cells*, **95**, 2200 (2011);
101. M. Albrecht, E. P. Urriolabeitia, M. R. Meneghetti, J. Dupont & M. Pfeffer (Eds.), *Palladacycles: Synthesis, Characterization and Applications*, Wiley-VCH: Weinheim, Germany (2008);
102. T. Pugliese, N. Godbert, I. Aiello, M. La Deda, M. Ghedini, M. Amati, S. Belviso, F. Lelj, *Dalton Transactions*, **2008**, 6563;
103. J. Pommerehne, H. Vestweber, W. Guss, R. F. Mahrt, H. Bäessler, M. Porsch, J. Daub, *Advanced Materials*, **7**, 551 (1995);
104. Z. Miskolczy, L. Biczók, I. Jablonkai, *Chemical Physics Letters*, **440**, 92 (2007);
105. J. Zhou, X. Wan, Y. Liu, Y. Zuo, Z. Li, G. He, G. Long, W. Ni, C. Li, X. Su, Y. Chen, . *Journal of the American Chemical Society*, **134**, 16345 (2012);
106. M. Riede, T. Mueller, W. Tress, R. Schueppel, K. Leo, *Nanotechnology*, **19**, 424001,

107. O. P. Lee, A. T. Yiu, P. M Beaujuge, T. W. Holcombe, J. E. Millestone, J. D. Douglas, M. S. Chen, J. M. J. Frechet, *Advanced Materials*, **23**, 5359 (2011);
108. N. Cho, K. Song, J. K. Lee, J. Ko, *Chemistry-A European Journal*, **18**, 11433 (2012);
109. H. Shang, H. Fan, Y. Liu, W. Hu, Y. Li, X. Zhan, *Advanced Materials*, **23**, 1554 (2011);
110. G. C. Welch, L. A. Perez, C.V. Hoven, X-D. Dang, A. Sharenko, M. F. Toney, E. J. Kramer, T-Q. Nguyen, G. C. Bazan., *Journal of Materials Chemistry*, **21**, 12700 (2011);
111. J. W. Lee, Y. S. Choi, W. H. Jo, *Organic Electronics*, **13**, 3060 (2012);
112. Y. Huang, L. Li, X. Peng, J. Peng, Y. Cao, *Journal of Materials Chemistry*, **22**, 21841 (2012);
113. G. Chen, H. Sasabe, Z. Wang, X-F Wang, Z. Hong, Y. Yang, J. Kido, *Advanced Materials*, **24**, 2768 (2012);
114. V. Steinmann, N .M. Kronenberg, M. R. Lenze, S. M. Graf, D. Hertel, K. Meerholz, H. Bürckstümmer, E. V. Tulyakova, F. Würthner, *Advanced Energy Materials*, **1**, 888 (2011);
115. W.-Y. Wong, C.-L. Ho, *Accounts of Chemical Research*, **43**,1246 (2010);
116. W.-Y. Wong, X.-Z. Wang, Z. He, A. B. Djuricic , C.-T. Yip, K.-Y. Cheung, K.-Y, H. Wang, C. S. K. Mak, W.-K. Chan, *Nature Materials*, **6**, 521 (2007);
117. X. Huang, C. Zhu, S. Zhang, W. Li, Y. Guo, X. Zhan, Y. Liu, Z. Bo, *Macromolecules*, **41**, 6895 (2008);
118. C. Wanzhu, W. Ming, Z. Jie, W. Ergang, Y. Tingbing, H. Chao, S. M. Ji, W. Hongbin, G. Xiong, C. J. Yong, *Physical Chemistry C*, **115**, 2314 (2011);
119. S. Kim, B. Kim, J. Kim, *Applied Materials*, **6**, 1264 (2010);
120. H. Y. Chen, J. Hou, S. Zhang, Y. Liang, G. Yang, Y. Yang, L. Yu, Y. Wu, G. Li, *Nature Photonics*, **3**, 649 (2009);
121. E. Verploegen, R. Mondal, C. Bettinger, S. Sok, M. Toney, Z. Bao, *Advanced Functional Materials*, **20**, 3519 (2010);
122. G. Dennler, K. Forberich, M. Scharber, et al., *Journal of Applied Physics*, **102**, 054516 (2007);
123. J. Natera, L. Otero, L. Sereno, F. Fungo, N. S. Wang, Y-M. Tsai, T-Y. Hwu, K-T. Wong, *Macromolecules*, **40**, 4456 (2007);



124. L. Otero, L. Sereno, F. Fungo, Y.-L. Liao, C.-Y. Lin, K.-T. Wong *Chemical Materials*, **18**, 3495, (2006);
125. C. W. Huang, K. Y. Chiu, S. H. Cheng, *Dalton Transactions*, 2417 (2005);
126. N. Vettorazzi, J. J. Silber, L. Sereno, *Journal of Electroanalytical Chemistry*, **125**, 459 (1981);
127. E. T. Seo, R. F. Nelson, J. M. Fritsch, L. S. Marcoux, D. W. Leedy, R. N. Adams, *Journal of the American Chemical Society*, **88**, 3498 (1966);
128. M.-K. Leung, M.-Y. Chou, Y. O. Su, C. L. Chiang, H.-L. Chen, C. F. Yang, C.-C. Yang, C.-C. Lin, H.-T. Chen., *Organic Letters*, **5**, 839 (2003);
129. G. Sanchez, J. Vives, G. Lopez, L. Serrano, L. Garcia, J. Perez., *European Journal of Inorganic Chemistry*, 2360 (2005);
130. M. Oyama, K. Nozaki, S. Okazaki, *Analytical Chemistry*, **63**, 1387 (1991);
131. T. V. Arjunan, T. S. Senthil, *Materials Technology*, **28**, 9 (2013);
132. G. Hagfeldt, L. Boschloo, L. Sun, L. Sun, H. Kloo, H. Pettersson, *Chemical Reviews*, **110**, 6595 (2010);
133. S. Ardo, G. J. Meyer, *Chemical Society Reviews*, **38**, 115 (2009);
134. P. Pechy, F. P. Rotzinger, M. K. Nazeeruddin, O. Kohle, S. M. Zakeeruddin, R. Humphry-Baker, M. Grätzel. *Journal of Chemical Society, Chemical Communications*, **1**, 65 (1995);
135. J. Cong, X. Yang, J. Liu, Zhao, Y. Hao, Y. Wang, L. Sun, *Chemical Communications*, **48**, 6663 (2012);
136. A. Sepehrifard, A. Stublla, S. Haftchenary, S. Chen, P. G. Potvin, S. Morin, *Journal of New Materials for Electrochemical Systems*, **11**, 281 (2008);
137. E. Galoppini, *Coordination Chemistry Reviews*, **248**, 1283 (2004);
138. K. Hara, H. Sugihara, Y. Tachibana, A. Islam, M. Yanagida, K. Sayama, H. Arakawa, *Langmuir*, **17**, 5992 (2001);
139. P. E. Eaton, G. R. Carlson, J. T. Lee, *Journal of Organic Chemistry*, **38**, 23 (1973);
140. K. Meyer, H. S. Bloch, *Organic Synthesis*, Coll. **3**, 637 (1955);
141. a) N. Koumura, Z.-S. Wang, S. Mori, M. Miyashita, E. Suzuki, K. Hara, *Journal of the American Chemical Society*, **128**, 14256 (2006); b) Q. Feng, G. Zhou, Z.-S. Wang, *Journal of Power Sources*, **239**, 16 (2013);
142. M. Chandrasekharam, G. Rajkumar, C. S. Rao, G. Rajkumar, C. S. Rao, P. Y. Reddy, M. L. Kantam, *Advances in OptoElectronics* **2011**, 432803, (2011);

143. G. C. Vougioukalakis, A. I. Philippopoulos, T. Stergiopoulos, P. Falaras, *Coordination Chemistry Reviews*, **255**, 2602 (2011);
144. M. La Deda, A. Crispini, I. Aiello, M. Ghedini, M. Amati, S. Belviso, F. Lelj, *Dalton Transactions*, **40**, 5259 (2011);
145. E. F. Schubert, J. K. Kim, *Science*, **308**, 1274 (2005);
146. S. Nakamura, M. Senoh, T. Mukai, *Japanese Journal of Applied Physics*, **32**, L8 (1993); S. Nakamura, T. Mukai, M. Senoh, *Applied Physics Letters*, **64**, 1687 (1994);
147. L. Chen, C.-C. In, C.-W. Yeh, R.-S. Liu, *Materials*, **3**, 2172 (2010);
148. M. Pope, H. P. Kallmann, P. Maganate, *Journal of Chemical Physics*, **38**, 2042 (1963);
149. C. W. Tang, S. A. VanSylke, *Applied Physics Letters*, **51**, 913 (1987);
150. a) H. Sasabe, J. Kido, *Chemical Materials*, **23**, 621 (2011); b) A. Kohler, H. Bassler, *Materials Science and Engineering R*, **66**, 71 (2009);
151. J. H. Burroughess, D. D. C. Bradley, A. R. Brown, R. N. Marks, K. Mackay, R. H. friend, P. L. Burns, A. B. holmes, *Nature*, **347**, 539 (1990);
152. E. Holder, B. M. W. Langeveld, U. S. Schubert, *Advanced Materials*, **17**, 1109 (2005);
153. M. E. Kondakova, J. C. Deaton, T. D. Pawlik, D. J. Giesen, D. Y. Kondakov, R. H. Young, T. L. Royster, D. L. Comfort, J. D. Shore *Journal of Applied Physics*, **107**, 014515 (2000);
154. U. Giovanella, C. Botta, F. Galeotti, B. Vercelli, S. Battiato, M. Pasinia, *Journal of Materials Chemistry C*, **1**, 5322 (2013);
155. J. Slinker, D. Bernards, P. L. Houston, H. D. Abruna, S. Bernhard, G. G. Malliaras, *Chemical Communications*, **2003**, 2392 (2003);
156. V. I. Adamovich, S. R. Cordero, P. I. Djurovich, A. Tamayo, M. E. Thompson, B. W. D'Adrade, S. R. Forrest, *Organic Electronics*, **4**, 77 (2003);
157. a) S. Lamansky, P. Djurovich, D. Murphy, H. E. Lee, C. Adachi, P. E. Burrows, S. R. Forrest, M. E. Thompson, *Journal of the American Chemical Society*, **12**, 4304 (2001); b) H. Becker, H. Vestweber, A. Gerhard, P. Stossel, R. Fortte, *Digital Technology Pap.-Society Information Display International Symposium*, **35**, 796 (2004);
158. L. Yu, J. Liu, S. Hu, R. He, W. Yang, H. Wu, J. Peng, R. Xia, D. D. C. Bradley, *Advanced Functional Materials*, **23**, 4366 (2013);
159. D. Y. Kondakov, W. C. Lenhart, W. F. Nichols, *Journal of Applied Physics*, **101**, 024512 (2007);

160. Y.-S. Tyan, *Journal of Photonics for Energy*, **1**, 011009 (2011);
161. Q. Pei, G. Yu, C. Zhang, Y. Yang, A. J. Heeger, *Science*, **269**, 1086 (1995);
162. a) N. D. Robinson, J. H. Shin, M. Berggren, L. Edman, *Physical Review Letters*, **74**, 155210, (2006); b) G. G. Malliaras, J. D. Slinker, J. A. De Franco, M. J. Jaquith, W. R. Silveira, Y.-W. Zhong, J. M. Moran-Mirabal, H. G. Craighead, H. D. Abruna, J. A. Marohn, *Nature Materials*, **7**, 168 (2008); M. Lenes, G. Garcia-Belmonte, D. Tordera, A. Pretegas, J. Bisquert, H. J. Bolink, *Advanced Functional Materials*, **21**, 1581 (2011);
163. R. D. Costa, E. Orti, H. J. Bolink, *Pure Applied Chemistry*, **83**, 2115 (2011);
164. Y. Yang, Q. Pei, *Journal of Applied Physics*, **81**, 3294 (1997);
165. D. C. Harris, M. D. Bertolucci, *Symmetry and Spectroscopy*, Dover Publications, Inc., New York, 1989;
166. M. A. Baldo, D. F. O'Brien, Y. You, A. Shoustikov, S. Sibley, M. E. Thompson, S. R. Forrest, *Nature*, **395**, 151 (1998);
167. X. Yang, C. Yao, G. Zhou, *Platinum Metals Reviews*, **57**, 2 (2013);
168. a) M. A. Baldo, S. Lamansky, P. E. Burrows, M. E. Thompson, S. R. Forrest, *Applied Physics Letters*, **75**, 4 (1999); b) C. Adachi, M. A. Baldo, M. E. Thompson, S. R. Forrest, *Journal of Applied Physics*, **90**, 10 (2001);
169. *Photofunctional Transition Metal Complexes*, in *Structure and Bonding*, Editor: V.W.W. Yam, Vol. **123**, Springer, 2007;
170. N. Thejo Kalyani, S. J. Dhoble, *Renewable and Sustainable Energy Reviews*, **16**, 2696 (2012);
171. T. Peng, G. Li, K. Ye, K. Ye, S. Huang, Y. Wu, Y. Liu, Y. Wang, *Organic Electronics*, **14**, 1649 (2013);
172. S. Welter, K. Brunner, J. W. Hofstraat, L. De Cola, *Nature*, **421**, 54 (2003);
173. K. Kalyanasundaram, *Photochemistry of Polypyridine and Porphyrin Complexes*, Academic Press, London, 1992;
174. a) F. Dumur, D. Bertin, C. R. Mayer, A. Guerlin, G. Wantz, G. Nasr, E. Dumas, F. Miomandre, G. Clavier, D. Gigmes, *Synthetic Metals*, **161**, 1934 (2011); b) D. Tordera, S. Meier, M. Lenes, R.D. Costa, E. Ortí, W. Sarfert, H.J. Bolink, *Advanced Materials*, **24**, 897 (2012);

**175.** a) S. Bernhard, X. Gao, G. G. Malliaras, H. D. Abruna, *Advanced Materials*, **14**, 433 (2002); b) N. Armaroli, G. Accorsi, M. Holler, O. Moudam, J. F. Nierengarten, Z. Zhou, R. T. Wegh, R. Welter, *Advanced Materials*, **18**, 1313 (2006); c) A. R. Hosseini, C. Y. Kohn, J. D. Slinker, S. Flores-Torres, H. D. Abruna, G. G. Malliaras, *Chemical Materials*, **17**, 6114 (2005); d) Q. Zhang, Q. Zhou, Y. Cheng, L. Wang, D. Ma, X. Jing, F. Wang, *Advanced Functional Materials*, **16**, 1203 (2006); e) Y.-M. Wang, F. Teng, Y.-B. Hou, Z. Xu, Y.-S. Wang, W.-F. Fu, *Applied Physical Letters*, **87**, 233512 (2005); f) O. Moudam, A. Kaeser, B. Delavaux-Nicot, C. Duhavon, H. Holler, G. Accorsi, N. Armaroli, I. Seguy, J. Navarro, P. Destruels, J.-F. Nierengarten, *Chemical Communications*, 2007, 3077 (2007); g) F. G. Gao, A. J. Bard, *Chemical Materials*, **14**, 3465 (2002); e) R. D. Costa, D. Tordera, E. Orti, H. J. Bolink, J. Schonle, S. Graber, C. E. Housecroft, E. C. Constable, J. A. Zampese, *Journal of Materials Chemistry*, **21**, 16108 (2011);

**176.** J. D. Slinker, J. Rivnay, J. S. Moskowitz, J. B. Parker, S. Bernhard, H. D. Abruna, G. G. Malliaras, *Journal of Materials Chemistry*, **17**, 2976 (2007); J. D. Slinker, A. A. Gorodetsky, M. S. Lowry, J. Wang, S. Parker, R. Rohl, S. Bernhard, G. G. Malliaras *Journal of the American Chemical Society*, **126**, 2763 (2004);

**177.** a) H.-F. Chen, C. Wu, M.-C. Kuo, M.E. Thompson, K.-T. Wong, *Journal of Materials Chemistry*, **22**, 9556 (2012); b) F. Dumur, Y. Yuskevitch, G. Wantz, C. R. Mayer, D. Bertin, D. Gigmès, *Synthetic Metals*, **177**, 100 (2013);

**178.** a) G. Kalyuzhny, M. Buda, J. McNeill, P. Barbara, A. J. Bard, *Journal of the American Chemical Society*, **125**, 6272 (2003); b) L. J. Soltzberg, J. Slinker, S. Flores-Torres, D. Bernardis, G. G. Malliaras, H. D. Abruna, J. S. Kim, R. H. Friend, M. D. Kaplan, V. Goldberg, *Journal of the American Chemical Society*, **128**, 7761 (2006); c) J. D. Slinker, J.-S. Kim, S. Flores-Torres, J. H. Delcamp, H. D. Abruna, R. H. Friend, G. G. Malliaras, *Journal of Materials Chemistry*, **7**, 76 (2007);

**179.** F. Alary, J. L. Heully, L. Bijeire, P. Vicendo, *Inorganic Chemistry*, **46**, 3154 (2007); B. Durham, J. V. Caspar, J. K. Nagle, T. J. Meyer, *Journal of the American Chemical Society*, **104**, 4803 (1982); D. W. Thompson, J. F. Wishart, B. S. Brunshwig, N. Sutin, *Journal of Physical Chemistry A*, **105**, 8117 (2001); J. Van Houten, R. J. Watts, *Journal of the American Chemical Society*, **98**, 4853 (1976);

- 180.** a) H. J. Bolink, E. Coronado, R. D. Costa, E. Ortí, M. Sessolo, S. Graber, K. Doyle, M. Neuburger, C. E. Housecroft, E. C. Constable, *Advanced Materials*, **20**, 3910 (2008); b) S. Graber, K. Doyle, M. Neuburger, C. E. Housecroft, E. C. Constable, R. D. Costa, E. Ortí, D. Repetto, H. J. Bolink, *Journal of the American Chemical Society*, **130**, 14944 (2008); c) M. Lenes, G. Garcia-Belmonte, D. Tordera, S. A. Pertega, J. Bisquert, H. J. Bolink, *Advanced Functional Materials*, **21**, 1581 (2011); d) D. Tordera, S. Meier, M. Lenes, R. D. Costa, E. Ortí, W. Sarfert, H. J. Bolink, *Advanced Materials*, **24**, 897 (2012);
- 181.** H. J. Bolink, E. Coronado, R. D. Costa, N. Lardies, E. Orti, *Inorganic Chemistry*, **47**, 9149 (2008);
- 182.** R. D. Costa, G. Fernandez, L. Sanchez, N. Martin, E. Orti, H. J. Bolink, *Chemistry -A European Journal*, **16**, 9855 (2010);
- 183.** E. Zysman-Colman, J. D. Slinker, J. B. Parker, J. B. Parker, G. G. Malliaras, S. Bernhard, *Chemical Materials*, **20**, 388 (2008);
- 184.** H. C. Su, H. F. Che, C. C. Wu, K. T. Wong, *Chemistry-An Asian Journal*, **3**, 1922 (2008);
- 185.** C. Ulbricht, B. Beyer, C. Friebe, A. Winter, U. S. Schubert, *Advanced Materials*, **21**, 4418 (2009);
- 186.** I. M. Dixon, J.-P. Collin, J.-P. Sauvage, J.-P. Sauvage, L. Flamigni, S. Encinas, F. Barigeletti, *Chemical Society Review*, **29**, 385 (2000);
- 187.** a) V. V. Grushin, N. Herron, D. D. LeCloux, W. J. Marshall, V. A. Petrov, Y. Wang, *Chemical Communications*, **2001**, 1494 (2001); b) K. Dedeian, P. I. Dhurovic, F. O. Garces, G. Carlson, R. J. Watts, *Inorganic Chemistry*, **30**, 1685 (1991);
- 188.** S. Lamansky, P. I. Djurovich, D. Murphy, F. Abdel-Razzaq, R. Kwong, I. Tysba, M. Bortz, B. Mui, R. Bau, M. E. Thompson, *Inorganic Chemistry*, **40**, 704 (2001);
- 189.** a) F. Neve, A. Crispini, *European Journal of Inorganic Chemistry*, **2000**, 1039 (2000); b) D. Di Censo, S. Fantacci, F. De Angelis, C. Klein, N. Evans, K. Kalyanasundaram, H. J. Bolink, M. Graetzel, *Inorganic Chemistry*, **47**, 980 (2008);
- 190.** K. A. King, P. J. Spiliane, R. J. Watts, *Journal of the American Chemical Society*, **107**, 1431 (1985);

- 191.** R. Ragni, E. A. Plummer, K. Brunner, J. W. Hofstraat, F. Babudri, G. F. Farinola, F. Naso, L. De Cola, *Journal of Materials Chemistry* **16**, 161 (2006); Y. J. Su, H. L. Huang, C. L. Li, et al., *Advanced Materials*, **15**, 884 (2003); G. Y. Park, Y. Kim, Y. Ha, *Molecular Crystals Liquid Crystals*, **462**, 179 (2007); J. Otsuki, T. Tokimoto, Y. Noda, H. Tomohiro, C. Takeshi, X. Chen, Y. Okamoto., *Chemistry-A European Journal*, **13**, 2311 (2007); K. Ono, M. Joho, K. Saito, et al. *European Journal of Inorganic Chemistry*, **2006**, 3676 (2006); H. C. Bottcher, M. Graf, H. Kruger, C. Wagner, *Inorganic Chemical Communications*, **8**, 278 (2005);
- 192.** a) C. Zhou, W.-Y. Wong, B. Yao, Z. Xie, L. Wang, *Angewandte Chemie International Edition*, **46**, 1149 (2007); b) Y. You, C.-G. An, D.-S. Lee, J.-J. Park, S. Y. Park, *Journal of Materials Chemistry*, **46**, 4706 (2006); S. Bettington, M. Tavasli, et al., *Chemistry-A European Journal*, **13**, 1423 (2007);
- 193.** L. Chen, C. Yang, J. Qin, J. Gao, H. You, D. Ma, *Journal of Organometallic Chemistry*, **691**, 3591 (2006);
- 194.** X.-Y. Wang, R. N. Prabhu, R. H. Schmel, M. Weck, *Macromolecules*, **39**, 3140 (2006); X.-Y. Wang, A. Kimyonok, M. Weck, *Chemical Communications*, **2006**, 3933 (2006);
- 195.** K. Dedeian, J. Shi, N. Shepard, E. Forsythe, D. C. Morton, *Inorganic Chemistry*, **44**, 4445 (2005);
- 196.** A. B. Tamayo, B. D. Alleyne, P. I. Djurovic, P. I. Djurovic, S. lamansky, I. Tysba, N. N. Ho, R. Bao, M. E. Thompson, *Journal of the American Chemical Society*, **125**, 7377 (2003);
- 197.** A. J. Wilkinson, H. Puschmann, J. A. K. Howard, C. E. Forster, J. A. G. Williams, *Inorganic Chemistry*, **43**, 8685 (2006);
- 198.** H. J. Bolink, E. Coronado, S. G. Santamaria, M. Sessolo, N. Evans, C. Klein, E. Baranoff, K. Kalyansundaram, M. Gaetzel, M. K. Nazeeruddin, *Chemical Communications*, **2007**, 3249 (2007);
- 199.** S. Ladouceur, S. Zysman-Colman, *European Journal of Inorganic Chemistry*, **17**, 2985, (2013);
- 200.** M. Yu, Q, Zhao, L. Shi, et al., *Chemical Communications*, **2008**, 2115 (2008);
- 201.** H. J. Bolink, L. Cappelli, E. Coronado, M. Graetzel, E. Ortì, R. D. Costa, P. M. Vinuela, M. K. Nazeeruddin, *Journal of the American Chemical Society*, **128**, 14786 (2006);

- 202.** M. K. Nazeeruddin, R. T. Wegeh, Z. Zhou, C. Kein, Q. Wang, F. De Angelis, S. Fantacci, M. Graetzel, *Inorganic Chemistry*, **45**, 9245 (2006);
- 203.** L. Xiao, Z. Chen, B. Qu, J. Luo, S. Kong, Q. Gong, J. Kido, *Advanced Materials*, **23**, 926 (2011);
- 204.** R. D. Costa, E. Orti, H. J. Bolink, F. Monti, G. Accorsi, N. Armaroli, *Angewandte Chemie International Edition*, **51**, 8178 (2012);
- 205.** F. Dumur, D. Bertin, D. Gigmes, *International Journal of Nanotechnology*, **9**, 377-395 (2012);
- 206.** Z. Liu, Z. Bian and C. Huang, *Top Organometallic Chemistry*, **28**, 113 (2010);
- 207.** a) M. Mauro, K. C. Schermann, R. Pretot, R. Pretot, A. Hafner, P. Mercandelli, A. Sironi, L. De Cola, *Angewandte Chemie International Edition*, **49**, 1222 (2010); b) M. K. Nazeeruddin, E. D. Baranoff, M. Graetzel, Complex salts for light emitting devices, World patent WO2010089393 A2;
- 208.** M. L. H. Green, A. Hamnett, J. Qin, P. Baird, J. A. Bandy, K. Prout, E. Marseglia, S. D. Obertelli, *Journal of the Chemical Society, Chemical Communications*, 1809 (1987)
- 209.** a) C. Wu, H.-F. Chen, K.-T. Wong, M. E. Thompson, *Journal of the American Chemical Society*, **132**, 3133 (2010); b) G. Nasr, A. Guerlin, F. Dumur, L. Beouch, E. Dumas, G. Clavier, F. Miomandre, F. Goubard, D. Gigmes, D. Bertin, G. Wantz and C.R. Mayer, *Chemical Communications*, **47**, 10698 (2011); c) F. Dumur, G. Nasr, G. Wantz, C.R. Mayer, E. Dumas, A. Guerlin, F. Miomandre, G. Clavier, D. Bertin and D. Gigmes, *Organic Electronics*, **12**, 1683 (2011); d) M. K. Nazeeruddin, R. Humphrey-Baker, D. Berner, S. Rivier, L. Zuppiroli, M. Graetzel, *Journal of the American Chemical Society*, **125**, 8790 (2003);
- 210.** E. I. Szerb, A. Ionescu, N. Godbert, Y. J. Yadav, A. M. Talarico, M. Ghedini, *Inorganic Chemistry Communications*, **37**, 80 (2013);
- 211.** C. G. Pierpont, *Coordination Chemistry Reviews*, **219-221**, 415 (2001);
- 212.** F. Blasberg, M. Bolte, H.-W. Lerner, M. Wagner, *Organometallics*, **31**, 3213 (2012);
- 213.** A. M. Talarico, E. I. Szerb, T. F. Mastropietro, I. Aiello, A. Crispini, M. Ghedini, *Dalton Transactions*, **41**, 4919 (2012);
- 214.** W. J. Geary, *Coordination Chemistry Reviews*, **7**, 81 (1971);

215. B. Hirani, J. Li, P. I. Djurovich, M. Yousufuddin, J. Oxgaard, P. Persson, S.R. Wilson, R. Bau, W.A. Goddard III, M.E. Thompson, *Inorganic Chemistry*, **46**, 3865 (2007);
216. a) P. Barbaro, B. Claudio, K. Linn, C. Mealli, A. Meli, F. Vizza, F. Laschi, P. Zanello, *Inorganica Chimica Acta*, **198–200**, 31 (1992); b) P. Barbaro, C. Bianchini, C. Mealli, A. Meli, *Journal of the American Chemical Society*, **113**, 3181 (1991); c) A. Bencini, E. Bill, F. Mariotti, F. Totti, A. Scorzzafava, A. Vargas, *Inorganic Chemistry*, **39**, 1418 (2000);
217. A. Ruggi, M. Mauro, F. Polo, D.N. Reinhoudt, L. De Cola, A.H. Velders, *European J. Inorganic Chemistry*, **2012**, 1025 (2012);
218. T. Grygar, S. Kuckova, D. Hradil, D. Hradilova, *Journal of Solid State Electrochemistry*, **7**, 706 (2003);
219. J. B. Birks, *Excimers, Reports Progress Physics*, **38**, 903 (1975);
220. a) B. Schmid, F.O. Garces, R. J. Watts, *Inorganic Chemistry*, **33**, 9 (1994); b) D. L.Ma, W. L.Wong, W. H. Chung, F.Y. Chan, P.-K. So, T. S. Lai, Z. Y. Zhou, Y. C. Leung, K.Y. Wong, *Angewandte Chemie International Edition*, **47** 3735 (2008);
221. (a) M. Epstein, S. Yariv, *J. Colloid Interface Science*, **263**, 377 (2004); b) A. Del Medico, E. S. Dodsworth, A. B. P. Lever, W. J. Pietro, *Inorganic Chemistry*, **43**, 2654 (2004);
222. a) S.-J. Yun, H.-J. Seo, M. Song, S.-H. Jin, S. K. Kang, Y.-I. Kim, *Journal of Organometallic Chemistry*, **724**, 244 (2013); b) R. Zhu, J. Lin, G.-A. Wen, S.-J Liu, J.-H. Wan, J.-C. Feng, Q.-L Fan, G.-Y. Zhong, W. Wei, W. Huang, *Chemistry Letters*, **34**, 1668 (2005);
223. a) G. Maistralis, A. Koutsoodimou, N. Katsaros, *Transition Metal Chemistry*, **25**, 166 (2000); b) R. Hilal, Z.M. Zaky, S.A.K. Elroby, *Spectrochimica Acta Part A*, **63**, 740 (2006); c) S. L. James, D. M. P. Mingos, X. Xu, A. J. P. White, D. J. Williams, *Dalton Transactions*, **27**, 1335 (1998);
224. Y. Ohsawa, S. Sprouse, K. A. King, M. K. DeArmond, K. W. Hanck, R. J. Watts, *Journal of Physical Chemistry*, **91**, 1047 (1987);
225. S. Jung, Y. Kang, H.-S. Kim, Y.-H. Kim, C.-L. Lee, J.-J. Kim, S.-K. Lee, and S.-K. Kwon, *European Journal of Inorganic Chemistry*, **2004**, 3415 (2004);
226. Y. You, S. Y. Park, *Dalton Transactions*, **38**, 1267 (2009);



227. a) T. F. Mastropietro, Y. J. Yadav, E. I. Szerb, A. M. Talarico, M. Ghedini, A. Crispini, *Dalton Transactions*, **41**, 8899 (2012); b) Y.J. Yadav, B. Heinrich, G. De Luca, A. M. Talarico, T. Mastropietro, M. Ghedini, B. Donnio, E. I. Szerb, *Advanced Optical Materials*, **1**, 844 (2013);
228. F. O. Garces, K. A. King, R. J. Watts, *Inorganic Chemistry*, **27**, 3464 (1988);
229. a) K. R. Schwartz, R. Chitta, J. N. Bohnsack, D. J. Ceckanowicz, P. Mirò, C. J. Cramer and K.R. Mann, *Inorganic Chemistry*, **51**, 5082 (2012); b) S. Ladouceur, D. Fortin, E.Zysman-Colman, *Inorganic Chemistry*, **50**, 11514 (2011);
230. a) B. Valeur, *Molecular Fluorescence: Principle and Application*; Wiley-VCH: Weinheim, Germany (2002); b) Lakowicz J.R., *Principle of Fluorescence Spectroscopy*; Kluwer Academic/Plenum Publishers: New York, 1999;
231. H-F. Chen, C. Wu, M-C. Kuo, M.E. Thompson and K-T. Wong, *Journal of Materials Chemistry*, **22**, 9556 (2012);
232. H. Sasabe, J. Kido, *Chemistry of Materials*, **23**, 621 (2011); Y. Shirota, H. Kageyama, *Chemistry Reviews*, **107**, 953 (2007);
233. C. L. Yang, X. W. Zhang, H. You, L. Y. Zhu, L. Q. Chen, L. N. Zhu, Y. T. Tao, D. G. Ma, Z. G. Shuai, J. G. Qin, *Advanced Funcional Materials*, **17**, 651 (2007);
234. M. A. Baldo, C. Adachi, S. R. Forrest, *Physical Review B*, **62**, 10967 (2000); X. Gong, J. C. Ostrowski, G. C. Bazan, D. Moses, A. J. Heeger, M. S. Liu, A. K.-Y. Jen, *Advanced Materials*, **15**, 45 (2003);
235. a) P. T. Furuta, L. Deng, S. Garon, M. E. Thompson, J. M. J. Frechet, *Journal of the American Chemical Society*, **126**, 15388 (2004); b) M.-J. Park, J. Lee, J. Kwak, I. H. Jung, J.-H. Park, H. Kong, C. Lee, D.-H. Hwang, H.-K. Shim, *Macromolecules*, **42**, 5551 (2009); c) F. Xu, H. U. Kim, D. Mi, J. M. Lim, J. H. Hwang, N. S. Cho, J-L Lee, D.-H. Hwang, *Bulletin of the Korean Chemical Society*, **34**, 39 (2013);
236. a) G. L. Schulz, X. Chen, S.-A. Chen, S. Holdcroft, *Macromolecules*, **39**, 9156 (2006); b) H. Zhen, W. Xu, W. Yang, Q. Chen, Y. Xu, J. Jiang, J. Peng, Y. Cao, *Macromolecuar Rapid Communications*, **27**, 2095 (2006); c) K. Zhang, Z. Chen, C. Yang, Y. Tao, Y. Zou, S. Gong, J. Qin, Y. Cao, *Journal of Materials Chemistry*, **18**, 291 (2008);

- 237.** a) R. Guan, Y. Xu, L. Ying, W. Yang, H. Wu, Q. Chen, Y. Cao, *Journal of Materials Chemistry*, **19**, 531 (2009); b) F. Xu, D. Mi, H.-R. Bae, M.-C. Suh, U.-C. Yoon, D.-H. Hwang, *Bulletin of the Korean Chemical Society*, **34**, 9 (2013); c) A.-H. Liang, S. Dong, K. Zhang, X. Xiao, F. Huang, X.-H. Zhu, Y. Cao, *Macromolecular Rapid Communications*, **34**, 130 (2013); d) W. Cho, N. S. Karthikeyan, S. Kim, S. Kim, Y.-S. Gal, J. W. Lee, S.-H. Jin, *Synthetic Metals*, **175**, 68 (2013);
- 238.** Y. Zhang, M. Song, L. Huang, *Journal of Luminescence*, **132**, 2242 (2012);
- 239.** C. Fan, L. Zhu, B. Jiang, Y. Li, F. Zhao, D. Ma, J. Qin, C. Yang, *Journal of Physical Chemistry C*, **117**, 19134 (2013);
- 240.** G. M. Sheldrick, SADABS, Version 2.10, Bruker AXS Inc., Madison, WI, USA, 2003; SHELXTL-NT, Version 5.1, Bruker Analytical X-ray Systems Inc., 1999;
- 241.** J. Pommerehne, H. Vestweber, W. Guss, R. F. Mahrt, H. Bassler, M. Porsch, J. Daub, *Advanced Materials*, **7**, 555 (1995);
- 242.** a) Y. S. Gerasymchuk, V. Y. Chernii, L. A. Tomachynskii, M. Kowalska, J. Legendziewics. St. Radzki, *Optical Materials*, **32**, 1193 (2010); b) M. Gervaldo, M. Funes, J. Durantini, L. Fernandez, F. Fungo, L. Otero, *Electrochimica Acta*, **55**, 1948 (2010);
- 243.** a) J. W. Ondersma, Thomas W. Hamann, *Coordination Chemistry Reviews*, **257**, 1533 (2013); b) E. A. Gibson, A. L. Smeigh, L. Le Pleux, et al., *Journal of Physical Chemistry C*, **115**, 9772 (2011);
- 244.** C. H. Law, S. C. Pathirana, X. Li, A. Y. Anderson, P. R. F. Barnes, A. Listorti, T. H. Ghaddar, B. C. O' Regan *Advanced Materials*, **22**, 4505 (2010);
- 245.** M. Wang, C. Grätzel, S. M. Zakeeruddin, M. Grätzel, *Energy Environmental Science*, **5**, 9394 (2012);
- 246.** D. P. Hagberg, X. Jiang, E. Gabrielsson, M. Linder, T. Marinado, T. Brinck, A. Hagfeldt, L. Sun, *Journal of Materials Chemistry*, **19**, 7232 (2009);

## Acknowledgments

During these three years, I received a constant support from my supervisors and my colleagues.

I am very grateful to Prof. Mauro Ghedini for guiding me with his knowledge and his experience and to Dr. Nicolas Godbert for his continuous innovative ideas and constructive comments. They have decisively improved my research work. Moreover, I want to thank them both for sharing with me their passion for Chemistry.

I would like to thank Dr. Petra Cameron and Prof. Laurence Peter from the University of Bath (U.K.) for allowing me to spend four useful months in their group.

Heartfelt acknowledgments go to all people from the CEMIF.Cal group with whom I have profitably collaborated: Dr. Iolinda Aiello, Prof. Alessandra Crispini, Prof. Attilio Golemme, Raffaella Lento, Dr. Upendra K. Pandey, Dr. Elisabeta Szerb, Dr. Anna Maria Talarico, Dr. Roberto Termine and Dr. Yogesh J. Yadav.

Special thanks to Prof. Daniela Pucci and Dr. Massimo La Deda and to my colleagues and friends Caterina Tone, Barbara Sanz, Loredana Ricciardi, Eugenia Giorno & Emanuela Gionfriddo, Teresa Mastropietro, Paola Liguori, Sante Pirillo, and Luigi Rizzuti.

Finally, thanks to all the people, family and friends who stood by me day after day.

## List of publications

1. A. Ionescu, E. I. Szerb, Y. J. Yadav, A. M. Talarico, M. Ghedini and N. Godbert, "Orotate containing anionic luminescent Iridium(III) complexes and their use in soft salts", *Dalton Trans.*, DOI: 10.1039/c3dt52077c;
2. E. I. Szerb, A. Ionescu, N. Godbert, Y. J. Yadav, A. M. Talarico and M. Ghedini, "Anionic cyclometallated Iridium(III) complexes containing substituted bivalent orthohydroquinones", *Inorg. Chem. Commun.*, **37**, 80-83 (2013);
3. A. Ionescu, N. Godbert, A. Crispini, R. Termine, A. Golemme and M. Ghedini, "Photoconductive Nile Red Cyclopalladated Metallomesogens", *J. Mater. Chem.*, **22**, 23617–23626 (2012);
4. A. Ionescu, N. Godbert, I. Aiello, A. Crispini and M. Ghedini, "Neutral and Cationic Cyclopalladated Nile Red Complexes and Metallomesogens: Synthesis and Characterization", *Mol. Cryst. Liq. Cryst.*, **558**, 84-92 (2012);
5. U. K. Pandey, R. Termine, A. Ionescu, N. Godbert, M. P. De Santo, M. Ghedini and A. Golemme, "Enhancement of exciton dissociation efficiency in bulk heterojunction solar cell by using an intrinsic photoconductor component", *Mol. Cryst. Liq. Cryst.*, **558**, 148-159 (2012);